NUREG/CR-6511, Vol. 9
ANL-01/26

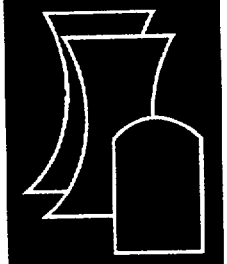

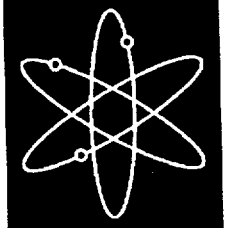

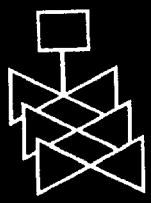

Steam Generator Tube Integrity Program

Semiannual Report October 1999 — March 2000

Argonne National Laboratory

U.S. Nuclear Regulatory Commission
Office of Nuclear Regulatory Research
Washington, DC 20555-0001

AVAILABILITY OF REFERENCE MATERIALS IN NRC PUBLICATIONS

NRC Reference Material

As of November 1999, you may electronically access NUREG-series publications and other NRC records at NRC's Public Electronic Reading Room at www.nrc.gov/NRC/ADAMS/index.html.
Publicly released records include, to name a few, NUREG-series publications; *Federal Register* notices; applicant, licensee, and vendor documents and correspondence; NRC correspondence and internal memoranda; bulletins and information notices; inspection and investigative reports; licensee event reports; and Commission papers and their attachments.

NRC publications in the NUREG series, NRC regulations, and *Title 10, Energy*, in the Code of *Federal Regulations* may also be purchased from one of these two sources.

1. The Superintendent of Documents
   U.S. Government Printing Office
   Mail Stop SSOP
   Washington, DC 20402–0001
   Internet: bookstore.gpo.gov
   Telephone: 202-512-1800
   Fax: 202-512-2250
2. The National Technical Information Service
   Springfield, VA 22161–0002
   www.ntis.gov
   1–800–553–6847 or, locally, 703–605–6000

A single copy of each NRC draft report for comment is available free, to the extent of supply, upon written request as follows:

Address: Office of the Chief Information Officer,
Reproduction and Distribution
Services Section
U.S. Nuclear Regulatory Commission
Washington, DC 20555-0001
E-mail: DISTRIBUTION@nrc.gov
Facsimile: 301–415–2289

Some publications in the NUREG series that are posted at NRC's Web site address www.nrc.gov/NRC/NUREGS/indexnum.html are updated periodically and may differ from the last printed version. Although references to material found on a Web site bear the date the material was accessed, the material available on the date cited may subsequently be removed from the site.

Non-NRC Reference Material

Documents available from public and special technical libraries include all open literature items, such as books, journal articles, and transactions, *Federal Register* notices, Federal and State legislation, and congressional reports. Such documents as theses, dissertations, foreign reports and translations, and non-NRC conference proceedings may be purchased from their sponsoring organization.

Copies of industry codes and standards used in a substantive manner in the NRC regulatory process are maintained at—

The NRC Technical Library
Two White Flint North
11545 Rockville Pike
Rockville, MD 20852–2738

These standards are available in the library for reference use by the public. Codes and standards are usually copyrighted and may be purchased from the originating organization or, if they are American National Standards, from—

American National Standards Institute
11 West 42nd Street
New York, NY 10036–8002
www.ansi.org
212–642–4900

Legally binding regulatory requirements are stated only in laws; NRC regulations; licenses, including technical specifications; or orders, not in NUREG-series publications. The views expressed in contractor-prepared publications in this series are not necessarily those of the NRC.

The NUREG series comprises (1) technical and administrative reports and books prepared by the staff (NUREG–XXXX) or agency contractors (NUREG/CR–XXXX), (2) proceedings of conferences (NUREG/CP–XXXX), (3) reports resulting from international agreements (NUREG/IA–XXXX), (4) brochures (NUREG/BR–XXXX), and (5) compilations of legal decisions and orders of the Commission and Atomic and Safety Licensing Boards and of Directors' decisions under Section 2.206 of NRC's regulations (NUREG–0750).

NUREG/CR-6511, Vol. 9
ANL-01/26

Steam Generator Tube Integrity Program

Semiannual Report October 1999 — March 2000

Manuscript Completed: October 2001
Date Published: June 2002

Prepared by
D. R. Diercks, S. Bakhtiari, K. E. Kasza, D. S. Kupperman,
S. Majumdar, J. Y. Park, W. J. Shack

Argonne National Laboratory
9700 South Cass Avenue
Argonne, IL 60439

J. Muscara, NRC Project Manager

Prepared for
Division of Engineering Technology
Office of Nuclear Regulatory Research
U.S. Nuclear Regulatory Commission
Washington, DC 20555-0001
NRC Job Code W6487

NUREG/CR-6511, Volume 9, has been reproduced from the best available copy.

Steam Generator Tube Integrity Program
Semiannual Report October 1999–March 2000

by

D. R. Diercks, S. Bakhtiari, K. E. Kasza, D. S. Kupperman,
S. Majumdar, J. Y. Park, and W. J. Shack

Abstract

This report summarizes work performed by Argonne National Laboratory on the Steam Generator Tube Integrity Program for the period October 1999 through March 2000. The program is divided into five tasks: (1) Assessment of Inspection Reliability, (2) Research on ISI Technology, (3) Research on Degradation Modes and Integrity, (4) Development of Methodology and Technical Requirements for Current and Emerging Regulatory Issues, and (5) Program Management. Under Task 1, progress is reported on the round-robin analysis of the steam generator tube mockup, in which a total of seven teams have participated to date. The format for the tables necessary to carry out the statistical analysis of the round-robin data has also been established. Activities under Task 2 were concerned primarily with multiparameter analysis of eddy current NDE results. Calculations were performed on the applicability of pseudoinverse filters for improving the spatial resolution of rotating probes, analytical procedures for the elimination of unwanted signals were explored, the conversion of data analysis results into calibrated profiles for more direct deduction of estimated flaw size and extent was examined, and inspection data obtained from laboratory-degraded tubes were analyzed. Under Task 3, the production and characterization of laboratory-degraded tubes continued. Further testing of tubes with electro-discharge machined and laser-cut notches, as well as laboratory-degraded tubes, was carried out in the High-Pressure Test Facility, and an exploratory test was conducted to evaluate the potential for erosion resulting from a jet of water from a leaking tube impinging on an adjacent tube, Finally, a model was developed to calculate crack-opening area as a function of time for axial cracks under severe-accident conditions, and the ligament-rupture behavior observed in laboratory tests on tubes with EDM and laser-cut notches was modeled.

Contents

Figures

Tables

Executive Summary

Assessment of Inspection Reliability

A steam generator mock-up has been assembled under Task 1 for round-robin studies that use currently practiced techniques and commercial teams. The mock-up will also be used as a test bed for evaluating emerging technologies for the ISI of SG tubes. The completed mock-up tube bundle consists of nine levels, each consisting of 400 Alloy 600 test sections, each 0.3 m (1 ft.) long. Above the ninth level is a 0.91-m (3-ft.)-long run-out section. In addition to stress corrosion cracks (SCCs), test sections with dents (cracked and uncracked) have been installed in levels with tube support plate (TSP) simulations. Magnetite in the tube support plate crevice was simulated by filling the crevice with magnetic tape or a ferromagnetic fluid. A mixture of magnetite and copper simulates sludge deposits.

Input from the NDE Task Group was used to ensure that the set of round robin documents are representative of a field inspection. The documents cover all aspects of an eddy current inservice inspection and include the analysis guideline, the data collection guideline degradation assessment and technique qualification, training manual, and Examination Technique Specification Sheets (ETSS).

The round-robin analysis began on January 10, 2000. One team was from FTI in Lynchburg, VA, a second team from FTI in Benicia, CA, and a third team from ABB-CE in Chattanooga, TN. Four more teams participated in February: two from Zetec, one from Anatec, and one from KAITEC of South Korea. Teams participating in the round-robin had to commit seven or eight working days to complete the data analysis. Before evaluating the round-robin data, the analysts were provided with a training manual, received additional training at their site, and were required to pass a site-specific exam. Argonne proctors administered the exam and monitored the data analysis process.

A review has been conducted of the bobbin coil voltages for axial OD indications at TSPs that were called by the teams analyzing the mock-up data. In most cases, variations in the voltages identified by the teams were fairly small. The cumulative distribution of the normalized standard deviations can be fit well by a Weibull distribution. For almost 85% of all indications, the normalized standard deviation in the reported voltages is less than 0.1. Indications with larger variations are not associated with particularly low or high voltages, but rather with the complexity of the signal and the difficulty of identifying the peak voltage.

The format for the tables necessary to carry out the statistical analysis has been established. Five tables are required. One is the Flaw Table, which identifies every flaw in mock-up. The second table is the Grading Unit Table, which divides up the mock-up and provides the location and dimension of each segment of the mock-up to be graded. Next is the Inspection Table, which provides the detailed information regarding the inspection being graded. The fourth is the Indication Table, which provides the essential information from the inspection. The final table is the Scoring Table, in which each row describes how a particular inspection team performed on a grading unit.

Research on ISI Technology

Task 2 activities during the present reporting period were concerned primarily with multiparameter analysis of eddy current (EC) NDE results. Sample calculations are presented in a follow-up study to demonstrate the applicability of pseudoinverse filters for improving the spatial resolution of rotating probes. Recent investigations have in part dealt with evaluating the effectiveness of approximate deconvolution methods for enhancing the spatial resolution and, in turn, sizing accuracy for crack-like indications. The deconvolution scheme has been incorporated into a rule-based multiparameter data analysis algorithm. Preliminary results are provided on a limited set of laboratory-grown specimens with axial and circumferential OD/ID cracking; they suggest that improved spatial resolution and sizing accuracy could be achieved through proper application of pseudoinverse filters. More extensive studies in this area are currently underway and the results will be provided in our future reports.

Preliminary results are presented on another study that was undertaken to explore potential advantages of two-dimensional (2-D) suppression over conventional 1-D mix schemes for elimination of unwanted signals. Preliminary test case results are presented from an ongoing investigation on the application of signal decomposition and factor analysis techniques for selective suppression of unwanted indications from rotating probe data. Initial studies suggest that 2-D multiple-frequency factor-based techniques could provide substantial improvement over conventional 1-D mix procedures for the analysis of EC rotating probe inspection data. Preliminary evaluation of the two techniques discussed here was based on analyses of simulated composite signals from a rotating probe that were produced from the available readings on a calibration standard.

Initial evaluations on conversion of data analysis results into calibrated profiles for more direct deduction of estimated flaw size and extent are also discussed in this report. Selected test cases from a data set that was analyzed earlier were used for this purpose. Modifications and refinements of computer codes that facilitate more convenient display of the sizing results are briefly discussed here. Representative test cases on analyses of laboratory-grown specimens exhibit the current state of graphical display of the sizing results. Further refinement of display routines is underway to allow for direct comparison of NDE with destructive examination profiles in a more practical manner.

Samples are currently being manufactured under Task 3 to augment the library of tubes for NDE studies with a wider range of degradation morphologies. Flaw types in these tubes are, in general, representative of those incorporated into the ANL tube bundle mock-up. Results are presented in this report on analyses of rotating probe inspection data from three separate batches of laboratory-grown specimens. Manufactured flaws in the first batch of tubes were composed primarily of circumferential cracks and those in the second batch of axially oriented cracking. A collection of 31 tubes was also produced recently to carry out blind studies to help further assess the performance of alternate data analysis schemes to detect and size SG tubing degradations. Initial results on analyses of NDE data from this set of tubes are presented. A more detailed description of ongoing investigations on the analysis of multiple-frequency eddy current rotating probe data will be provided in our subsequent reports.

Research on Degradation Modes and Integrity

Production of laboratory-degraded 22.2-mm (7/8-in.)-diameter Alloy 600 tube specimens continued using material from three heats. The cracking is accomplished using a 1M aqueous solution of sodium tetrathionate at room temperature and atmospheric pressure. The material was first mill-annealed for 2-3 min at 940-1060°C, depending upon the material heat. All specimens were then sensitized by heat-treating at 600°C (1112°F) for 48 h prior to exposure to the sodium tetrathionate solution to produce a susceptible microstructure. During this reporting period, 101 tubes were processed in an attempt to produce axial outer diameter stress corrosion cracking, or ODSCC (76 specimens), axial inner diameter stress corrosion cracking, or IDSCC (12 specimens), circumferential ODSCC (5 specimens), and circumferential IDSCC (8 specimens). Four of the specimens were dented tubes (25-100 μm [1-4 mils]-deep semicircular dents on the OD).

To accelerate cracking, some of the specimens from one heat were additionally solution-heat-treated at 1010-1100°C for 10-20 min before the sensitization heat treatment at 600°C for 48 h. The specimens that received this high-temperature solution heat treatment cracked in shorter times than those without the solution heat treatment. However, this solution heat treatment caused a reduction in flow stress of up to ≈20%. The sensitization heat treatment at 600°C for 48 h did not weaken the material.

The cracked tubes were examined by eddy current NDE and dye-penetrant techniques. Following this, the laboratory-degraded tubes were destructively analyzed to provide detailed comparisons with the eddy current NDE measurements. The cracks were opened by internal pressurization and examined macroscopically and by scanning electron microscopy (SEM). The samples were heat tinted prior to loading to permit differentiation of the SCC surface from that produced by subsequent fracture during opening. Detailed results from all of these examination procedures are presented.

The heat treatments used to make the tubes more susceptible to SCC can influence the electromagnetic properties of the material and thus the baseline EC signal and signal-to-noise ratio. However, this problem is not evident when using mag-biased BC and +Point probes, except for a small baseline shift with the BC probe.

At the beginning of this reporting period, efforts focused on additional testing of Alloy 600 tubes with OD axial EDM notches in the High-Pressure Test Facility. More than forty 22.2-mm (7/8-in.)-diameter flawed tubes of several different designs were fabricated and tested, with some flaw geometries made in triplicate to evaluate test reproducibility. The EDM notches were all 0.19 mm (0.0075 in.) wide and had lengths of 6.35, 12.7, 19.1, and 25.4 mm (0.25, 0.5, 0.75, and 1.0 in.), and most had uniform depths of 60, 80, 90, and 100% TW. However, some axial notches of nonuniform depth were also tested. These tests generated information on the influence of various test parameters such as flaw geometry, bladder/backup foil characteristics, and pressurization rate on flaw behavior. The data indicate that under some conditions, flaw tearing pressure and opening area can be quite sensitive to pressurization rate and bladder/backup foil characteristics.

After testing the EDM flaws, 24 Alloy 600 tubes were pressure-tested with a variety of laser-cut OD flaws in the High-Pressure Test Facility. The flaws included simple single axial and circumferential notches, as well as complex OD patterns of axial and circumferential

notches separated by various ligament sizes. Ten different generic flaw geometries were evaluated. The laser-cutting technique permits considerably more complex flaws to be fabricated than are possible using EDM, and the flaws are also considerably tighter than EDM notches. The data obtained address the question of how far apart multiple cracks must be to behave as individual noninteracting flaws without creating a larger zone of greater weakness. The laser-cut tubes were first subjected to Stage 1 testing, which consisted of pressurization at a quasi-steady-state rate without the use of internal bladders until ligament tearing occurred. This was followed, where possible, by Stage 2 testing in which the specimens were pressurized to unstable burst with the aid of internal bladders and reinforcing foils as needed. Thus, for most of the specimens, this combination of tests yielded data on ligament tearing pressure, leak rate at ligament tearing, and unstable burst pressure for the variety of flaw configurations tested.

Tests were also conducted on 14 laboratory-degraded tubes with SCC flaws in the High-Pressure Test Facility. These tubes contained flaws of several types, including OD axial and circumferential cracks and combinations of these types, as well as OD flaws in the roll transition. The tubes underwent extensive pretest characterization, pressure testing, and posttest examination using metallographic and fractographic techniques to characterize the flaw morphologies. The overall goal of this series of tests was to relate pretest NDE information to failure behavior and the actual crack morphologies and improve the techniques for predicting leak and burst pressures. The tubes were tested without bladders by using a quasi-steady pressurization rate involving 0.69 MPa (100 psi) increments in pressure with a 10-s hold before each increase. Data on pressure at first leak, leak flow rate vs. pressure differential, and pressure for sudden flaw opening and unstable tearing (if observed) were also obtained.

Finally, an exploratory test was conducted to evaluate the potential for erosion resulting from a jet of water from a leaking tube impinging on an adjacent tube. The test was conducted in the High-Pressure Test Facility at room temperature using a single-phase water jet issuing from a sharp-edged circular orifice of 0.79 mm (1/32-in.) diameter under 17.2 MPa (2500 psi) pressure. The leak rate for this test was held constant for the 4-h duration of the experiment and was measured to be 3.6 L/min (0.95 gpm), which corresponds to a jet velocity of about 116 m/s (380 ft/s). Evidence of slight erosion was seen. This surface erosion is undergoing further evaluation, and additional tests will be conducted with single-phase water and with a steam/liquid combination under main steam line break elevated-temperature conditions in the high-temperature Pressure and Leak-Rate Test Facility.

To determine the leak rate after throughwall penetration of axial cracks during severe accidents, it is necessary to estimate the crack opening area as a function of time. A simple model is proposed to calculate the crack opening area as a function of time. It is derived by analogy from a model that is applicable to cracks in a rectangular plate. A total of six isothermal and nonisothermal tests were conducted to validate the approach. The model was used to analyze crack opening area for tubes subjected to SBO Case 6RU transient. The analysis shows that for a final temperature of ≥750°C, throughwall cracks greater than 15 mm (0.6 in.) long will have crack opening areas that are greater than the tube cross-sectional flow area of a 22.2-mm (7/8-in.)-diameter tube.

Pressure tests at room temperature were conducted on notched tubes in the ANL High-Pressure Test Facility. In addition to part-throughwall EDM notches, laser-cut notches were used. The widths of the laser-cut notches were significantly less than the 0.19-mm

(0.0075–in.)-wide EDM notches. A significant number of specimens with short and deep notches were tested. The tests showed that the ligament rupture pressures of the laser-cut notches were within but at the lower end of the scatter band of the EDM notch data. The factor β used in the ANL correlation for m_p was updated on the basis of the tests. It was determined that either $k = 0.55$ and $\beta = 1$ or $k = 0.595$ and $\beta = 0.83$ give reasonable predictions for the ligament rupture pressures (k is the flow stress factor). However, $k = 0.55$ gives more accurate predictions for unstable burst pressures of throughwall notches than $k = 0.595$.

Acknowledgments

The authors gratefully acknowledge the contributions of J. E. Franklin, L. Knoblich, D. R. Perkins, and C. W. Vulyak to the experimental work described in this report. This work is sponsored by the Office of Nuclear Regulatory Research, U.S. Nuclear Regulatory Commission, under Job Code W6487; Program Manager: Dr. J. Muscara, who provided helpful guidance in the performance of this work.

Acronyms and Abbreviations

1-D	one-dimensional
2-D	two-dimensional
ABBCE	ASEA Brown-Boveri Combustion Engineering
AECL	Atomic Energy of Canada, Ltd.
ANL	Argonne National Laboratory
BC	bobbin coil
DTI	distorted tube support plate indication
EC	eddy current
EDM	electrodischarge machining
EM	electromagnetic
EPRI	Electric Power Research Institute
ETSS	examination technique specification sheet
FTI	Framatome Technologies, Inc.
ID	inner diameter
IDSCC	inner diameter stress corrosion cracking
IGA	intergranular attack
IGSCC	intergranular stress corrosion cracking
ISG-TIP-2	International Steam Generator Tube Integrity Program—2
ISI	inservice inspection
LOD	longitudinal/axial outer diameter
LS	least squares
MRPC	motorized rotating pancake coil
NDE	nondestructive evaluation
NQI	nonquantifiable indication
NRC	U.S. Nuclear Regulatory Commission
OD	outer diameter
ODSCC	outer-diameter stress corrosion crack/cracking
PNNL	Pacific Northwest National Laboratory
POD	probability of detection
PWR	pressurized water reactor
PWSCC	primary-water stress corrosion cracking
QDA	qualified data analyst
RR	round-robin
RT	room temperature
SCC	stress corrosion cracking
SEM	scanning electron microscopy
SG	steam generator
S/N	signal-to-noise ratio
SS	stainless steel
SSPD	site-specific performance documentation
SVD	singular value decomposition
TSP	tube support plate
TW	throughwall
UT	ultrasonic testing

1 Introduction

The objective of this program is to provide the experimental data and predictive correlations and models needed to permit the U.S. Nuclear Regulatory Commission (NRC) to independently evaluate the integrity of steam generator (SG) tubes as plants age and degradation proceeds, new forms of degradation appear, and new defect-specific management schemes are implemented. The areas addressed by the program include assessment of procedures and equipment used for inservice inspection (ISI) of SG tubes, and recommendations for criteria and requirements to improve the reliability and accuracy of ISI; validation and improvement of correlations and models that are used to evaluate integrity and leakage of degraded SG tubes; and validation and improvement of correlations and models that predict the generation and progression of degradation in SG tubes as a function of aging.

This program is divided into four technical tasks and one management task:

1. Assessment of Inspection Reliability
2. Research on ISI Technology
3. Research on Degradation Modes and Integrity
4. Integration of Results, Methodology, and Technical Assessments for Current and Emerging Regulatory Issues
5. Program Management.

This semiannual report describes program activities and results from October 1999 through March 2000.

2 Assessment of Inspection Reliability (D. S. Kupperman and S. Bakhtiari)

The objective of the inspection task is to evaluate and quantify the reliability of current and emerging inspection technology for current-day flaws, i.e., establish the probability of detection (POD) and the capability to size cracks. Both eddy current (EC) and ultrasonic testing (UT) techniques will be evaluated.

A steam generator mock-up has been assembled for round-robin (RR) studies that use currently practiced techniques and commercial teams. The mock-up will also be used as a test bed for evaluating emerging technologies for the ISI of SG tubes. Teams report flaw types, sizes, and locations, as well as other commonly used parameters such as voltage responses, from the EC tests.

2.1 Steam Generator Tube Mock-Up Facility

The mock-up consists of nine levels, each consisting of 400 Alloy 600 test sections, each measuring 0.3 m (1 ft.) in length. Above the ninth level is a 0.91-m (3-ft.)-long run-out section (see Fig. 2.1 for tube bundle diagram). In addition to stress corrosion cracks (SCCs), test sections with dents (cracked and uncracked) have been installed in levels with tube support plate (TSP) simulations. Magnetite in the TSP crevice was simulated by filling the crevice with magnetic tape or a ferromagnetic fluid. A mixture of magnetite and copper used to simulate sludge was placed above the tube sheet roll transition and above the TSP in some cases. Further details of the mock-up can be found in Ref. 1.

2.2 Round Robin Documentation

One of the key goals for the steam generator mock-up NDE RR exercise is to ensure that documentation used for the RR is comparable to documentation used during field examinations. To help achieve this goal, documentation for the RR and their revised versions were distributed periodically to the NDE Task Group, a group organized to provide input on the Argonne SG tube mock-up NDE round-robin and made up of industry, utility, NRC, and Argonne personnel. Input from the Task Group was used to prepare the set of representative documents that cover all aspects of an eddy current ISI inspection. The document "Analysis Guideline (ANL001)" provides the technical direction for the performance of eddy current examinations of the mockup. The "Multi-Frequency Eddy Current Examination of Tubing within the ANL SG Mock-up (ANL002)" governs the EC examination in accordance with the ASME Boiler and Pressure Vessel Code, Sections V and XI, 1980 through 1995 editions, with all addenda through 1997; the ASME Boiler and Pressure Vessel Code Cases N-401, N-401-1, N-402, and N-402-1; and NRC Regulatory Guide 1.83, July 1975, Rev.1. The "Steam Generator Mock-up Tubing Degradation Assessment and Technique Qualification (ANL003)" identifies the degradation mechanisms in the tubing of the steam generator mock-up. This assessment also identifies the inspection methods to be used to ensure that the inspection techniques and personnel used for the detection and sizing of tube flaws is appropriate for all degradation mechanisms. The "Training Manual (ANL004)" provides information on the mock-up design, format for entering data, degradation mechanisms, and examples of EC signals from flaws in the mock-up. Examination Technique Specification Sheets (ETSS) for flaw detection

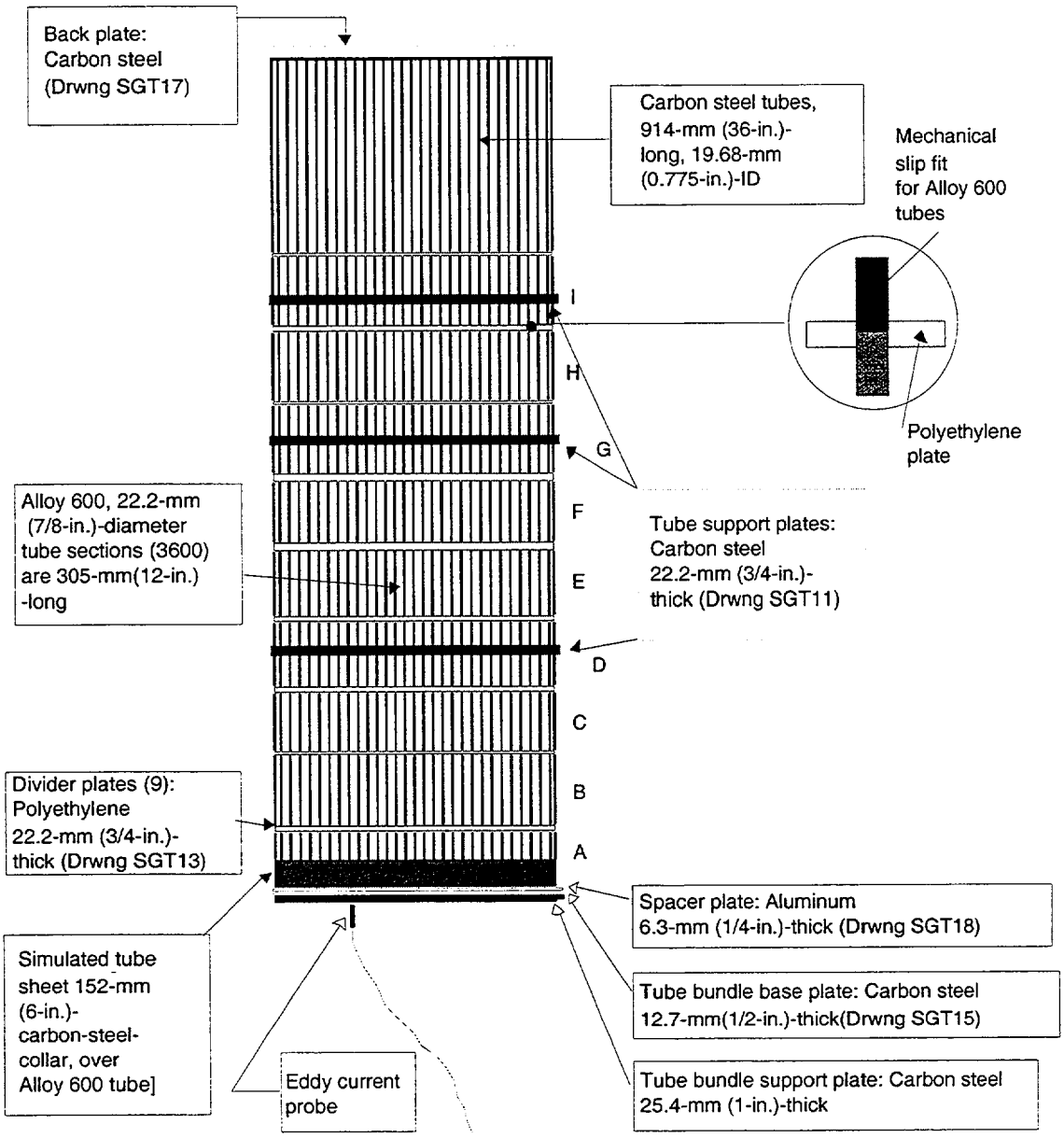

Fig. 2.1. Schematic representation of steam generator mock-up tube bundle.

provide the examination scope, including specifications for probes, electronics, instrument settings, and procedures for identifying flaws. In addition, ETSSs for sizing circumferential and axial flaws have been prepared. These ETSSs are based on EPRI ETSSs 96702 and 96703, which have been developed for sizing PWSCC. While qualified only for primary water SCC (PWSCC), these ETSSs will form the basis for profiling both ODSCC and PWSCC.

After completion of the bobbin and motorized rotating pancake coil (MRPC) data acquisition task by qualified Zetec personnel, a meeting of NDE Task Group was held on January 5, 2000, in anticipation of the beginning of the RR exercise on January 10, 2000. Final comments and suggestions for the RR documentation were provided. The sequence of

events for the RR exercise was set, and a schedule for organizations committed to participate was presented. The practical exam, which the analysts are required to take before participating in the RR, was reviewed. Several comments led to modification of the exam and preparation of a retest for those analysts who do not pass the first exam. One member of the Task Group was elected to represent the entire group to acknowledge, by signature, that the documentation prepared for the RR is acceptable to the Task Group. The documents were approved after receiving further revisions. Approval acknowledged that the Argonne RR documents are comparable to those used for a field inspection.

2.3 Status of Round Robin Exercise

The RR analysis began on January 10, 2000. One team was from FTI in Lynchburg, VA, the second team was from FTI in Benicia, CA, and the third team was from ABB-CE in Chattanooga, TN. Four more teams participated in February: two from Zetec, one from Anatec, and one from KAITEC in Korea. The KAITEC team analyzed the data at Argonne. Participation at a later date is expected from Duke Engineering and Services, Westinghouse Nuclear Services, and Ontario Power Generation. The initial effort by FTI and ABB-CE showed that all of the data could not be analyzed in the one week initially allowed for the RR. However, the analysis of all bobbin coil and all tube sheet data was completed in one week. Analysis of MRPC special interest (spin call) data was to be completed at another time for those three teams. Teams participating later committed seven or eight working days to complete the data analysis.

Each RR team consists of five analysts: a primary and secondary analyst, two resolution analysts, and an independent qualified data analyst (QDA). Data were analyzed at the analysts' home base (except for Kaitec). To carry out the analysis, an Argonne proctor brought optical disks to the analysts' site. The first disk to be analyzed contained the bobbin coil data from all 3600 of the 30.5-cm (1-ft.)-long test sections. The special interest (spin call) data were analyzed using the second mock-up optical disk. The third optical disk contained MRPC data from all 400 simulated tube sheet test sections. Before evaluating the RR data, the analysts were provided with a training manual and were required to pass a site-specific examination. Argonne proctors administered the exam and monitored the data analysis. Training session prepared the proctors involved in the RR.

More specifically, the tasks involved in carrying out the RR are summarized as follows:

1. Provide training manual, training optical disk, and supplemental schematics to participating teams for review.

2. Collect certifications and have nondisclosure agreements signed by all analysts participating in the RR.

3. Administer written and practical exams graded by the Argonne proctor.

4. Provide mock-up data on optical disks and have analysts' reports recorded on disks, along with a hard copy of the reports.

5. Return disks to Argonne for analysis of reports using the EPRI data management program. At this stage, team reports are compared to expert opinion. These results do

not provide probability of detection (POD), because they do not reflect the true state of the mock-up, but they are useful for comparing team responses. Data provided by Argonne using a multivariate approach to EC sizing to obtain maximum depth and crack length will be used to obtain true state and allow for a complete analysis of team reports, including POD, as function of flaw size and type.

The tasks described above are accomplished following this sequence of events for the RR.

1. The training manual with examples of flaws on an optical disk (DISK #1), supplemental schematics, and final reports for the training data are sent to the teams for review before the RR exercise is started,

2. On the first day, the Argonne proctor collects certifications, and nondisclosure agreements are signed.

3. Analysts finish studying training manual, analyst guidelines, training disk, and supplemental schematics.

4. Analysts take a written exam graded by the Argonne proctor together with the practical exam from DISK #2 provided by the proctor. For the written exam, a score of 80% is passing, and for the practical exam, all "I" codes must be called. Some overcalls are allowed. The Argonne proctor, who retrieves DISK #2 after testing is completed, grades the results.

5. The Argonne proctor provides DISK #3 that contains all bobbin coil data. The primary and secondary analysts analyze the BC data, and their reports are recorded on DISK #3. The resolution analysts resolve the primary/secondary discrepancies, and a resolution analyst's report is provided. DISK #3 now contains primary, secondary, and resolution analysts' reports for the BC data. Hard copies of these reports are given to the proctor and disk #3 is returned to the proctor.

6. The Argonne proctor provides DISK #4 containing MRPC special interest (spin call) data. The MRPC data are analyzed by the primary and secondary analysts, and their reports are recorded on DISK #4 except for the tube sheet level (Level A), which is analyzed later. Analysts report depth at maximum amplitude.

7. The resolution analysts resolve the primary/secondary discrepancies, and a resolution analyst's report is provided. DISK #4 now contains primary, secondary, and resolution analysts' reports for MRPC data other than the tube sheet level. Disk #4 is returned to the proctor, and hard copies of reports are printed and given to the Argonne proctor.

8. The Argonne proctor provides DISK #5 containing only tube sheet MRPC data, but from all 400 tubes. The primary and secondary analysts analyze the data of Level A and provide their report. The resolution analysts resolve any discrepancies and provide their report. DISK #5 now contains primary, secondary, and resolution analysts' reports.

9. The Argonne proctor returns to Argonne for analysis of team reports with the EPRI "SSPD Shell" data management program.

10. Data are analyzed by PNNL statistical analysis software to obtain POD as a function of flaw size and type.

Table 2.1 shows the number of reports provided from the seven teams participating to date.

2.4 Management of Mock-up Eddy Current Data

The EPRI Data Management SSPD "Shell" program previously loaded onto an Argonne computer successfully handled the analyses that were completed by each team. This program compares the results of expert opinion against the round-robin reports from the primary analyst, the secondary analyst, and the final report of the resolution analysts. A total of three reports are analyzed for each team for each of the three parts of the RR; the bobbin coil data, the MRPC tube sheet data, and the MRPC spin call (special interest) data. The raw data and reports for each part are provided on a single optical disk managed by the Argonne proctor present during the round-robin exercise. The Shell program sorts the data by degradation and, for axial ODSCC at the tube support plate, by voltage. The Shell program reports the percentage of correct matches to expert opinion for each degradation and the overcalls. Note that, at this time, analysts' reports are compared to expert opinion and not to the true state of the mock-up, which will be established at a later date. Table 2.2 summarizes the reporting format.

A review has been carried out of BC voltages that were called for longitudinal outer-diameter stress corrosion cracking (LODSCC) indications at tube support plates by the teams analyzing the mock-up data. In most cases, the variations in the voltages identified by the teams were fairly small. For each LOD, an average BC voltage for the teams and a corresponding standard deviation were computed. The cumulative distribution of the normalized standard deviations (i.e., the standard deviation divided by the corresponding value of the average voltage) can be fit well by a Weibull distribution, and the root mean square (RMS) difference between the observed distribution and the Weibull fit is <0.03. The fitted distribution is shown in Fig. 2.2. For almost 85% of the indications, the normalized standard deviation in the reported voltages is <0.1. The indications with larger variations are not associated with particularly high or low voltages (i.e., approximately half the signals with standard deviations >0.1 have voltages >2 V), but rather are associated with the complexity of the signal and the difficulty of identifying the peak voltage.

2.5 Statistical Analysis

A meeting was held at ANL on November 18, 1999, with Pacific Northwest National Laboratory (PNNL) personnel to discuss statistical analysis methods for evaluating of mock-up inspection RR data and to develop an outline for a statistical analysis protocol document. The following issues were discussed:

1. How should grading units be defined?

2. What definitions of detection will be used?

3. What algorithms should be used to describe POD?

Table 2.1. Number of round-robin analyst reports for the three data sets from the first seven participating teams.

Mock-up Data Set	Number of **Primary** Analyst Reports To Date	Number of **Secondary** Analyst Reports To Date	Number of **Resolution** Analyst Reports To Date
Bobbin Coil (all tubes)	7	7	7
MRPC (all tube sheet test sections)	7	7	7
MRPC (all special interest, i.e., spin calls)	6	6	6

Table 2.2. Information provided by EPRI Data Management "SSPD Shell" program using results from RR analysts' reports. At present, analysts' reports are compared to expert opinion and not to true state of mock-up, which will be established later.

Flaw Type → (see footnotes)	2	3	4	5	6	7	8	9	10	11	12	13	14	26	27	28	Total	31	32	Total	33	34	Total
No. of Expert Opinion Calls	*	*	*	*	*	*	*	*	*	*	*	*	*	*	*	*	*	*	*	*	*	*	*
No. of Analyst Calls	*	*	*	*	*	*	*	*	*	*	*	*	*	*	*	*	*	*	*	*	*	*	*
RMSE Volts	*	*	*	*	*	*	*																
No. of Overcalls	*	*	*	*	*	*	*	*	*	*	*	*	*	*	*	*	*	*	*	*	*	*	*

*Data Generated

2. TSP/BC/ODSCC 0.25-0.49 V.
3. TSP/BC/ODSCC 0.50-0.74 V.
4. TSP/BC/ODSCC 0.75-0.99 V.
5. TSP/BC/ODSCC 1.00-.1.49 V.
6. TSP/BC/ODSCC 1.50-2.99 V.
7. TSP/BC/ODSCC > 3.00 V.
8. TSP/BC/PWSCC-Dent < 2.0 V.
9. BC/ODSCC/Free Span
10. BC/PWSCC-Ding/Free Span
11. TSP/BC/Wear/Free Span
12. TSP/BC/IGA/Free Span
13. BC/ODSCC/Sludge Pile
14. Expansion/BC/PWSCC
26. BC/ All Dents
27. BC/Other
28. TSP/BC/thinning-Wastage/Free Span
31. +Point/PWSCC
32. +Point/ODSCC
33. +Point/Expansion/PWSC
34. +Point/Expansion/ODSCC

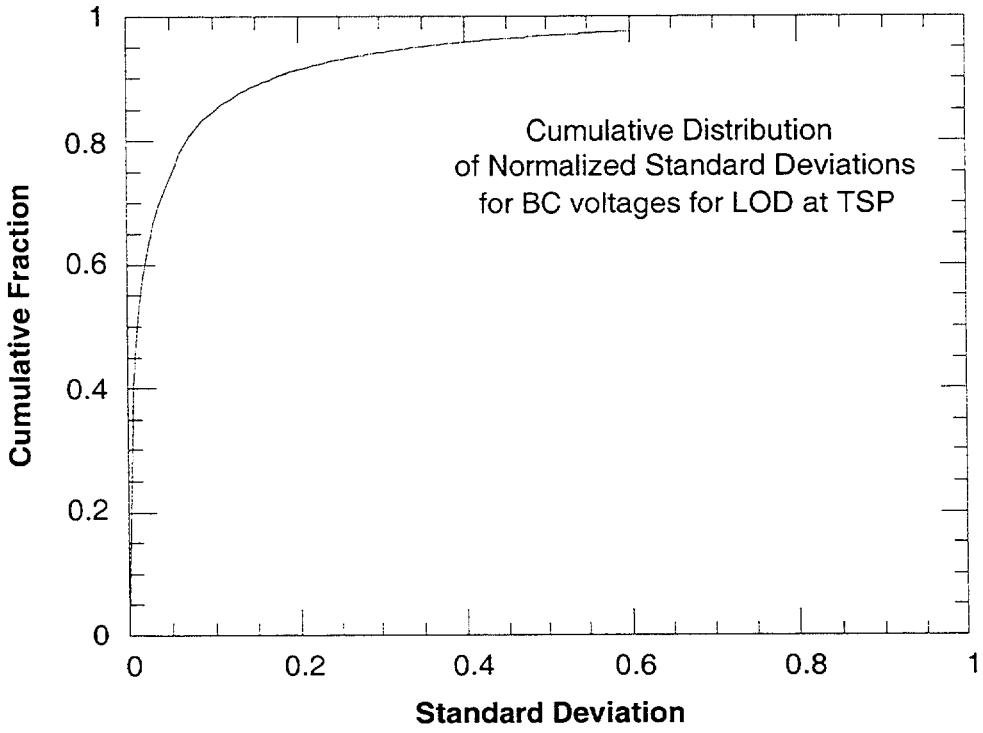

Fig. 2.2. Cumulative distribution of normalized standard deviations for bobbin coil voltages for LODSCC at tube support plates.

4. How many blank areas for false call estimation are required?

5. Does the false call probability describe all aspects of false calls we want to evaluate?

6. How should the true state of the tubes be characterized?

7. What flaw sizing parameters will be evaluated (length, depth, area, etc.)?

8. Should the relationship between burst pressure and inspection results be evaluated?

9. How many flaws need to be destructively evaluated to be confident of the true state of the mock-up?

The format for the tables necessary to carry out the statistical analysis has been established. Five tables are required. The first is the Flaw Table, which identifies every flaw in mock-up. Each row of the Flaw Table describes one flaw in the mock-up. The columns of the Flaw Table provide the flaw identification, flaw type, location, orientation, size, and true state call. The second table is the Grading Unit Table, which divides the mock-up into segments and provides the location and dimension of each segment of the mock-up to be graded. Each row of the Grading Unit Table defines an area evaluated by the scoring program to produce statistics. The Grading Unit Table has the tube identification, segment identification, upper and lower dimensions, and flaw information.

The third table is the Inspection Table, which provides the detailed information regarding the inspection being graded (probe type, area inspected, etc.). The fourth table is the Indication Table, which provides the essential information from the inspection. Each row of the Inspection Table describes one analyst's call. The columns provide analyst's information on location, volts, phase, ID/OD, depth, length, orientation and three-letter code. The fifth table is the Scoring Table. Each row in the Scoring Table describes how a particular inspection performed on a grading unit. A scoring algorithm to be prepared by PNNL generates the Scoring Table.

Tables 2.3 and 2.4 show simulated inputs to the Flaw Table and the Flaw Indication Table for a bobbin coil inspection. Table 2.4 shows a flaw in row A, column 7, at TSP level D. The maximum BC voltage is at data point 1865. The flaw is a longitudinal ID with a BC voltage of 2.04 v and phase angle of 25°. The flaw begins at data point 1839 and ends at 1873. About 3600 data points are stored for each tube examined with the BC (nine test sections). Table 2.3 shows a depth estimated to be 40% TW, as determined by application of a multivariate algorithm to MRPC data for the flaw. The expert opinion for the BC call is NQI (nonquantifiable indication). An "I" code triggers an inspection with an MRPC. The true state three-letter code is SAI (single axial indication). A second example is also provided.

The second flaw, a longitudinal ODSCC, is at row M, column 14, and at free span level F. The result for the BC inspection is shown in Table 2.4. An indication was found in row A, column 7 at data point 1855, close to the correct flaw location. The ID/OD call is correct, and an "I" code is also called, although in this case it is distorted TSP indication (DTI). The DTI call also requires MRPC data to be acquired. The second indication would also be graded as a correct call. Indication tables are generated for both bobbin coil and MRPC data and compared with the Flaw Indication Table, which contains all information needed to estimate POD.

2.6 Emerging Technology

Interest has been shown by AECL in using the mock-up to evaluate the X-probe, a transmit-receive array probe that obtains coverage by having multiple coils, whereas the rotating probes, such as the +Point, uses a single coil that spins to provide full coverage. An array probe can move through the tube more quickly than a rotating coil because the latter is slowed by its helical spin. In March 2000, a team from AECL (Chalk River, Canada) brought the X-probe to Argonne. Mock-up data from the test sections used for training were collected. A detailed procedure was provided by AECL and followed during collection of the training data. For this exercise, data were taken at more frequencies than will be used to examine the entire mock-up. The evaluation of training data will lead to the selection of frequencies to be used when data from the entire mock-up is collected. Evaluation of the training data may also lead to modification of the data acquisition and analysis procedures for the X-probe.

AECL plans to return to Argonne at a later date to collect data from the entire mock-up using the final procedure. RDTech (Quebec, Canada) and Nuson (Netherlands) have also expressed interest in evaluating ultrasonic inspection technology using the Argonne mock-up.

Table 2.3. Simulated input to flaw table for bobbin coil inspection.

Flaw ID	Flaw Type	BC Volts	BC Phase	ID/ OD	Beg. Data Pt.	End Data Pt.	Depth (%TW)	Expert BC Call	True State Call
A07D1865	LID	2.04	25	ID	1839	1873	40	NQI	SAI
M14F3177	LOD	2.61	70	OD	3157	3192	90	NQI	SAI

Table 2.4. Simulated bobbin coil input to flaw indication table.

Indication	BC Volts	BC Phase	ID/ OD	Beg. Data Point	End Data Point	Depth Est.	Call
AO7 1855	2.14	29	ID	-	-	50	DTI
M14 3157	2.68	60	OD	-	-	80	NQI

2.7 Meetings and Travel

D. Kupperman visited the Indian Point 2 site on March 9-10, 2000, to assist in the NRC review of eddy current data taken from U-bends in 1997 and 2000. Selected +Point data from the 1997 and 2000 inspections were brought to Argonne for subsequent review.

An ISG-TIP-2 meeting was held October 20-21, 1999. Presentations were made on NDE activities by D. Kupperman (progress on mock-up and RR) and S. Bakhtiari (sizing and profiling cracks). Participation in the RR by AECL (using the X-probe array) was discussed at this meeting. AECL indicated that they might want to use the mock-up as a test bed for the X-probe.

3 Research on ISI Technology (S. Bakhtiari and D. S. Kupperman)

The objective of this task is to evaluate advanced NDE and signal analysis techniques for the reliable ISI of original and repaired SG tubes. Improved correlations between EC probe response and flaw morphology, leak rate, and failure pressure will be developed and validated. In addition, the reliability of the voltage parameter and other EC parameters and techniques will be evaluated with respect to their ranges of applicability.

The present research on improved ISI of SG tubes focuses on four primary areas: (1) implementation of analytical methods for prediction of EC response as a function of probe design, flaw characteristics, and material properties; (2) development of effective signal analysis procedures; (3) development of flaw imaging and display methods for simple and accurate flaw characterization; and (4) evaluation of improved probe designs that use directional arrays so that defects of arbitrary orientation can be examined simultaneously. The reliability and effectiveness of improved inspection techniques and the robustness of potential correlations will ultimately be substantiated through laboratory testing of the SG tube bundle mock-up and of SG tubes that contain various flaw morphologies. Final validation will also utilize in–service-degraded SG tubes.

A description of Task 2 activities during the past reporting period is provided here. Research efforts that are associated primarily with multiparameter analysis of eddy current NDE results are discussed. Sample calculations are presented in Section 3.1 in a follow-up study to demonstrate the applicability of pseudoinverse filters for improving the spatial resolution of rotating probes. Preliminary results are presented in Section 3.2 on another study that was initiated to explore potential advantages of 2-D suppression over conventional 1-D mix schemes for elimination of unwanted signals. Initial evaluations regarding conversion of data analysis results into calibrated profiles for more direct deduction of estimated flaw size and extent is discussed in Section 3.3. Selected test cases from a data set that was analyzed earlier were used for this purpose.

Samples are currently being manufactured under Task 3 activities to augment the library of tubes for NDE studies with a wider range of degradation morphologies. Flaw types in these tubes are, in general, representative of those incorporated into ANL tube bundle mock-up. Results are presented in Section 3.4 on analyses of rotating-probe inspection data from three separate batches of laboratory-grown specimens. Manufactured flaws in the first batch of tubes were composed primarily of circumferential and those in the second batch of axially oriented cracking. A collection of 31 tubes was also produced recently to carry out blind studies to help further assess the performance of alternate data analysis schemes to detect and size SG tubing degradations. Initial results on analyses of NDE data from this set of tubes is presented in Section 3.4. A more detailed description of ongoing investigations on the analysis of multiple-frequency eddy current rotating-probe data will be provided in our subsequent reports.

3.1 Follow-Up Studies on the Enhancement of Spatial Resolution of Rotating Probes

Application of pseudoinverse filters to the restoration of flaw signals from rotating-probe inspections was discussed in an earlier report.[1] Recent investigations have, in part, dealt with

evaluating the effectiveness of approximate deconvolution methods to improve spatial resolution and, in turn, sizing accuracy for crack-like indications. Initial studies using a collection of laser-cut specimens with machined flaws of various geometries were described in preceding reports. The deconvolution scheme has been incorporated into a rule-based multiparameter data analysis algorithm to study potential improvements in sizing accuracy. Preliminary results provided next on a limited set of laboratory-grown specimens with axial and circumferential OD/ID cracking suggest that improved spatial resolution and sizing accuracy could be achieved through proper application of pseudoinverse filters. More extensive studies in this area are currently underway and the results will be provided in our future reports.

3.1.1 Analyses of laboratory-grown specimens.

Eddy current readings on a collection of 22.2-mm (0.875-in.)-diameter Alloy 600 tubes with laboratory-produced cracking were analyzed by using a multiparameter data analysis scheme described in our earlier reports. Flaws in this small set of six samples consisted primarily of OD axial cracking in free-span and circumferential cracking in roll transition regions, plus a single specimen with axial ID cracking at a dented TSP region. Multiple-frequency NDE data used in this study were acquired with a standard three-coil rotating probe that contains a 2.92-mm (0.115-in.)-pancake, a mid-range +Point, and 2.03-mm (0.080-in.)-high-frequency pancake coil. The primary pancake coil readings were utilized for analyses. The calibration standard tube contained 18 EDM notches of axial and circumferential orientation ranging in depth from 20% ID to 20% OD, with all being 6.35 mm (0.25 in.) in length. Data analysis results here are presented as an isometric display of relative depth profile for the flawed region of the tube. Estimated profiles are shown both with and without signal restoration by inverse filtering.

Figure 3.1 shows the normalized depth profile for a laboratory-grown specimen with longitudinal ODSCC. For all test cases, only the portion of tube in the vicinity of the flaw is displayed. In reference to the calibration standard, the maximum flaw depth in the laboratory-grown specimen was estimated to be >80% TW. Figures 3.1(a) and (b) display, respectively, the estimated 2-D profiles of the flawed segment without and with the deconvolution process being applied. Unlike the gradual tapering of the flaw depth seen in Fig. 3.1(a), restored depth profile of Fig. 3.1(b) shows the flaw to have a rather uniform depth in the center, with a sharp drop in the estimated depth at the two ends of the crack.

Figure 3.2 shows the results of analyses for the second axial ODSCC flaw with estimated maximum depth of ≈80% TW. Comparison of the restored depth profile in Fig. 3.2(b) with that in Fig. 3.2(a) suggests the crack to be composed of a series of axial segments with the one crack being nearly separated from the rest. Similar results are shown in Fig. 3.3 for another specimen with axial ODSCC flaw. Terrain plots of the depth profile, however, suggest the orientation of the crack to be approximately at 45° with respect to the tube axis.

Figures 3.4 and 3.5 show the results of analyses for two specimens with circumferential ODSCC at the roll transition region of tube. The processed data clearly indicates complete suppression of the roll transition that is the primary signal feature in the amplitude trace. The maximum flaw depths were estimated to be ≈60% and ≈80% TW, respectively. Based on the terrain plots in Figs. 3.4(a) and 3.5(a), both cracks extend nearly 120° around the

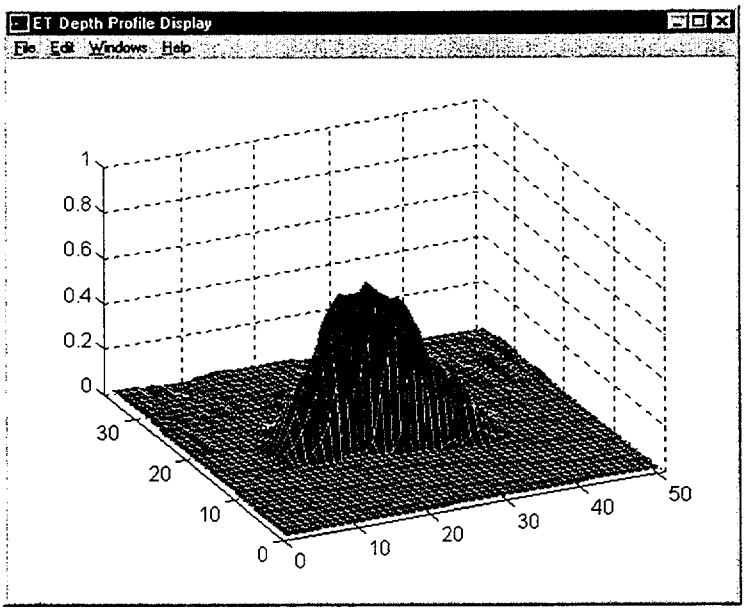

(a)

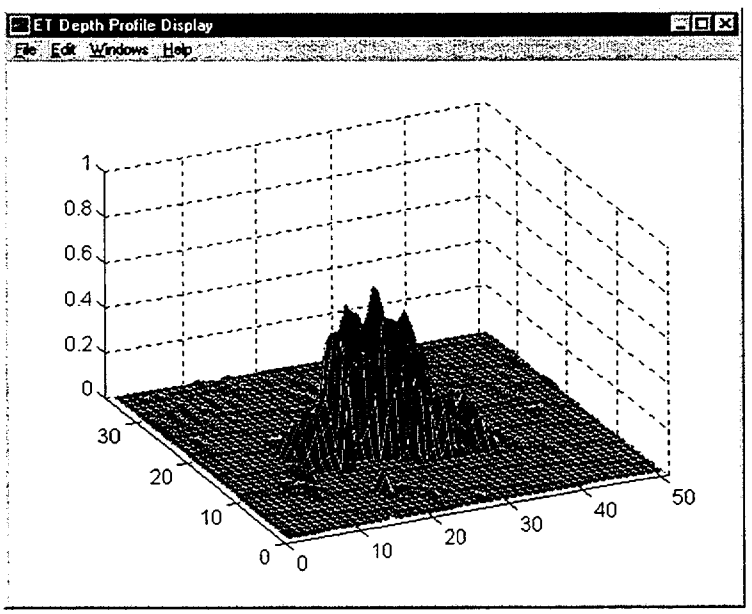

(b)

Fig. 3.1. Data analysis results for specimen with laboratory-grown longitudinal ODSCC showing (a) terrain plot of relative depth profile for cracked zone and (b) restored profile by inverse filtering. Maximum crack depth is estimated to be >80% TW. Isometric display of results shows finer details in restored profile.

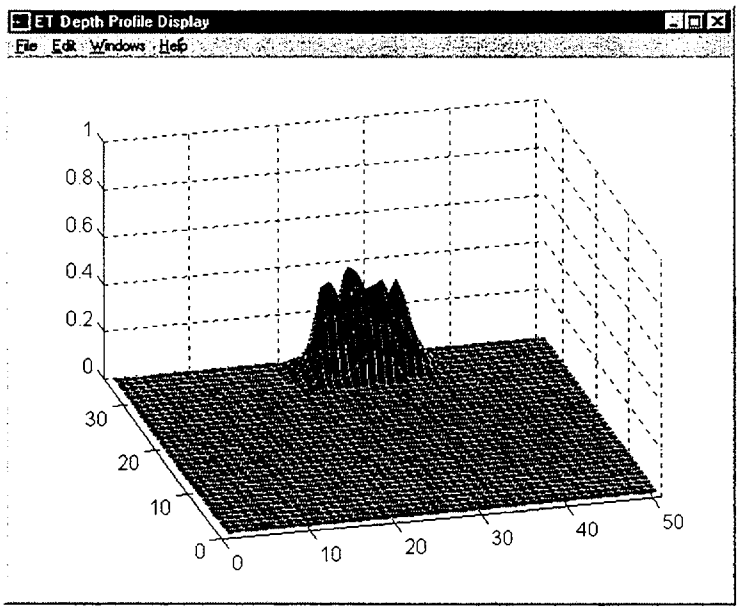

(a)

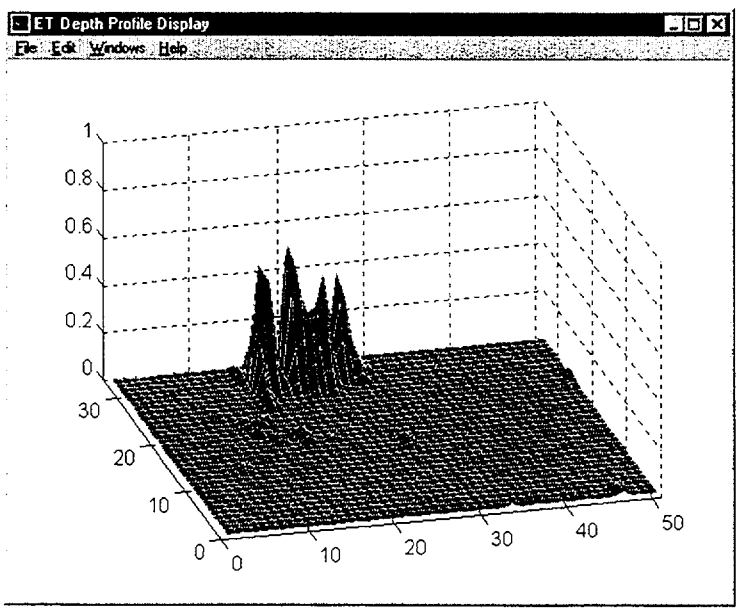

(b)

Fig. 3.2. Data analysis results for specimen with laboratory-grown longitudinal ODSCC showing (a) terrain plot of relative depth profile for cracked zone and (b) restored profile by inverse filtering. Maximum crack depth is estimated to be ≈80% TW. Isometric display of results shows finer details in restored profile.

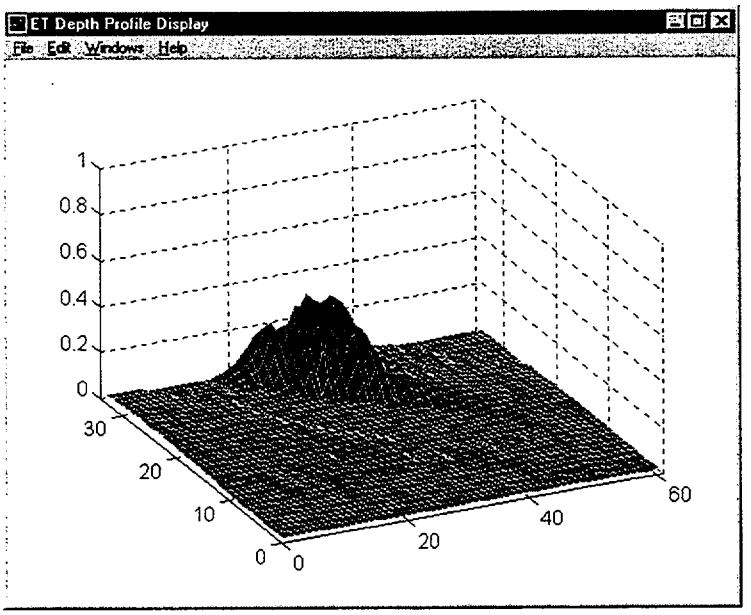

(a)

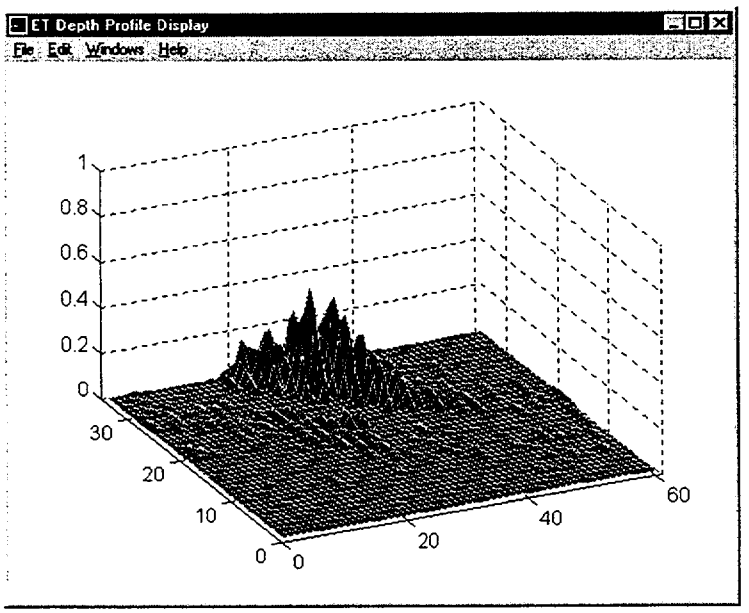

(b)

Fig. 3.3. Data analysis results for specimen with laboratory-grown skewed ODSCC showing (a) terrain plot of relative depth profile for cracked zone and (b) restored profile by inverse filtering. Maximum crack depth is estimated to be ≈80% TW. Isometric display of results shows finer details in restored profile.

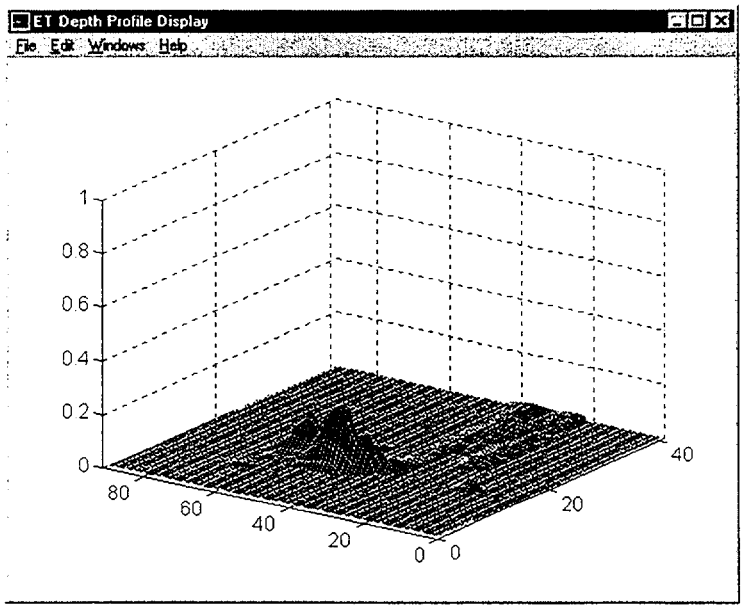

(a)

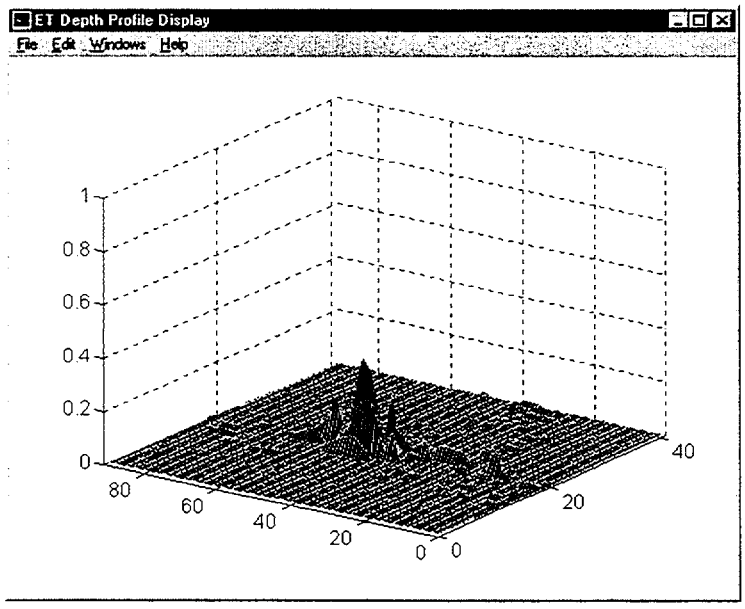

(b)

Fig. 3.4. Data analysis results for specimen with laboratory-grown circumferential ODSCC showing (a) terrain plot of relative depth profile for cracked zone and (b) restored profile by inverse filtering. Maximum crack depth is estimated to be ≈60% TW. Isometric display of results shows finer details in restored profile.

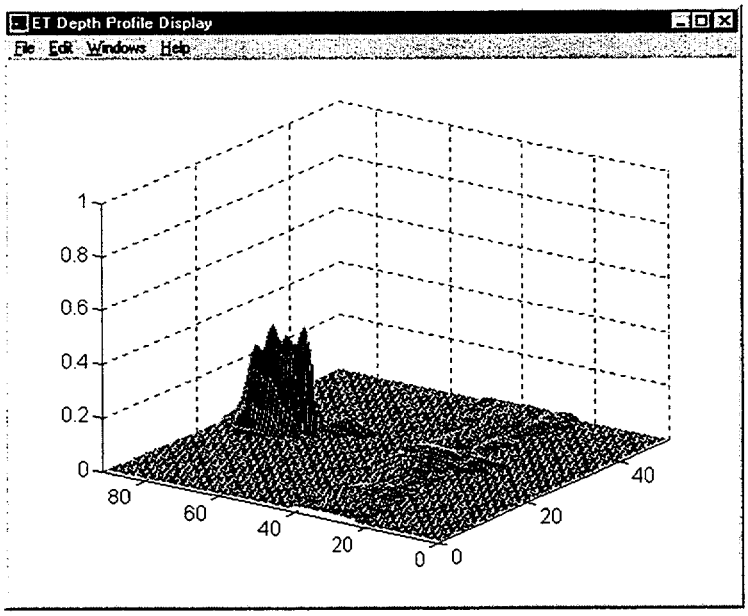

(a)

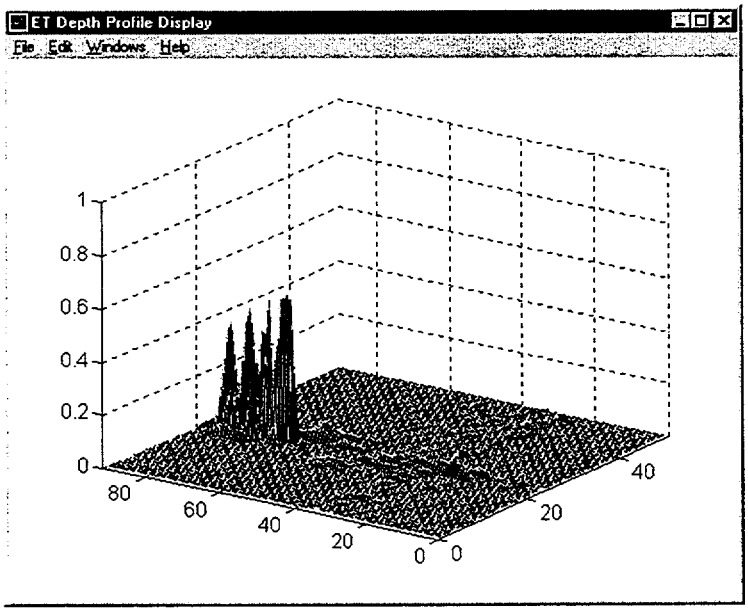

(b)

Fig. 3.5. Data analysis results for specimen with laboratory-grown circumferential ODSCC showing (a) terrain plot of relative depth profile for cracked zone and (b) restored profile by inverse filtering. Maximum crack depth is estimated to be ≈80% TW. Isometric display of results shows finer details in restored profile.

circumference. The depth profiles of the restored signals shown in Figs. 3.4(b) and 3.5(b) suggest both circumferential cracks to be composed of multiple segments. The maximum depth of the flaw displayed in Fig. 3.4(b) appears to be near the center. The profile of the estimated depth for the restored signal in Fig. 3.5(b), however, suggests that the circumferential crack consists of four closely spaced short segments with comparable maximum depths.

Finally, Fig. 3.6 shows the results of analysis for an ID axial crack in a dented region at the tube support plate intersection. The maximum flaw depth was predicted to be ≈40% TW. In this case, a terrain plot of the defected segment was constructed from the estimated ID profile. Comparing the restored profile of Fig. 3.6(b) with that of 3.6(a) indicates some improvement of spatial resolution following signal restoration. Once again, complete suppression of the TSP and dent signals is clearly evident in both cases.

3.2 Preliminary Investigations on 2-D Suppression of Unwanted Signals

Preliminary test case results are presented here from an ongoing investigation on the application of signal decomposition and factor analysis techniques for selective suppression of unwanted indications from rotating-probe data. Initial studies suggest that 2-D multiple-frequency factor-based techniques could provide substantial improvement over conventional 1-D mix procedures for the analysis of rotating-probe EC inspection results. Preliminary evaluation of the two techniques discussed here was based on analyses of simulated composite signals from a rotating-probe that were produced from the available readings on a calibration standard. Further investigations will be carried out by using laboratory-produced specimens.

Conventional regression-based mix algorithms were initially developed to aid in suppression of unwanted signals (e.g., external support structures and, to a lesser extent, tube dimensional variations) from EC signals. Multifrequency mix procedures that typically involve combining the information from a primary/base frequency and one or two auxiliary frequency channels have been fairly effective for the processing of BC readings. However, independent evaluations at ANL suggest that 1-D mix algorithms are not as effective for the processing of higher resolution rotating-probe inspection results. In particular, unlike the situation for the BC, mixes for rotating-probe C-scan data are quite subtle and routinely fail to produce consistent outcomes. Also, when mix coefficients are applied to the entire signal trace, significant distortion of both the amplitude and phase-angle information of the original readings could result. The nature of instability of traditional mix schemes for the processing of rotating-probe data becomes somewhat apparent when one compares a 1-D BC signal (i.e., each measurement point along the tube axis is an integration of coil response over the circumference) with 2-D readings (i.e., measurements along both axial and circumferential directions) from a rotating probe. To improve rotating-probe mixes, specially designed simulated TSP rings (e.g., a 270° ring as opposed to an axisymmetric 360° ring used for bobbin mixes) are often utilized. Nevertheless, the mix results could vary substantially, depending on the selected portion of signal for the calculation of mix coefficients. For this reason, mix channel information is not currently used for reporting of rotating-probe inspection results.

A study was initiated recently at ANL to evaluate potential alternatives to 1-D conventional mix procedures for suppression of unwanted signals from RPC data. Two approaches based on 2-D factor analysis techniques were considered. Both methods utilize

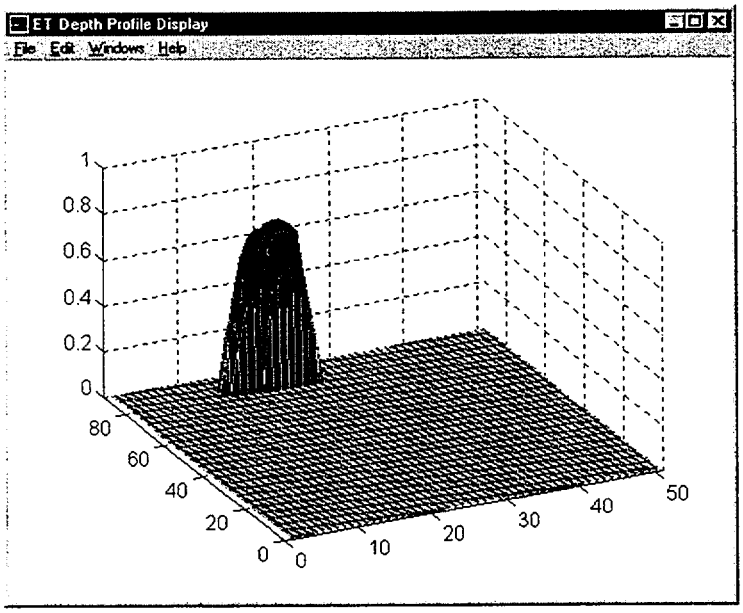

(a)

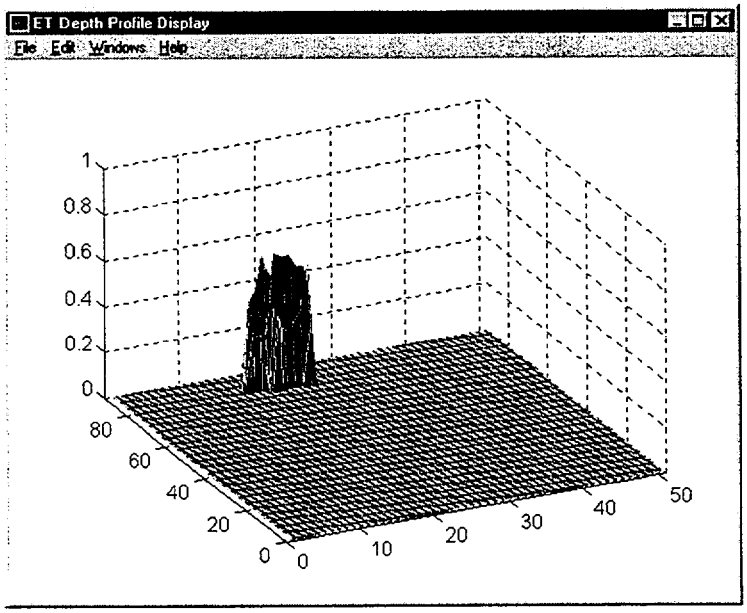

(b)

Fig. 3.6. Data analysis results for specimen with laboratory-grown longitudinal IDSCC at dented TSP intersection showing (a) terrain plot of relative depth profile for cracked zone and (b) restored profile by inverse filtering. Maximum crack depth is estimated to be <40% TW. Isometric display of results shows finer details in restored profile.

spectral decomposition, also referred to as singular value decomposition (SVD) or outer product expansion. However, they differ significantly in their analysis of factors. The first method is based on a standard decomposition at a single-frequency and subsequent selection of appropriate coefficients. The second method, on the other hand, uses a least-squares (LS) regression approach with two frequencies.

Spectral decomposition methods serve as the fundamental numerical technique in a wide range of applications from solution of linear system of equations to problems in signal and image processing such as restoration, compression, denoising, pattern recognition, and feature extraction. Such transformation algorithms basically attempt to decompose an often ill-conditioned data matrix to an outer product expansion of left- and right-hand unitary matrices of orthonormal eigenvectors with a matrix of pseudo-eigenvalues. With the underlying assumption that the basis functions that span the signal and noise subspaces are orthogonal, this mapping should then provide improved separation of relevant signal features from inconsequential trends. Following the decomposition, selection of appropriate factors allows for the preservation of relevant signal features and in effect elimination of background noise. Factor analysis methods that use spectral decomposition together with multivariate regression schemes offer a more robust method for the analysis of factors through recursive regression between the independent and dependent variable matrices. The basic formulation of LS-based factor analysis method used here for the processing of RPC data was described in our earlier reports.

In practice, selection of appropriate factors often poses the greatest challenge when spectral decomposition alone is used. This is particularly true for the EC inspection results with rotating probes in which flaw and artifacts at one frequency are often described by common factors. This means that it is not always possible to select a set of factors that reasonably separate consequential indications from artifacts and background fluctuations. Therefore, factors cannot be applied blindly, and some form of discretion is necessary in deciding which factors to keep. For this reason, multiple-frequency LS-based factor analysis method should provide a more robust and systematic approach to suppression of unwanted signals in rotating-probe data.

The two approaches that were described above, namely, single-frequency spectral decomposition and a two-frequency decomposition with LS-based regression, were initially tested on simulated composite signals from RPC readings on a 22.2-mm (7/8-in.)-OD tube standard with machined notches and a 270° support plate slip ring. Various combinations of OD and ID notches within the TSP region were produced. This was done by vectorial addition of data segments with notches at various frequencies with that from the TSP segment. It is worth noting that the nonaxisymmeteric geometry of the TSP ring used here poses a greater challenge to any signal suppression scheme in comparison to axisymmetric drilled support plates. However, it is expected that such nonuniform and overwhelming EC indications could be encountered in the field from external structures such as broached support plates.

Initial results on the suppression of TSP indication at a single frequency by using a standard SVD algorithm did not produce acceptable results. Specifically, in several test cases a reasonable degree of suppression of TSP indications introduced substantial degradation of the flaw signal. As mentioned earlier, the primary limitation of this method arises from the lack of separation of factors that describe artifact and flaw signals.

With the same simulated data, the two-frequency LS-based factor analysis method, on the other hand, rendered a systematic approach for repeatable suppression of TSP indications with acceptable degradation of flaw signals. Figures 3.7 and 3.8 show the results for two test cases by using the composite signal described above. In both cases, single and multiple flaws that were arbitrarily placed within the TSP region were recovered with a high level of suppression of TSP indications. Selection of primary and auxiliary frequencies for 2-D suppression is analogous to that used by standard 1-D mix procedures. Also, in a similar manner to conventional mix procedures, multiple unwanted indications could be suppressed by successive application of this method. Further studies in this area will be carried out by using laboratory-produced flawed specimens and with various forms of simulated artifacts. Results of these investigations will be provided in our future reports.

3.3 Display of Data Analysis Results

Modifications and refinements of computer codes that facilitate more convenient display of the sizing results are briefly discussed here. Representative test cases on analyses of laboratory-grown specimens are shown that exhibit the current state of graphical display of the sizing results. Further refinement of display routines is underway to allow for direct comparison of NDE with destructive examination results in a more practical manner. Validation of NDE sizing results is being made through comparison with destructive examination of tubes currently being performed under Task 3 of this program.

Earlier estimates of flaw size by multiparameter analysis of rotating-probe data were made by direct comparison of a flawed-tube profile with that of an in-line standard. A series of modifications was recently incorporated to allow for more quantitative mapping of NDE estimates to destructive examination results. Subsequent to calculation of relative depth profile, a curve-fitting routine is used to convert the results to percent of tube wall thickness. Transformation/calibration function is generated through a multiple linear regression fit to known values of flaw depths from an in-line standard. Upon reconstruction of helically scanned data into terrain plots, the sizing profiles may then be observed from any azimuth and elevation view angle and for any axial or circumferential cross section of the tube. Scaling of data in axial and circumferential directions is based on user-defined locations and data acquisition sampling rate, respectively. This allows for direct deduction of sizing information on axial (in millimeters) and circumferential (in degrees) extent of each flaw in the tube.

Eddy current readings on two representative 22.2-mm (0.875-in.)-diameter Alloy 600 tubes with laboratory-produced flaws were analyzed with the multiparameter data analysis scheme. Flaws in both tubes were identified as OD axial cracking. Multiple frequency NDE data were acquired with a standard three-coil rotating probe that contains a 2.92-mm (0.115–in.) pancake, a mid-range +Point, and 2.03-mm (0.080-in.) high-frequency pancake coil. The primary pancake coil readings were utilized for analysis. Data analysis results in the form of normalized depth profile for each tube were then transformed to throughwall depth estimates according to the process described above.

Figure 3.9 displays the analysis results from two arbitrarily selected views of tube profile for the first sample. Only the section of tube in the vicinity of the crack is shown. From Fig. 3.9(b), the axial length and maximum flaw depth are estimated to be ≈25 mm (1.0 in.) and ≈85% TW, respectively. Similar display of the NDE results for the second specimen are shown

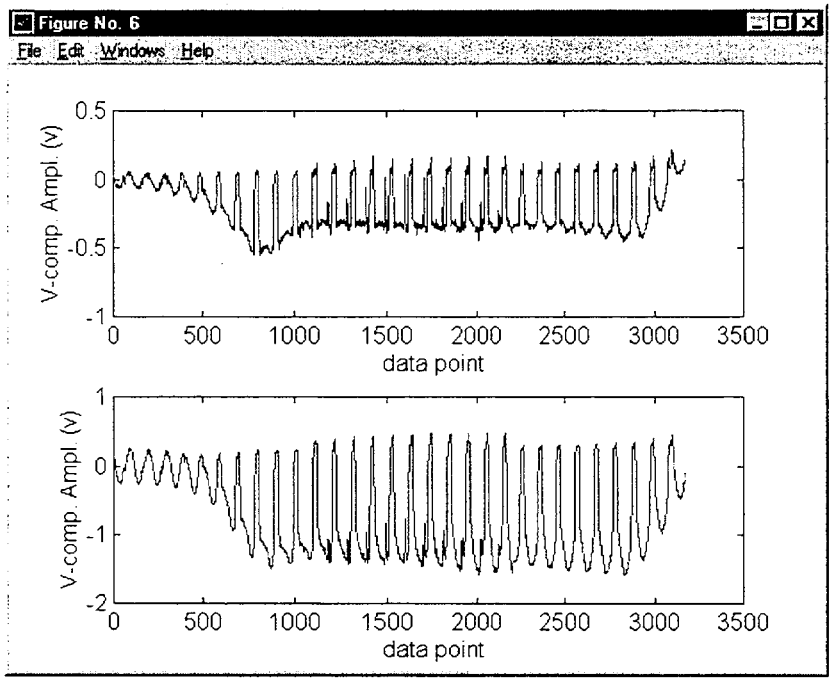

(a)

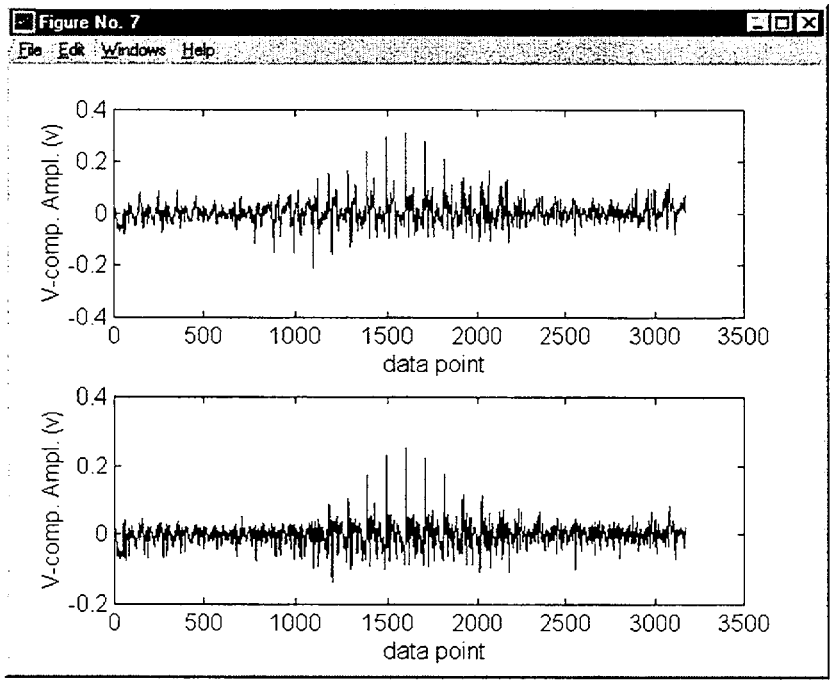

(b)

Fig. 3.7. Demonstration of 2-D signal suppression on RPC traces of (a) simulated raw data at 400 kHz (top) and 200 kHz (bottom) frequencies composed of a 40% TW axial OD notch at an arbitrarily selected location within a 270° tube support ring and (b) processed data using 400 kHz primary and 200 kHz auxiliary frequency (top) and 300 kHz primary and 100 kHz auxiliary frequency (bottom). In both cases, the processed data indicate substantial improvement of S/N ratio over original readings.

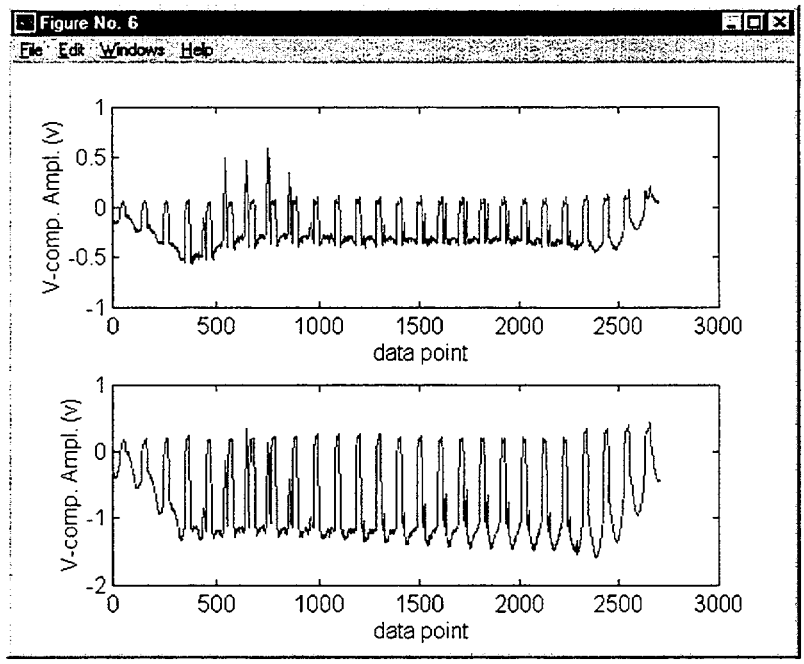

(a)

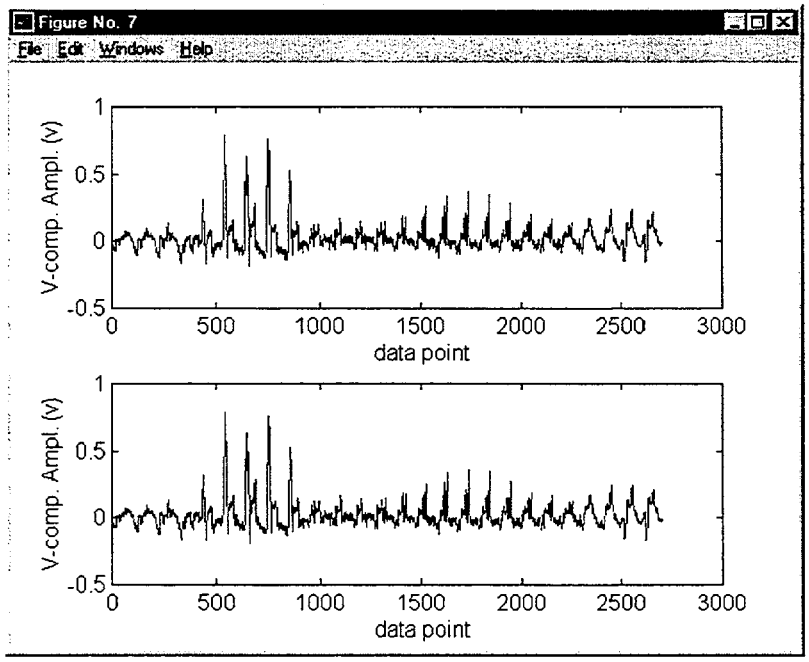

(b)

Fig. 3.8. Demonstration of 2-D signal suppression on RPC traces of (a) simulated raw data at 400 kHz (top) and 200 kHz (bottom) frequencies composed of a 40% TW axial OD notch and 40% TW circumferential ID notch at an arbitrarily selected locations within a 270° tube support ring and (b) processed data using 400 kHz primary and 200 kHz auxiliary frequency (top) and 300 kHz primary and 100 kHz auxiliary frequency (bottom). In both cases, the processed data indicates substantial improvement of S/N ratio over the original data.

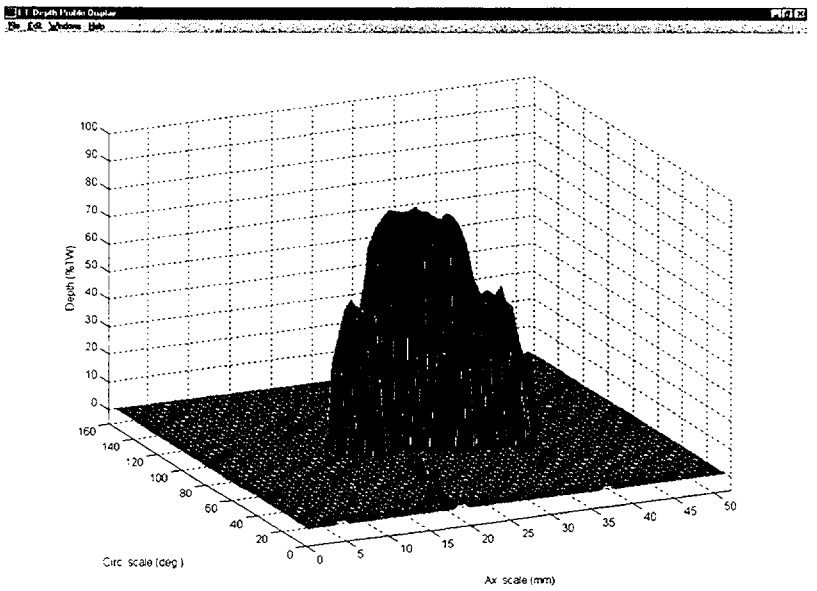

(a)

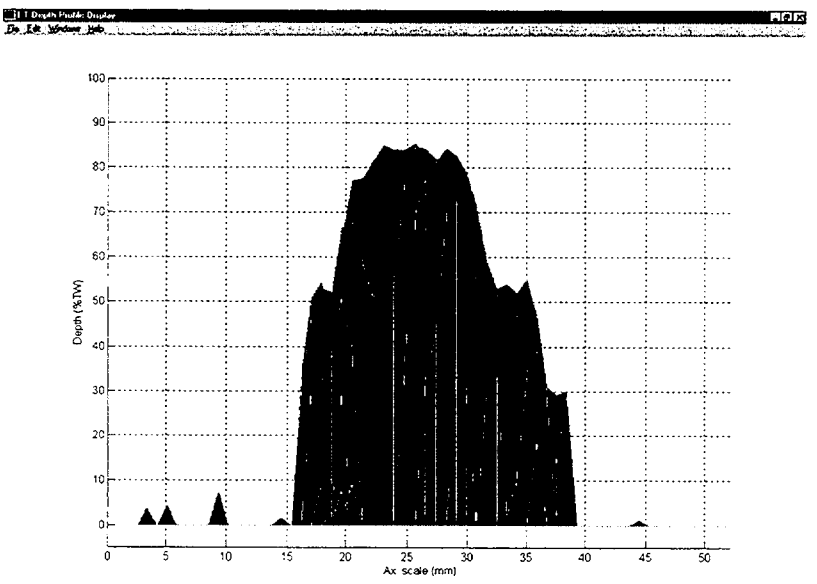

(b)

Fig. 3.9. Representative display of data analysis results for a laboratory-grown specimen with longitudinal ODSCC showing two views of estimated depth profile of cracked region. Figure 3.9(b) is a cross-sectional view of the terrain plot in Fig. 3.9(a). Profile indicates a ≈25-mm (1.0 in.)-long axial crack with maximum depth >80% TW.

in Fig. 3.10. Flaw length and maximum depth in this case are estimated to be 12.0 mm (0.5 in.) and ≈75% TW, respectively. Closer examination of this flaw through observation of graphics from various view angles revealed that the crack is composed of multiple axial segments. Further demonstration of the display format described here is provided in the following sections from profiling of various laboratory-grown specimens.

3.4 Analysis of Rotating-Probe Data from Laboratory-Grown Specimens

Data analysis results are presented next on representative samples from three separate batches of specimen with laboratory-grown SCC. Flaw types in these tubes are representative of those incorporated into the ANL tube bundle mock-up. All specimens used so far were made of 22.2-mm (0.875-in.)-diameter Alloy 600 tubing. Multiple-frequency NDE data was acquired with a standard three-coil rotating probe that incorporates a 2.92-mm (0.115-in.) pancake, a mid-range +Point, and 2.03-mm (0.080-in.) high-frequency pancake coil. The primary pancake coil readings were utilized for analyses.

Manufactured flaws in the first batch were composed primarily of circumferential and those in the second batch of axially oriented cracking. Additional samples are currently being produced under Task 3 activities to augment the library of tubes for NDE studies with a wider range of degradation morphologies. In particular, a batch of 31 tubes was produced recently to carry out blind studies for better assessment of the performance of alternate data analysis schemes in detection and sizing of various flaw types. Preliminary results are also presented here on the analysis of EC rotating-probe data on representative specimens from this collection of tubes. Analyses of laboratory-produced flaw types will aid incorporation of necessary refinements to rule-based algorithms for multiparameter analysis of NDE results currently under evaluation at ANL. Validation of NDE sizing results will be made through comparison with destructive examinations being performed as part of Task 3 activities.

Figures 3.11-3.15 display the results for selected tubes from the first batch of NDE samples containing OD- and ID-initiated cracks of primarily circumferential orientation. Figure 3.11 displays results of the analysis for a laboratory-grown specimen with circumferential ODSCC. The sizing profile is shown for two arbitrarily selected views of the estimated depth. Only the section of tube in the vicinity of the crack is shown. Figure 3.11(a) shows a representative display of intermediate results in image format. Preprocessed images at different stages of analysis for both the in-line standard (left) and the flawed tube (right) are shown. Presentation of data in this format provides a useful tool for visual identification of potential flaws that often show up as structured indications within the baseline signal. Figure 3.11(b) shows terrain plots of the estimated flaw profile from two different azimuth and elevation angles. Analysis results in this case indicate presence of ≈360° multiple parallel circumferential cracks with maximum depth of ≈80% TW. Figures 3.12 and 3.13 display the sizing results for three other specimens with circumferential cracking. Finally, Figs. 3.14 and 3.15 show the profile of an axial crack from the same batch of tubes. Analyses of EC inspection data on this set suggest that a majority of flaws are quite complex in nature.

Figure 3.16 displays the analysis results for a laboratory-degraded specimen with circumferential ODSCC degradation. Estimated depth profiles are shown as a terrain plot, as well as axial and circumferential cross sections of the tube. Only the section of tube in the vicinity of the crack is shown here. Figure 3.16(a) shows a terrain plot of the estimated flaw

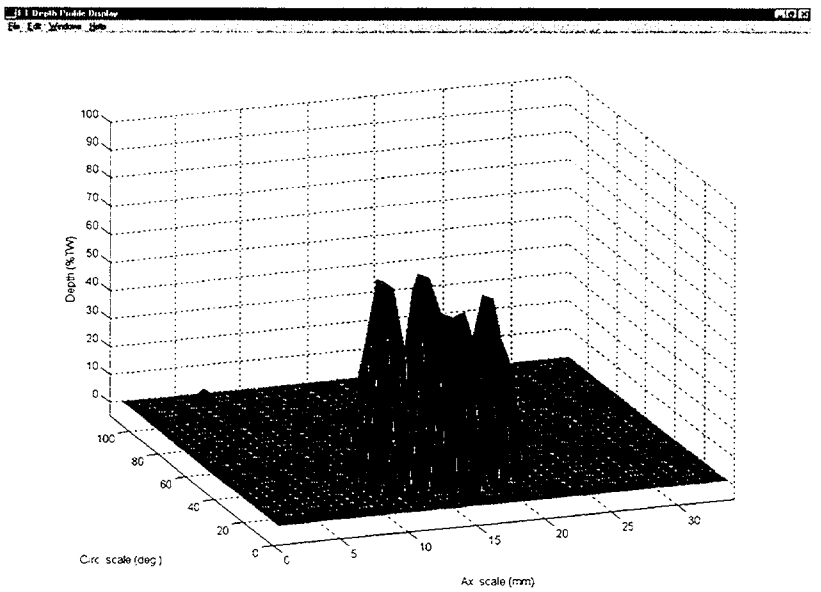

(a)

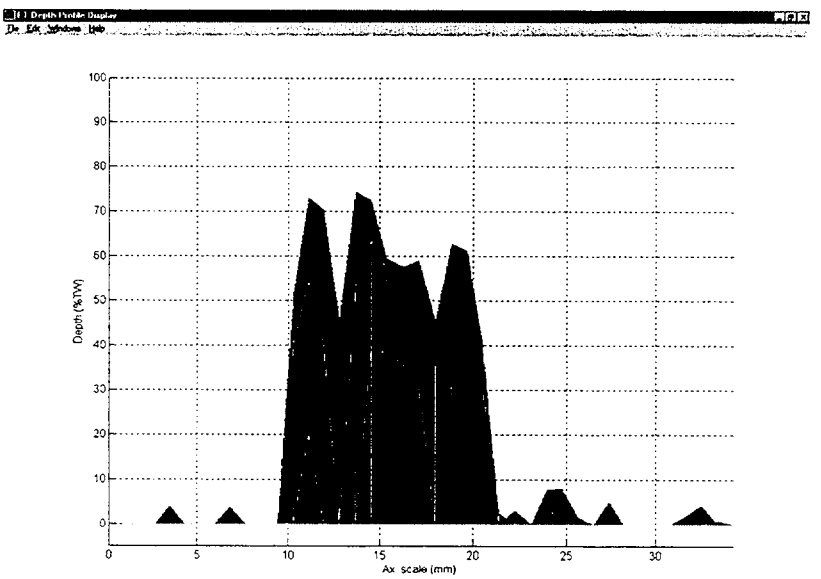

(b)

Fig. 3.10. Representative display of data analysis results for a specimen with laboratory-grown longitudinal ODSCC showing two views of estimated depth profile of cracked region. Figure 3.10(b) is a cross-sectional view of the terrain plot in Fig. 3.10(a). The profile indicates a total flaw length of ≈12 mm (0.5 in.), with maximum depth >70% TW. Close observation of graphics from various view angles reveals the axial crack to be composed of multiple segments.

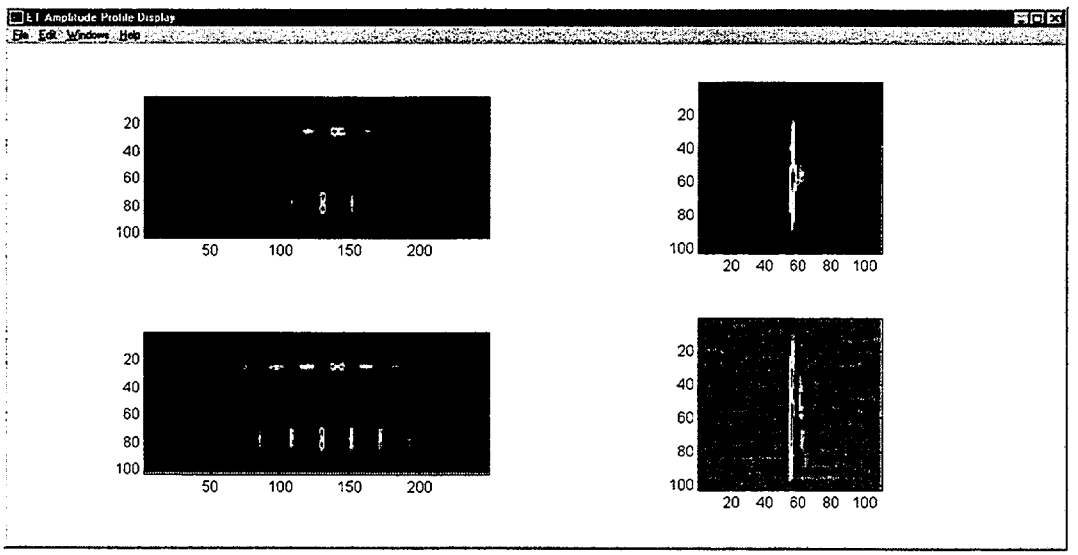

(a)

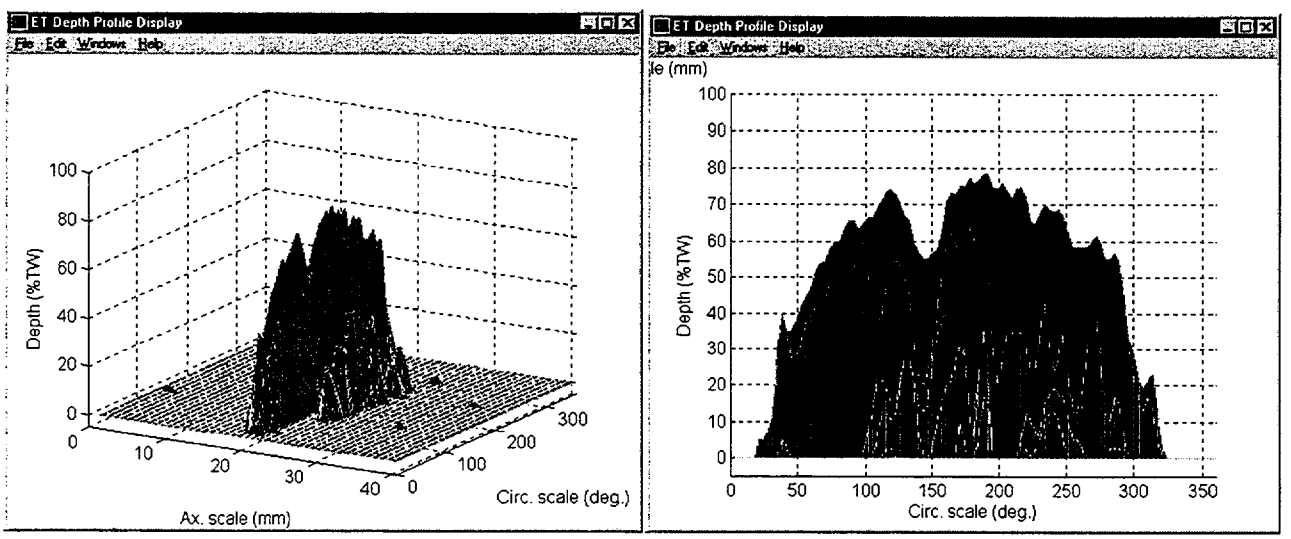

(b)

Fig. 3.11. Representative display of data analysis results for specimen with laboratory-grown circumferential ODSCC showing (a) pre- (top) and post-processed (bottom) images of normalized data and (b) terrain and cross sectional plots of estimated flaw profile. Results indicate ≈360° circumferential cracking, with maximum depth of ≈80% TW.

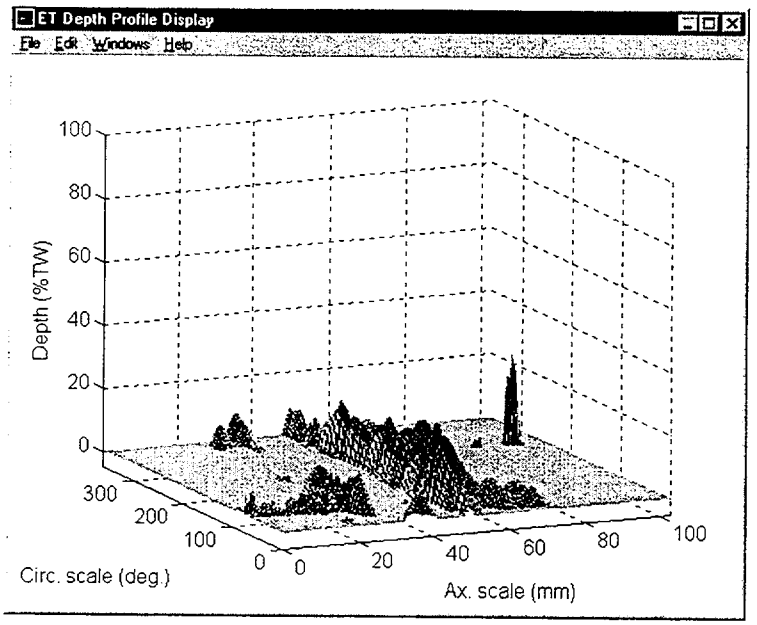

(a)

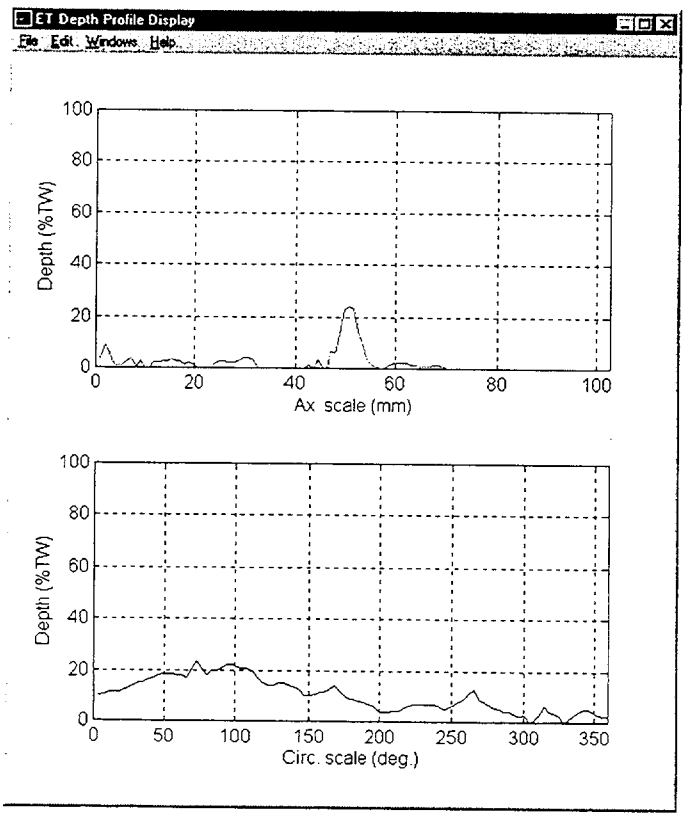

(b)

Fig. 3.12. Representative display of data analysis results for specimen with laboratory-grown shallow circumferential IDSCC showing (a) terrain and (b) cross-sectional plots of estimated flaw profile. Results indicate ≈360° circumferential cracking with maximum depth of >20% TW.

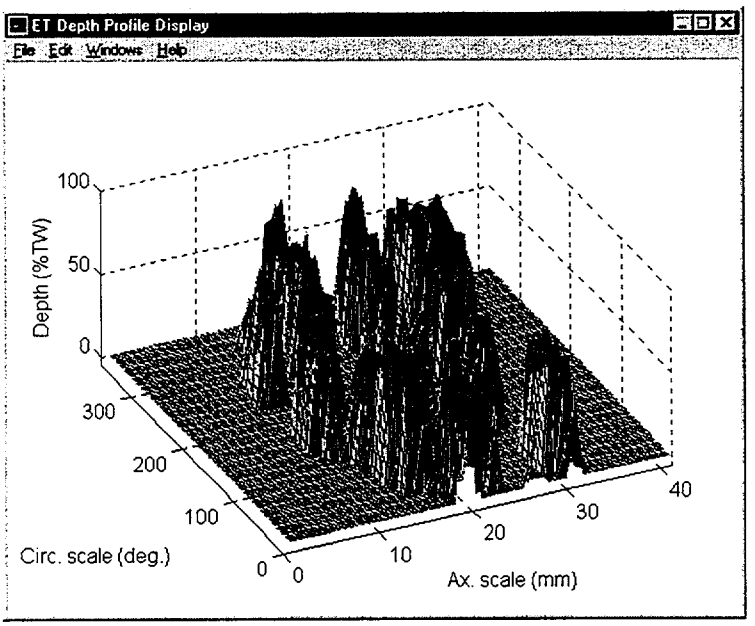

(a)

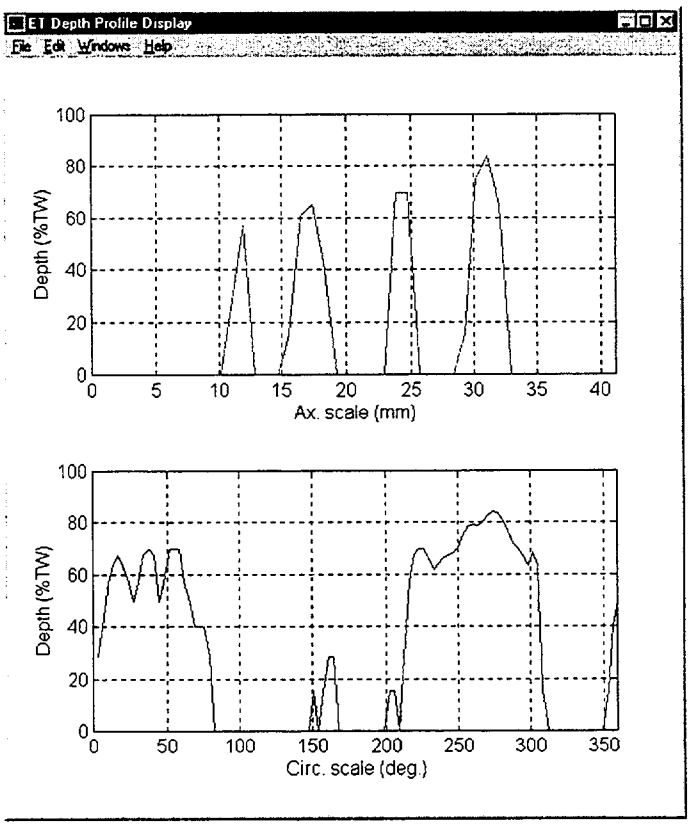

(b)

Fig. 3.13. Representative display of data analysis results for specimen with laboratory-grown circumferential ODSCC showing (a) terrain and (b) cross-sectional plots of estimated flaw profile. Results indicate ≈360° staggered circumferential cracking with maximum depth of >80% TW.

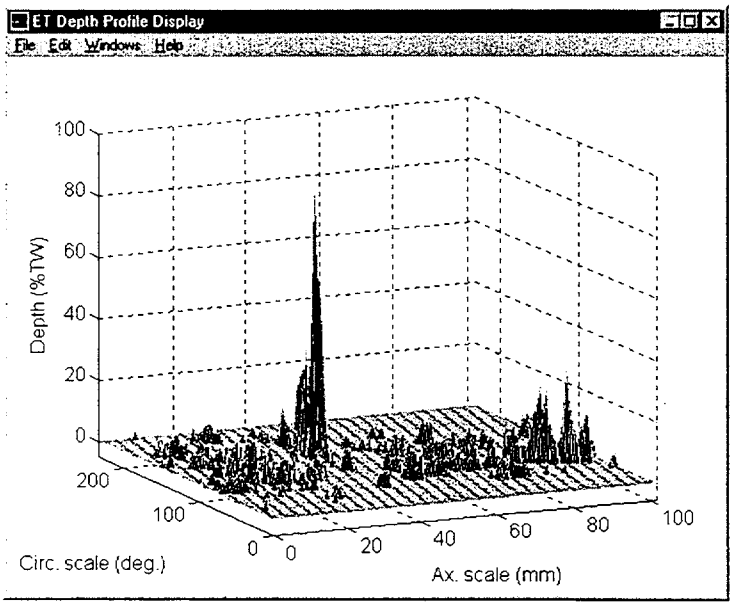

(a)

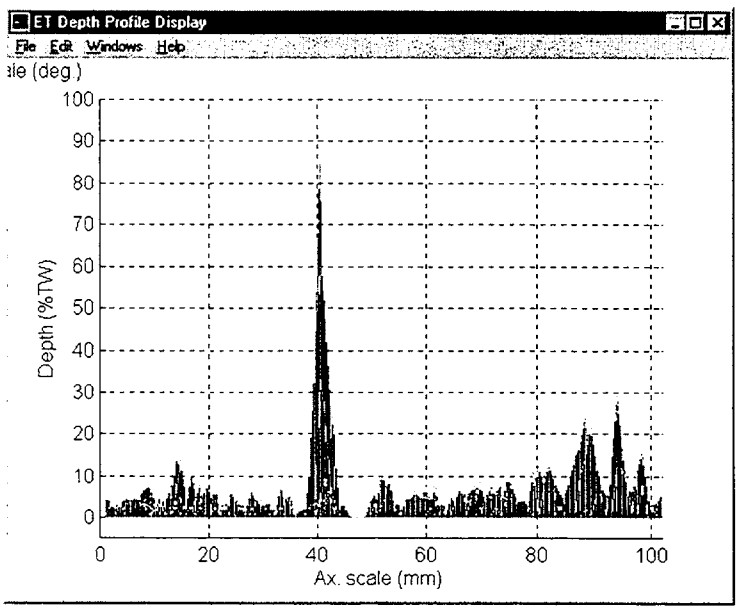

(b)

Fig. 3.14. Representative display of data analysis results for specimen with laboratory-grown axial IDSCC showing (a) terrain plot and (b) cross-sectional view of estimated flaw profile. Results indicate dominant single axial crack with maximum depth of >80% TW.

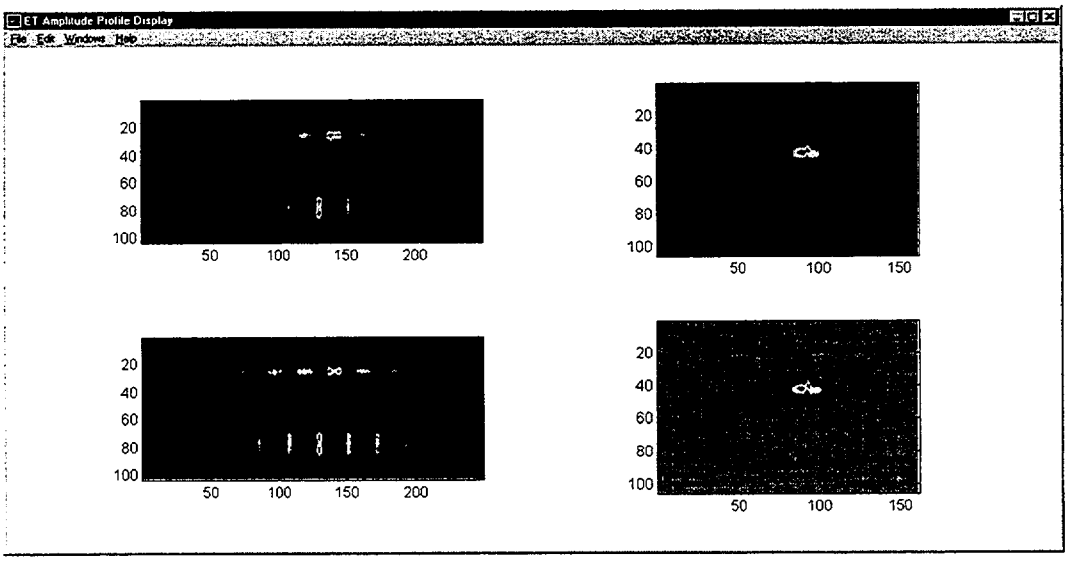

(a)

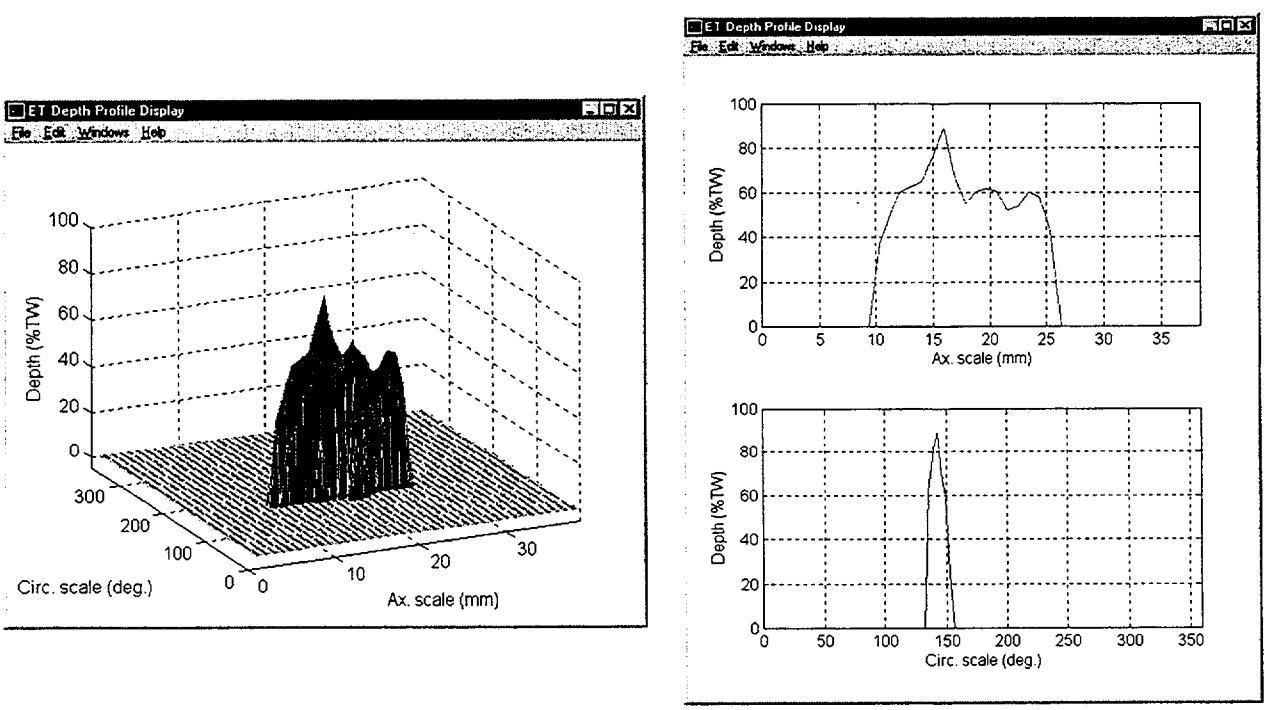

(b)

Fig. 3.15. Representative display of data analysis results for specimen with laboratory-grown axial ODSCC showing (a) pre- (top) and post-processed (bottom) images of normalized data and (b) terrain and cross-sectional plots of estimated flaw profile. Results indicate >15-mm (0.6-in.)-long axial crack with maximum depth of ≈90% TW.

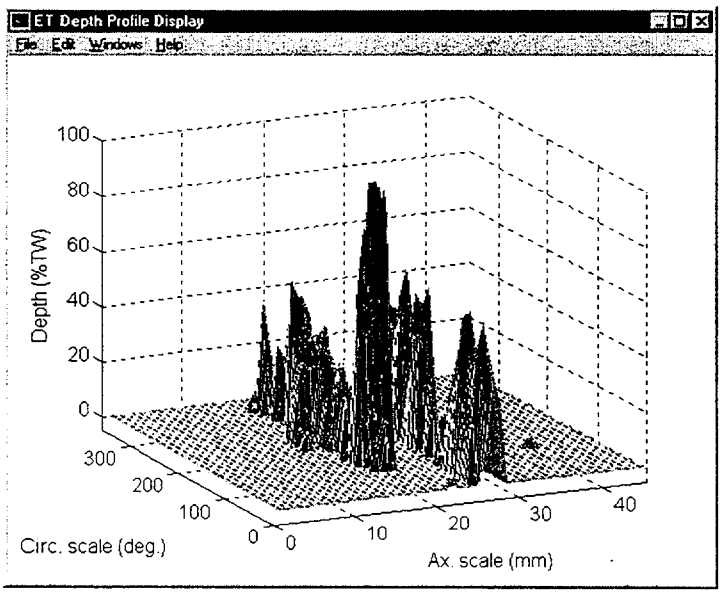

(a)

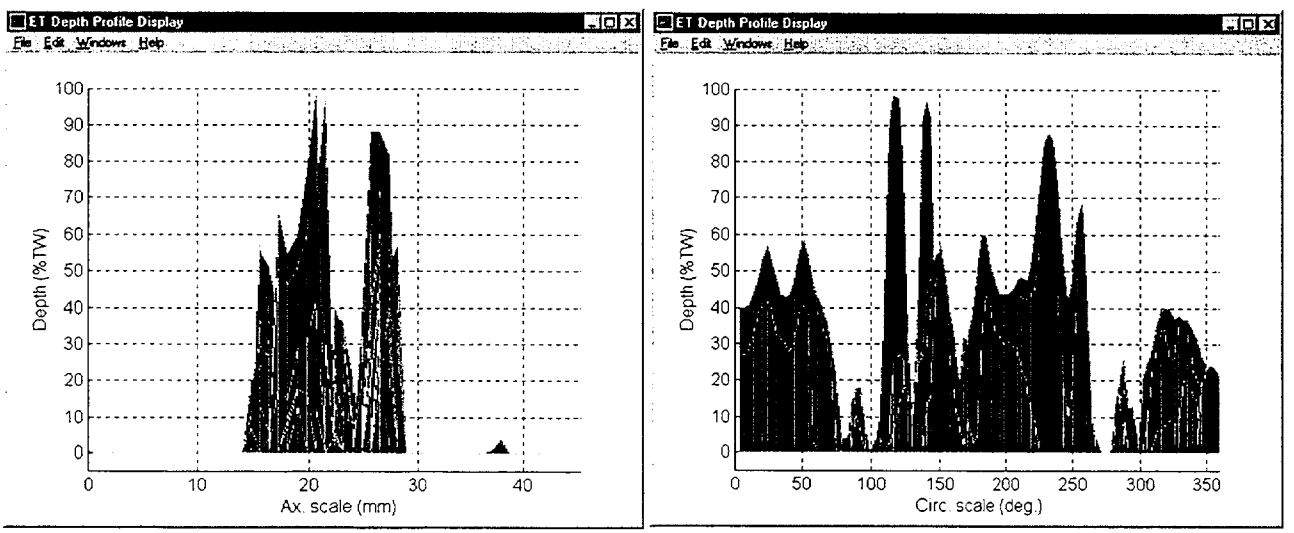

(b)

Fig. 3.16. Representative display of data analysis results for specimen with laboratory-grown circumferential ODSCC showing (a) terrain and (b) cross-sectional views of estimated flaw profile. Results indicate the ≈360° circumferential cracking with maximum depth >90% TW.

depth profile from an arbitrarily chosen azimuth and elevation angle. Figure 3.16(b) shows the same data from axial and circumferential viewpoints, respectively. Analysis results in this case indicate the presence of 360° multiple circumferential cracking with a maximum depth exceeding 90% TW.

Figure 3.17 shows similar results for a specimen with multiple axial ODSCC degradation. The dominant indications are two parallel axial cracks with maximum depths estimated to be ≈90% TW. Figures 3.18-3.20 display sizing results for three other representative specimens from this sample set that contain multiple axial indications. Eddy current inspection results from this second batch of tubes generally indicate that the majority of flaws are less complex in their morphology than the earlier batch of NDE tubes that contained mostly circumferentially oriented cracking.

A batch of 31 tubes containing various crack types and sizes are being utilized to further assess the capability of computer-aided data analysis algorithms that are being evaluated at Argonne. Flawed tubes in this set have been augmented with blank specimens having no visible damage, to better test the techniques. Eddy current readings on these tubes were acquired with and without simulated artifacts such as TSP, sludge, magnetite, and copper deposits that may be present to different degrees during field inspections. The effect of tube dimensional variations on detection and sizing of indications is also simulated by producing flaws within the transition zone of mechanically rolled tube sections. Initial results are presented next on multiparameter analysis of RPC data on selected specimens from the 31-tube set of laboratory-grown flaws. Efforts are currently underway to characterize flaws in the remaining samples.

Figures 3.21-3.29 display the analysis results for a subset of the 31-tube laboratory-grown specimens. In all cases, the results are shown as amplitude image displays of the standard and flawed tube at intermediate stages of processing, along with the estimated 3-D depth profile in the vicinity of the flawed region. The terrain plot is also displayed from two different view angles to provide axial and cross-sectional profiles. For the set of samples shown here, the profile of degraded regions suggests the presence of OD-initiated SCC in all tubes except one, which seems to contain cracks that originate from the ID side of the tube. Eddy current inspection results from this batch of samples show a wide range of complexity in the geometry of flaws, varying from single axial/circumferential to multiple and mixed-mode cracking.

Efforts are being made in parallel under Task 3 of this program to provide metallography/fractography results for these specimens. Feedback from these efforts will aid in assessing the results of NDE analyses and to help identify potential refinements for improvement of the RPC profiling algorithm. A more comprehensive description of the analytical results for all the specimens from the set of 31 tubes will be presented in our follow-up reports.

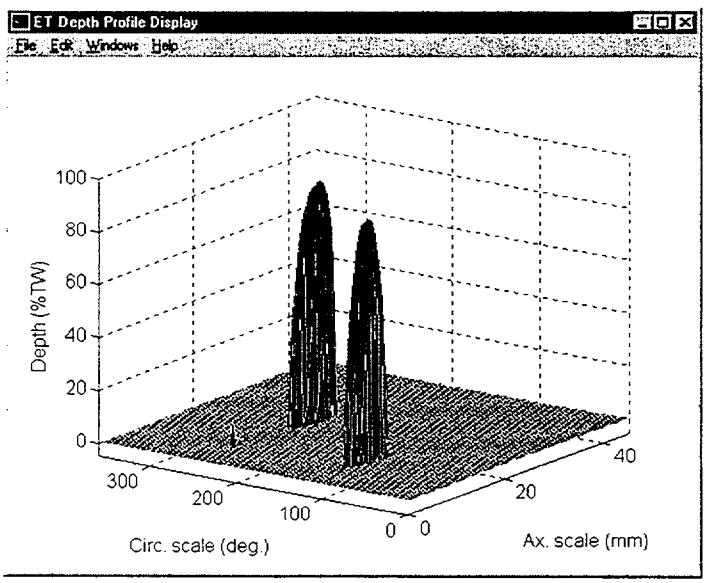

(a)

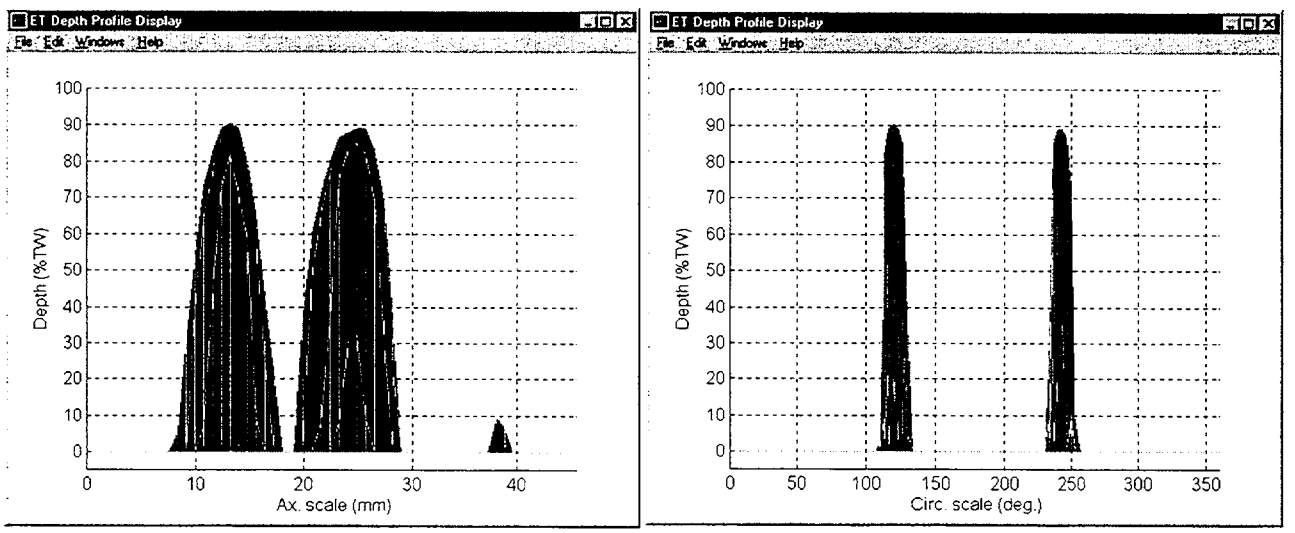

(b)

Fig. 3.17. Representative display of data analysis results for specimen with laboratory-grown axial ODSCC showing (a) terrain and (b) cross-sectional views of estimated flaw profile. Results show two indications with maximum depths >80% TW.

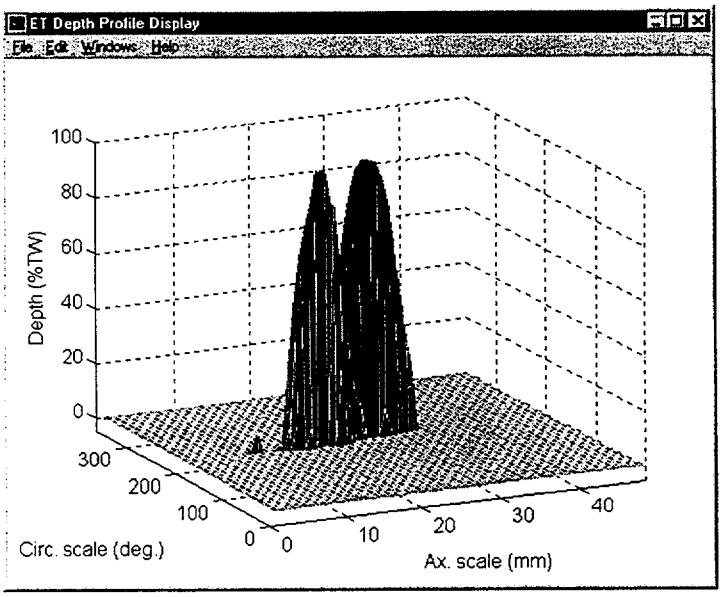

(a)

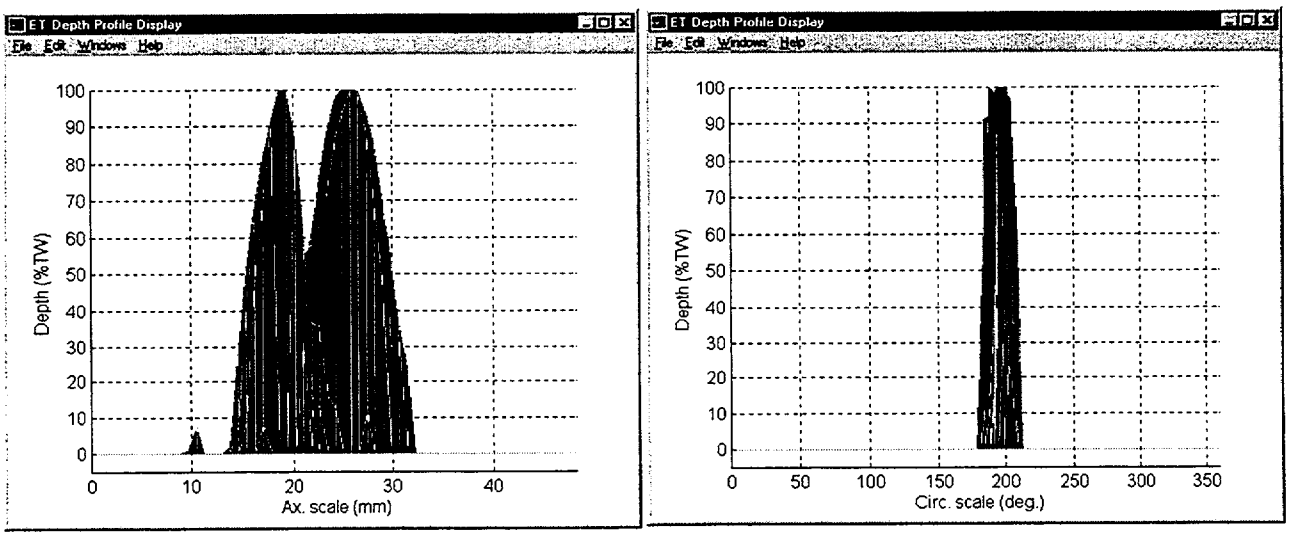

(b)

Fig. 3.18. Representative display of data analysis results for specimen with laboratory-grown axial ODSCC showing (a) terrain and (b) cross-sectional views of estimated flaw profile. Results indicate two closely spaced parallel (axially offset) cracks with maximum depths reaching 100% TW.

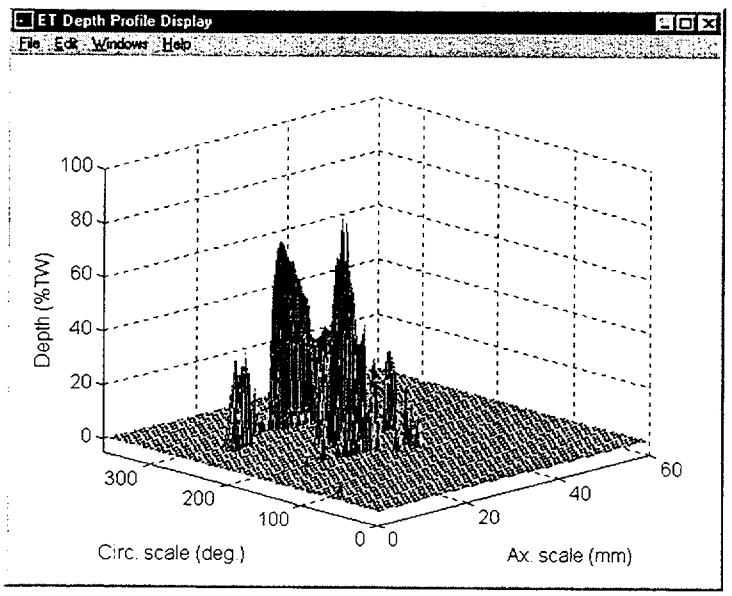

(a)

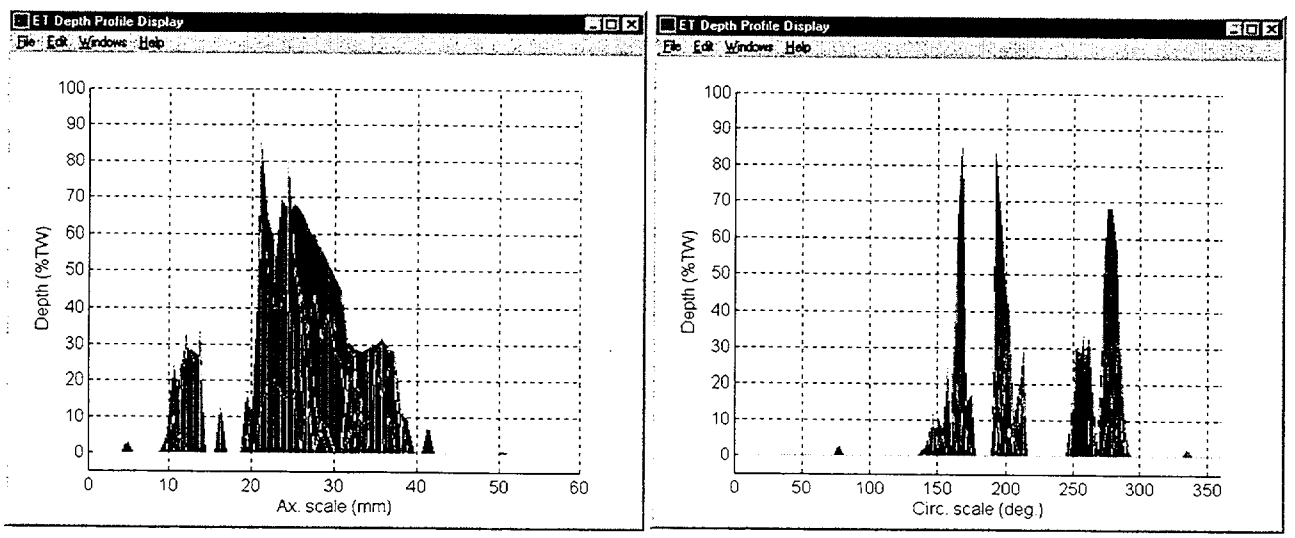

(b)

Fig. 3.19. Representative display of data analysis results for specimen with laboratory-grown axial ODSCC showing (a) terrain and (b) cross-sectional views of estimated flaw profile. Results indicate multiple axial cracks with maximum depths >80% TW.

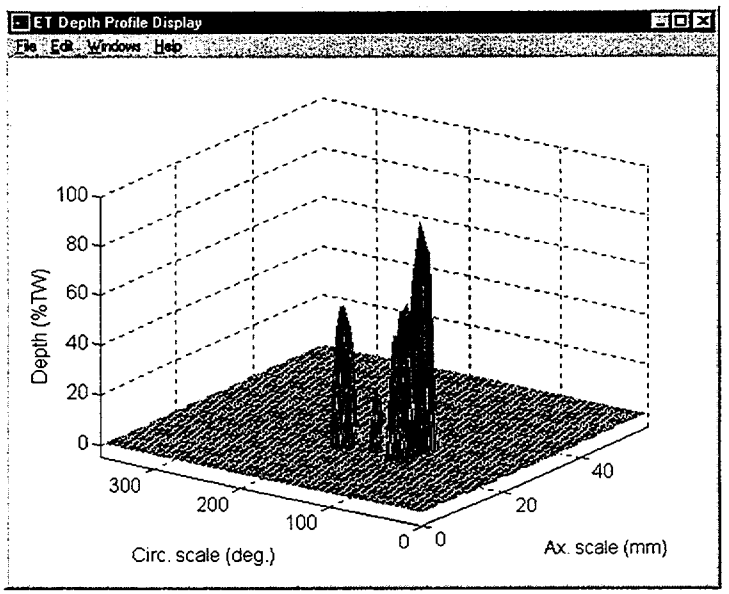

(a)

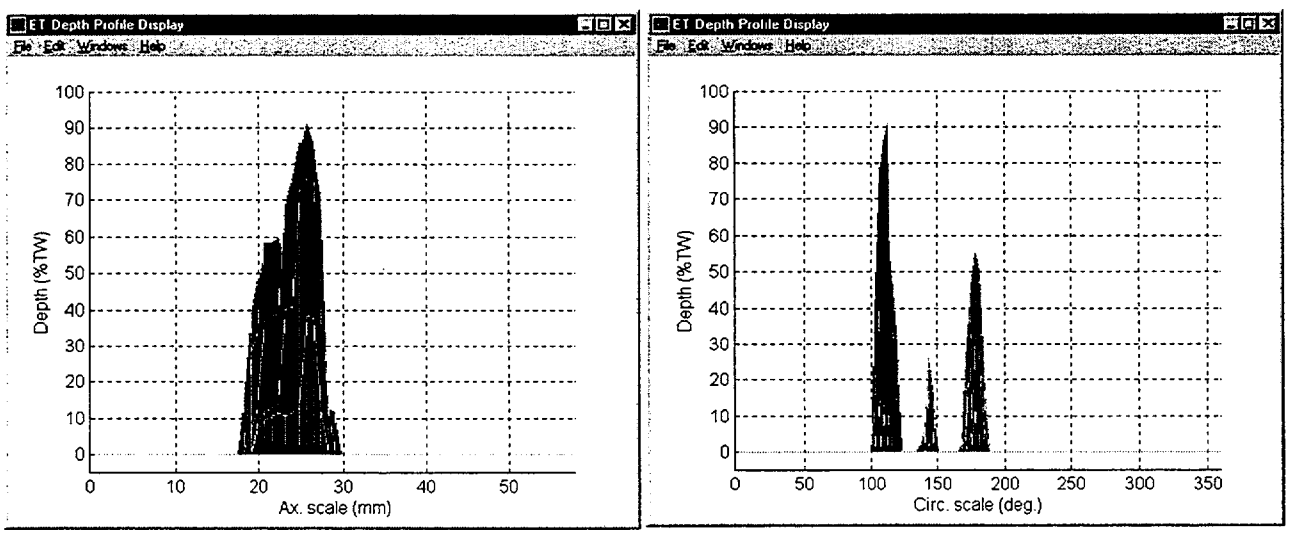

(b)

Fig. 3.20. Representative display of data analysis results for specimen with laboratory-grown axial ODSCC showing (a) terrain and (b) cross-sectional views of estimated flaw profile. Results indicate multiple axial cracks with maximum depths >80% TW.

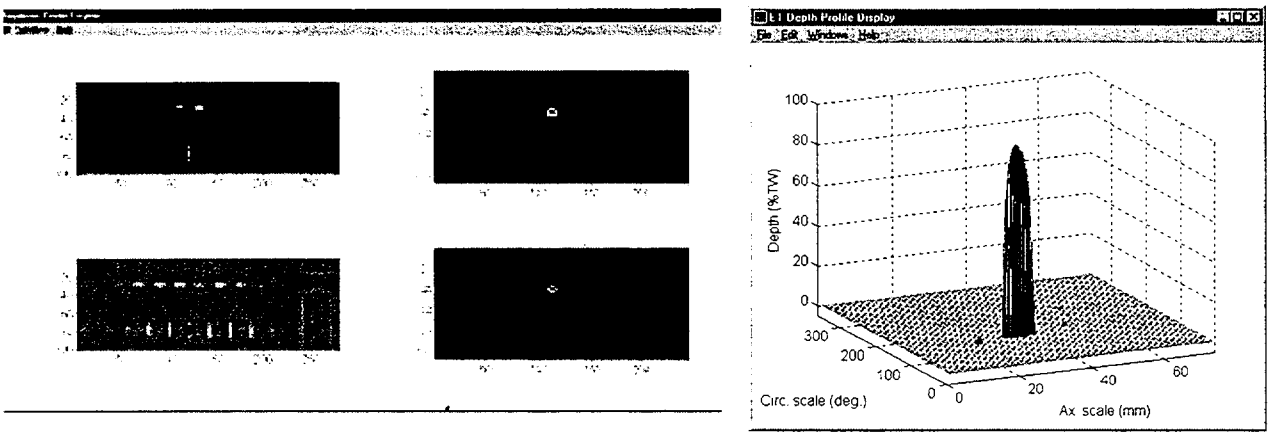

(a)

(b)

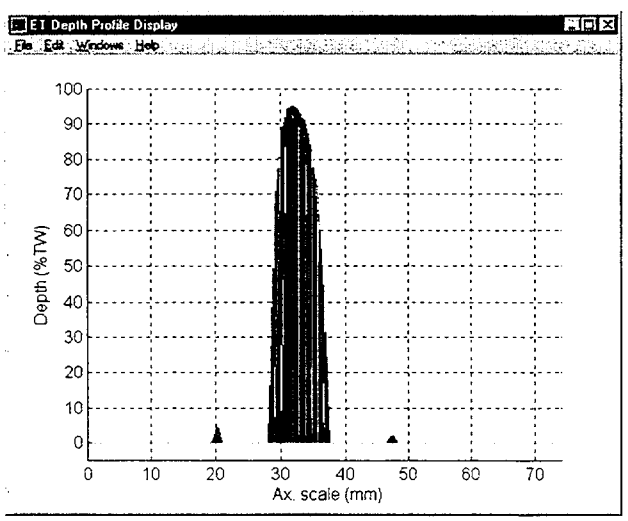

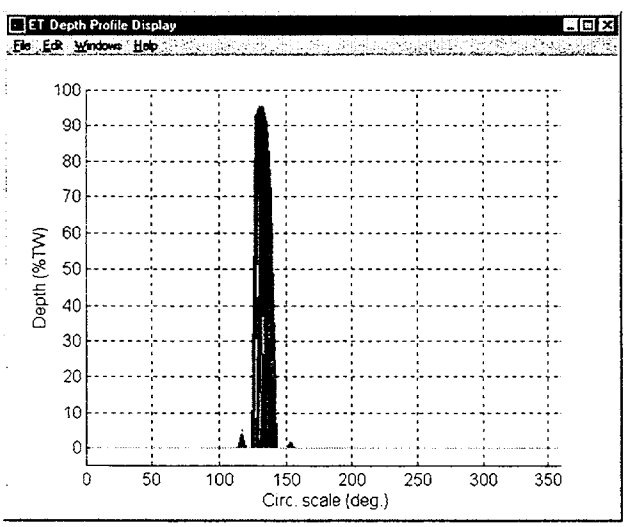

(c)

Fig. 3.21. Representative display of data analysis results for specimen with laboratory-grown ODSCC degradation showing (a) image display, (b) terrain profile, and (c) cross-sectional views of estimated flaw size. Results indicate single crack with maximum depth >90% TW.

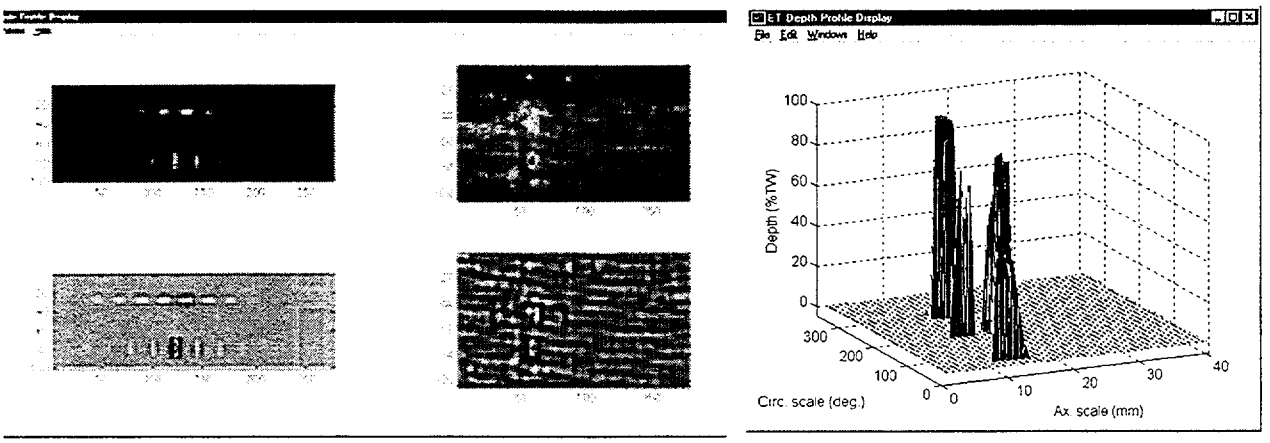

(a)

(b)

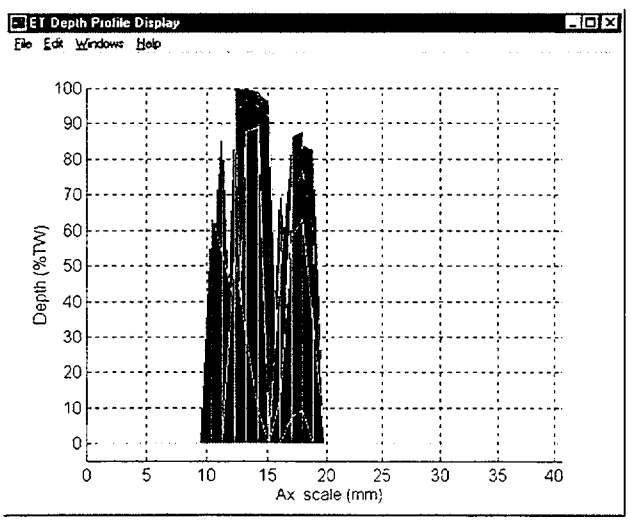

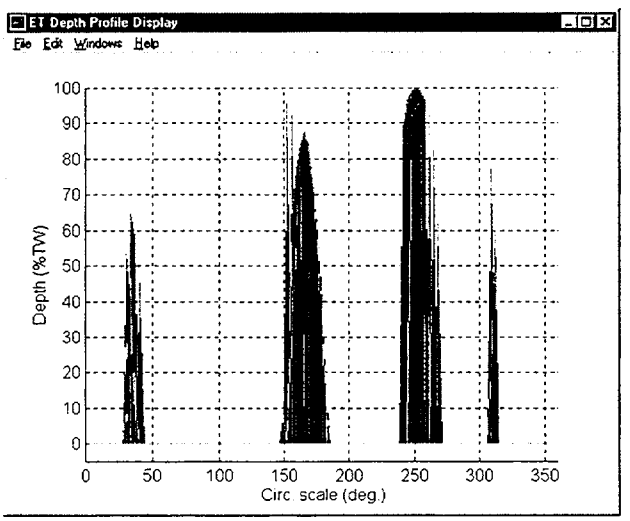

(c)

Fig. 3.22. Representative display of data analysis results for specimen with laboratory-grown ODSCC degradation showing (a) image display, (b) terrain profile, and (c) cross sectional views of estimated flaw size. Results indicate multiple cracks around circumference, with maximum depth of dominant flaw reaching 100% TW.

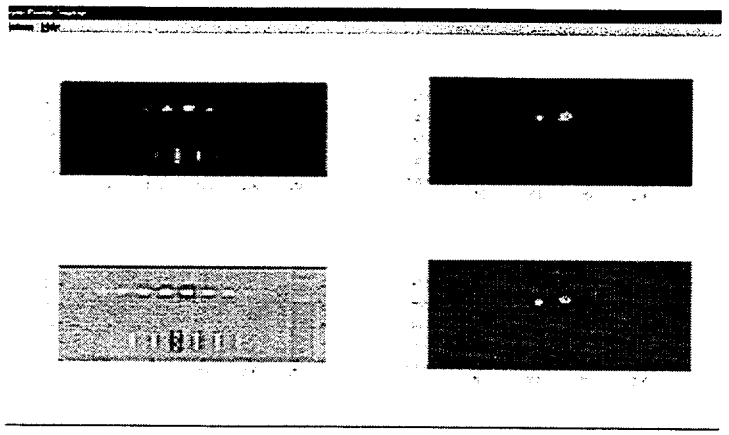

(a)

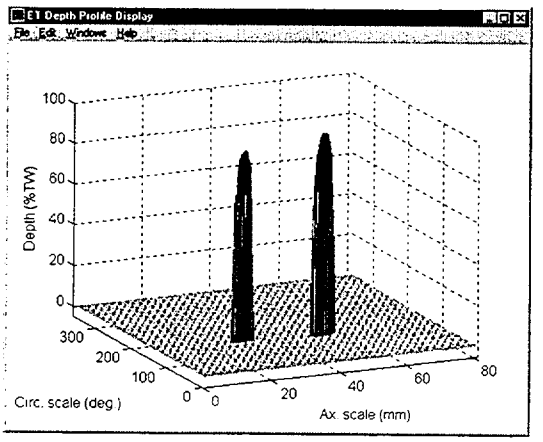

(b)

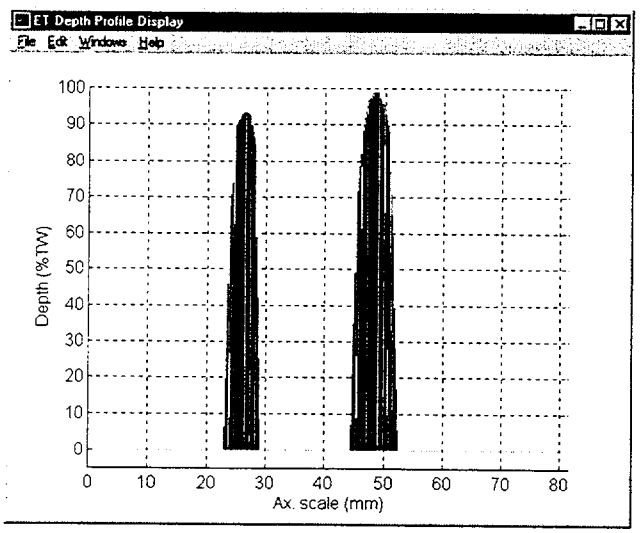

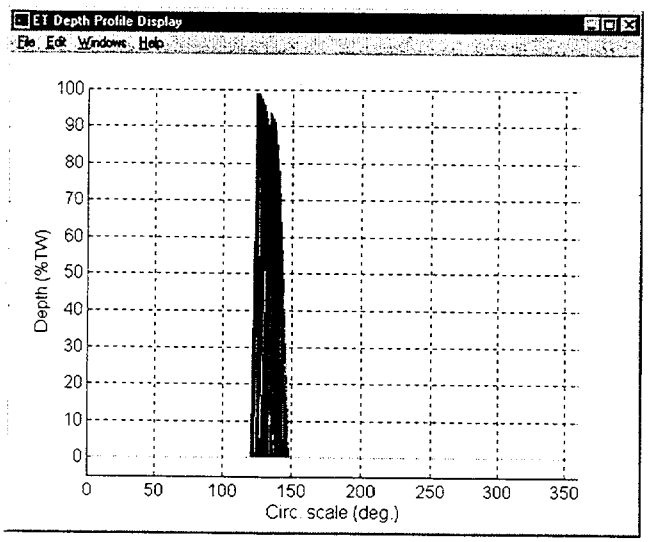

(c)

Fig. 3.23. Representative display of data analysis results for specimen with laboratory-grown ODSCC degradation showing (a) image display, (b) terrain profile, and (c) cross-sectional views of estimated flaw size. Results indicate two circumferentially offset cracks, with maximum depth reaching ≈100% TW.

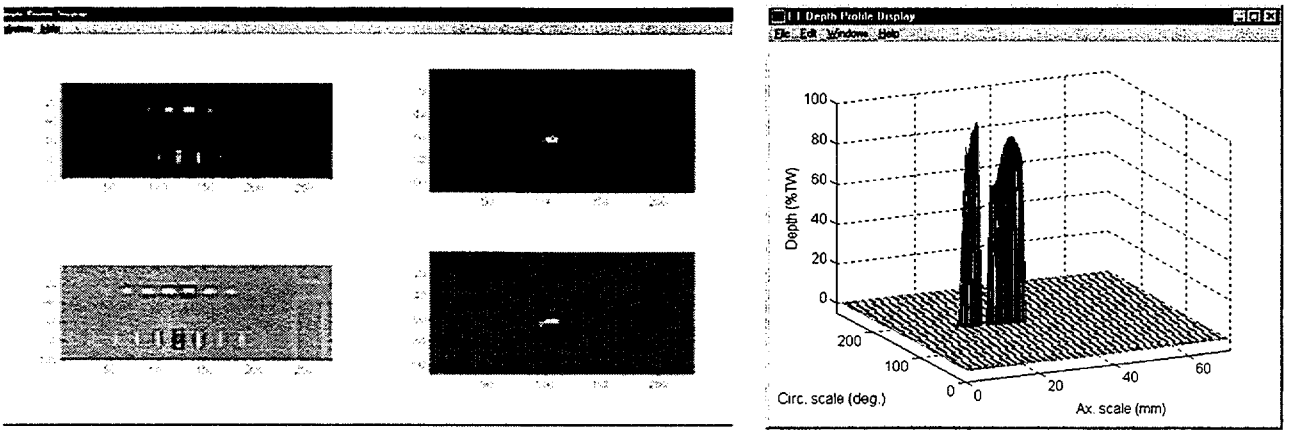

(a) (b)

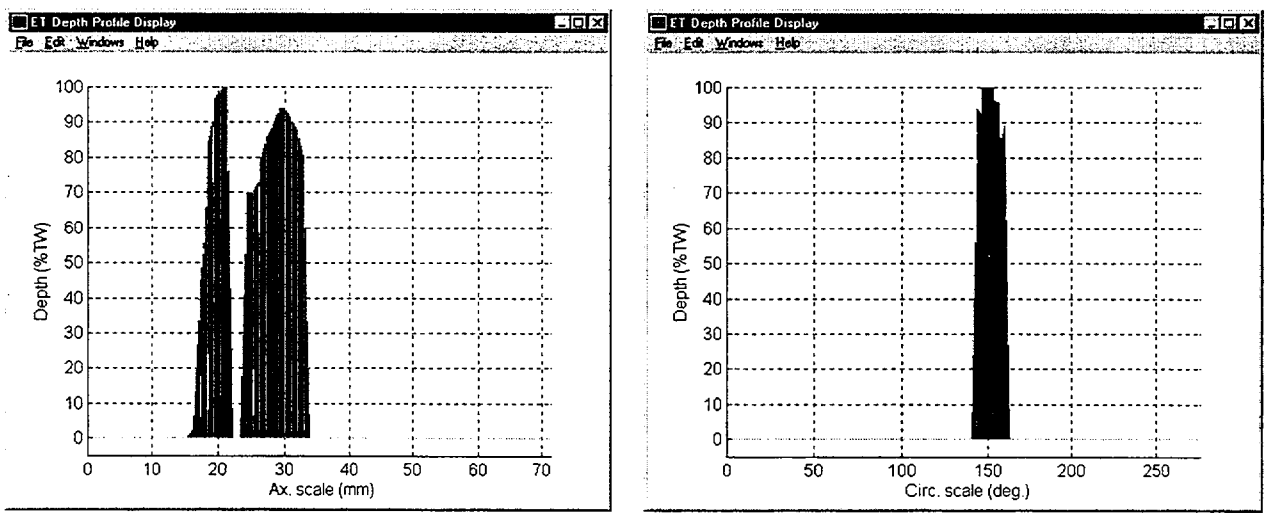

(c)

Fig. 3.24. Representative display of data analysis results for specimen with laboratory-grown ODSCC degradation showing (a) image display, (b) terrain profile, and (c) cross-sectional views of estimated flaw size. Results indicate segmented crack with maximum depth of ≈100% TW.

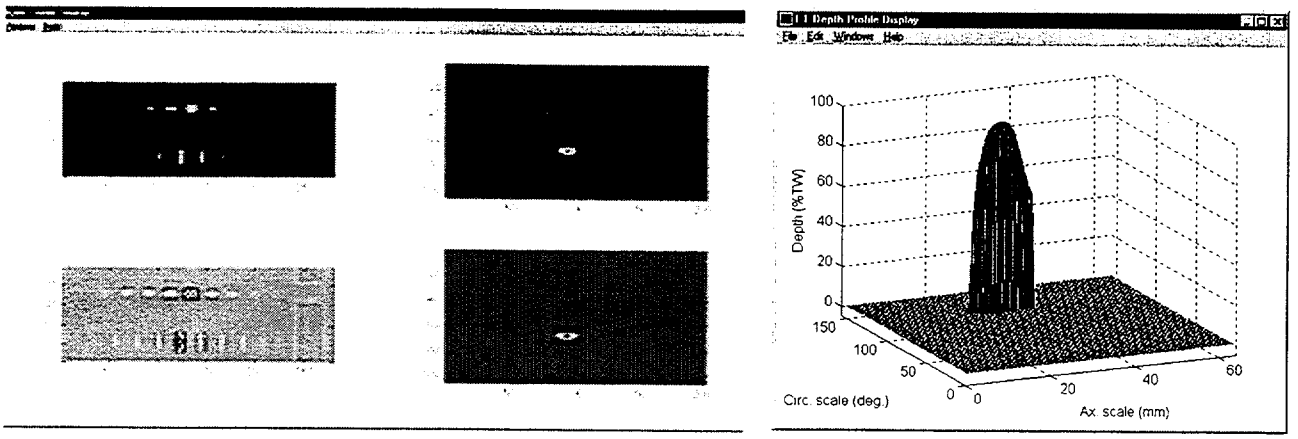

(a)

(b)

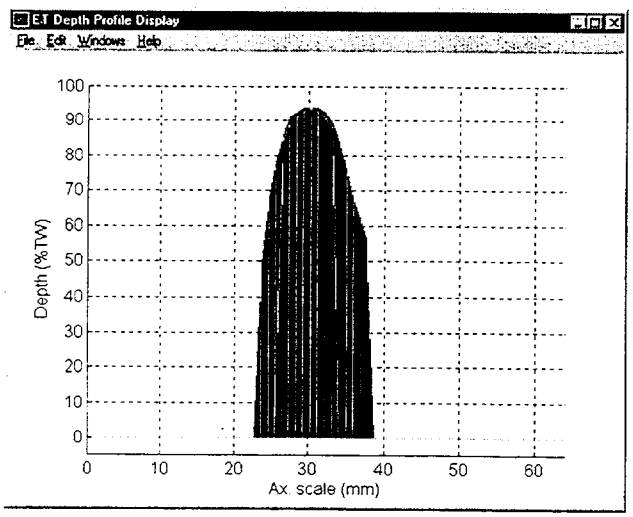

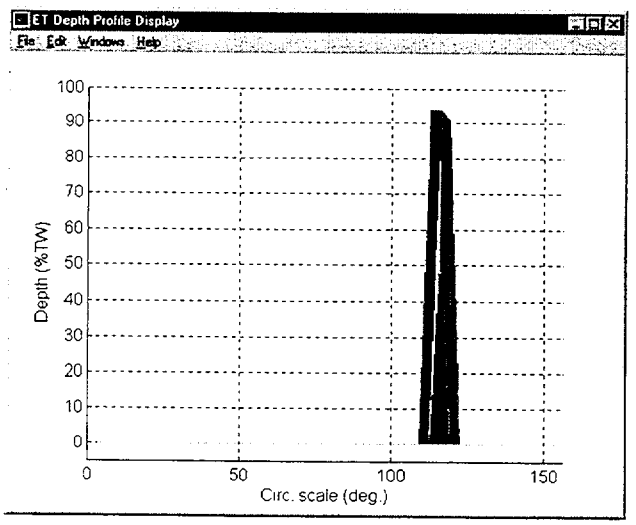

(c)

Fig. 3.25. Representative display of data analysis results for specimen with laboratory-grown ODSCC degradation showing (a) image display, (b) terrain profile, and (c) cross-sectional views of estimated flaw size. Results indicate single crack with maximum depth >90% TW.

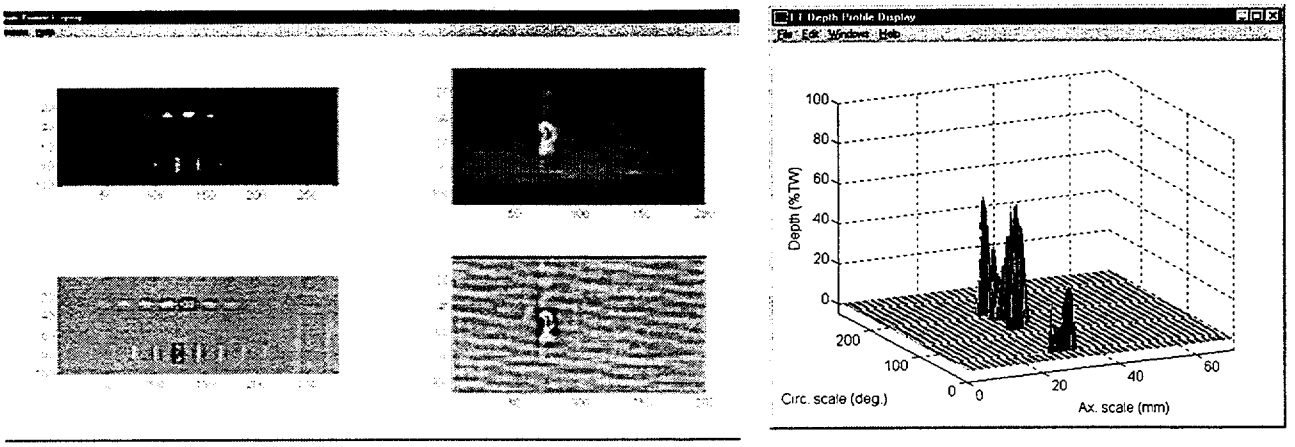

(a)

(b)

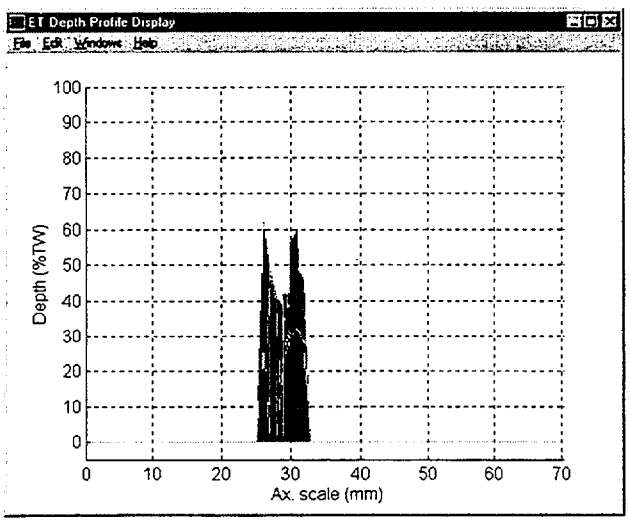

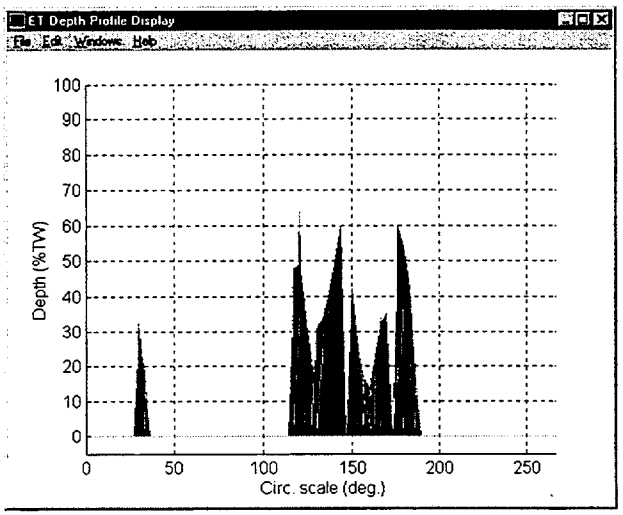

(c)

Fig. 3.26. Representative display of data analysis results for specimen with laboratory-grown ODSCC degradation showing (a) image display, (b) terrain profile, and (c) cross-sectional views of estimated flaw size. Results indicate multiple cracks around circumference, with maximum depth >60% TW.

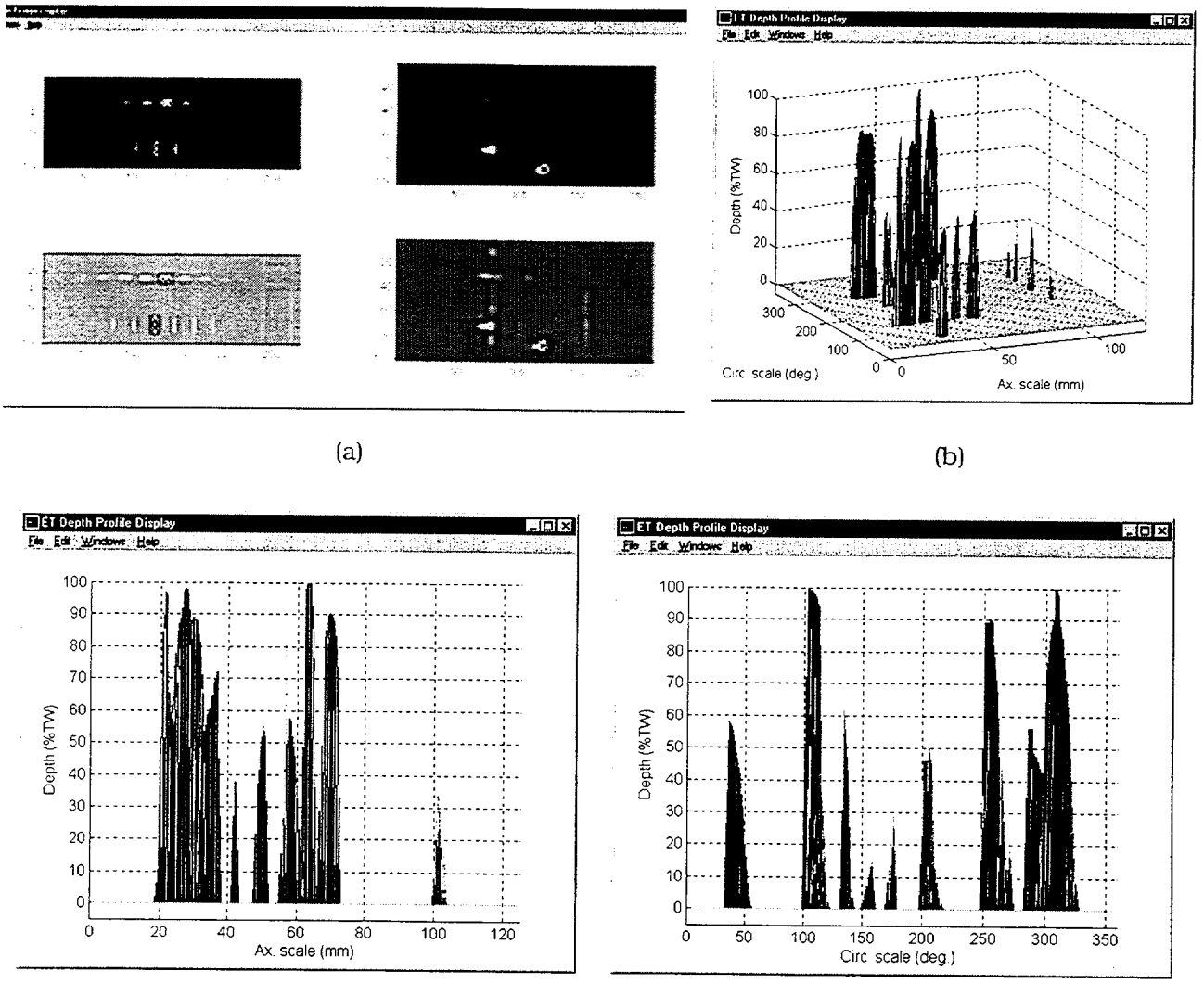

Fig. 3.27. Representative display of data analysis results for specimen with laboratory-grown ODSCC degradation showing (a) image display, (b) terrain profile, and (c) cross-sectional views of estimated flaw size. Results indicate multiple cracks around circumference, with maximum depth of dominant flaws reaching ≈100% TW.

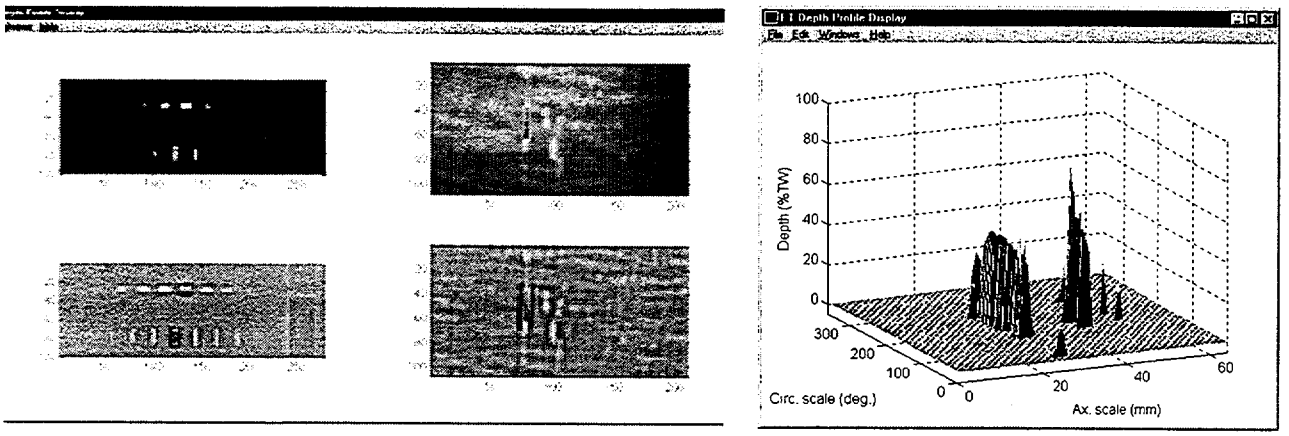

(a)

(b)

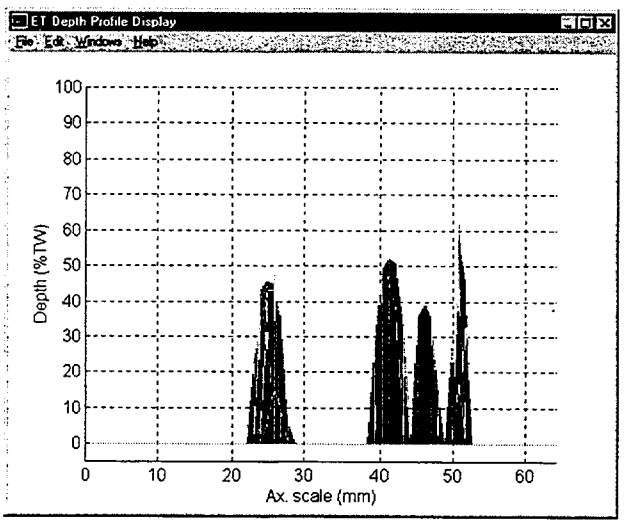

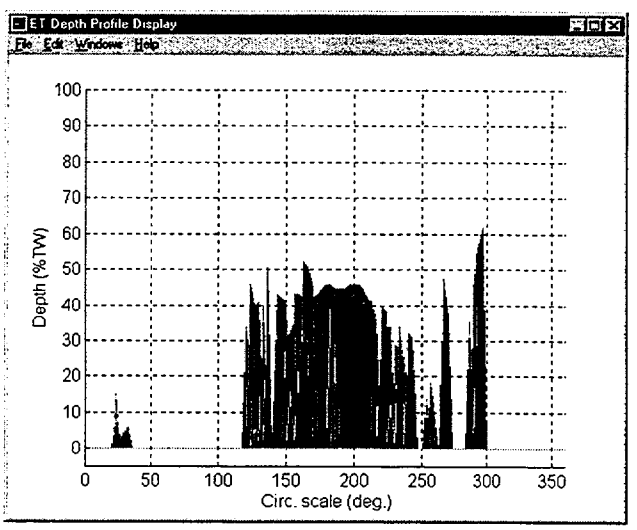

(c)

Fig. 3.28. Representative display of data analysis results for specimen with laboratory-grown ODSCC degradation showing (a) image display, (b) terrain profile, and (c) cross-sectional views of estimated flaw size. Results indicate multiple cracks at several axial locations around circumference, with maximum depth >60% TW.

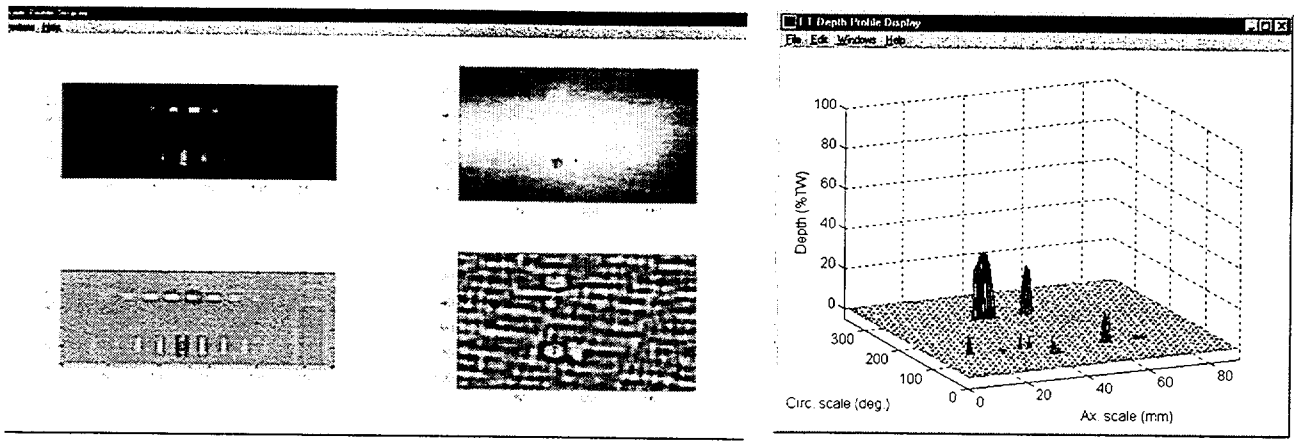

(a)

(b)

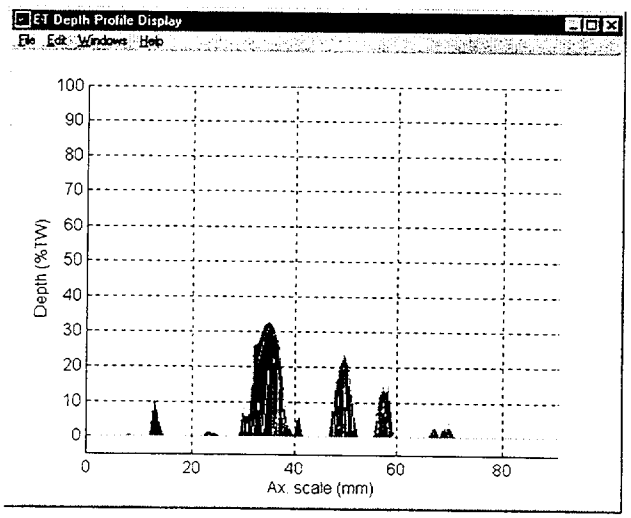

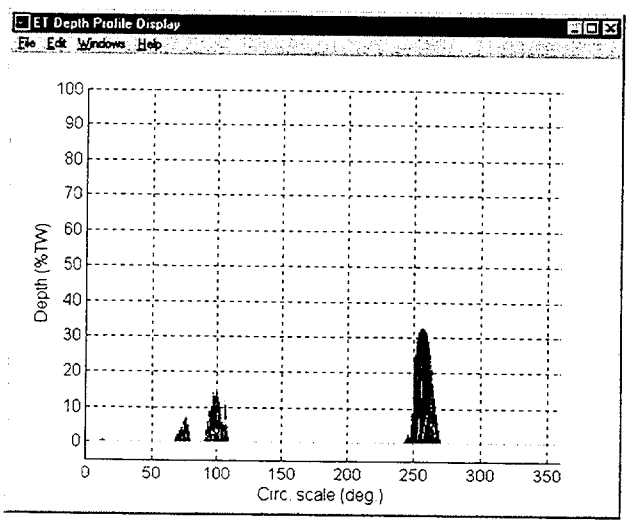

(c)

Fig. 3.29. Representative display of data analysis results for specimen with laboratory-grown IDSCC degradation showing (a) image display, (b) terrain profile, and (c) cross-sectional views of estimated flaw size. Results indicate multiple cracks, with dominant crack depth >30% TW.

4 Research on Degradation Modes and Integrity (K. E. Kasza, S. Majumdar, J. Y. Park. W. J. Shack, and D. R. Diercks)

4.1 Production and Characterization of Laboratory-Degraded Tubes

Production of laboratory-degraded 22.2-mm (7/8-in.)-diameter Alloy 600 tube specimens continued with material from Heats NX8527, NX8520L, and NX8520H. Cracking is accomplished using a 1M aqueous solution of sodium tetrathionate at room temperature and atmospheric pressure. The material was first mill-annealed for 3 min at 940°C for Heat NX8527, 3 min at 980°C (1796°F) for Heat NX8520L and for 2 min at 1060°C (1940°F) for Heat NX8520H. All specimens were then sensitized by heat-treating at 600°C (1112°F) for 48 h prior to exposure to the sodium tetrathionate solution to produce a microstructure that is susceptible to cracking. During this reporting period, 101 tubes were exposed in an attempt to produce axial ODSCC (76 specimens), axial IDSCC (12 specimens), circumferential ODSCC (5 specimens), and circumferential IDSCC (8 specimens). Four specimens were dented tubes (25-100 μm [1-4 mil]-deep semicircular dents on OD).

To accelerate cracking, some specimens from Heat NX8527 were additionally solution-heat-treated at 1010-1100°C for 10-20 min before the sensitization heat treatment at 600°C for 48 h. Cracking time ranged from 17 to 2389 h. The specimens that received the high-temperature solution heat treatment cracked in shorter times than those without the solution heat treatment. However, this solution heat treatment caused a reduction in flow stress of up to ≈20%, as previously reported,[1] and its avoidance eliminated this reduction in strength. The sensitization heat treatment at 600°C for 48 h did not weaken the material. For example, the Vickers hardness of tubes from Heat NX8520L was 160 and 165 before and after the sensitization heat treatment, respectively. Various techniques, including localized environmental exposure, low applied load, and controlled electrochemical potential, have been utilized in an effort to produce segmented SCC.

The cracked tubes were examined by eddy current NDE. Figure 4.1 shows the eddy current NDE result for Specimen SGL717 with an axial ODSCC indication having an estimated depth of 90% TW. Figures 4.2 and 4.3 show EC results for Specimens SGL473 and SGL492 with axial ODSCC indications ≈95% TW. Figure 4.3 also indicates that the axial ODSCC in Specimen SGL492 has a segmented secondary crack. Figures 4.4 and 4.5 show EC results for Specimens SGL748 and SGL757 with axial ODSCC indications estimated to be 60 and 85% TW, respectively. Multiple segmented cracks are indicated for both specimens. Figures 4.6 and 4.7 show eddy current NDE results for Specimens SGL737 and SGL776. A segmented OD axial indication ≈85% TW is seen in Specimen SGL737 and a complicated OD axial and circumferential indication ≈60% TW is seen in Specimen SGL776. Specimens SGL741, SGL786 and SGL795 (Figs. 4.8, 4.9, and 4.10) show circumferential ODSCC (≈90% TW), circumferential IDSCC (≈20% TW), and axial IDSCC (≈80% TW) indications, respectively. Specimen SGL795 shows multiple axial IDSCCs. Figures 4.11-4.14 show EC results for Specimens SGL808, SGL809, SGL816, and SGL817. Axial IDSCC indications are seen for Specimens SGL808 and SGL809 (Figs. 4.11 and 4.12), with two axial SCCs in each specimen. The depth of the SCC is estimated to be ≈60% TW for Specimen SGL808 and 100% TW for Specimen SGL809. Figures 4.13 and 4.14 show axial ODSCC indications for Specimens SGL816 and SGL817 with estimated depths of ≈85 and 95% TW, respectively.

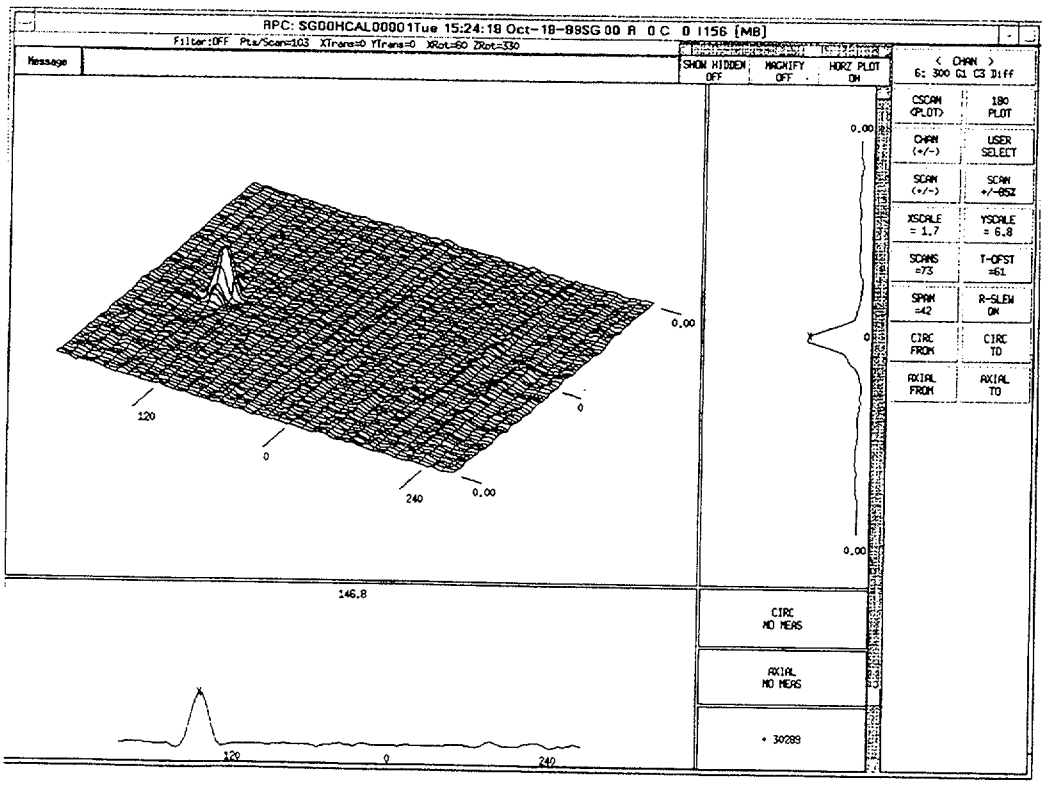

Fig. 4.1. EC NDE test results for Specimen SGL717 with 90% TW axial ODSCC indication.

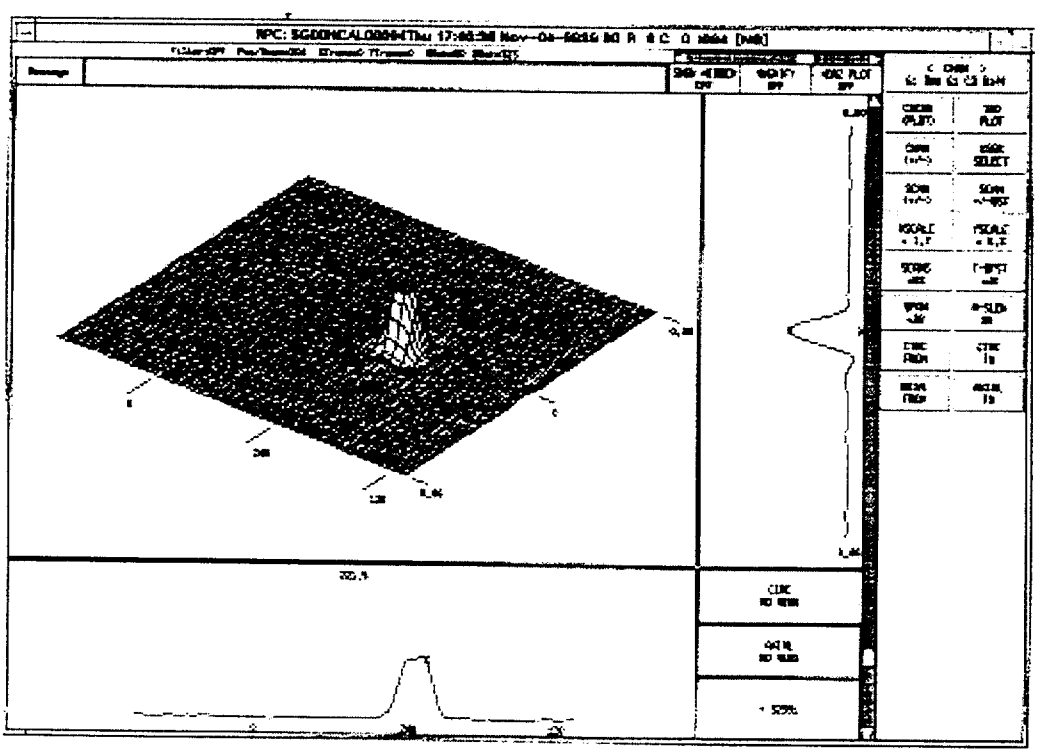

Fig. 4.2. EC NDE test results for Specimen SGL473 with ≈95% TW axial ODSCC indication.

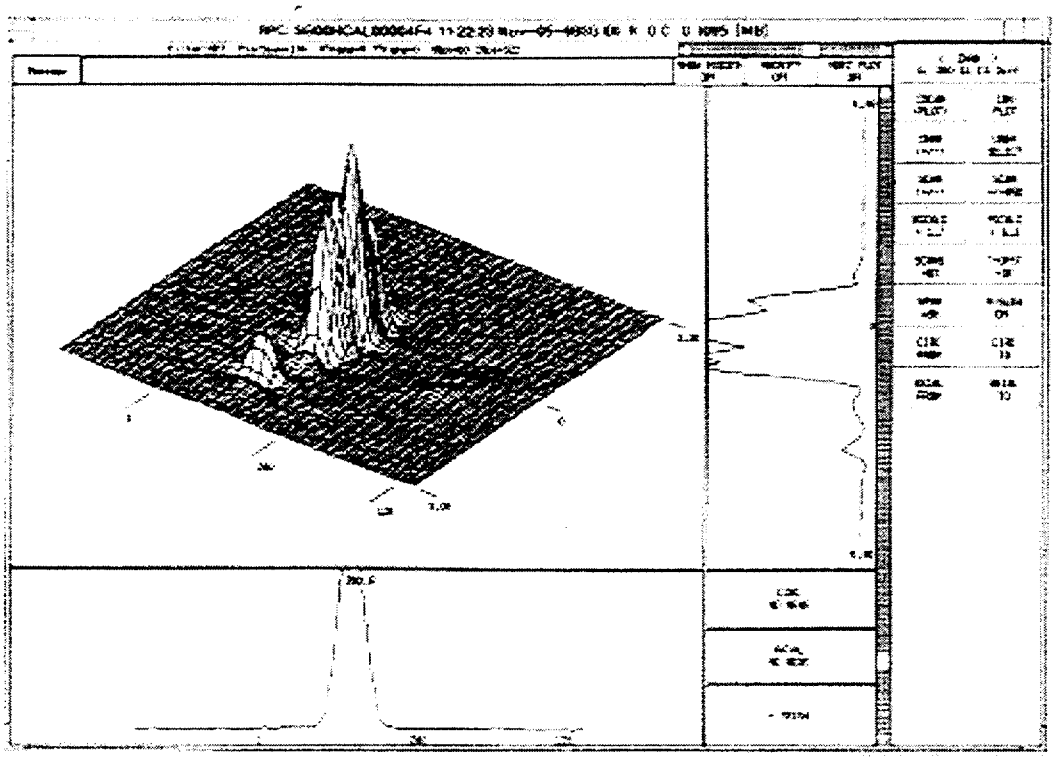

Fig. 4.3. EC NDE test results for Specimen SGL492 with ≈95% TW axial ODSCC indication.

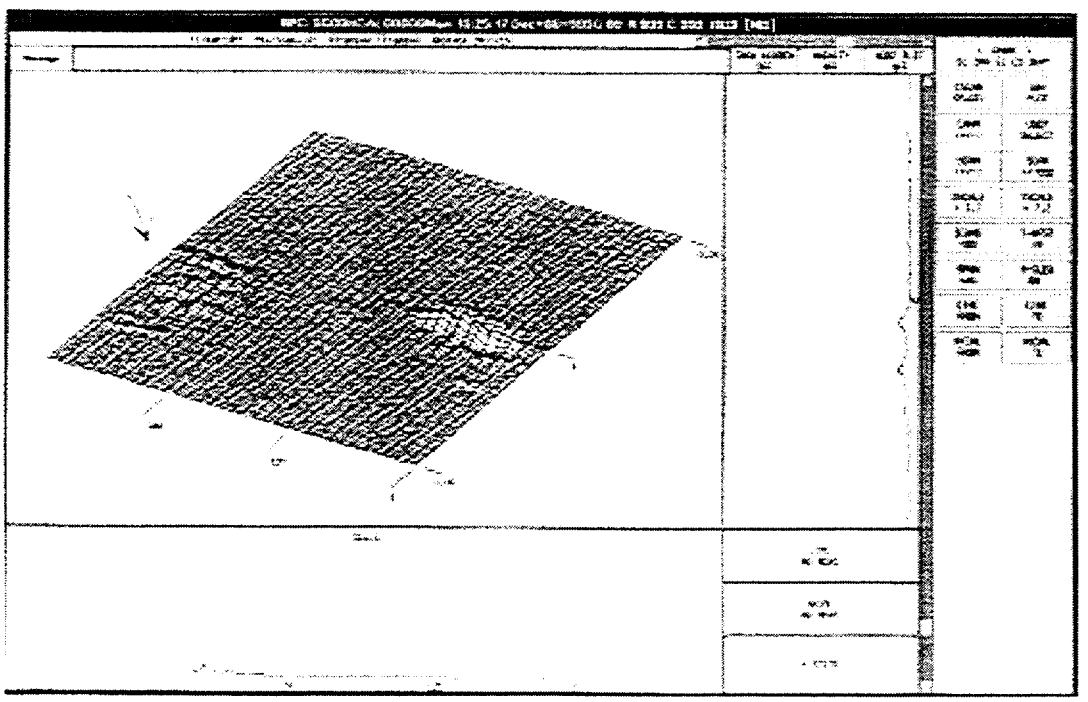

Fig. 4.4. EC NDE test results for Specimen SGL748 with 60% TW axial ODSCC indication 60%.

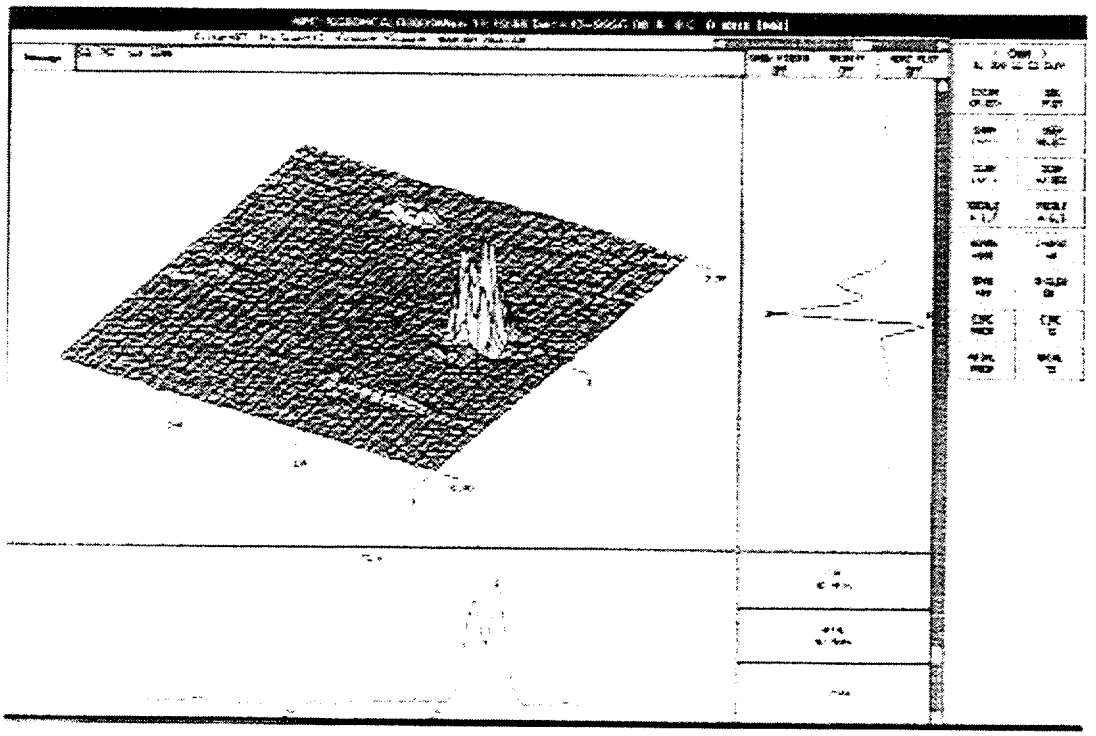

Fig. 4.5. EC NDE test results for Specimen SGL757 with 85% TW axial ODSCC indication.

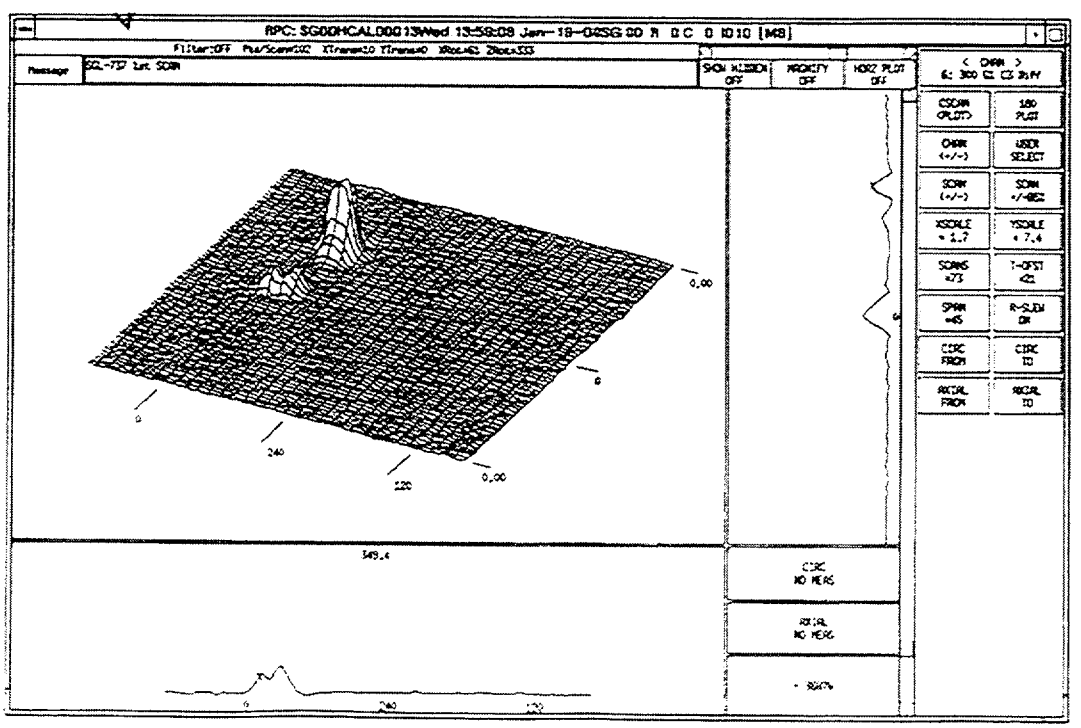

Fig. 4.6. EC NDE test results for Specimen SGL737 with segmented 85% TW axial ODSCC indication.

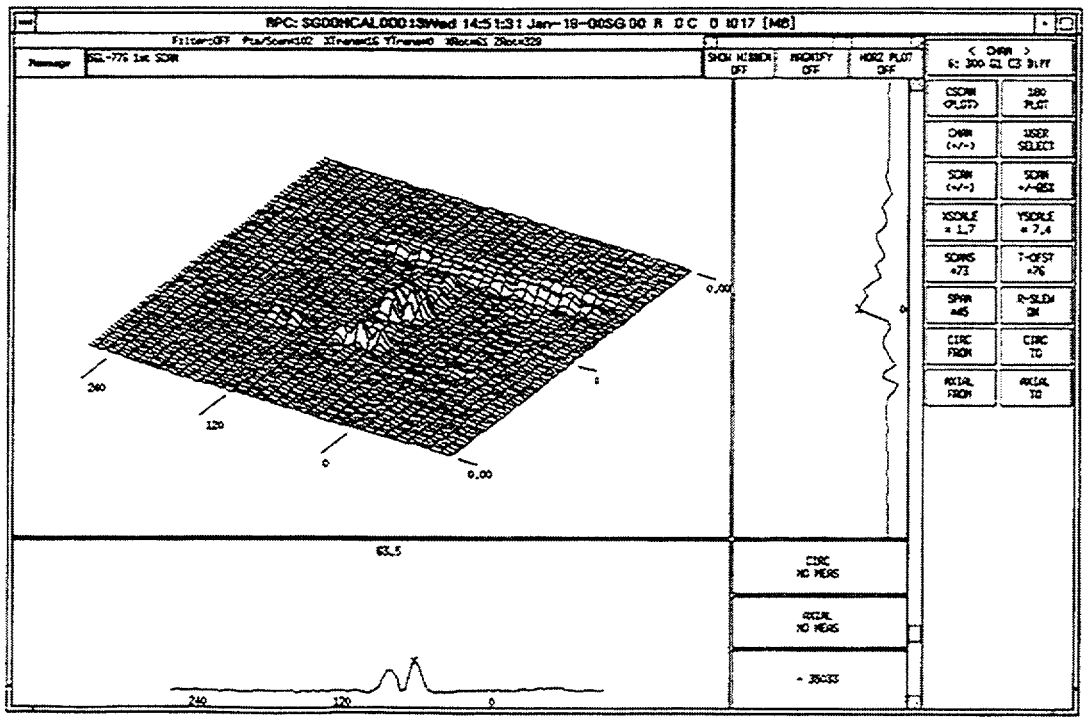

Fig. 4.7. EC NDE test results for Specimen SGL776 with 60% TW axial and circumferential ODSCC indications.

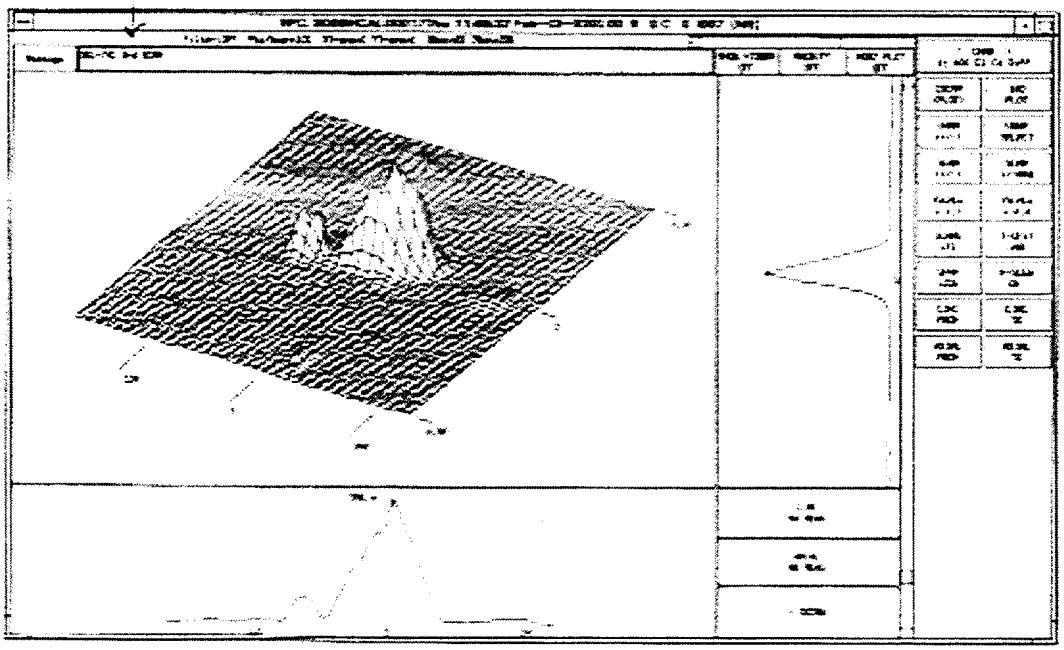

Fig. 4.8. EC NDE test results for Specimen SGL741 with 90% TW circumferential ODSCC indication.

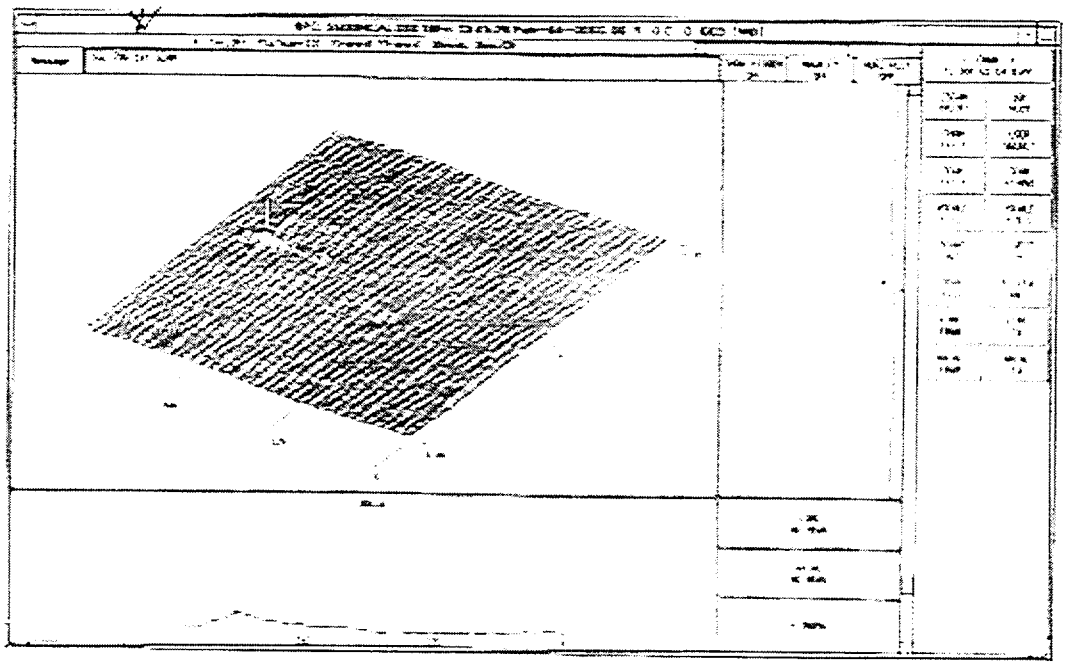

Fig. 4.9. EC NDE test results for Specimen SGL786 with a 20% TW circumferential IDSCC indication.

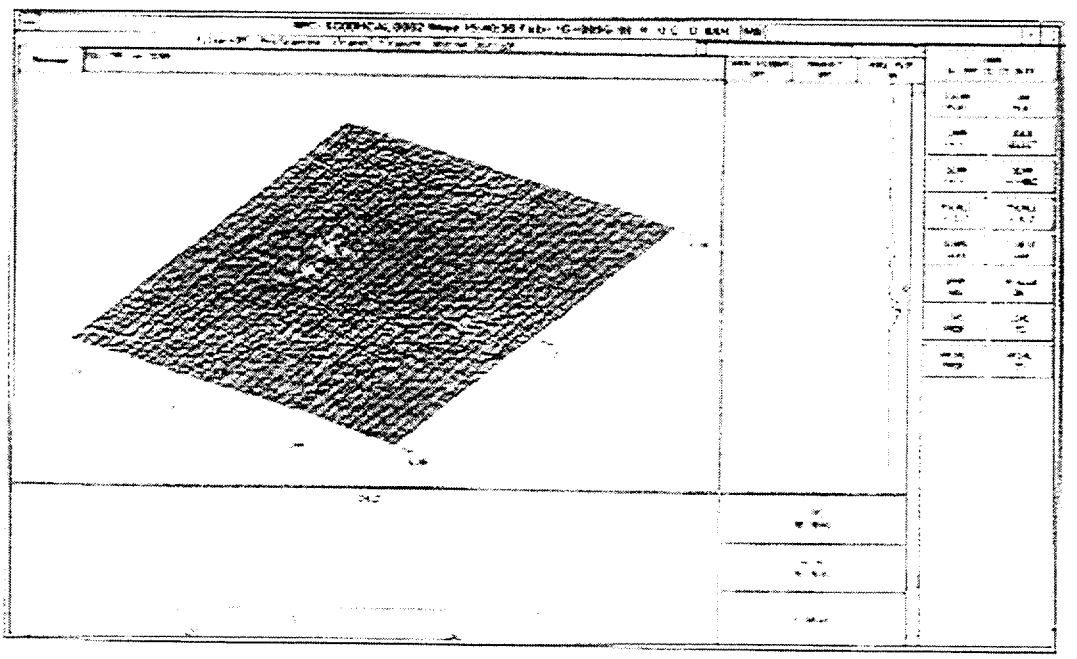

Fig. 4.10. EC NDE test results for Specimen SGL795 with an 80% TW axial IDSCC indication.

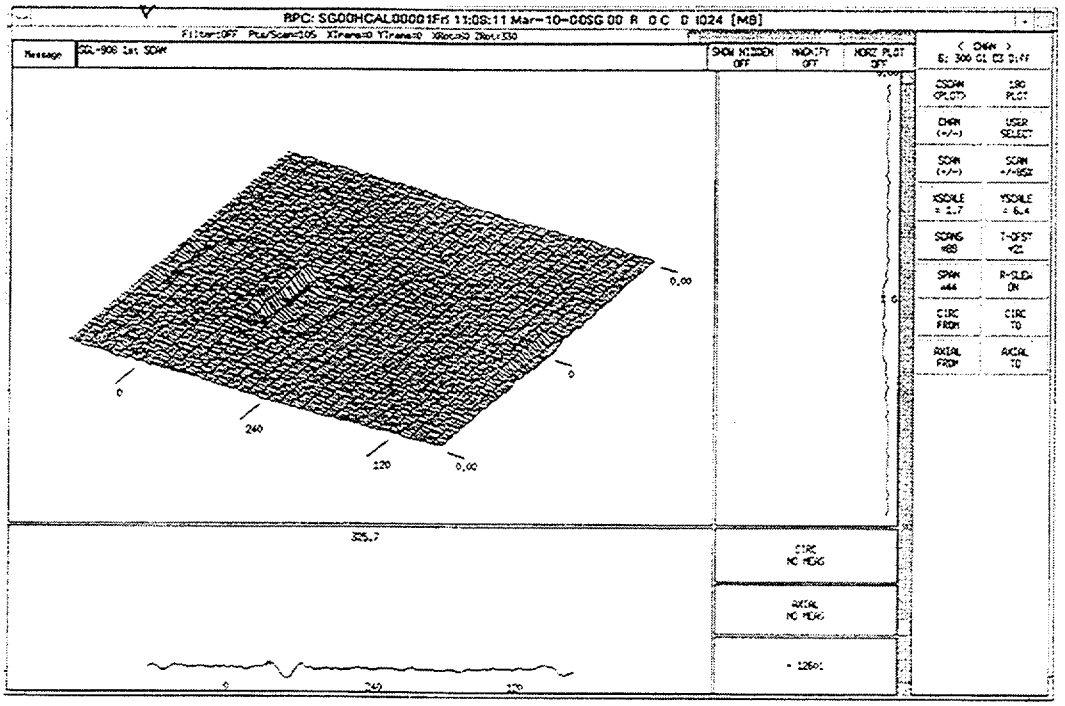

Fig. 4.11. EC NDE test results for Specimen SGL808 with 60% TW axial IDSCC indications.

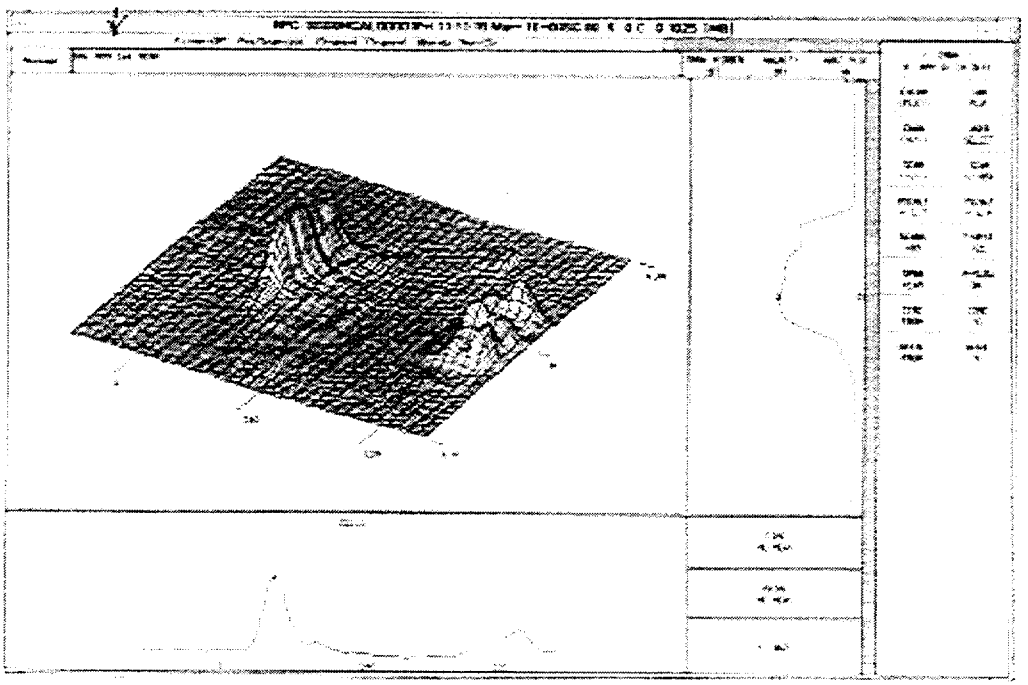

Fig. 4.12. EC NDE test results for Specimen SGL809 with 100% TW axial IDSCC indications.

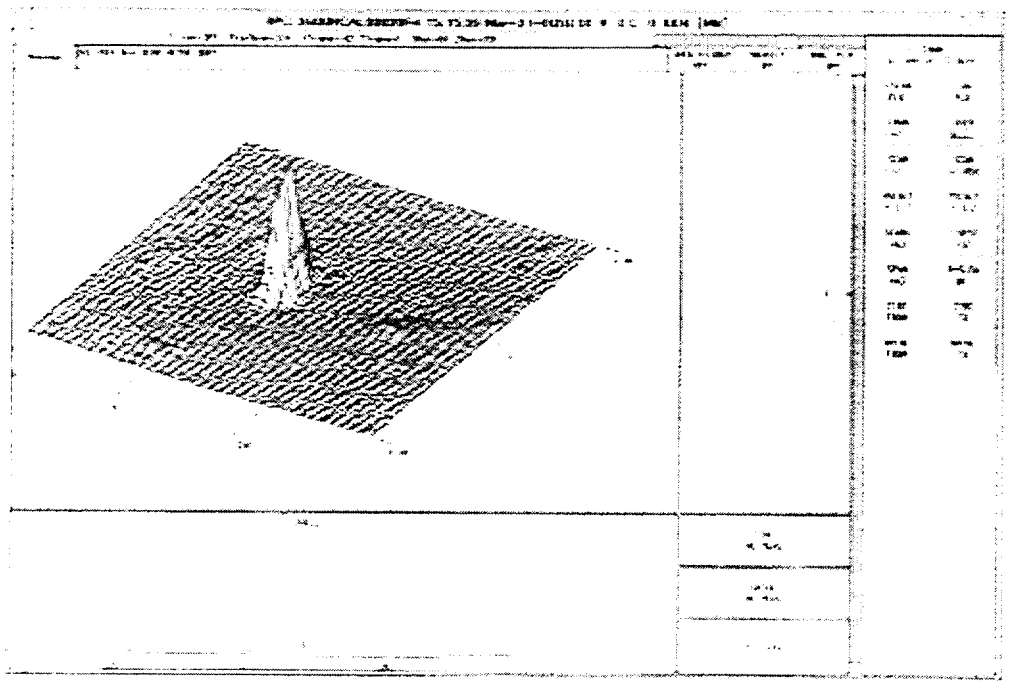

Fig. 4.13. EC NDE test results for Specimen SGL816 with 85% TW axial ODSCC indication.

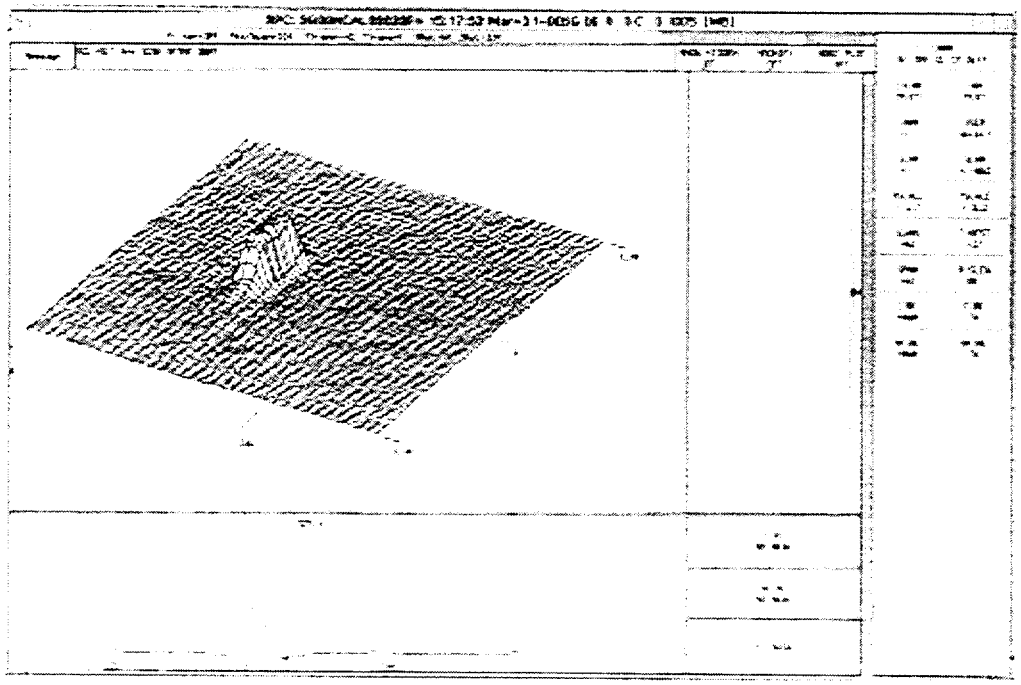

Fig. 4.14. EC NDE test results for Specimen SGL817 with 95% TW axial ODSCC indication.

The degraded tubes were also examined by a dye-penetrant technique. Figure 4.15 shows an example of the dye-penetrant examination of axial ODSCC in Specimen SGL717. The crack is ≈9 mm (0.35 in.) in length and is segmented. Figure 4.16 shows the dye-penetrant result for an ≈25-mm (1-in.)-long axial ODSCC in Specimen SGL473. Dye-penetrant examination indicates that the axial ODSCC in Specimen SGL492 (Fig. 4.17) consists of two segmented cracks ≈18 and 6 mm (0.71 and 0.24 in.) long, respectively. The axial ODSCC present in Specimens SGL748 and SGL757 (Figs. 4.18 and 4.19) appear to be ≈4 and 11 mm (0.16 and 0.43 in) long, respectively. The ODSCC in Specimen SGL737 (Fig. 4.20) is ≈25 mm (1 in.) long, with two major and multiple minor segmentations. Figure 4.21 shows a dye-penetrant indication of segmented circumferential ODSCC ≈23 mm (0.91 in.) long in Specimen SGL741. The dye-penetrant examinations of Specimens SGL816 and SGL817 (Figs. 4.22 and 4.23) reveal axial, segmented ODSCC, with lengths of ≈10 and 14 mm (0.39 and 0.55 in.), respectively.

The laboratory-degraded tubes were destructively analyzed to provide detailed comparisons with the eddy current NDE measurements. The cracks were opened by internal pressurization and examined macroscopically and by SEM. The samples were heat-tinted prior to loading to permit differentiation of the SCC surface from that produced by subsequent fracture during opening. The results of these destructive examinations are summarized in Table 4.1.

Figure 4.24 shows the results of the EC, dye-penetrant, and macroscopic surface and fractographic examinations of Specimen SGL226. This specimen contains both circumferential and axial ODSCCs. The main circumferential crack extends 360° around the OD, with a maximum penetration depth of 100% TW. The axial ODSCC is perpendicular to the circumferential crack, has a maximum length of ≈9 mm (0.35 in.), and is 100% TW. Many secondary axial cracks are connected with or away with the main circumferential crack. Some branching of the circumferential crack is also seen. Figure 4.25 shows results from similar examinations for roll-expanded Specimen SGL363. The roll expansion had been introduced to the specimen after sensitization but before cracking, and the resulting residual stresses produced SCC without applying an external load. Networks of axial-circumferential cracks are seen around the roll expansion area. The circumferential OD crack extends for 360°, with a maximum penetration depth of 100% TW. The associated network of axial ODSCCs are up to 14-mm long and 100% TW, and many secondary and branching cracks are seen in the roll expansion area.

Figure 4.26 shows eddy current NDE results for Specimen SGL494. The macroscopic appearance of the OD surface and the macroscopic appearance of the fracture surface of this specimen after internal pressurization are seen in Fig. 4.27. The specimen contains a main axial ODSCC and multiple secondary ODSCCs. Branching and segmentation of the cracks are also seen. The maximum penetration depth of the main crack was measured to be 90% TW by EC and 85% TW by optical fractography. The length of the main crack was found to be 11 mm (0.43 in.) by eddy current NDE and 17 mm (0.67 in.) by fractography. The axial ODSCC is perpendicular to the circumferential crack and is 9 mm (0.35 in.) long and 100% TW. The EC bobbin coil voltage for these cracks was only 0.09 V. No detectable dye-penetrant indication was observed. Figure 4.28 is a scanning electron photomicrograph of the fracture surface of Specimen SGL494 showing a 30-40% TW IGSCC that initiated at the OD surface. Figure 4.29 shows results of eddy current NDE for Specimen SGL480. Figure 4.30 shows the macroscopic

Table 4.1. Characterization of laboratory degradation in SG tube specimens

Specimen ID	Crack Type	Max. Depth (%)		Length (mm)		EC Voltage (V)	
		EC	Fractography	EC	Fractography	Bobbin	RPC
SGL099	Circ OD	97	90-100	70	70	2.52	-
SGL104	Axial OD	-	100	-	13		
SGL105	Circ ID	38	-	70	-	7.25	-
SGL177	Axial OD	-	100	-	12	-	-
SGL179	Axial ID	53	-	77	-	0.87	-
SGL226	Circ OD	88	100	70	70	11.67	-
SGL413	Axial OD	89/90	100	10/11	9/11	1.53	-
SGL425	Axial OD	100	100	18	13	2.23	-
SGL480	Axial OD	100	100	13	15	3.39	-
SGL493	Axial OD	93	100	17	16	3.94	-
SGL494	Axial OD	90	100	12	16	0.09	-
SGL719	Axial OD	85	40/80	5/20	17/20	0.39	-
SGL728	Axial OD	97	100	30	22	2.07	-
SGL730	Axial OD	98	100	26	-	0.98	-
SGL731	Axial OD	97	100	16	14	2.57	-
SGL734	Axial OD	90	100	12	16	1.71	-
W-2-10	Axial OD	-	100	-	11.6	-	-
5528-2-1	Axial laser	-	64	-	6.4	-	-
5528-2-2	Axial laser	-	55	-	6.4	-	-

appearance of the OD surface of this specimen after pressurization, as well as optical fractography of the fracture surface. The specimen contains an axial ODSCC with a maximum depth of 100% TW for the main crack, as determined by both eddy current NDE and optical fractography. The length of the crack is measured as 13 mm (0.51 in.) by eddy current NDE and 15 mm (0.59 in.) by fractography. The EC bobbin coil voltage was 4.39 V.

Figure 4.31 shows the eddy current NDE for Specimen SGL413. Figure 4.32 is a macroscopic view of the OD surface of this specimen after pressurization, together with the results of optical fractography. The specimen contains two main axial ODSCCs with maximum depths of ≈90% TW from eddy current NDE and 100% TW from optical fractography. The length of the main crack is measured to be 10-11 mm (0.39-0.43 in.) as measured by eddy current NDE and 9-11 mm (0.35-0.43 in.) by fractography. The BC eddy current voltage was 1.53 V. The eddy current NDE for Specimen SGL493 is shown in Fig. 4.33, and a macroscopic view of the OD surface after pressurization and a fractographic image of the crack/fracture surface are seen in Fig. 4.34. The specimen contains main and branched axial ODSCCs. The maximum penetration depth of the main crack is measured as 93% TW by eddy current NDE

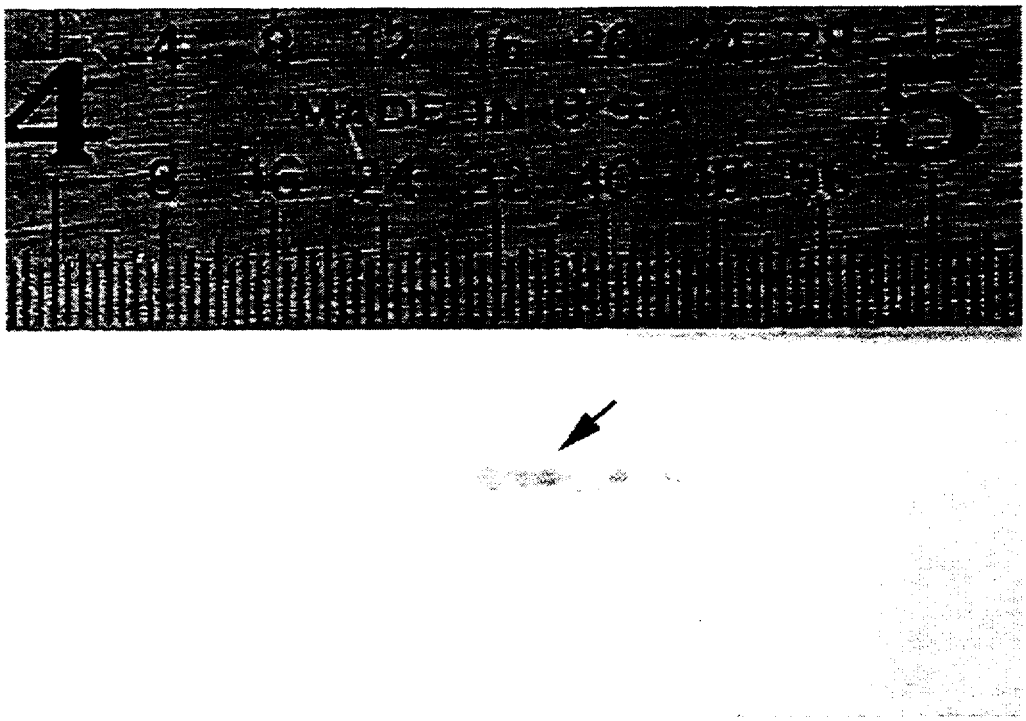

Fig. 4.15. Dye-penetrant examination of Specimen SGL717 with 9-mm-long axial ODSCC indication.

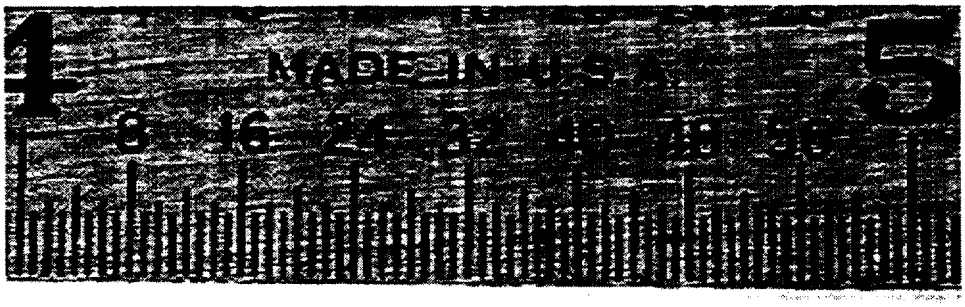

Fig. 4.16. Dye-penetrant examination of Specimen SGL473 with 25-mm-long axial ODSCC indication.

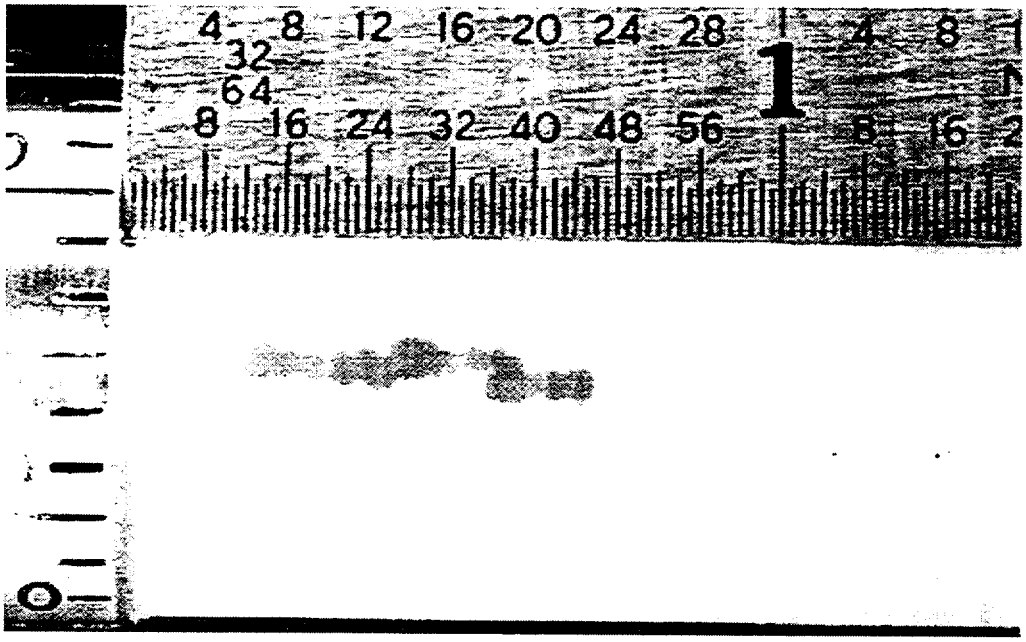

Fig. 4.17. Dye-penetrant examination of Specimen SGL492 with 18- and 6-mm-long axial ODSCC indications.

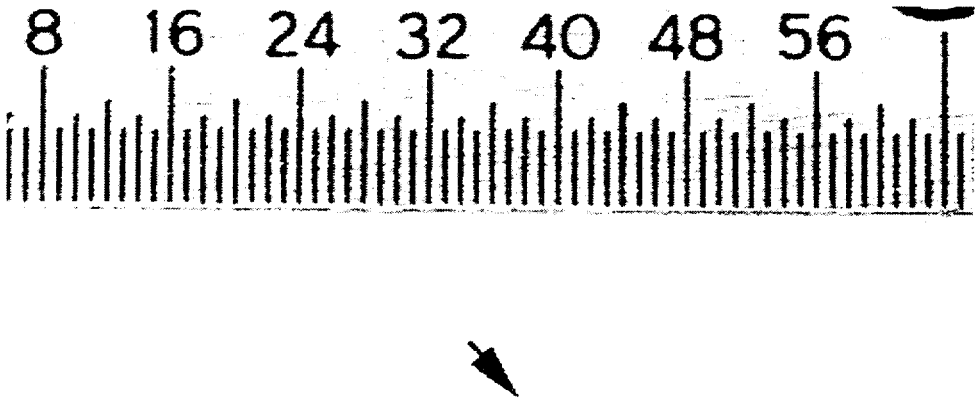

SGL748

Fig. 4.18. Dye-penetrant examination of Specimen SGL748 with 4-mm-long axial ODSCC indication.

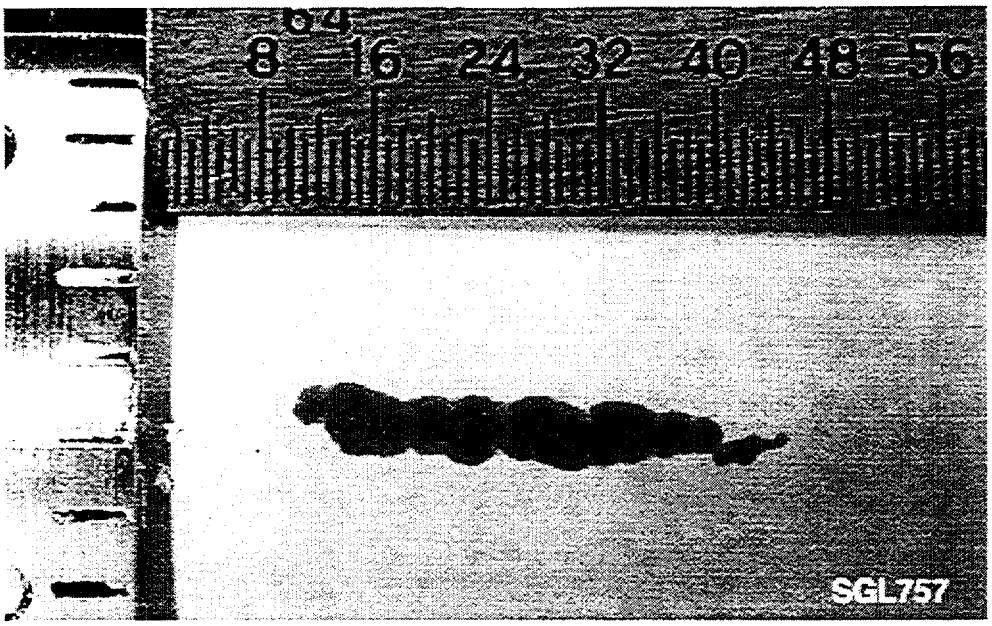

Fig. 4.19. Dye-penetrant examination of Specimen SGL757 with 11-mm-long axial ODSCC indication.

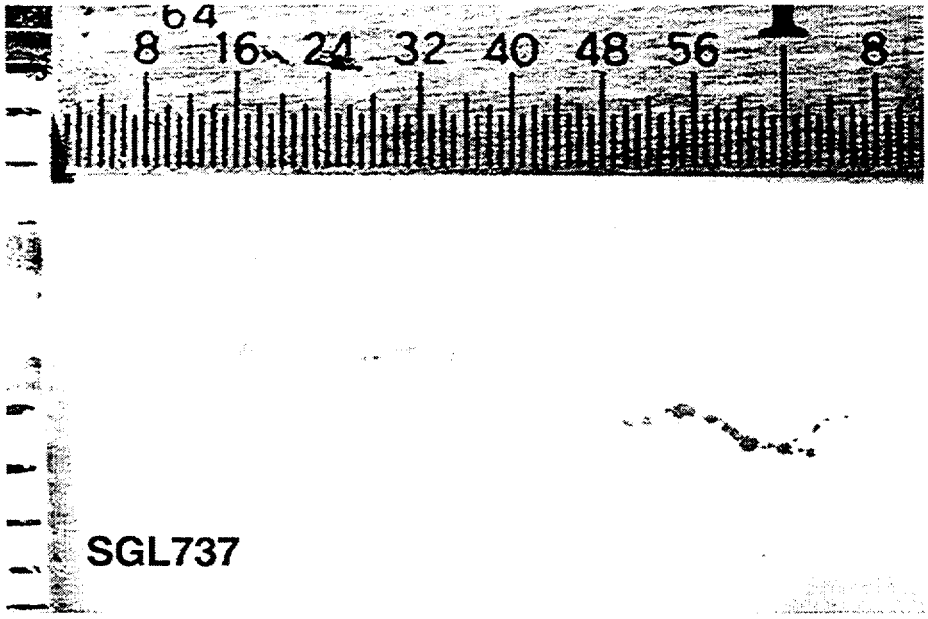

Fig. 4.20. Dye-penetrant examination of Specimen SGL737 with segmented 25-mm-long axial ODSCC indication.

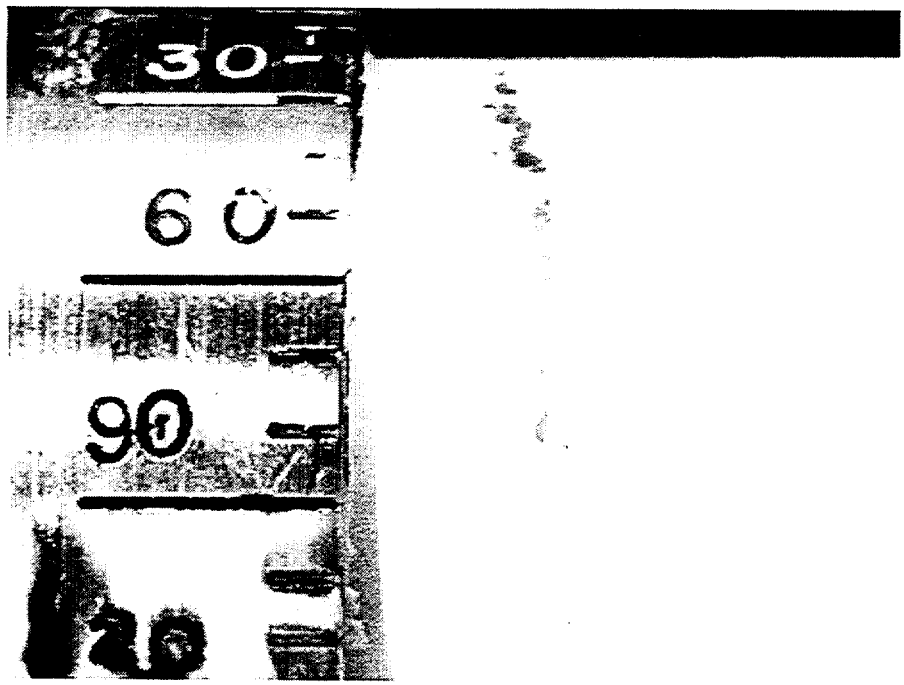

Fig. 4.21. Dye-penetrant examination of Specimen SGL741 with 23-mm-long circumferential ODSCC indication.

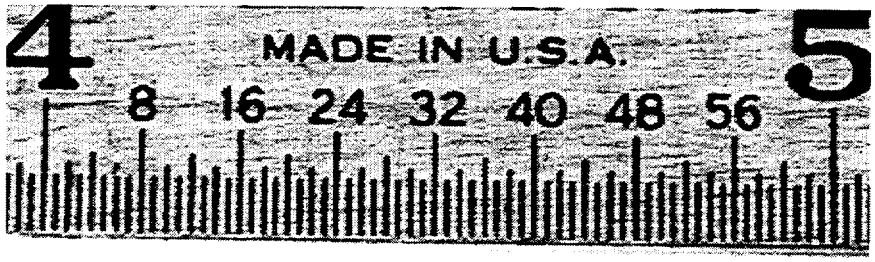

Fig. 4.22. Dye-penetrant examination of Specimen SGL816 with 10-mm-long axial ODSCC indication.

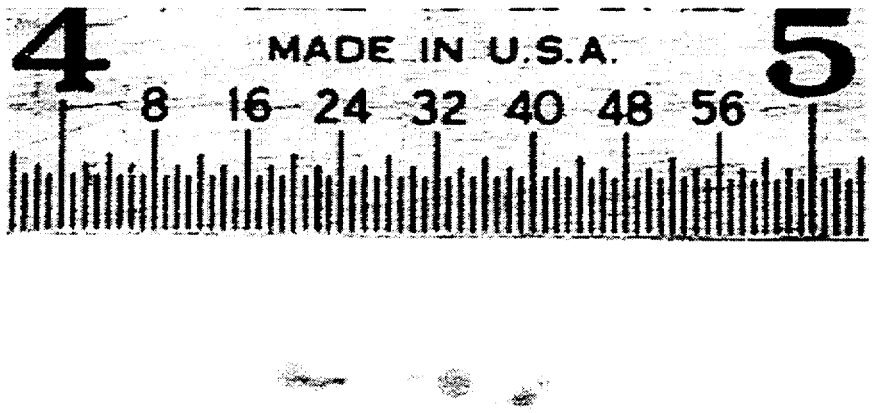

Fig. 4.23. Dye-penetrant examination of Specimen SGL817 with 14-mm-long axial ODSCC indication.

and 100% TW by optical fractography. The length of the main crack is measured to be 17 mm (0.67 in.) by eddy current NDE and 16 mm (0.63 in.) by fractography. The EC BC voltage was 3.94 v. The preliminary results of EC NDE, macroscopic examination, and SEM for the various tubes that have been characterized are summarized in Table 4.I. Characterization of additional specimens is in progress, and these results will be presented in future reports.

The heat treatments used to make the tubes more susceptible to SCC can influence the electromagnetic properties of the material and thus the baseline EC signal and signal-to-noise ratio. Figures 4.35-4.37 show examples of this effect. However, this problem is not evident when using mag-biased BC and +Point probes, except for a small baseline shift with the BC coil, as reported previously.[1]

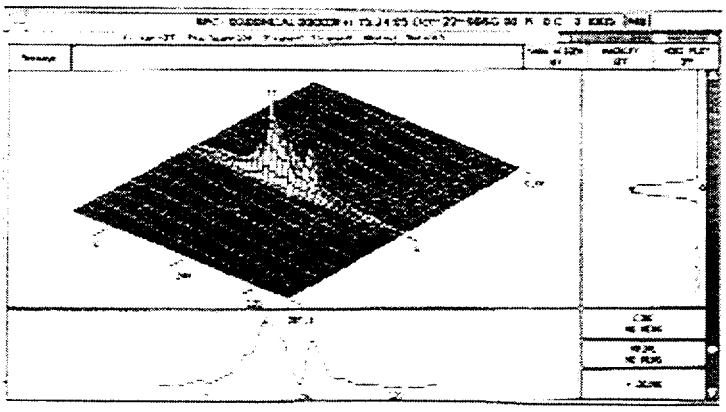

Eddy Current NDE, 7.80 V

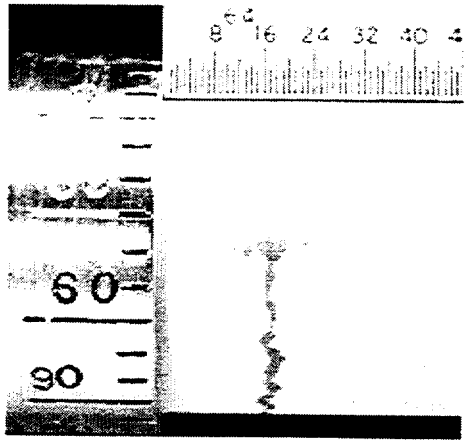

Dye-Penetrant Examination

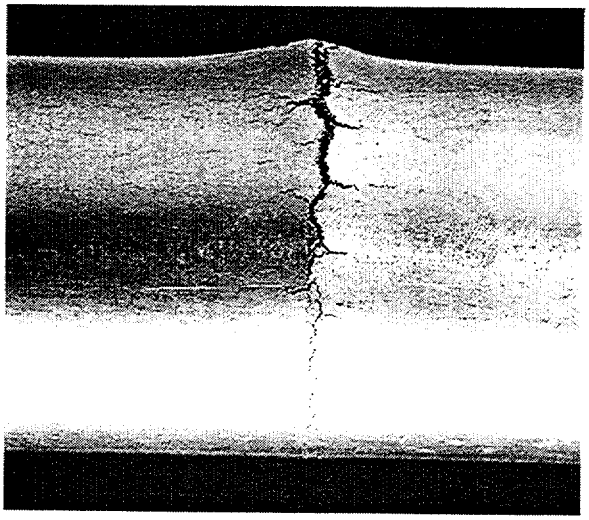

OD after High-Pressure Testing

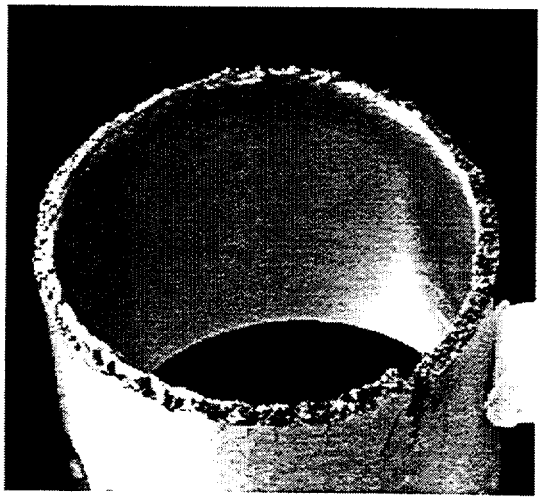

Macroscopy of Fracture Surface

Fig. 4.24. Eddy current NDE, dye-penetrant examination, macroscopic appearance of OD surface after pressure testing, and macroscopic fractography of fracture surface of Specimen SGL226.

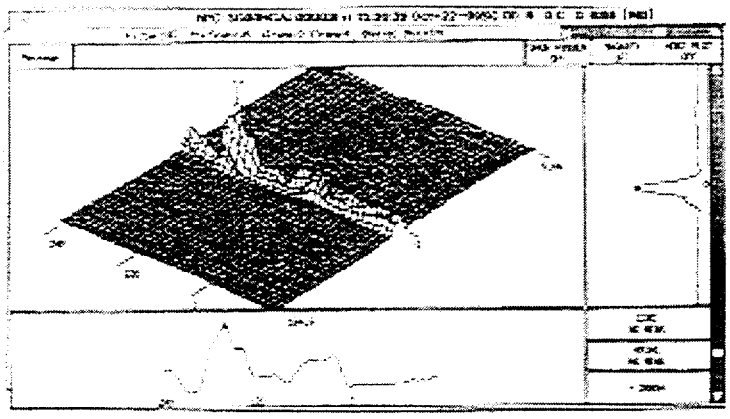

Eddy Current NDE, 3.10 V

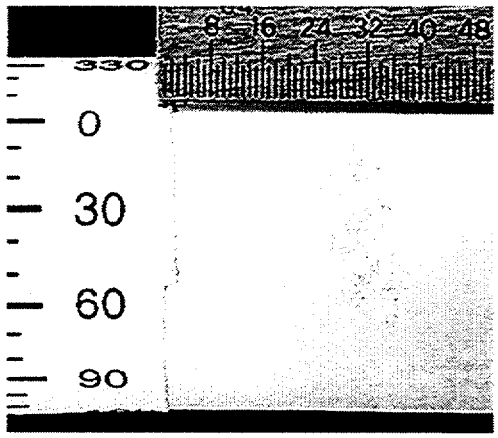

Dye-Penetrant Examination

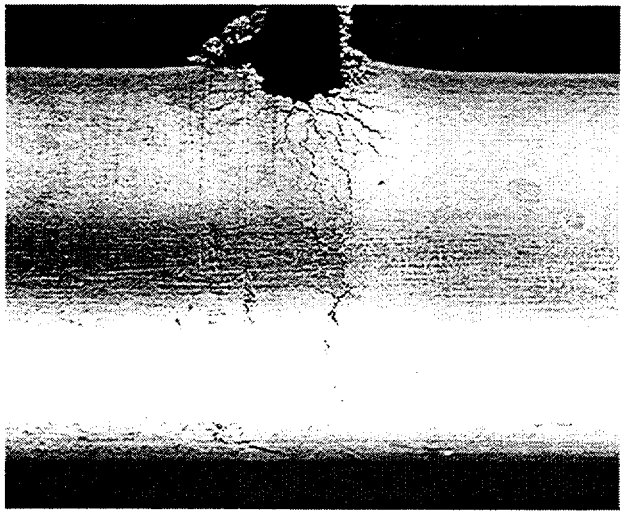

OD after High-Pressure Testing

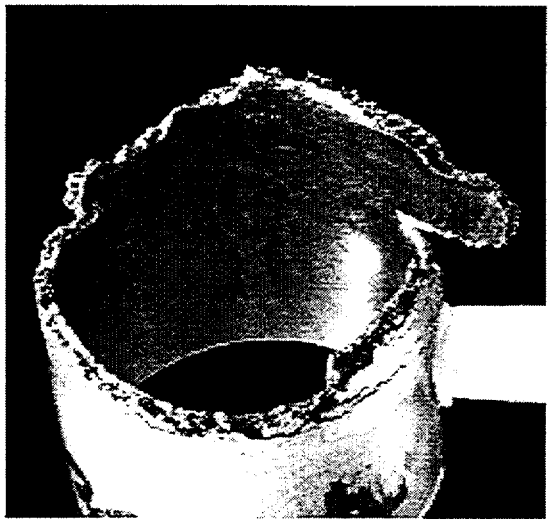

Macroscopy of Fracture Surface

Fig. 4.25. Eddy current NDE, dye-penetrant examination, macroscopic appearance of OD surface after pressure testing, and macroscopic fractography of fracture surface of Specimen SGL363.

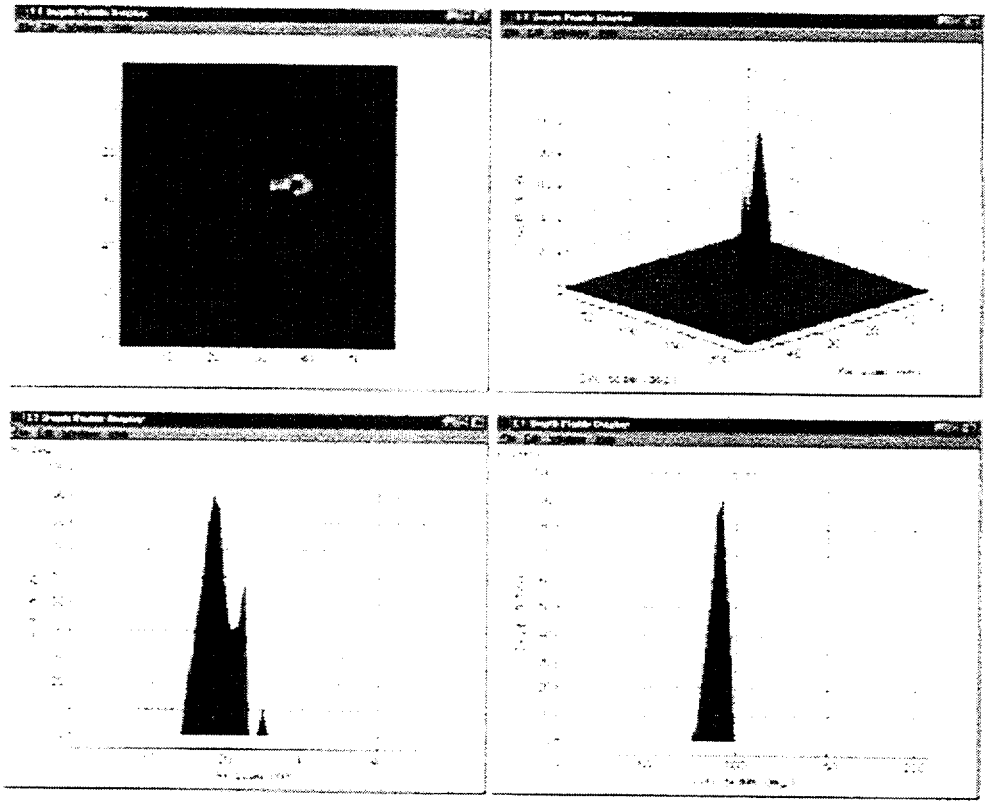

Fig. 4.26. Eddy current NDE of Specimen SGL494.

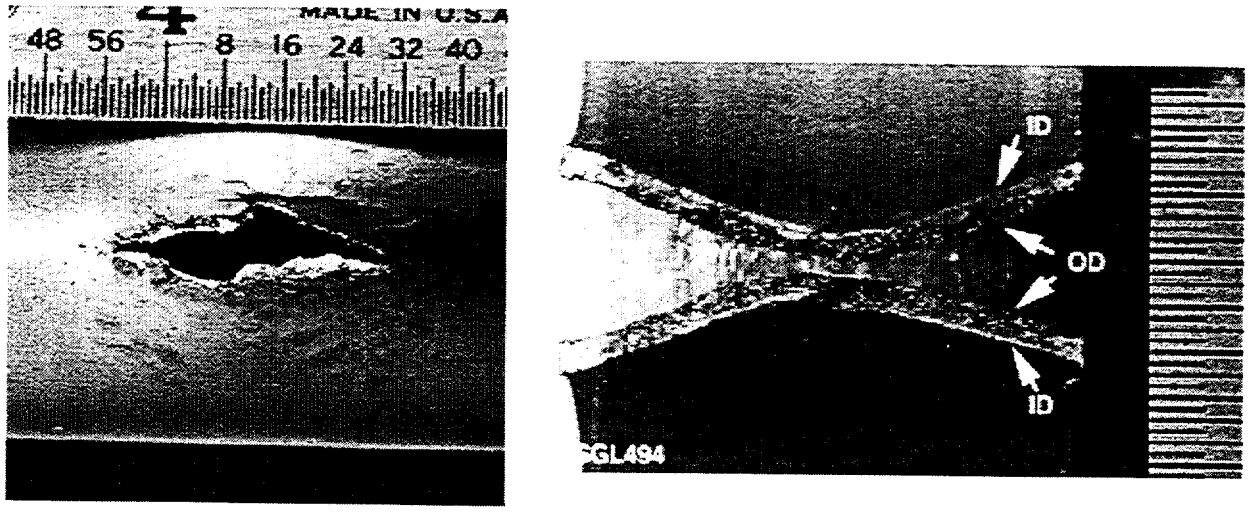

OD after High-Pressure Rupture

Fractography of Crack/Fracture Surface

Fig. 4.27. Macroscopic appearance of OD surface after high-pressure testing (left) and fractography of fracture surface (right) of Specimen SGL494.

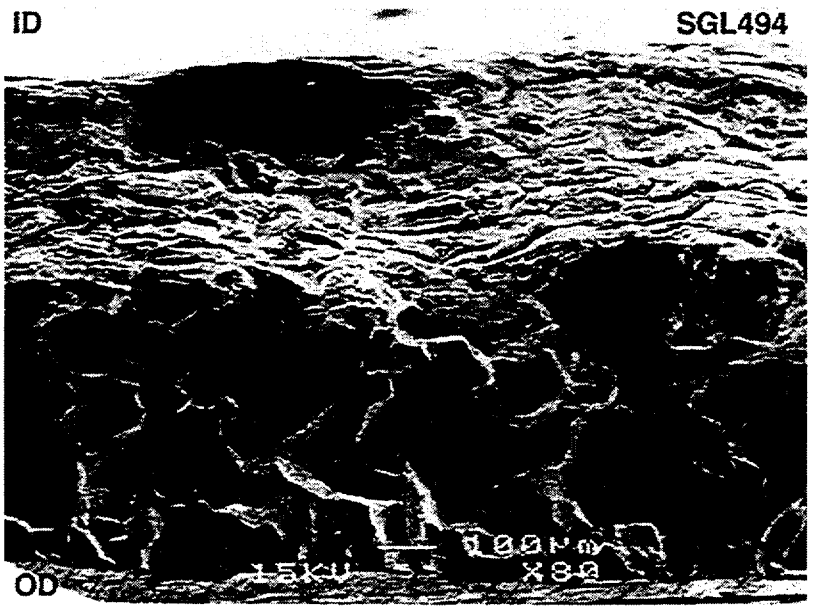

Fig. 4.28. Scanning electron photomicrograph of fracture surface of Specimen SGL494.

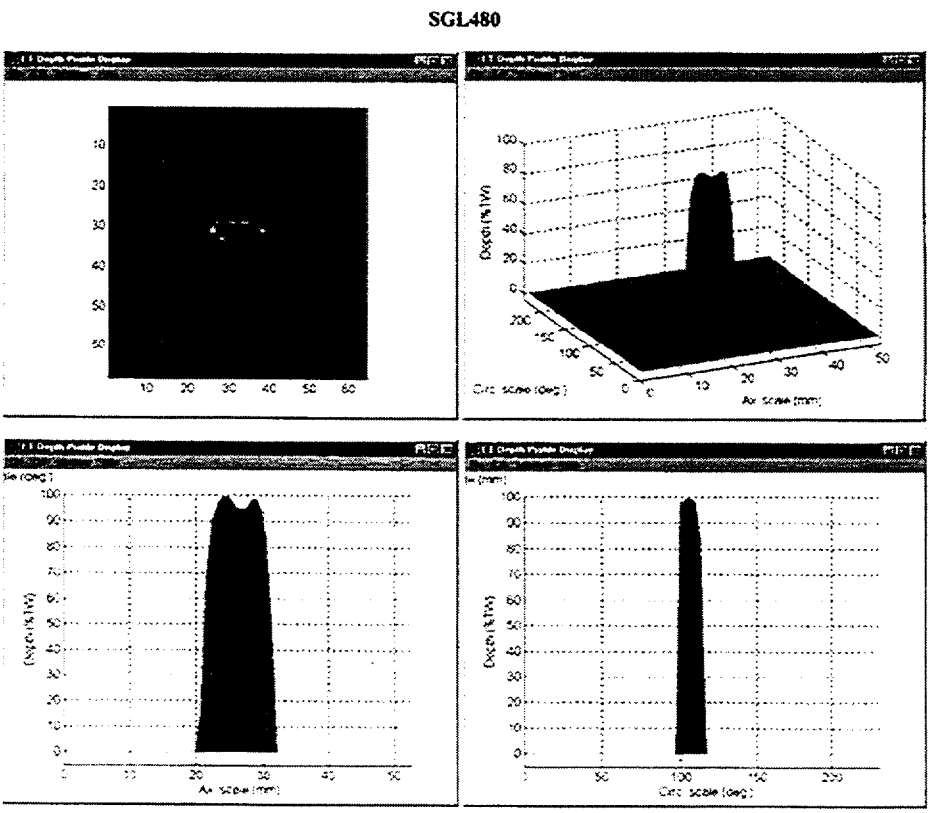

Fig. 4.29. Eddy current NDE of Specimen SGL480.

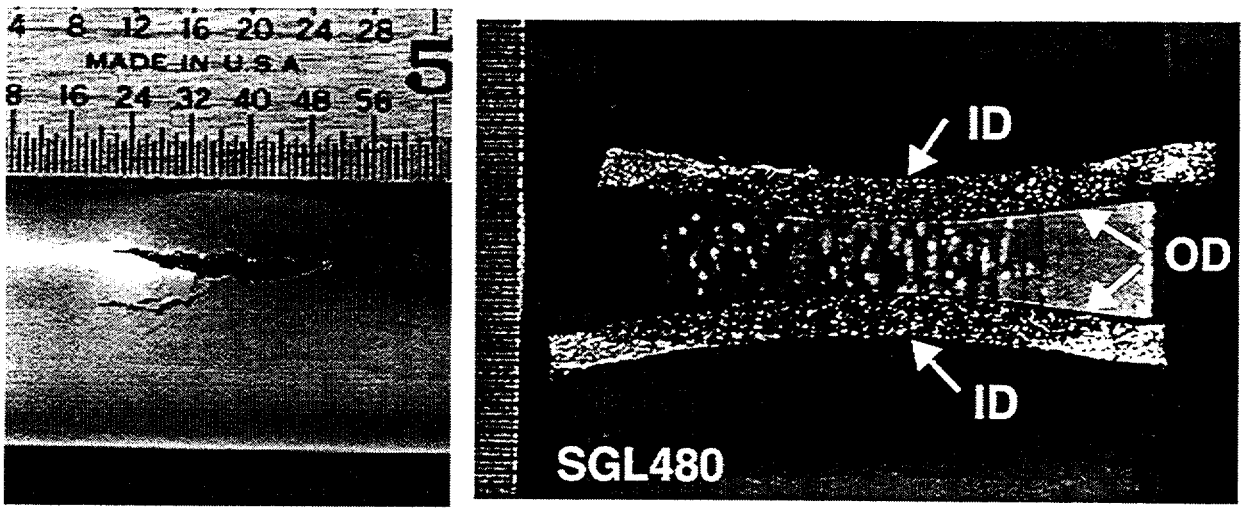

OD after High-Pressure Testing

Fractography of Crack/Fracture Surface

Fig. 4.30. Macroscopic appearance of OD surface after high-pressure testing (left) and fractography of crack/fracture surface (right) of Specimen SGL480.

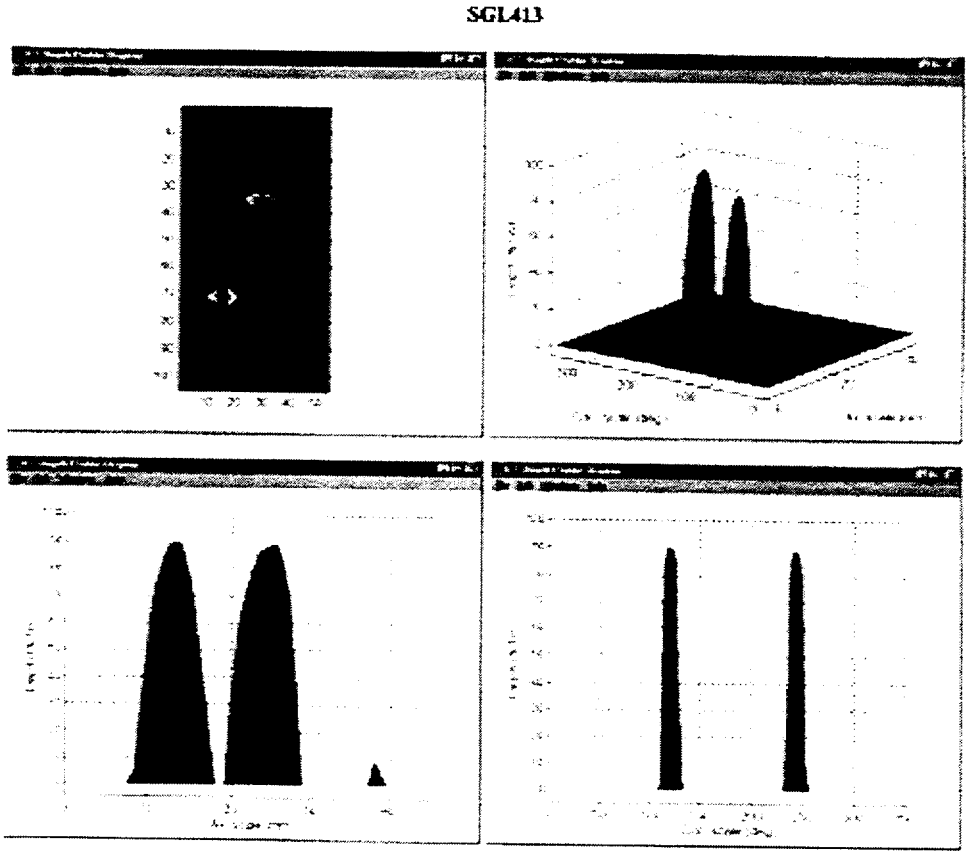

Fig. 4.31. Eddy current NDE of Specimen SGL413.

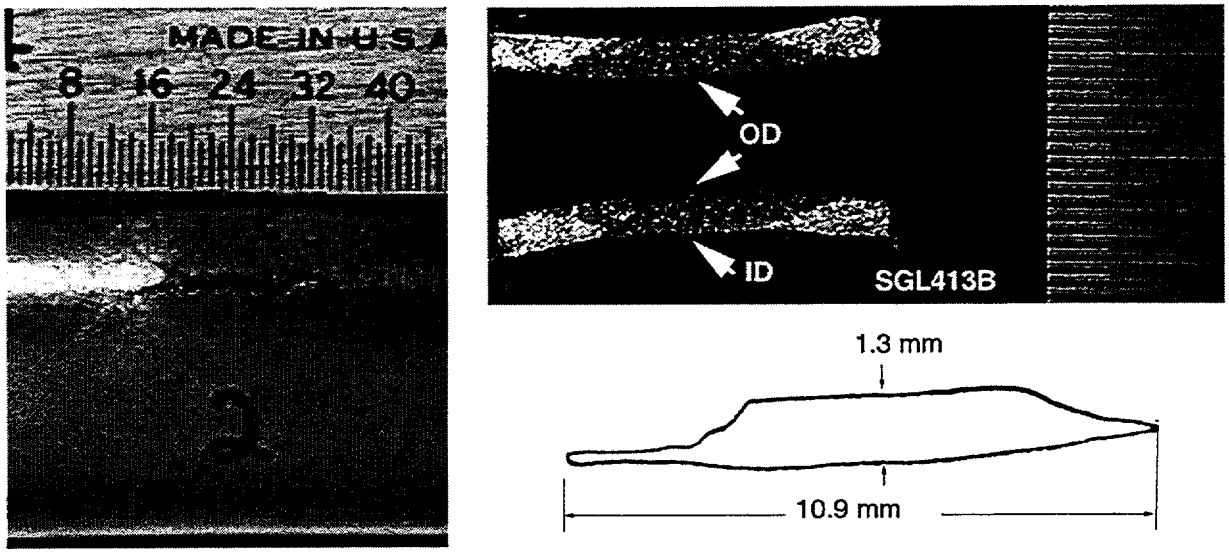

OD after Pressure Testing

Fractography of Fracture Surface

Fig. 4.32. Macroscopic appearance of OD surface after high-pressure testing and fractography of fracture surface of Specimen SGL413.

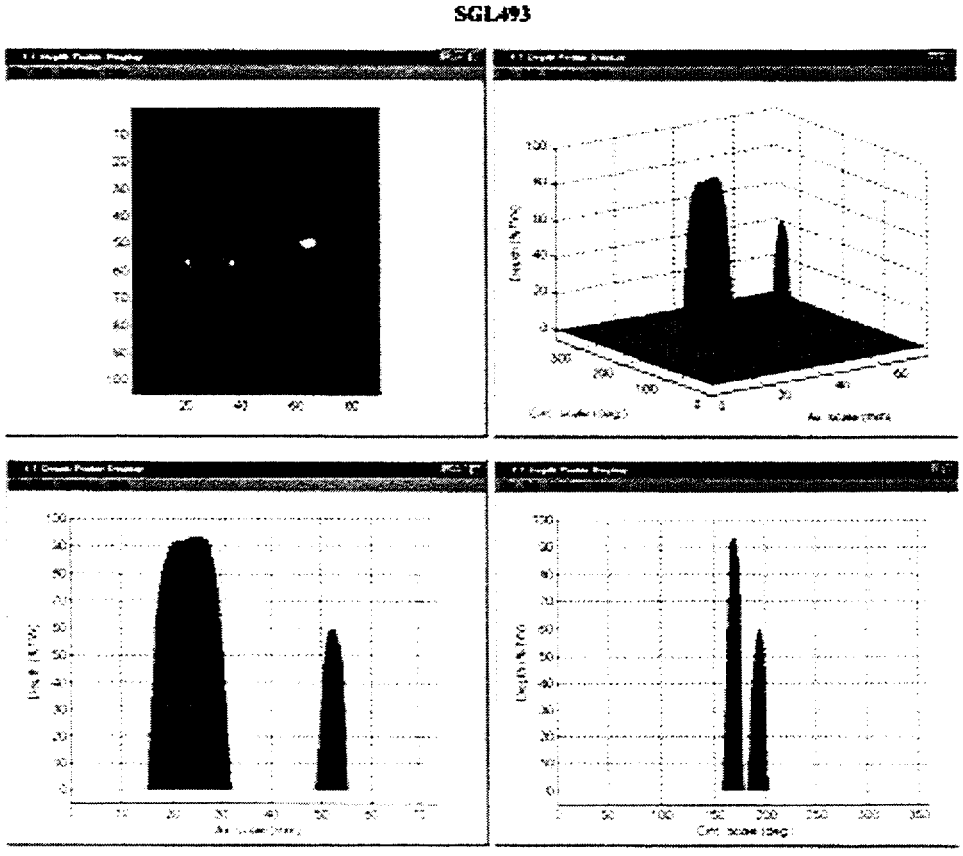

Fig. 4.33. Eddy current NDE of Specimen SGL493.

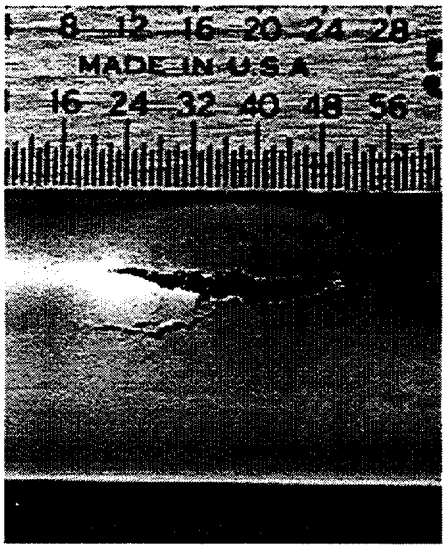

OD after High-Pressure Testing

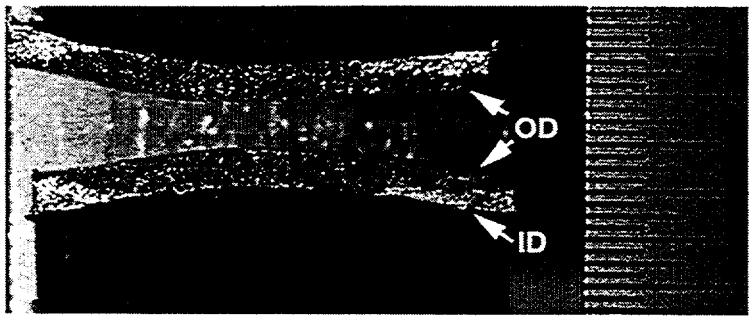

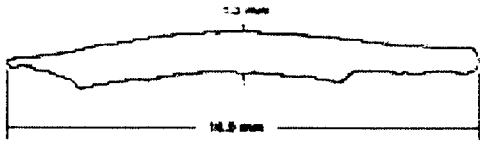

Fractography of Fracture Surface

Fig. 4.34. Macroscopic view of OD surface after high-pressure testing and fractography of fracture surface of Specimen SGL493.

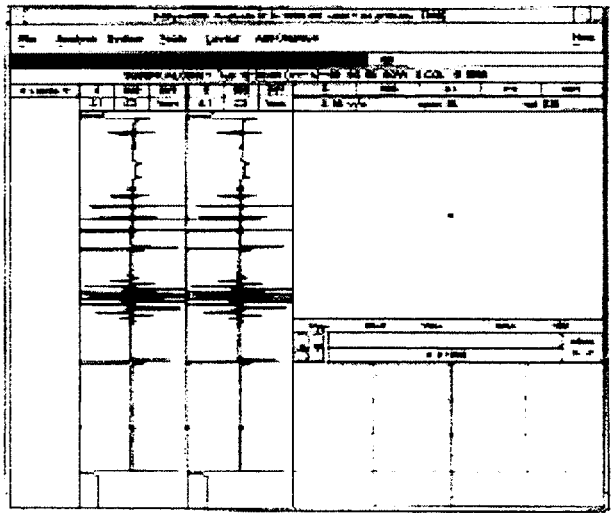

Specimen SGL515 (Mill Annealed)

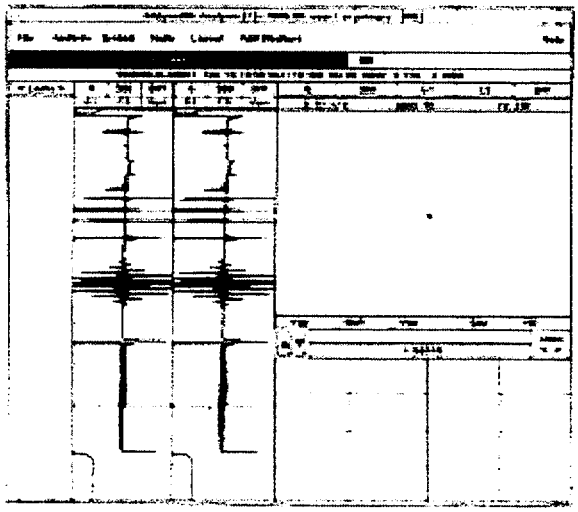

Specimen SGL472 (1100°C 10 min and 600°C 48 h)

Fig. 4.35. Eddy current NDE results showing effect of heat treatment on specimens from Heat NX8527. Note the slightly higher noise level in the lower part of the trace for Specimen SGL472.

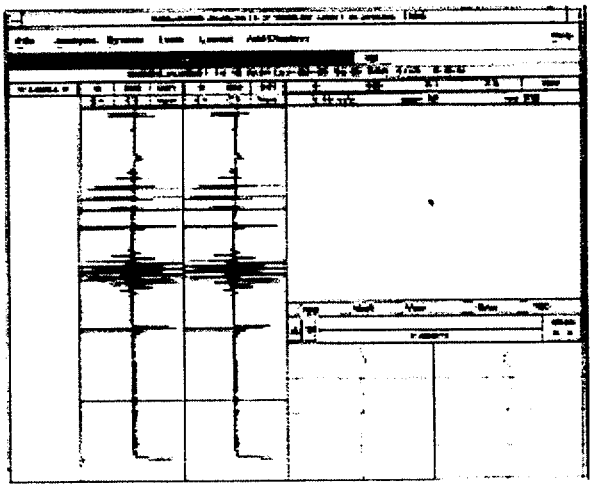

Specimen SGL743 (Mill Annealed)

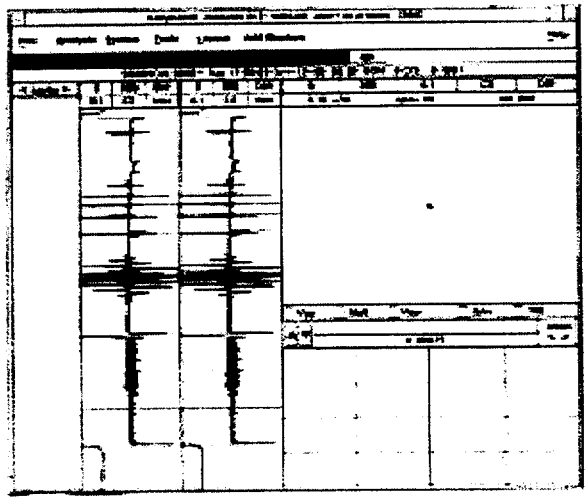

Specimen SG734
(Heat Treated 600°C 48 h)

Fig. 4.36. Eddy current NDE results showing effect of heat treatment on specimens from Heat NX8520LT.

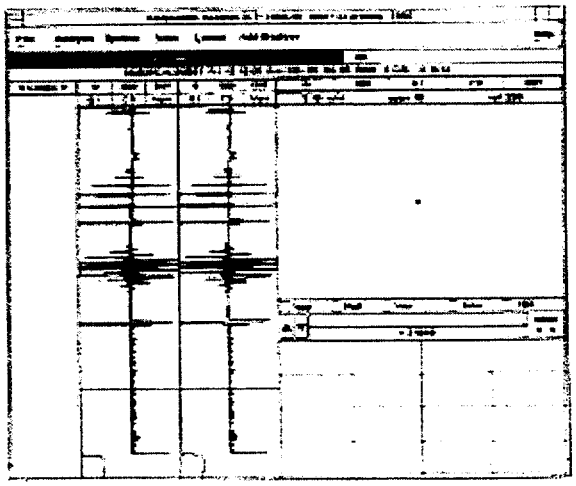

Specimen SGL741 (Mill Annealed)

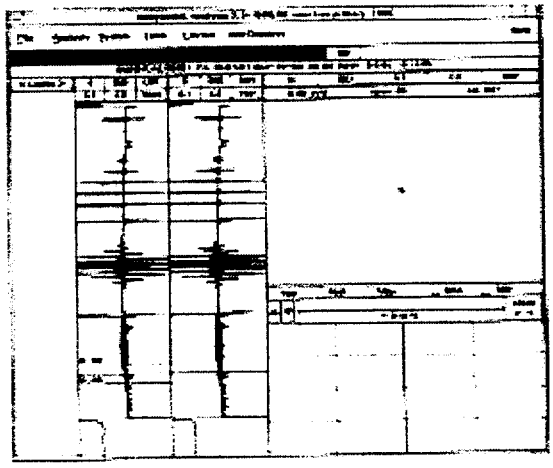

Specimen SGL741
(Heat Treated 600°C 48 h)

Fig. 4.37. Eddy current NDE results showing effect of heat treatment on specimens from Heat NX8520HT.

4.2 High-Pressure Test Facility

The room-temperature High-Pressure Test Facility was described in detail in the previous annual report.[1] This facility complements the elevated-temperature Pressure and Leak-Rate Test Facility in that its maximum operating pressure of 53.1 MPa (7700 psi) enables the testing of tubes that cannot be failed under the maximum pressure of 20.7 MPa (3000 psi) provided by the latter facility. These include tubes with shorter or shallower flaws that are of particular interest to the present program. In addition, its room-temperature operation provides a more rapid turnaround time for testing, and its ability to be continuously resupplied with water permits very long duration tests. The High-Pressure Test Facility was used during the present reporting period to conduct extensive tests on tubes with EDM and laser-cut notches and on tubes with laboratory-induced SCC. In addition, preliminary experiments were conducted on the erosion of steam generator tubing under water jet impingement.

4.2.1 Testing of tubes with EDM notches

Initial testing in the High-Pressure Test Facility following shakedown focused on the testing of 22.2-mm (7/8-in.)-diameter Alloy 600 tubes with EDM notches. These tests were conducted to study the influence of various test parameters such as flaw geometry, bladder/backup foil characteristics, and pressurization rate on flaw behavior. More than 40 flawed specimens of several different designs were fabricated and tested, with some flaw geometries tested in triplicate to evaluate reproducibility. These notches were all 0.19-mm (0.0075-in.) wide and had lengths of 6.35, 12.7, 19.3, and 25.4 mm (0.25, 0.5, 0.75, and 1.0 in.). The notches had uniform depths of 60, 80, 90, and 100% TW. Some axial notches of nonuniform depth were also tested. The results of some of these tests were described in the previous annual report,[1] and some of these results are repeated here along with results from additional tests.

As described in the previous report,[1] one of the first EDM notch tests was conducted on a tube with a 12.7-mm (0.5-in.)-long 60% TW OD flaw that was predicted to exhibit unstable tearing or bursting at a pressure of 38.6 MPa (5,600 psi) simultaneously with ligament tearing. Thus, this flaw geometry could be tested with and without a bladder to assess the influence of the bladder on the flaw opening pressure. The test without the bladder was conducted on Specimen OM113 at a pressurization rate of 13.8 MPa/s (2000 psi/s), and the tube burst unstably at 40.7 MPa (5900 psi). The resulting failure is shown in Fig. 4.45 of Ref. 1. A similar test on an identical Specimen OM112 with a 2.4-mm (3/32-in.)-thick hard Tygon bladder resulted in unstable burst at 41.4 MPa (6000 psi), but with a significantly larger opening area (see Fig. 4.46 of Ref, 1). However, the similar failure pressures for the two tubes suggests that the bladder has only a small influence on this parameter.

A subsequent pair of tests on identical specimens with different bladders confirmed the lack of effect of the bladder characteristics on failure pressure. Specimen OM102 with a 12.7–mm (0.5-in.)-long 100% TW EDM notch was tested at a pressurization rate of 13.8 MPa/s (2000 psi/s) with a hard Tygon bladder having a 2.4-mm (3/32-in.)-thick wall. The tube failed at 29.65 MPa (4300 psi), as compared to the predicted failure pressure of 30.3 MPa (4400 psi). As seen in Fig. 4.47 of Ref. 1, the flaw exhibited only a small amount of tearing at the ends, and the bladder extruded through the opening. In contrast, an identical Specimen OM101 tested under the same conditions but with a hard bladder having a 3.2-mm (1/8-in.)-thick wall exhibited significant flaw tearing and bulging, and the thicker bladder did not extrude through

the opening (Fig. 4.48 of Ref. 1). However, the failure pressure of 29.62 MPa (4296 psi) was almost identical to that of the previous test, indicating little influence of the bladder.

These tests indicate that the proper use of bladders does not appear to significantly affect the burst pressure irrespective of the extent of tearing for a given flaw geometry. However, it is readily apparent that even though the same values of burst pressure are achieved, the resulting leak areas are significantly different. This raises questions as to the correct crack opening area to be used in predicting the leak rate at burst. A detailed simulation of flaw structure and fluid dynamic interactions during burst may be required to answer this question.

Backup foils are sometimes used to prevent premature bladder extrusion through throughwall flaws and resulting excessive water leakage that would prevent pressurization to a sufficient level to burst a tube. To evaluate the influence of foil backups, two tubes with identical flaw geometries (axial notch 12.7-mm [0.5-in.] long and 100% TW) were tested at a pressurization rate of 13.8 MPa/s (2000 psi/s) with 3.2-mm (1/8-in.)-thick bladders and two different designs of 0.13 mm (0.005-in.)-thick brass foil backups. Specimen OM133 had a foil that extended 6.35 mm (0.25 in.) beyond the defining dimensions of the axial notch, in conformance with EPRI guidelines. Specimen OM134 had a larger foil that extended circumferentially 90° to either side of the notch and 12.7 mm (0.5 in.) beyond the ends of the notch. The use of a larger size foil can be advantageous when dealing with large near-throughwall flaws that cover a large tube area and have additional secondary cracking that makes a precise determination of flaw extent by pretest NDE or dye penetrant uncertain. In both cases, the internal tube surface was lubricated with a multipurpose spray lubricant to reduce friction between the foil and the tube.

Figures 4.38 and 4.39 show post-test photographs of the failed tubes with bladders and foil still in place for tests OM133 (small foil) and OM134 (large foil), respectively. Both flaws exhibit more unstable tearing than test OM101, which used only a bladder (see Fig. 4.48 of Ref. 1). However, most important, the burst pressures of 30.0 MPa (4350 psi) for Specimen OM133 and 30.7 MPa (4450 psi) for Specimen OM134 are close to the observed failure pressure of 29.6 MPa (4296 psi) for Specimen OM101 tested without the foil. For the tube with the smaller foil (Fig. 4.38), it can be seen that the foil has unsymmetrically slipped partially through the flaw opening. In the tube with the larger foil (Fig. 4.39), the foil has torn axially and symmetrically along the entire flaw opening length, suggesting that this larger foil does not slip as easily through the opening flaw upon failure. Even though these tests show that the foil coverage area has not influenced the failure pressure, this behavior could change if larger foils were used or tubes that fail at considerably lower pressures were tested, in which case the greater extent of foil might produce local strengthening and erroneous flaw opening pressure data. Likewise, thicker foils or foils made of stronger material such as stainless steel could also produce unreliable data.

Tube failure tests were also conducted on nine tubes with EDM OD axial notches 6.35 mm (0.25 in.) long and 60, 80 and 90% TW. The tests were conducted with and without bladders and foil backups at various pressurization rates. Prior to these tests, the shortest flaw tested was 8.89 mm (0.35-in.) long and 90% TW, which could not be opened in the 20.7 MPa (3000 psi) Pressure and Leak-Rate Test Facility at either room or elevated temperature. In addition, this short flaw was considerably stronger than predicted by structural analysis, in contrast to the generally good agreement observed for longer flaws.

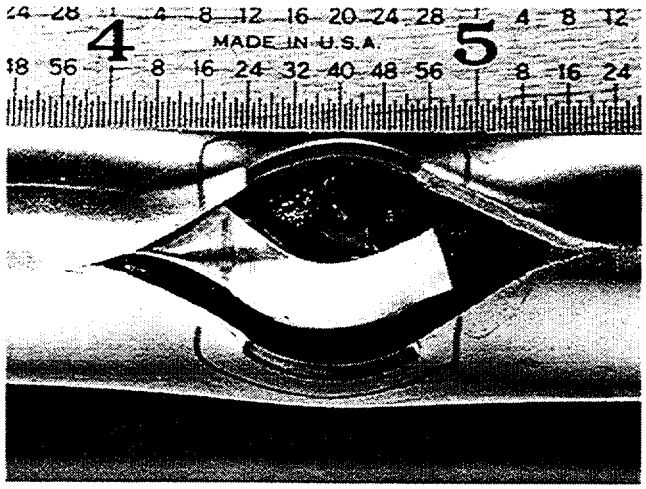

Fig. 4.38. Specimen OM133 with 12.7-mm (0.5-in.)-long 100% TW OD axial EDM notch tested with 3.2-mm (1/8-in.)-thick hard bladder and small backup foil at a pressurization rate of 13.8 MPa/s (2000 psi/s). Failure pressure was 30.0 MPa (4350 psi).

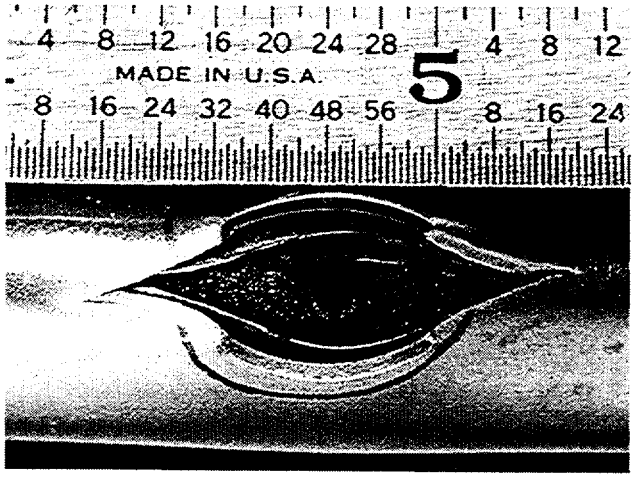

Fig. 4.39. Specimen OM134 with 12.7-mm (0.5-in.)-long 100% TW OD axial EDM notch tested with 3.2-mm (1/8-in.)-thick hard bladder and large backup foil at a pressurization rate of 13.8 MPa/s (2000 psi/s). Failure pressure was 30.7 MPa (4450 psi).

The results from the nine tests are summarized in Table 4.2, and post-test photographs of the flaws are shown in Figs 4.40-4.48. The 60% TW flaws (Specimens OM118 and OM119) were tested at fast pressurization rates without and with a bladder, respectively, and the flaws opened within 2.1 MPa (300 psi) of each other. These flaws were predicted to burst unstably at 45.4 MPa (6600 psi) before tearing, but the actual failure pressures were found to be somewhat higher. In addition, specimen OM118 (Fig. 4.40) exhibited no unstable tearing, but OM119 tested with a bladder (Fig. 4.41) exhibited significant tearing many times longer than the original flaw length. This effect of the bladder on flaw opening area is in agreement with the observations for Specimens OM113 and OM112 described above.

Table 4.2. Test results for flawed tubes containing 6.35-mm (0.25-in.)-long EDM OD axial notches.

Specimen ID	Flaw Depth, (% TW)	Pressurization Rate, MPa/s (psi/s)	Initial Flaw Tearing		Unstable Burst		Predicted Ligament Tear/Burst Press., MPa (psi)
			Pressure, MPa (psi)	Leak Rate, L/min (gpm)	Pressure, MPa (psi)	Leak Rate, L/min (gpm)	
OM118	60	13.6 (1970)	49.6 (7200)	46.9 (12.8)	d	d	48.3 (7000)/ 45.5 (6600)
OM119[a]	60	20.7 (3000)	47.6[a] (6900)[a]	>49[a] (13)[a]	47.6[a,e] (6900)[a,e]	>49[a,e] (>13)[a,e]	48.3 (7000)/ 45.5 (6600)
OM116	80	Quasi-steady	37.7 (5475)	12.5 (3.31)	d	d	37.2 (5400)/ 45.5 (6600)
OM117[a]	80	21.4 (3110)	43.1[a] (6252)[a]	>49[a] (13)[a]	43.1[a,e] (6252)[a,e]	>49[a,e] (>13)[a,e]	37.2 (5400)/ 45.5 (6600)
OM138	90	Quasi-steady	30.0 (4350)	4.2 (1.1)	42.7[d] (6200)[d]	45.0[d] (11.9)[d]	27.6 (4000)/ 45.5 (6600)
OM139	90	5.2 (750)	28.3 (4100)	2.8 (0.75)	43.8[d] (6356)[d]	45.4[d] (12.0)[d]	27.6 (4000)/ 45.5 (6600)
OM140	90	22.1 (3200)	33.8 (4900)	-	44.8[d] (6492)[d]	45.4[d] (12.0)[d]	27.6 (4000)/ 45.5 (6600)
OM141[b]	90	4.9 (705)	30.3[b] (4400)[b]	4.5[b] (1.2)[b]	45.0[b,e] (6520)[b,e]	48.4[b,e] (12.8)[b,e]	27.6 (4000)/ 45.5 (6600)
OM142[c]	90	6.3 (916)	27.6[c] (4008)[c]	4.9[c] (1.3)[c]	41.5[c,e] (6026)[c,e]	48.4[c,e] (12.8)[c,e]	27.6 (4000)/ 45.5 (6600)

[a]Tested with 2.38-mm (3/32-in.)-thick bladder.
[b]Tested with 3.18-mm (1/8-in.)-thick bladder.
[c]Tested with 3.18-mm (1/8-in.)-thick bladder with foil backing.
[d]No unstable burst.
[e]Unstable burst.

Specimens OM116 and OM117 with 80% TW flaws were tested at slow and fast pressurization rates without and with bladders, respectively. Specimen OM116 exhibited no unstable burst and opened at 37.7 MPa (5475 psi), whereas OM117 tested with a bladder exhibited unstable burst at 43.1 MPa (6252 psi). This flaw geometry was predicted to tear at 37.2 MPa (5400 psi) and to go unstable at 45.5 MPa (6600 psi). Specimen OM116, which could not be pressurized sufficiently rapidly to induce unstable burst because of the absence of a bladder, tore near the predicted value. Specimen OM117 tested with a bladder went unstable at a pressure ≈2.4 MPa (350 psi) lower than the predicted value for unstable burst. Again, as shown in Figs 4.42 and 4.43, the flaws exhibit greatly different flaw opening areas.

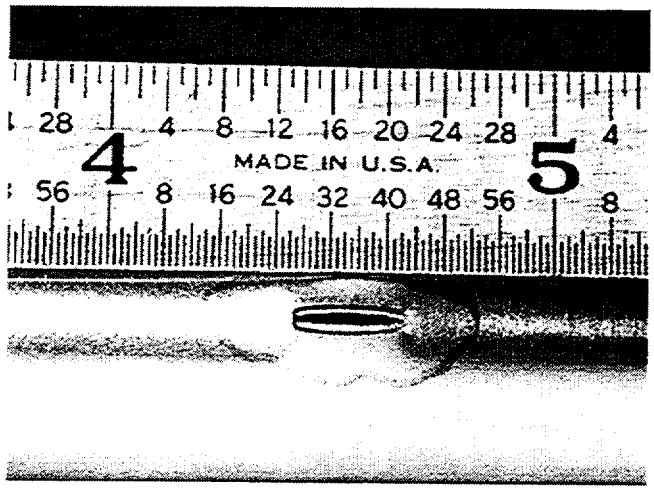

Fig. 4.40. Macroscopic appearance of Specimen OM118 after pressure testing. Initial flaw tearing occurred at 49.6 MPa (7200 psi). Specimen was tested without an internal bladder.

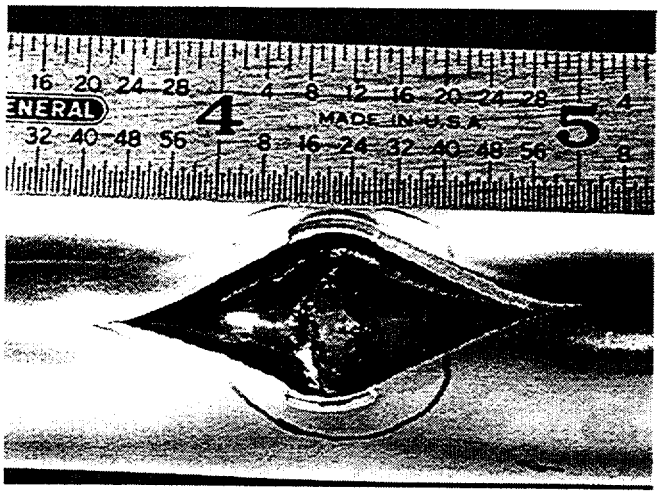

Fig. 4.41. Macroscopic appearance of Specimen OM119 after pressure testing. Flaw tearing and unstable burst occurred at 47.6 MPa (6900 psi). Specimen was tested with an internal bladder.

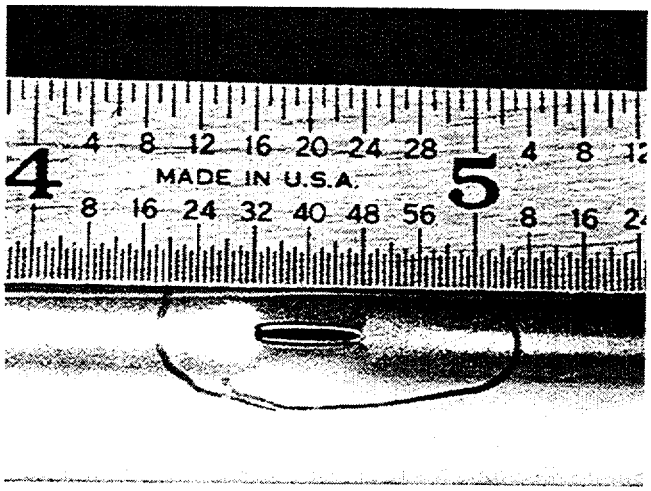

Fig. 4.42. Macroscopic appearance of Specimen OM116 after pressure testing. Initial flaw tearing occurred at 37.7 MPa (5475 psi).

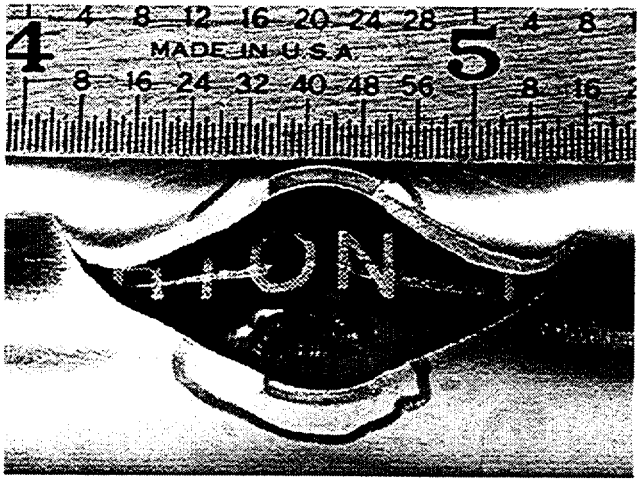

Fig. 4.43. Macroscopic appearance of Specimen OM117 after pressure testing. Flaw tearing and unstable burst occurred at 43.1 MPa (6252 psi). Specimen was tested with an internal bladder.

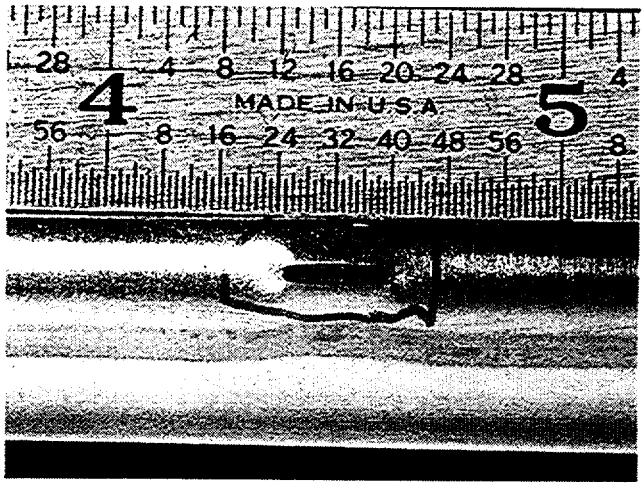

Fig. 4.44. Macroscopic appearance of Specimen OM138 after pressure testing. Initial flaw tearing occurred at 30.0 MPa (4350 psi), and additional deformation but no unstable burst occurred at maximum pressure of 42.7 MPa (6200 psi).

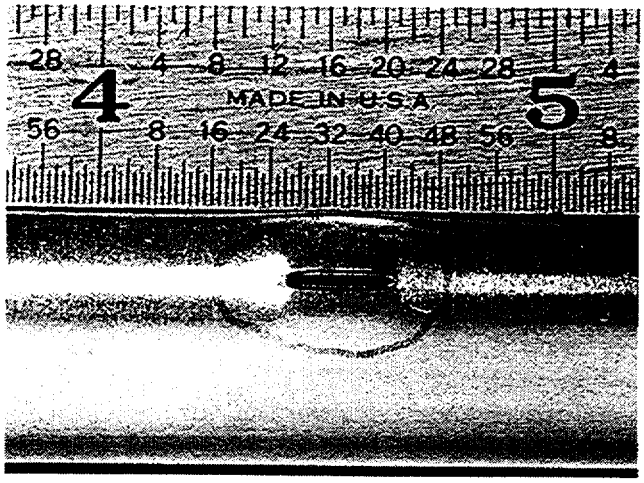

Fig. 4.45. Macroscopic appearance of Specimen OM139 after pressure testing. Initial flaw tearing occurred at 28.3 MPa (4100 psi), and additional deformation but no unstable burst occurred at maximum pressure of 43.8 MPa (6356 psi).

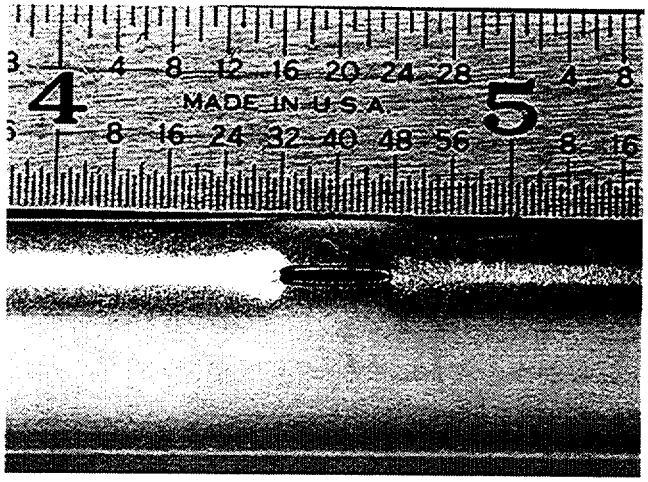

Fig. 4.46. Macroscopic appearance of Specimen OM140 after pressure testing. Initial flaw tearing occurred at 33.8 MPa (4900 psi), and additional deformation but no unstable burst occurred at maximum pressure of 44.8 MPa (6492 psi).

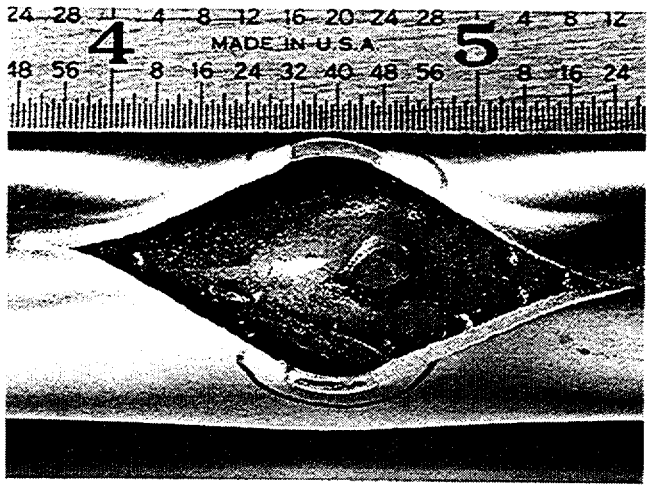

Fig. 4.47. Macroscopic appearance of Specimen OM141 after pressure testing. Initial flaw tearing occurred at 30.3 MPa (4400 psi), and unstable burst occurred at 45.0 MPa (6520 psi). Specimen was tested with an internal bladder.

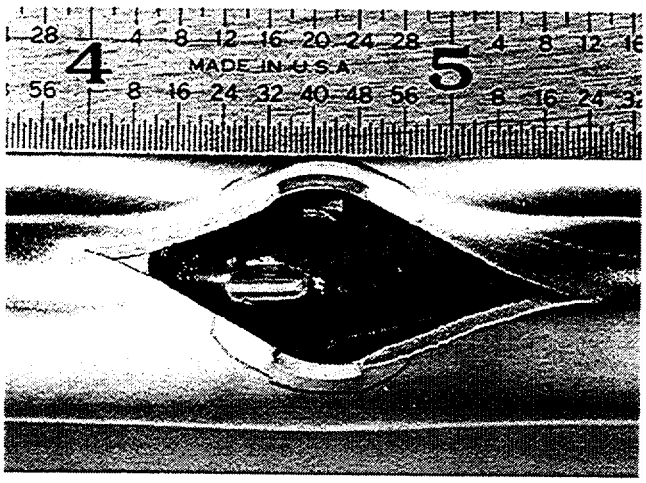

Fig. 4.48. Macroscopic appearance of Specimen OM142 after pressure testing. Initial flaw tearing occurred at 27.6 MPa (4008 psi), and unstable burst occurred at 41.5 MPa (6026 psi). Specimen was tested with an internal bladder with foil backing.

Three of the five 90% TW flaws (Specimens OM138, OM139, and OM140) were tested without bladders at progressively increasing pressurization rates of quasi-steady-state, 5.2 and 22.1 MPa/s (750 and 3200 psi/s), respectively. None of these flaws exhibited unstable burst. This flaw geometry was predicted to first tear at 27.6 MPa (4000 psi) and then to go unstable at 45.5 MPa (6600 psi). The specimens actually tore open at pressures of 30.0, 28.3, and 33.8 MPa (4350, 4100, and 4900 psi), respectively. Thus, the results for the tests conducted at the two slower pressurization rates were in good agreement with the predicted values, but the specimen tested at the fastest pressurization rate tore open at 6.2 MPa (900 psi) above the predicted value. This dependence of flaw opening pressure on pressurization rate has also been observed in previous tests conducted at ANL.[1] For all three specimens, the leak rates upon flaw opening were below the facility maximum of nominally 45 L/min (12.8 gpm), and the flaws were therefore pressurized to higher levels of 42.7, 43.8, and 44.8 MPa (6200, 6356, and 6492 psi), respectively. At this point, the flow rates reached the facility maximum, and further pressurization to unstable burst (≈45.5 MPa or 6600 psi) could not be achieved. The post-test appearances of these three specimens are shown in Figs. 4.44-4.46.

This same flaw geometry was tested with a bladder (Specimen OM141) and a bladder/foil combination (Specimen OM 142) using a pressurization rate of <6.9 MPa/s (<1000 psi/s). Both of these specimens went unstable and exhibited greatly increased flaw opening areas (Figs. 4.47 and 4.48). Both of these flaws first tore open near the predicted value of 27.6 MPa (4000 psi) and were then pressurized to higher levels. Specimen OM141, tested with only a bladder, exhibited unstable burst at 45.0 MPa (6520 psi), which is very near the predicted value of 45.4 MPa (6600 psi). However, Specimen OM142, which used a foil backup, burst at 41.5 MPa (6026 psi). The reason for this behavior is not clear.

Results are next presented from tests on three specimens, T29, T30, and T31, with OD axial EDM notches having nonuniform depths along the axial direction, which is in contrast to the above tests which all had uniform depth. All three notches were nominally 25.4-mm (1-in.) long and 0.19-mm (0.0075-in.) wide. This flaw geometry was tested to further evaluate an ANL equivalent notch analysis that was used to successfully predict flaw opening pressures in a previous series of five tests on SCC flaws.[1] For Specimens T30 and T31, the flaws were 0.635-mm (0.025-in.) deep at each end of the 25.4-mm (1-in.)-long notches and then deepened linearly to 1.14 mm (0.045 in.) at the midpoint of the notches. The flaw in Specimen T31 also had a 0.13-mm (0.005-in.)-diameter TW hole at the deepest midpoint of the notch. This hole was introduced to simulate TW pinholes that have been detected in previously tested nonuniform depth SCC flaws. The flaw in Specimen T29 was 1.04 mm (0.041-in.) deep at the ends and deepened linearly to 1.17 mm (0.046 in.) at the midpoint of the notch. It contained no TW hole. All three flaws were tested without bladders or foils using a quasi-steady pressurization rate consisting of increasing the pressure in 0.69 MPa (100 psi) increments, with a 5-s hold time between increases.

Figures 4.49 and 4.50 show the posttest appearance of Specimens T30 and T31, respectively. No unstable tearing into the ends of the notches occurred for either tube. Specimen T30 exhibited abrupt ligament tearing at 18.3 MPa (2650 psi) and T31 at 22.1 MPa (3200 psi), but the tearing did not extend into the notch ends for either flaw. However, tube T31, which had the 0.13-mm (0.005-in.)-diameter throughwall hole at the center of the flaw, exhibited greater ligament tearing, a wider crack opening, and a higher opening pressure. The reason for this behavior is being analyzed.

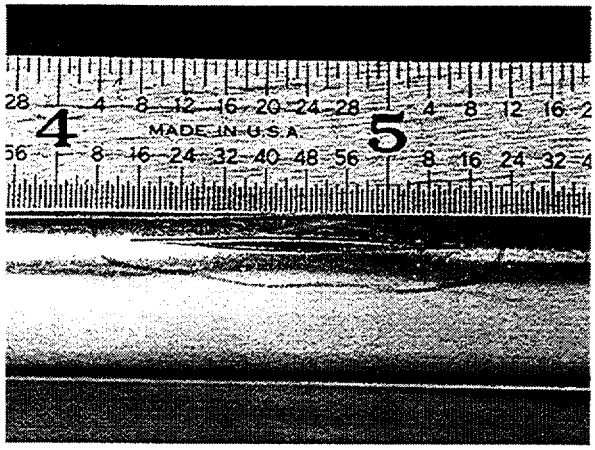

Fig. 4.49. Specimen T30 with nonuniform 25.4-mm (1-in.)-long OD axial EDM notch tested without bladder at quasi-steady-state pressurization rate. Failure pressure was 18.3 MPa (2650 psi).

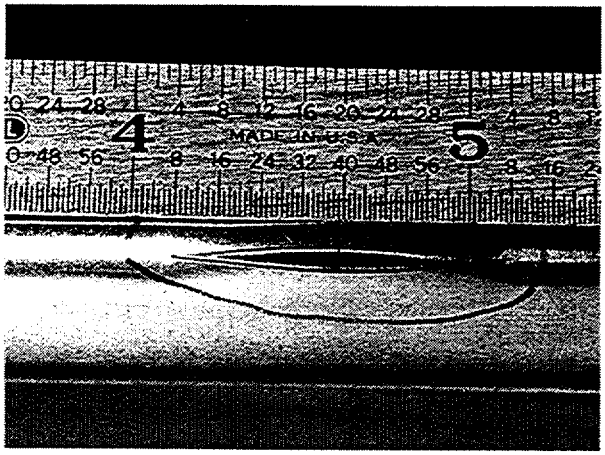

Fig. 4.50. Specimen T31 with nonuniform 25.4-mm (1-in.)-long OD axial EDM notch tested without bladder at quasi-steady-state pressurization rate. Flaw was identical to that in Specimen T30 (Fig. 4.49), except that it also had a 0.13-mm (0.005-in.)-diameter throughwall hole at its center. Failure pressure was 2.1 MPa (3200 psi).

The flaw in Specimen T29 opened gradually and began leaking at 8.3 MPa (1200 psi), then opened significantly at 9.7 MPa (1400 psi), with the flow rate exceeding 47.3 L/min (12.5 gpm). This is considerably lower than the opening pressure for the shallower flaws in Specimens T30 and T31. These data are also being analyzed by structural analysis.

4.2.2 Testing of tubes with complex interacting laser-cut notches

After testing the EDM flaws, pressure tests were performed on 24 22.2-mm (7/8-in.)-diameter Alloy 600 tubes with a variety of laser-cut OD flaws consisting of simple single axial and circumferential notches, as well as complex OD patterns of axial and circumferential notches separated by various ligament sizes. Ten different generic flaw geometries were tested. The laser cutting technique permits considerably more complex flaws to be fabricated than are

possible using EDM. These complex flaws are intended to more closely simulate the flaw patterns actually present in field-degraded tubes. The laser-cut flaws are also considerably tighter than the minimum 0.19-mm (0.0075-in.)-wide notches that can be achieved by EDM, and this flaw tightness may influence tube ligament tearing and unstable burst pressure behaviors. The laser-cut flaw data reported here complement the data reported above for tubes with EDM flaws.

The 24 laser-cut flaws were tested in two stages. The first stage consisted of pressurizing at a quasi-steady-state rate without the use of internal bladders. The pressurization protocol consisted of starting at an internal pressure of 0.34 MPa (50 psi) and increasing the pressure in 0.69 MPa (100 psi) increments after a 10 s dwell at each pressure plateau. This process continued until ligament tearing occurred, accompanied by an abrupt increase in flow. Data were thus obtained on the pressure at first ligament tearing, as well as the flow rate and sustainable pressure observed upon ligament tearing. Post-test photographs of the flaw opening yield information on flaw area, which is used to validate predictions from structural code analyses and from the Argonne sharp-edge orifice flow model.

The second stage of testing generated unstable burst pressure data by retesting the flaws that exhibited only stable ligament tearing and opening in the first stage tests. Excessive leakage through the flaws was prevented by using an internal bladder with a foil backup, if necessary, to prevent bladder wedging in the flaw opening. For tubes with complex flaws, the two-stage testing permitted an evaluation of the ligament tearing sequence that takes place as the flaw opens. It also permitted both the unstable burst as well as the stable ligament tearing pressures to be determined for flaws that do not immediately go unstable. If the testing had been conducted using only internal bladders and rapid pressurization rates (i.e., no Stage 1 testing), data on stable ligament tearing would not be obtained.

The results from the 24 Stage 1 tests are summarized in Table 4.3, and the detailed configurations of the ten different laser-notched specimen types tested are shown in Fig. 4.51. Pre- and post-test photographs of representative flaws of the ten types are shown in Figs. 4.52-4.61. The ten generic flaw geometries tested are indicated in the second column in Table 4.3 and shown in the pre-test photographs of Figs. 4.52-4.61. Table 4.3 gives the nominal flaw dimensions and the nominal sizes of ligaments separating the multiple notches of the more complex flaws. Table 4.3 also gives pre-test EC estimates of the maximum flaw depth. It should be noted that all of the laser-cut flaws exhibited pinhole laser burn-through at the ends of each notch. These pinholes were too small to be detected by EC techniques, but they leaked air at 0.34 MPa (50 psi). At a pressure of 6.9 MPa (1000 psi), the leak rate through these pinholes was typically in the range of 0.04-0.4 L/min (0.01-0.1 gpm or 14.4-144 gal per day).

The six Type 1 flaws (Fig. 4.51) were simple single axial notches of three different lengths (6.35, 8.9, and 12.7 mm [0.25, 0.35, 0.5-in.]) and all nominally 80% TW. Duplicate tests of each of the three flaw lengths were conducted to check on test reproducibility. Figure 4.52 shows the pre- and post-test flaw photographs for Specimen 5528-2-1, which had a 12.7-mm (0.5-in.)-long axial notch. The post-test photograph shows that the ligament has torn completely but that there is no unstable tearing at the notch ends. From Table 4.3, it is seen that the ligament tore open at 34.4 MPa (5000 psi) and that the sustained pressure and flow rate after opening were 3.4 MPa (500 psi) and 48.1 L/min (12.7 gpm), respectively. The observed flow rate was near the maximum 48.8 L/min (12.8 gpm) facility capacity. These data

Table 4.3. Test results from Stage 1 testing (without bladders and quasi-steady pressurization) of flawed tubes containing OD laser-cut notches. All notches had nominal depths of 80% TW except for Specimens 5528-3-3 and 5469-2-2, which had nominal depths of 40% TW. All tubes leaked air through laser burn pinholes at the ends of the laser-cut notches at 0.34 MPa (50 psi) except Specimen 5528-2-2.

Specimen Number	Flaw Type	Number of Notches	NDE Flaw Depth (% TW)	Nominal Flaw Length, mm (in.)	Ligament Width, mm (in.)	Max. Pressure at Ligament Tearing, MPa (psi)	Sust. Pressure after Ligament Tearing, MPa (psi)	Flow Rate after Ligament Tearing, L/min (gpm)
5528-1-1	1	1	75	6.35 (0.25)	NA	36.6 (5310)	36.5 (5300)	18.1 (4.78)
5528-1-2	1	1	74	6.35 (0.25)	NA	37.1 (5380)	37.0 (5360)	13.8 (3.65)
5528-1-3	1	1	76	8.89) (0.35	NA	31.7 (4600)	29.8 (4320)	32.6 (8.6)
5528-1-4	1	1	73	8.89) (0.35	NA	32.4 (4700)	31.2 (4530)	30.5 (8.05)
5528-2-1	1	1	69	12.7 (0.5)	NA	34.5 (5000)	3.5 (500)	48.1 (12.7)
5528-2-2	1	1	61	12.7 (0.5)	NA	38.6[b] (5600)[b]	1.4 (200)	48.4 (12.8)
5516-4-3	2	2	72	12.7 (0.5)	0.25 (0.01)	33.8 (4900)	7.2 (1040)	48.1 (12.7)
5516-4-2	2	2	70	12.7 (0.5)	0.13 (0.005)	33.8 (4900)	6.5 (940)	48.1 (12.7)
5528-3-1	3	6	70	12.7 (0.5)	0.13 (0.005)	29.0 (4200)	10.7 (1550)	48.1 (12.7)
5528-3-2	3	6	73	12.7 (0.5)	0.25 (0.01)	30.0 (4350)	8.5 (1240)	48.1 (12.7)
5528-3-3[a]	3	6	61	12.7 (0.5)	0.25 (0.01)	35.2 (5100)	3.7 (540)	48.4 (12.8)
5528-3-4	4	6	76	12.7 (0.5)	0.13 (0.005)	35.9 (5200)	2.7 (390)	48.4 (12.8)
5469-2-1	4	6	74	12.7 (0.5)	0.25 (0.01)	32.8 (4750)	6.0 (870)	48.4 (12.8)
5469-2-2[a]	4	6	60	12.7 (0.5)	0.25 (0.01)	37.6 (5450)	3.8 (550)	48.4 (12.8)
5469-2-3	5	6	79	12.7 (0.5)	0.25 (0.01)	33.5 (4860)	2.1 (800)	48.4 (12.8)
5469-2-4	5	6	78	12.7 (0.5)	0.51 (0.02)	39.3[b] (5700)[b]	1.0 (150)	48.4 (12.8)

[a]Laser-cut notches had nominal depths of 40% TW.
[b]Specimen exhibited unstable tearing without internal bladder.

Table 4.3. (Cont'd.)

Specimen Number	Flaw Type	Number of Notches	NDE Flaw Depth (% TW)	Nominal Flaw Length, mm (in.)	Ligament Width, mm (in.)	Max. Pressure at Ligament Tearing, MPa (psi)	Sust. Pressure after Ligament Tearing, MPa (psi)	Flow Rate after Ligament Tearing, L/min (gpm)
5469-3-1	6	6	80	12.7 (0.5)	0.25 (0.01)	28.3 (4110)	13.3 (1930)	46.9 (12.4)
5531-3-1	6	6	79	12.7 (0.5)	0.51 (0.02)	34.3 (4980)	5.2 (760)	48.4 (12.8)
5469-3-3	7	2	75	360°	0.13 (0.005)	51.4 (7450)	0.4 (60)	49.2 (12.99)
5469-3-4	7	2	74	360°	0.25 (0.01)	51.7 (7500)	did not fail	did not fail
5469-4-1	8	6	70	360°	0.13 (0.005)	39.2 (5680)	0.3 (50)	48.8 (12.9)
5469-4-2	8	6	70	360°	0.25 (0.01)	38.3 (5550)	0.3 (50)	48.8 (12.9)
5469-4-3	9	2	69	180° x 0.5	NA	30.8 (4475)	0.7 (100)	48.8 (12.9)
5469-4-4	10	2	72	180° x 0.5	NA	31.3 (4540)	0.7 (100)	48.8 (12.9)

[a]Laser-cut notches had nominal depths of 40% TW.
[b]Specimen exhibited unstable tearing without internal bladder.

can be used to calculate a flaw opening area, which can then be checked by actual measurement. The duplicate tests indicated reasonable reproducibility of the ligament tear pressure, with the observed variation for the 12.7-mm (0.5-in)-long flaws believed to be due to differences in actual flaw depth for the two tubes, based on NDE data.

The two Type 2 flaws (Fig. 4.51) consisted of two aligned axial notches each 6.35 mm (0.25 in.) in length and 80% TW, separated by a complete wall thickness ligament of lengths 0.25 or 0.13 mm (0.010 or 0.005-in.). Figure 4.53 shows the pre- and post-test flaw appearances of Specimen 5516-4-3, which had the 0.25-mm (0.010-in.)-long ligament. The post-test photograph indicates no unstable tearing at the notch ends and shows that the ligament between the two notches, as well as those at the bottom of each notch, have torn. During testing, no indication of progressive sequential tearing was evident; both types of ligaments tore simultaneously at 33.8 MPa (4900 psi).

The three Type 3 flaws (Fig. 4.51) consisted of six aligned equal-length axial notches separated by complete wall thickness ligaments. The total length of the composite flaw (notches plus ligaments) was 12.7 mm (0.5-in.). For two of the tubes, the flaws were 80% TW, and the interspersed ligaments were 0.13 or 0.25 mm (0.005 or 0.010 in.) in length. For the

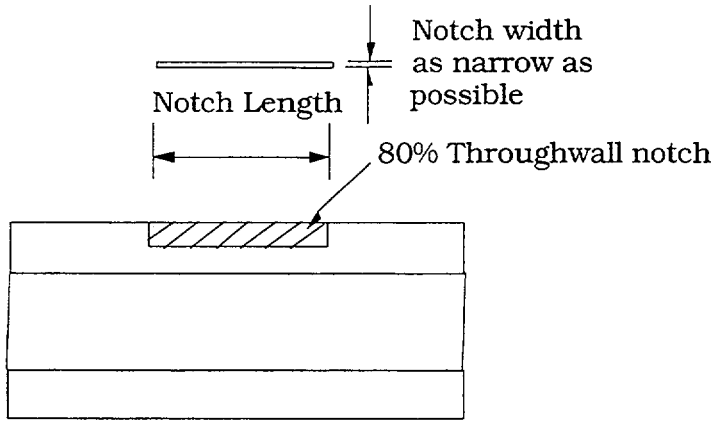

Type 1 specimen

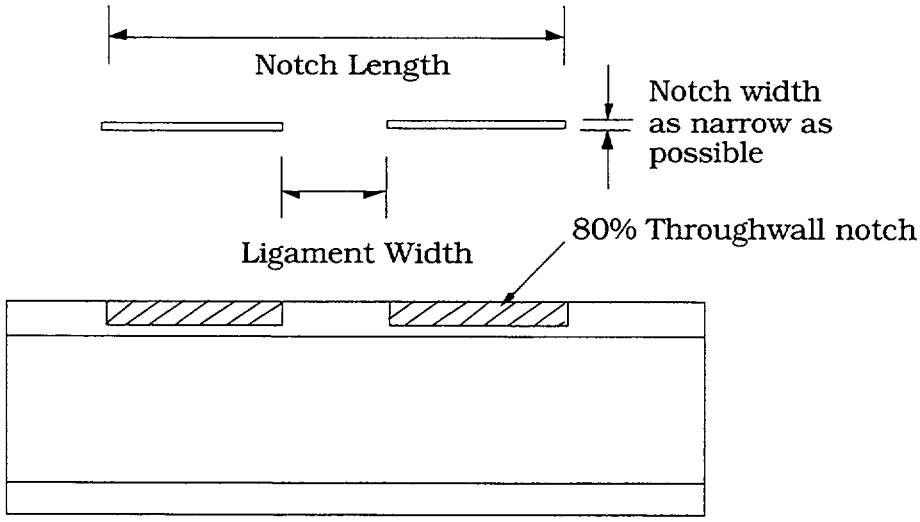

Type 2 specimen

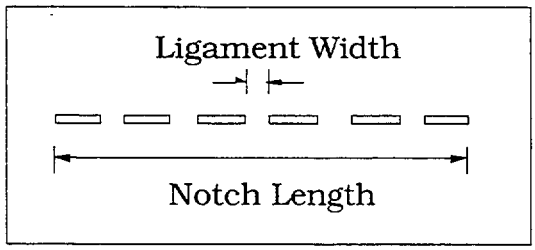

Type 3 specimen

Fig. 4.51. Configurations of notches in various types of laser-cut tube specimens.

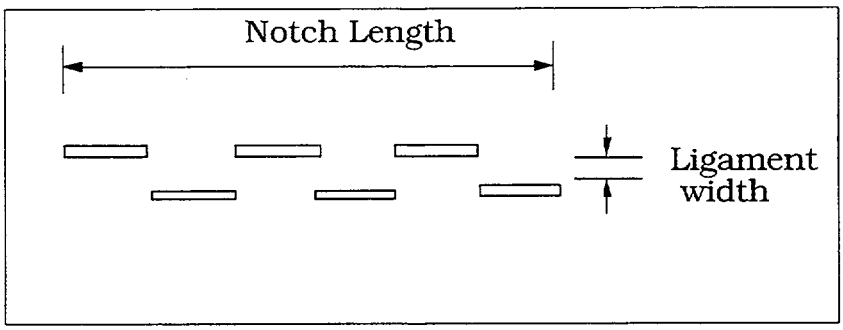

Type 4 specimen

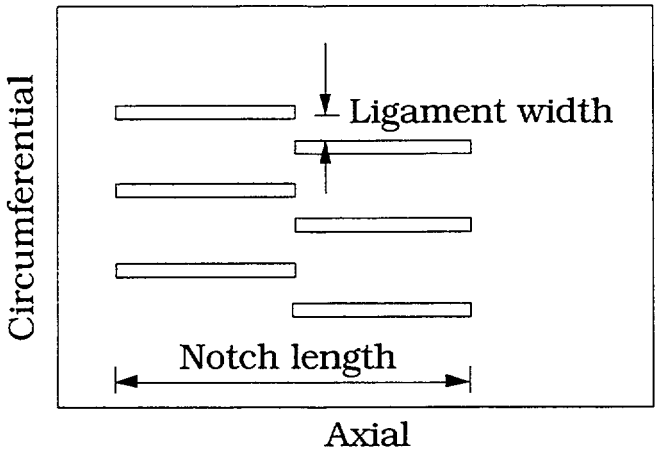

Type 5 specimen

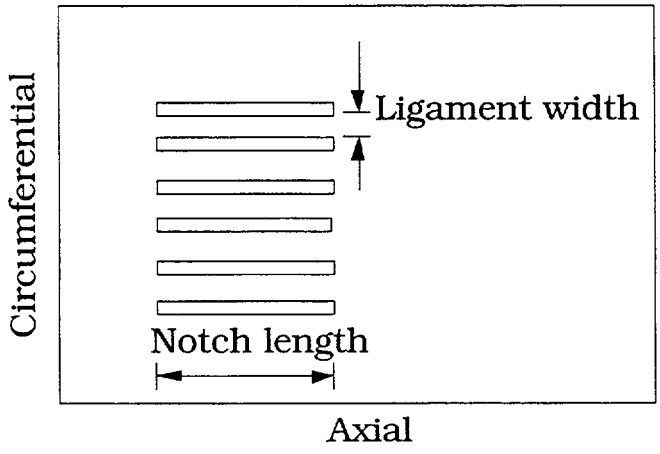

Type 6 specimen

Fig. 4.51. Configurations of notches in various types of laser-cut tube specimens (cont'd.).

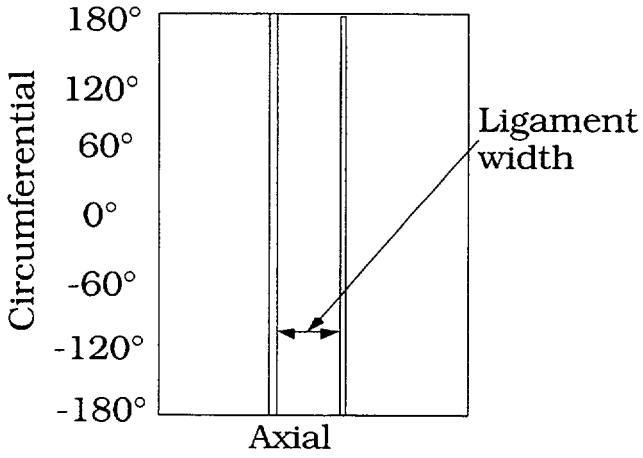

Type 7 specimen

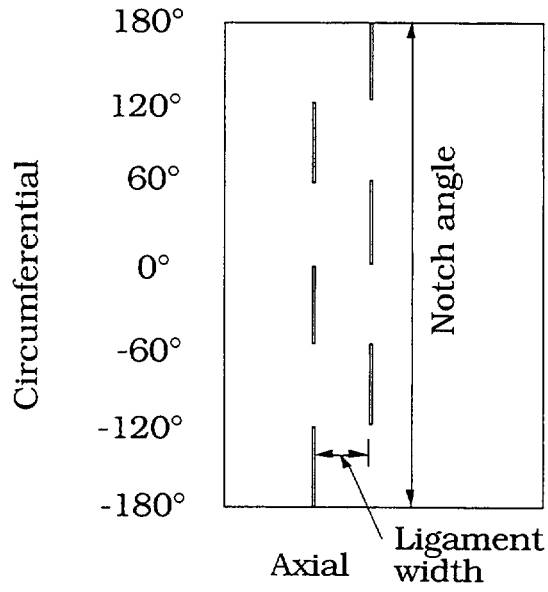

Type 8 specimen

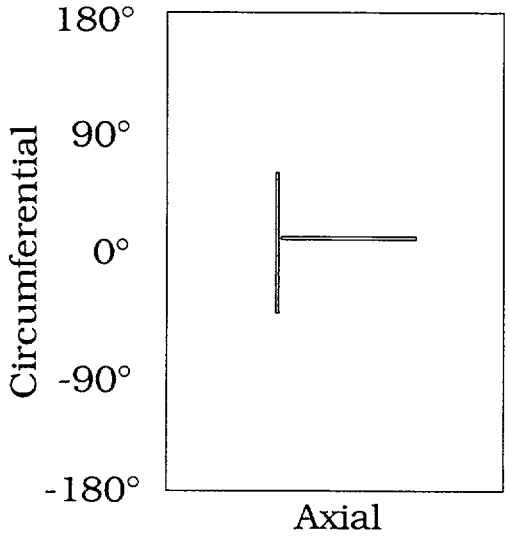

Type 9 specimen

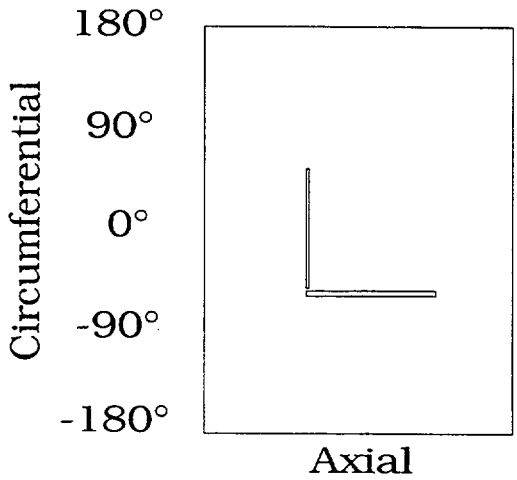

Type 10 specimen

Fig. 4.51. Configurations of notches in various types of laser-cut tube specimens (cont'd.).

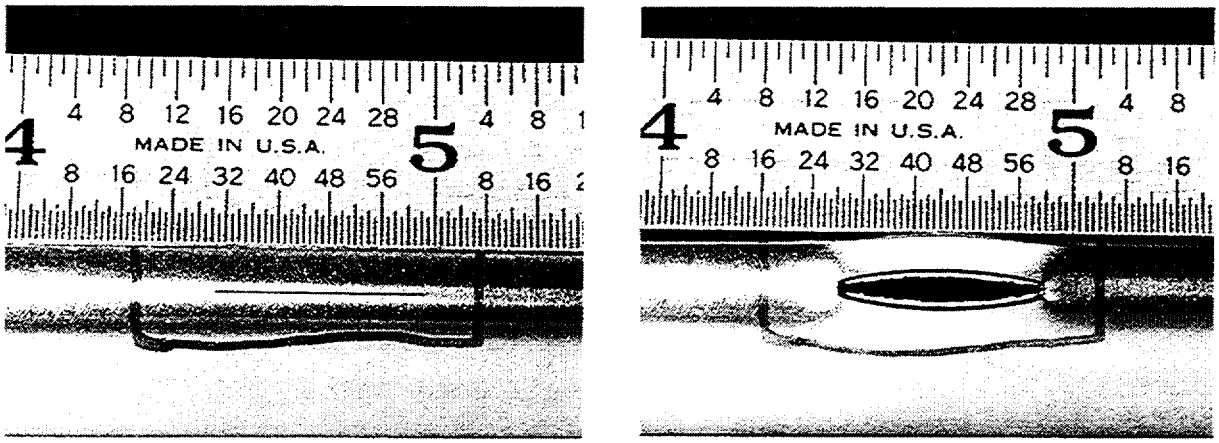

Fig. 4.52. Appearance of Specimen 5528-2-1 with Type 1 flaw before (left) and after (right) Stage 1 testing.

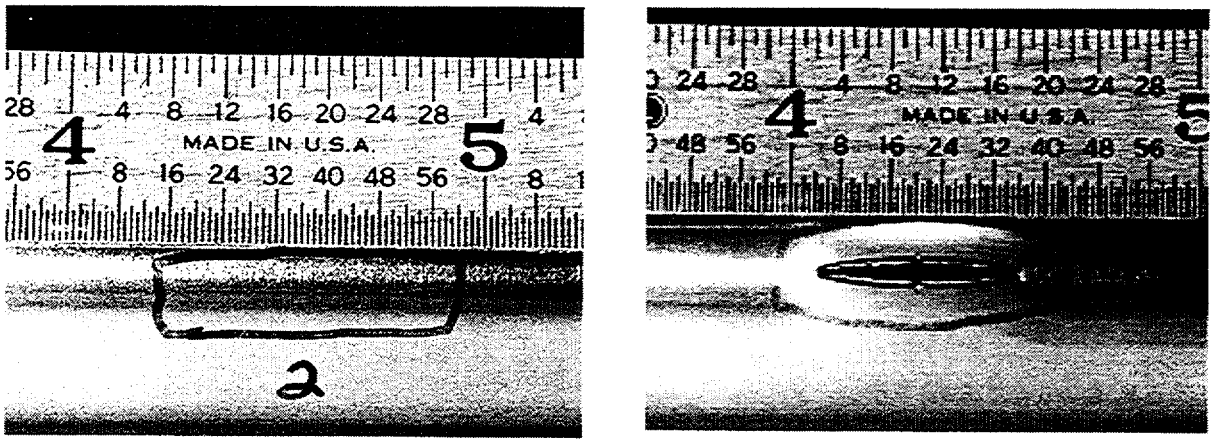

Fig. 4.53. Appearance of Specimen 5516-4-3 with Type 2 flaw before (left) and after (right) Stage 1 testing.

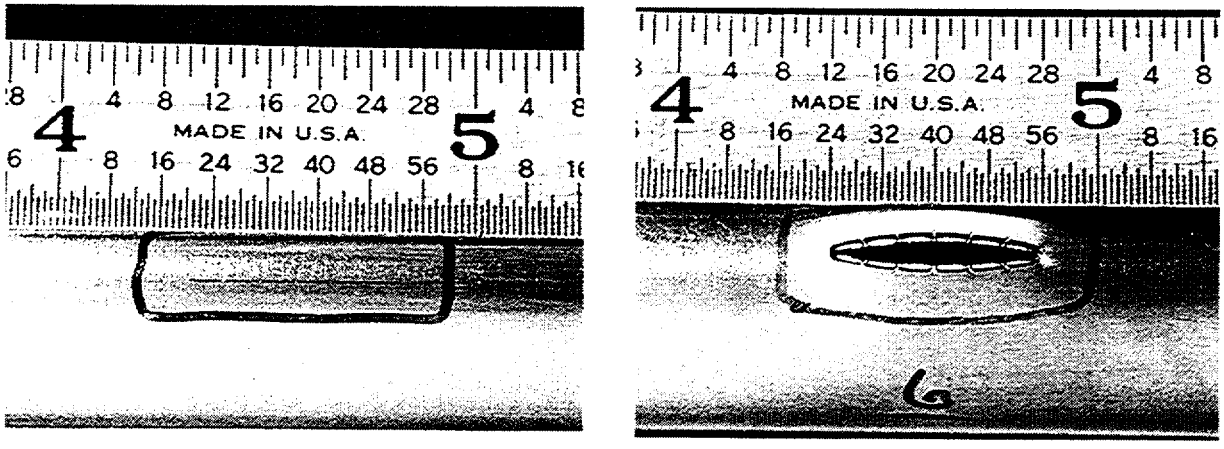

Fig. 4.54. Appearance of Specimen 5528-3-3 with Type 3 flaw before (left) and after (right) Stage 1 testing.

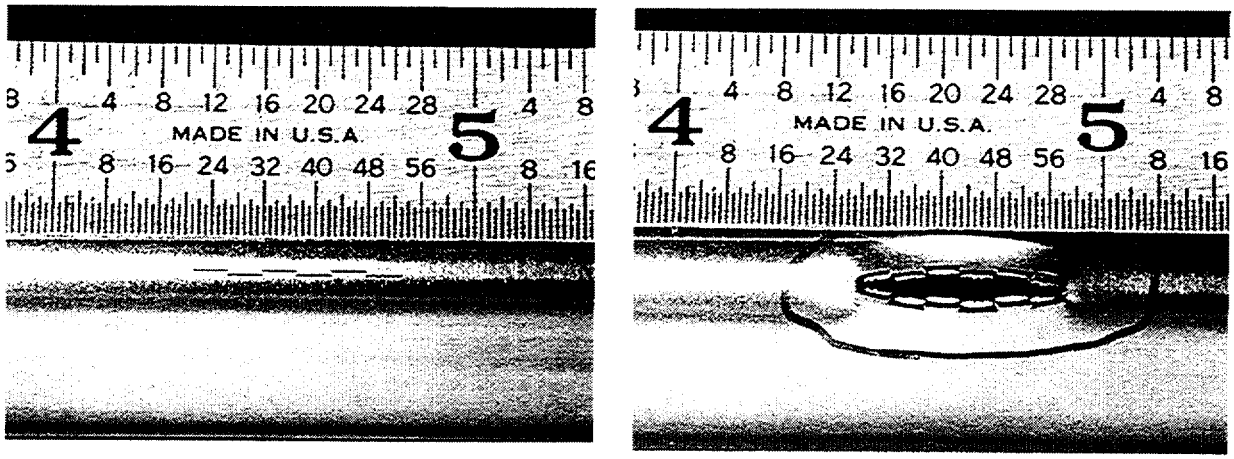

Fig. 4.55. Appearance of Specimen 5469-2-2 with Type 4 flaw before (left) and after (right) Stage 1 testing.

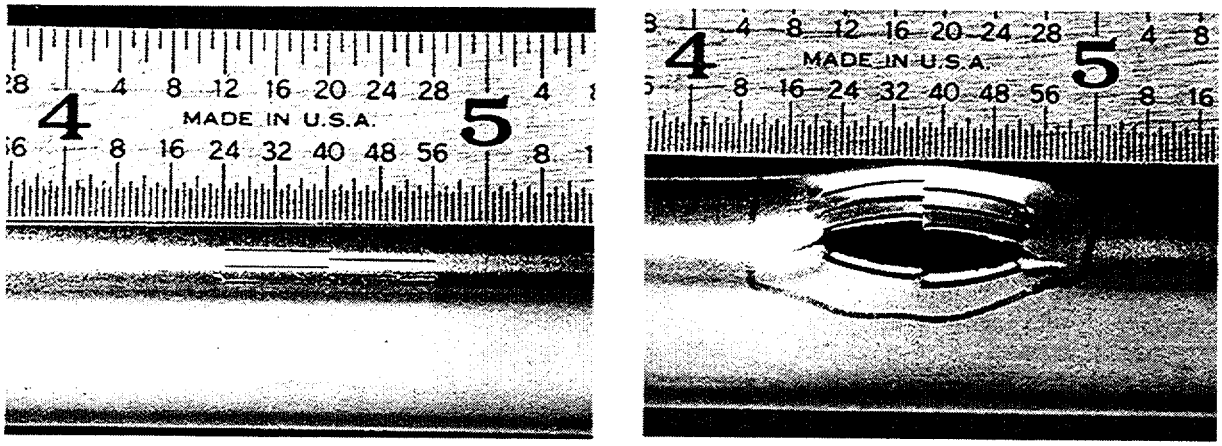

Fig. 4.56. Appearance of Specimen 5469-2-4 with Type 5 flaw before (left) and after (right) Stage 1 testing.

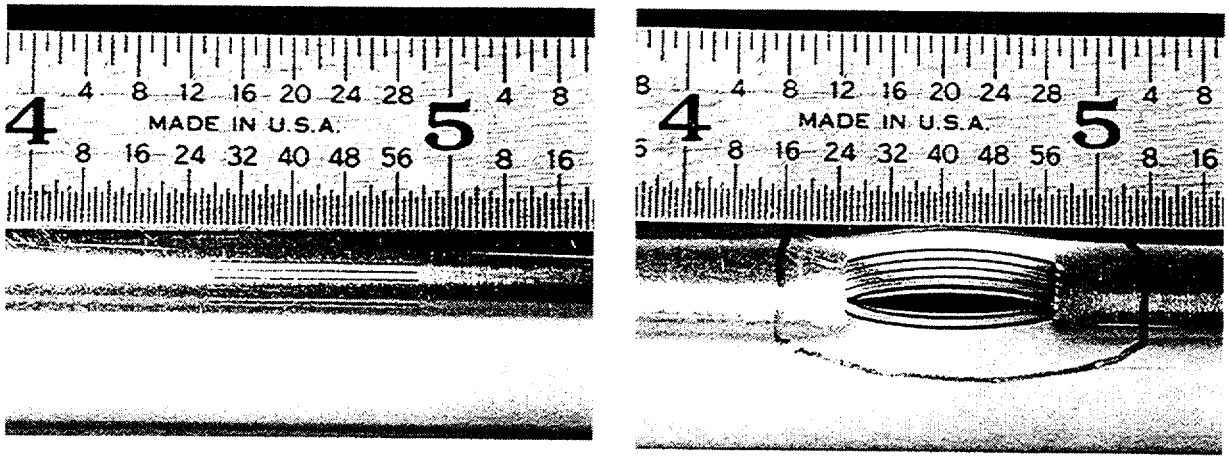

Fig. 4.57. Appearance of Specimen 5531-3-1 with Type 6 flaw before (left) and after (right) Stage 1 testing.

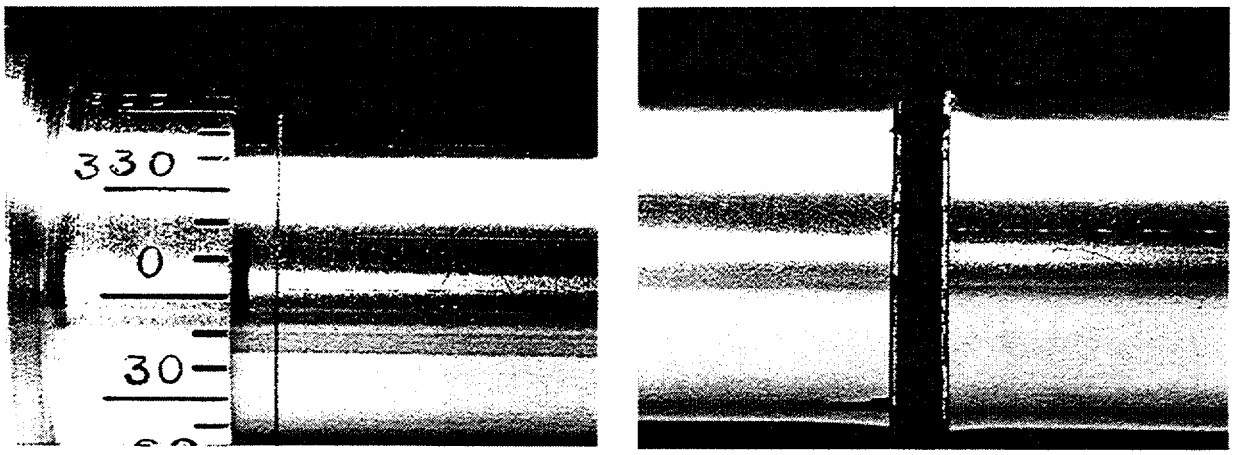

Fig. 4.58. Appearance of Specimen 5469-3-3 with Type 7 flaw before (left) and after (right) Stage 1 testing.

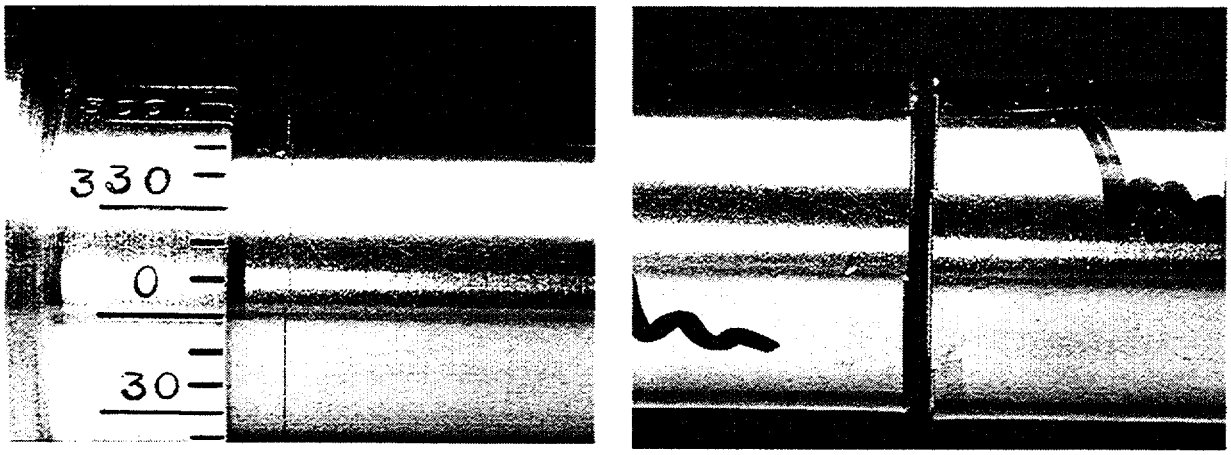

Fig. 4.59. Appearance of Specimen 5469-4-1 with Type 8 flaw before (left) and after (right) Stage 1 testing.

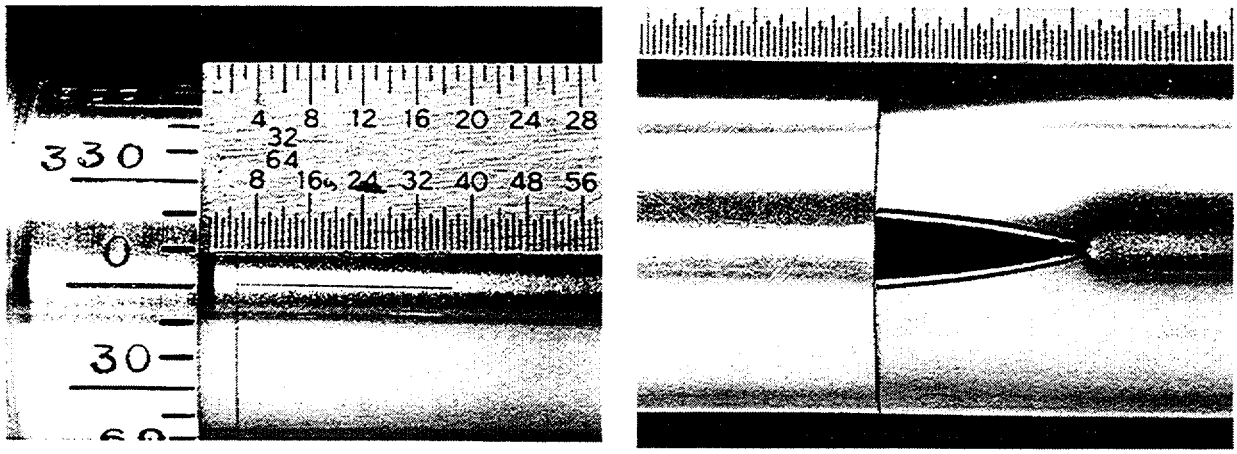

Fig. 4.60. Appearance of Specimen 5469-4-3 with Type 9 flaw before (left) and after (right) Stage 1 testing.

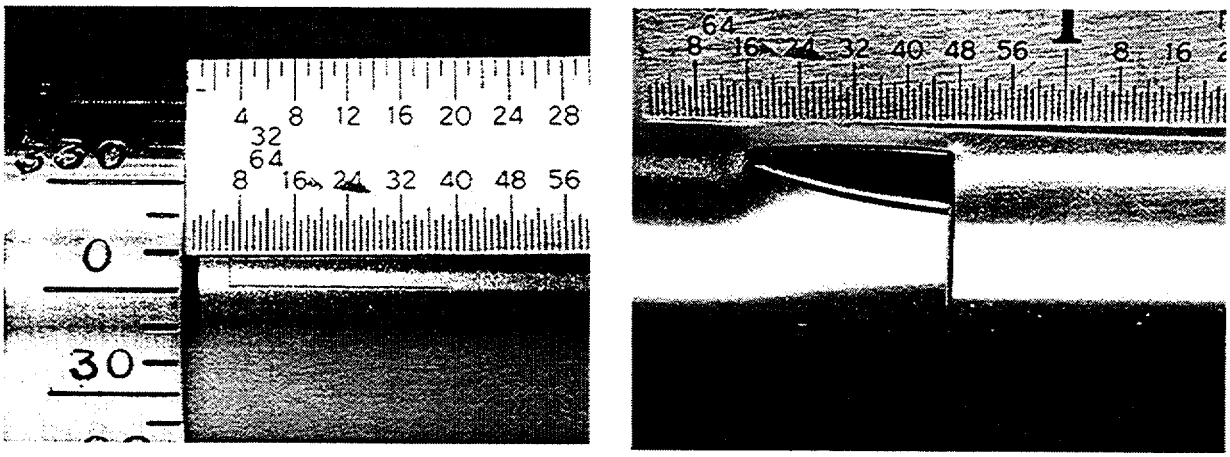

Fig. 4.61. Appearance of Specimen 5469-4-4 with Type 10 flaw before (left) and after (right) Stage 1 testing.

third tube, the six notches were only 40% TW, and the interspersed ligaments were 0.25 mm (0.010 in.) long. Figure 4.54 shows the pre- and post-test appearances of Specimen 5528-3-3, which had the 40% TW flaw depth. The post-test photograph indicates no unstable tearing at the notch ends and shows that the ligaments between the notches and those at the bottom of each notch have torn. Again, all of the ligaments tore simultaneously at the failure pressure of 35.2 MPa (5100 psi). For this type of flaw and the dimensions tested, the length of the ligaments separating the notches had little influence on failure pressure, but the depth of the notches exerted a noticeable influence.

The three Type 4 flaws (Fig. 4.51) consisted of six nonaligned side-step equal-length axial notches in two axial rows of three aligned flaws each separated by complete wall thickness ligaments. The overall length of the composite flaw was 12.7 mm (0.5 in.). In two of the three tubes, the individual notches were 80% TW, and the interspersed ligaments were 0.13 or 0.25 mm (0.005 or 0.010 in.) in length. In the third tube, the individual notches were only 40% TW, and the interspersed ligaments were 0.25 mm (0.010 in.) long. Figure 4.55 shows the pre- and post-test flaw appearances of Specimen 5469-2-2, which had the 40% TW flaw depth. The post-test photograph indicates no unstable tearing at the notch ends and shows that the ligaments between the notches and those at the bottom of each notch have torn. Again, all of the ligaments tore simultaneously at the failure pressure of 37.6 MPa (5450 psi), and the depth of the notches exerted a stronger influence on the failure pressure than did the length of the interspersed ligaments.

The two Type 5 flaws (Fig. 4.51) were made up of six individual notches of equal length in two parallel offset rows of three notches each. The laser-cut notches in both specimens were 80% TW, and the ligament lengths were either 0.25 or 0.51 mm (0.010 or 0.020 in.). Figure 4.56 shows the pre- and post-test appearances of Specimen 5469-2-4, which had the 0.51-mm (0.020-in.) ligaments. The post-test photograph shows that ligament tearing occurred along only one of the unaligned axial rows and that, in contrast to the previous tests, unstable tearing also occurred at the ends of flaw. This unstable tearing occurred without the use of an internal bladder. No indication of progressive sequential tearing was evident during testing; all ligaments tore simultaneously at 39.3 MPa (5700 psi). The other flaw of this type (5469-2-3) with the thinner 0.25-mm ligament between notches, did not tear unstably, and it opened at the considerably lower pressure of 33.5 MPa (4860 psi).

The two Type 6 flaws (Fig. 4.51) consisted of six axial parallel notches of equal 12.7-mm (0.50-in.) length and 80% TW depth with ligament widths of 0.25 or 0.51 mm (0.010 or 0.020 in.) (Table 4.3). Figure 4.57 shows the pre- and post-test flaw photographs for Specimen 5531-3-1, which had the 0.51-mm (0.020-in.)-long ligaments. The post-test photograph shows that ligament tearing occurred in only one of the parallel notches and that no unstable tearing occurred at the ends of notch. The flaw tore open at 34.3 MPa (4980 psi). The other flaw of this type (Specimen 5469-3-1) with the thinner 0.25-mm (0.010-in.)-long ligament between the notches behaved similarly but opened at the considerably lower pressure of 28.3 MPa (4110 psi).

The two Type 7 flaws (Fig. 4.51) consisted of two parallel 360° continuous circumferential notches of 80% TW depth separated by ligament widths of 0.13 or 0.25 mm (0.005 and 0.010 in). Figure 4.58 shows the pre- and post-test appearances of Specimen 5469-3-3, which had the thinner 0.13-mm (0.005-in.) ligament. The post-test photograph shows that ligament tearing occurred around the entire tube circumference, resulting in complete separation of the tube into two pieces. Failure occurred at 51.4 MPa (7450 psi), which is near the maximum 53.1 MPa (7700 psi) operating pressure of the facility. The other flaw of this type (Specimen 5469-3-4) but having the thicker 0.25-mm (0.010 in.) ligament could not be opened at the maximum facility pressure of 53.1 MPa (7700 psi).

The two Type 8 flaws (Fig. 4.51) consisted of six equal-length circumferential notches of 80% TW depth in two circumferential parallel rows having three notches each, separated by ligaments widths of 0.13 or 0.25 mm (0.005 or 0.010 in.). Figure 4.59 shows the pre- and post-test appearances of Specimen 5469-4-1, which had the thicker 0.25-mm (0.010-in.) ligament. The post-test photograph shows that ligament tearing occurred around the entire tube circumference, resulting in complete separation of the tube into two pieces. Failure occurred at 39.2 (5680 psi). The other flaw of this type (Specimen 5469-4-2) with the thinner 0.13-mm (0.005-in.) ligament opened at the slightly lower pressure of 38.3 MPa (5550 psi).

The single Type 9 flaw (Fig. 4.51) consisted of two intersecting notches, one extending 180° around the circumference and the second, perpendicular, notch extending 12.7 mm (0.5 in.) in the axial direction. The two notches were 80% TW and formed a tee. Figure 4.60 shows the pre- and post-test appearances of Specimen 5469-4-3. The post-test photograph shows that ligament tearing occurred primarily along the 12.7-mm (0.5-in)-long axial notch and only slightly along the circumferential notch. The flaw tore open at 30.9 MPa (4475 psi).

The single Type 10 flaw (Fig. 4.51) consisted of two intersecting notches similar to those in the Type 9 flaw. However, the notches in the Type 10 flaw were configured to form an ell rather than a tee. Figure 4.61 shows the pre- and post-test appearances of Specimen 5469-4-4. The post-test photograph shows that ligament tearing again occurred primarily along the 12.7-mm (0.5-in.)-long axial notch and only slightly along the circumferential notch. The flaw tore open at 31.3 MPa (4540 psi), very near the failure pressure for the Type 9 flaw.

Most of the tubes from the 24-tube set were subjected to Stage 2 testing after the above Stage 1 tests were completed. However, several tubes from Stage 1 were not capable of being tested under Stage 2. For example, Specimen 5528-2-2 exhibited unstable tearing in Stage 1 (without an internal bladder); its burst pressure is given in Table 4.3. Specimens 5528-2-1 and 5528-2-2 were destructively examined after Stage 1 testing to evaluate notch tear characteristics and the true depth of the laser cuts, and they could therefore not be tested in

Stage 2. Finally, Specimens 5469-3-3, 5469-4-1, 5469-4-2, 5469-4-3, and 5469-4-4 exhibited such large flaw tear openings from Stage 1 testing that they could not be sealed adequately with a bladder and foil to be unstably burst in Stage 2. As shown in Table 4.4, the remaining 17 flaws were Stage-2 tested and exhibited unstable tearing or burst, except for specimen 5469-3-4, which had a circumferential flaw that could not be opened at the maximum 53.1 MPa (7700 psi) pressure of the facility. Post-Stage 2 test photographs of the flaws are shown in Figs. 4.62-4.66.

Initially, the Stage 2 tests were conducted with only a bladder (3.2-mm [1/8-in.]-thick Tygon tubing) and without a foil backup (Specimens 5528-1-1 through 5528-3-1). However, all flaws after this were tested with the same bladder and a 0.13-mm (0.005-in)-thick brass foil backup. Specimens 5516-4-3, 5516-4-2, and 5528-3-1 all had 12.7-mm (0.5-in.)-long notches and exhibited appreciable notch width opening after Stage 1 testing. During the Stage 2 testing of these specimens, it was observed that the burst pressures were very low and that after testing, the bladders were wedged in the opening, a phenomenon that can result in atypical reduced burst pressures. The reported burst data for these three specimens are thus incorrect. Backup foils were used in the remaining tests. The 6.35-mm and 8.9-mm (0.25 and 0.35-in)-long single axial flaws tested with only a bladder (specimens 5528-1-1, 5528-1-2, 5528-1-3, and 5528-1-4) did not exhibit bladder wedging, probably because the flaw openings were much smaller after the Stage 1 tests than for the 12.7-mm (0.5-in.)-long flaws. The ligament tear data from Table 4.3 and the burst data shown in the last column of Table 4.4 are currently being compared with analytical predictions.

The following summarizes the combined results from the Stages 1 and 2 testing for each of the flaw types.

For the six Type 1 flaws, duplicate Stage 1 tests of each of the three flaw lengths were conducted to check test reproducibility. As described above, the ligaments tore completely in the Stage 1 tests and there was no unstable tearing at the notch ends. Under Stage 2 testing, five of the six flaws exhibited unstable burst (Table 4.4).

No unstable tearing at the notch ends of the two Type 2 flaws was observed after Stage 1 testing, though the ligament between the two notches, as well as those at the bottom of each notch, tore. No indication of progressive sequential tearing was evident; both types of ligaments tore simultaneously. In Stage 2 testing, both flaws burst unstably, but, as mentioned above, bladder wedging resulted in an artificially low value for the burst pressure. The Stage 2 post-test photograph of Specimen 5516-4-3 is shown in Fig. 4.62, and unstable tearing is evident into the ends of the notch.

For the three Type 3 flaws, no unstable tearing at the notch ends was observed under Stage 1 testing, and the ligaments between the notches and those at the bottom of each notch tore simultaneously at the failure pressure. For this type of flaw and the dimensions tested, the length of the ligaments separating notches had little influence on the failure pressure, but the depth of the notches exerted a noticeable influence. The Stage 2 post-test photograph of Specimen 5528-3-3 (Fig 4.63) shows significant unstable tearing into the ends of the notch.

The three Type 4 flaws exhibited no unstable tearing at the notch ends in Stage 1 testing, and the ligaments between the notches and those at the bottom of each notch again all tore

Table 4.4. Test results from Stage 2 testing of flawed tubes containing OD laser-cut notches. All notches had characteristics that existed after of Stage 1 testing (see Table 4.3).

Test Number	Flaw Type	Pressurization Rate MPa/s (psi/s)	Burst (Yes/No)	Maximum Pressure, MPa (psi)
5528-1-1	1	12.6 (1823)	Y	41.2 (5980)
5528-1-2	1	13.9 (2023)	Y	40.3 (5850)
5528-1-3	1	12.9 (1865)	Y	33.4 (4850)
5528-1-4	1	14.4 (2084)	Y	32.1 (4660)
5528-2-1	1	No Stage 2	-	-
5528-2-2	1	No Stage 2	-	-
5516-4-3	2	12.4 (1802)	Y	26.6 (3865)
5516-4-2	2	13.0 (1929)	Y	27.9 (4040)
5528-3-1	3	12.8 (1850)	Y	26.4 (3825)
5528-3-2[a]	3	13.3 (1928)	Y	30.4 (4409)
5528-3-3[a,b]	3	10.0 (1450)	Y	28.6 (4146)
5528-3-4[a]	4	12.2 (1776)	Y	30.0 (4346)
5469-2-1[a]	4	13.4 (1950)	Y	31,9 (4630)
5469-2-2[a,b]	4	10.3 (1497)	Y	33.4 (4850)
5469-2-3[a]	5	13.3 (1925)	Y	32.2 (4669)
5469-2-4[a]	5	13.3 (1930)	Y	26.8 (3893)
5469-3-1[a]	6	13.5 (1953)	Y	32.2 (4675)
5531-3-1[a]	6	13.2 (1909)	Y	29.0 (4200)
5469-3-3	7	Stage1 opened	-	-
5469-3-4	7	14.2 (2066)	N	53.1 (7700)
5469-4-1	8	Stage1 opened	-	-
5469-4-2	8	Stage1 opened	-	-
5469-4-3	9	Stage1 opened	-	-
5469-4-4	10	Stage1 opened	-	-

[a]Specimen tested in Stage 2 with internal bladder plus foil; all other Stage 2 tests conducted with internal bladder only.

[b]Specimen exhibited unstable tearing in Stage 1 testing without internal bladder.

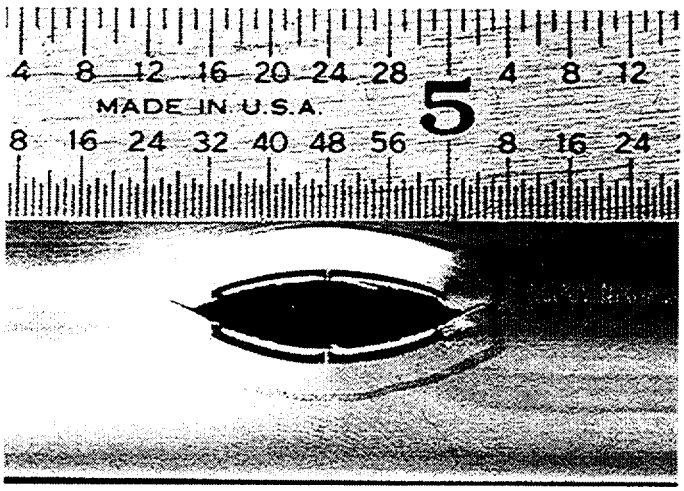

Fig. 4.62. Appearance of Specimen 5516-4-3 with Type 2 flaw after Stage 2 burst testing with bladder.

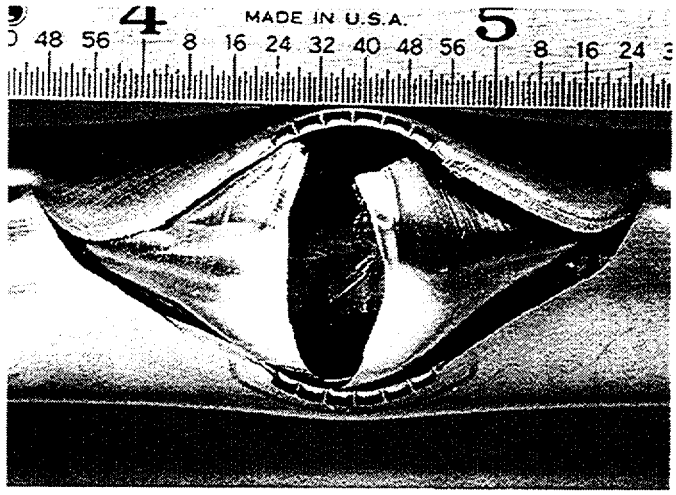

Fig. 4.63. Appearance of Specimen 5528-3-3 with Type 3 flaw after Stage 2 burst testing with bladder and foil.

simultaneously at the failure pressure. The depth of the notches exerted a stronger influence on the failure pressure than did the length of the interspersed ligaments. The Stage 2 post-test photographs of Specimen 5469-2-2 (Fig 4.64) indicates significant unstable tearing into the ends of the notch.

Stage 1 testing of the two Type 5 flaws resulted in ligament tearing along only one of the unaligned axial rows and, in contrast to the previous tests, unstable tearing also occurred at the ends of flaw, even though no internal bladder was used. No indication of progressive sequential tearing was evident during testing; all ligaments tore simultaneously. The other flaw of this type (Specimen 5469-2-3) with the thinner 0.25-mm (0.010 in.) ligament between notches did not tear unstably in Stage 1 testing, and it opened at the considerably lower pressure of 33.5 MPa (4860 psi). The Stage 2 testing (Fig. 4.65) for Specimen 5469-2-4 resulted in significant unstable tearing into the ends of the notch.

For the Type 6 flaw with the 0.51-mm (0.020-in.)-long ligaments, ligament tearing occurred in only one of the parallel notches and no unstable tearing occurred at the ends of notch. The flaw tore open at 34.3 MPa (4980 psi). The other flaw of this type (Specimen

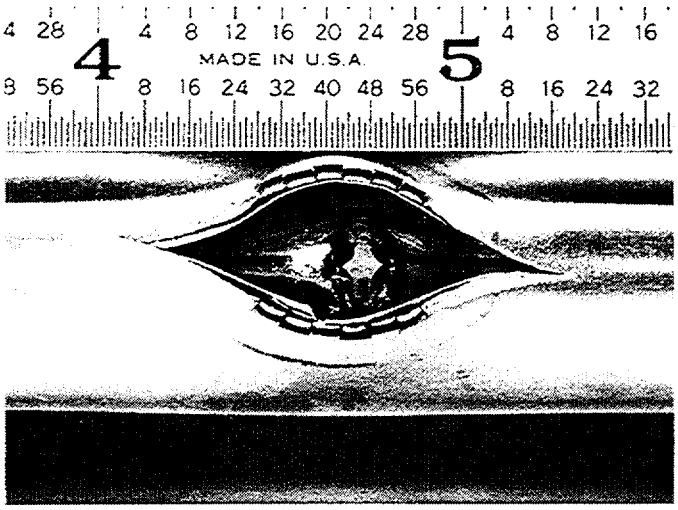

Fig. 4.64. Appearance of Specimen 5469-2-2 with Type 4 flaw after Stage 2 burst testing with bladder and foil.

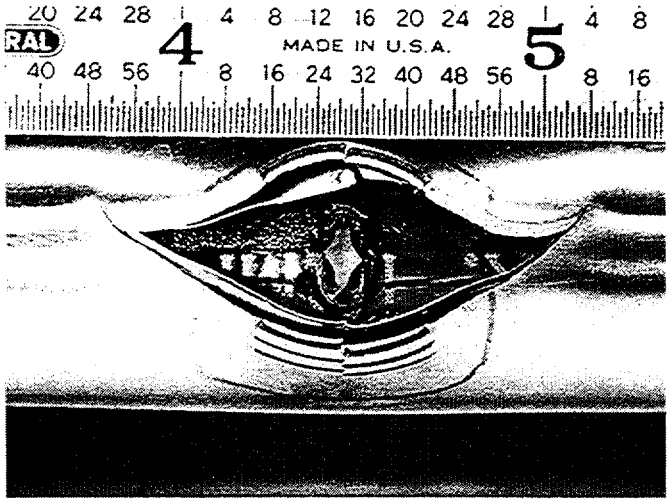

Fig. 4.65. Appearance of Specimen 5469-2-4 with Type 5 flaw after Stage 2 burst testing with bladder and foil.

5469–3-1) with the thinner 0.25-mm (0.010-in.)-long ligament between the notches behaved similarly but opened at the considerably lower pressure of 28.3 MPa (4110 psi). The Stage 2 testing of Specimen 5531-3-1 (Fig. 4.66) again produced significant unstable tearing at the ends of the notch.

For the two Type 7 flaws, Stage 1 testing of Specimen 5469-3-3, which had the thinner 0.13-mm (0.005-in.) ligament, resulted in ligament tearing around the entire tube circumference. Failure occurred at 51.4 MPa (7450 psi), close to the maximum 53.7 MPa (7700 psi) operating pressure of the facility. The other flaw of this type (Specimen 5469-3-4), but with a thicker 0.25-mm (0.010 in.) ligament could not be opened at the maximum facility pressure of 53.1 MPa (7700 psi). It was subsequently tested under Stage 2 conditions and again reached the same maximum pressure without failing

As stated above, the tubes containing Types 8, 9, and 10 flaws did not undergo Stage 2 testing.

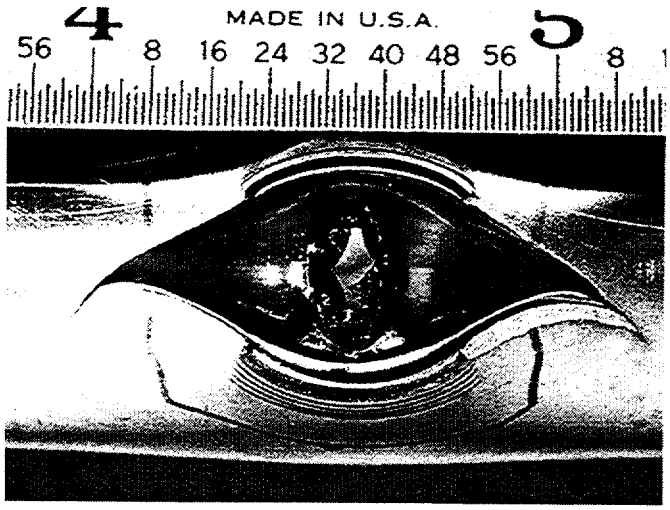

Fig. 4.66. Appearance of Specimen 5531-3-1 with Type 6 flaw after Stage 2 burst testing with bladder and foil.

4.2.3 Testing of tubes with SCC flaws

Tests were conducted at room temperature in the High-Pressure Test Facility on 14 tubes that are part of a 24-tube set of tubes with laboratory-induced SCC flaws. These tubes were produced at ANL using the room-temperature tetrathionate process described in earlier reports.[1] The 24-tube set contains flaws of several types, including OD axial and circumferential cracks and combinations of these types, as well as OD flaws in the roll transition. The tubes underwent extensive pretest characterization, pressure testing, and post-test examination using metallographic and fractographic techniques to characterize the flaw morphologies. The overall goal of this series of tests was to relate pretest NDE information to failure behavior and the actual crack morphologies and to improve the techniques for predicting leak and burst pressures. The general test procedures followed were similar to those used in an earlier testing of five SCC flaws tested at elevated temperature in the Pressure and Leak-Rate Test Facility. The tubes were tested without bladders using a quasi-steady pressurization rate with 0.69 MPa (100 psi) increments in pressure and a 10-s hold time after each increase.

Table 4.5 summarizes the results from the 14 tests, all on tubes with OD flaws. Specimens SGL226 and SGL363 contained complex flaws with combinations of axial and circumferential cracks, including cracking in the roll transition for Specimen SGL363. Specimens SGL413, 425, 480, 493, 494, 719, 728, 730, 731, and 734 involved axial flaws, and Specimens SGL099 and 158 involved circumferential cracks, based on dye-penetrant determinations. The tabulated maximum depths and the EC voltages represent pre-test characterizations using standard EC signal analysis procedures and software and do not reflect the new analysis techniques presently being developed in Task 2.

The information on pressure at first leak represents data obtained from visual observation of the flawed tube through observation windows for the first signs of water leakage. For Specimens SGL158, 413, 425, 480, 493, 728, 731, 226, and 363, first leak occurred in the form of one drop of water issuing from the flaw over a period of several minutes (a much lower leak rate than could have been detected in the Pressure and Leak-Rate Test Facility or by using the turbine flowmeter in the present facility). The frequency of drop formation increased with

Table 4.5. Summary of results from room-temperature pressure tests on 14 SCC flaws

Test No.	Flaw Type	Max. Flaw Depth (%)	BC Voltage	Pressure at First Leak (psi)	Max. Pressure Attained (psi)
099	OD/Circ	20	3.25	7400	7400
158	OD/Circ	60	4.32	3600[a,b]	4560
413	OD/Axial	90	1.57	1800[b]	3570
425	OD/Axial	<20	2.14	2400[b]	4350
480	OD/Axial	<20	3.08	900[b]	2200
493	OD/Axial	<20	3.84	80[b]	2550
494	OD/Axial	<20	0.54	4600	4880
719	OD/Axial	55	0.83	4200	4300
728	OD/Axial	90	1.97	2100[b]	3000
730	OD/Axial	100	1.10	5500	6050
731	OD/Axial	90	3.12	40[a,b]	3100
734	OD/Axial	55	1.71	5000	5300
226	OD/Axial/Circ	90	-	1750[b]	3800
363	OD/Axial/Circ/ Roll Trans.	90	-	2700[b]	3580

[a]Pre-test air bubble leak test at 40 psi indicated throughwall pinhole.

[b]First leak occurred as one drop of water issuing from the flaw over a period of several minutes.

increasing pressure, and the leaks often passed through a subsequent atomized small droplet spray stage, followed by a continuous leak stream jet stage. The tests were terminated when the flaw opened enough that the flow reached the maximum 48.4 L/min (12.8 gpm) capacity of the pressurizer pump. The tabulated maximum pressure for the tests represents the pressure at which the flow capacity of the facility was reached.

For Specimens SGL099, 494, 719, and 734, the pressure at first leak and maximum pressure achieved were the same or differed only slightly. These tests were characterized by essentially no leak prior to sudden rapid flaw opening, yielding a leak rate >48.4 L/min (12.8 gpm). All of the flaws tested in this 14-tube series exhibited significant tearing, with varying degrees of secondary cracking evident. Some tubes also exhibited evidence of unstable tearing without the use of bladders. More detailed results for two of the more complex flaws in Specimens SGL226 and SGL363 are presented below.

Specimen SGL226 contained an ODSCC flaw that, based on pretest dye-penetrant and NDE examinations, exhibited both axial and circumferential cracking. Figure 4.67, a posttest photograph of the flaw opening, shows a ≈6.35-mm (0.25-in.)-long axial crack intersected by a ≈1-in.-long circumferential crack. This flaw initially began to leak at a 12.1 MPa (1750 psi),

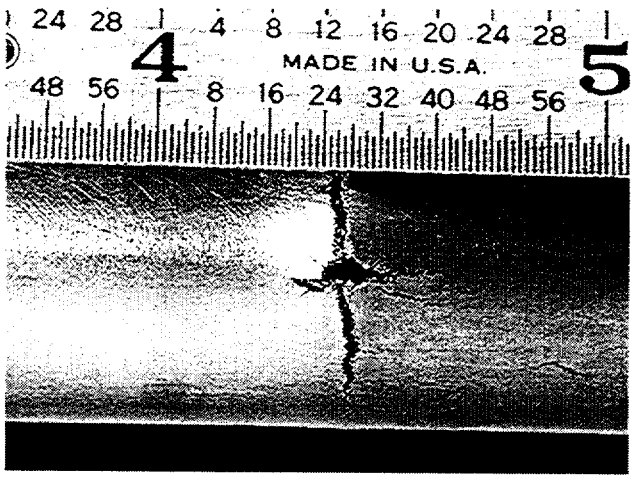

Fig. 4.67. Post-test appearance of complex ODSCC flaw in Specimen SGL226 exhibiting both axial and circumferential cracking.

with a leak rate of approximately one drop every few minutes. By the time the pressure had reached 20.7 MPa (3000 psi), the leak rate had increased to 4.39 L/min (1.16 gpm). The test was terminated at 26.2 MPa (3800 psi) when the flaw suddenly opened and the flow rate exceeded the 48.4 L/min (12.8 gpm) capacity of the facility.

Specimen SGL363 contained an ODSCC flaw at a roll transition that, based on pretest dye-penetrant and NDE examinations, was made up of a complex series of axial/circumferential cracks. Figure 4.68 shows the posttest photograph of the flaw opening, a large hole with both circumferential and axial ligament tearing with considerable secondary cracking. This flaw began to leak at 18.6 MPa (2700 psi) with a leak rate of approximately one drop every few minutes. The flaw abruptly opened at 24.7 MPa (3580 psi) and the flow rate again exceeded the facility capacity.

All of the SCC flaws are currently undergoing metallographic and fractographic examinations. The fracture surfaces of the failed specimens are being examined by fractography to determine the initial crack profile. This information will then be compared with the pre-test crack profile characterization profile obtained by EC techniques.

4.2.4 Jet impingement erosion

An exploratory test was conducted to evaluate the potential for jet erosion resulting from a jet of water from a leaking tube impinging on an adjacent tube. The test was conducted in the High-Pressure Test Facility at room temperature using a single-phase water jet issuing from a sharp-edged circular orifice of 0.79 mm (1/32-in.) diameter under 17.2 MPa (2500 psi) pressure. The leak rate for this test was held constant for the 4-h duration of the experiment and was measured at 3.6 L/min (0.95 gpm), which corresponds to a jet velocity of about 116 m/s (380 ft/s).

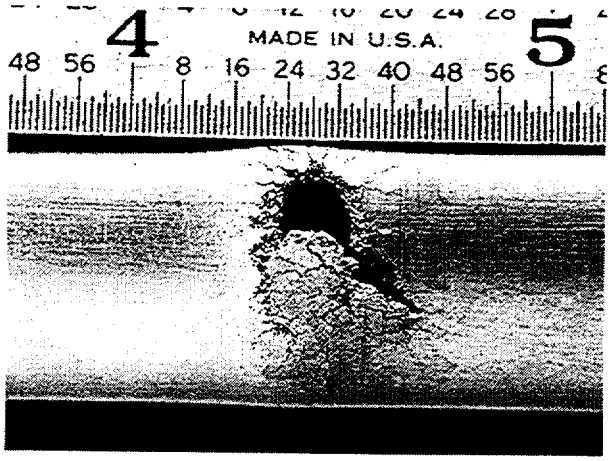

Fig. 4.68. Post-test appearance of complex ODSCC flaw in Specimen SGL363 exhibiting a large opening resulting from both axial and circumferential cracking.

The apparatus for this test is as shown in Fig. 4.69. Two 22.2-mm (7/8-in.)-diameter Alloy 600 tubes were held parallel in a fixture at a spacing of 6.35 mm (0.25 in.). The tube with the orifice hole is at the bottom in the figure. Figure 4.70 shows the post-test jet impact region after 4 h of continuous impact, and evidence of erosion is seen. The facility was very stable during the 4-h test, with little operator intervention required to maintain constant pressure. This surface erosion is undergoing further evaluation, and additional tests will be conducted with single-phase water and with a steam/liquid combination under main-steam-line-break elevated-temperature conditions in the Pressure and Leak-Rate Test Facility.

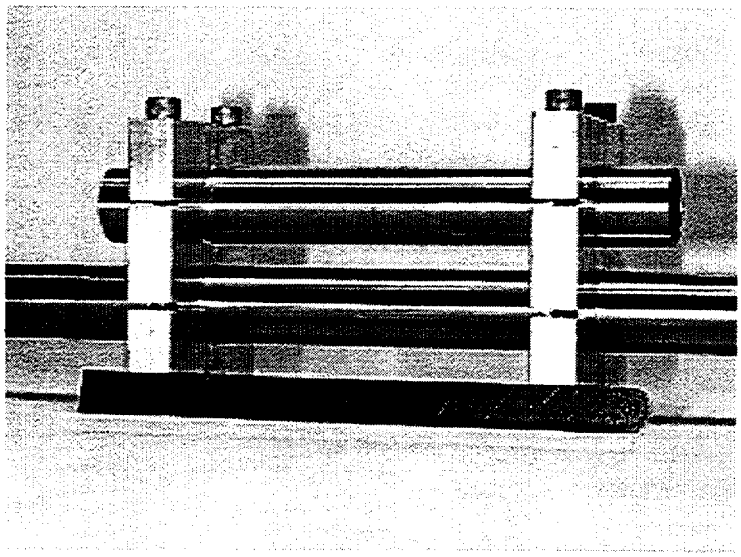

Fig. 4.69. Apparatus used for exploratory water-jet erosion test. Water is discharged from a sharp-edged orifice at top of lower tube and impacts upper tube, which is at a distance of 6.35 mm (0.25 in.).

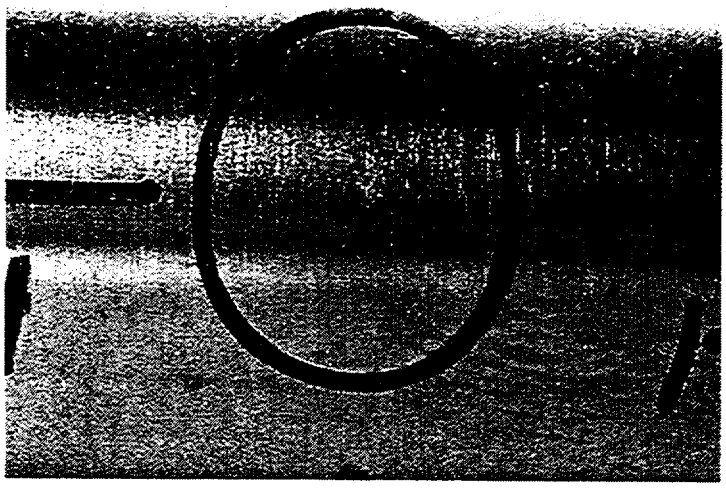

Fig. 4.70. Appearance of water-jet erosion specimen after 4 h of impact by room-temperature water jet discharged at 17.2 MPa (2500 psi) through a 0.79-mm (1/32-in.)-diameter orifice from a distance of 6.35 mm (0.25 in.)

4.3 Analysis of Crack Behavior during Severe Accidents

A model for predicting ligament rupture of part-throughwall cracks at high temperatures expected during severe accidents was developed and validated at ANL in the past.[2] To determine the leak rate after throughwall penetration of axial cracks during severe accidents, it is necessary to estimate the crack opening area as a function of time. A simple model is proposed to calculate the crack opening area as a function of time and to report results from tests for validating the approach. The model is derived by analogy from a model that is applicable to cracks in a rectangular plate.

4.3.1 Model for predicting crack opening area during severe accidents

Consider a throughwall central crack of length 2c in a rectangular plate of width 2b (b>>c) subjected to a remotely applied axial load P. For a material with stress-plastic strain law,

$$\frac{\varepsilon}{\varepsilon_0} = \alpha\left(\frac{\sigma}{\sigma_0}\right)^{m'}, \tag{4.1}$$

where

ε is the plastic strain,
ε_0 is the reference strain,
α is the stress-strain curve coefficient,
σ is the axial stress,
σ_0 is the reference stress, and
m' is the stress-strain curve exponent,

the crack opening displacement δ at the middle of the crack, ignoring elastic displacement, is given by[3]

$$\delta = \alpha\varepsilon_0 c h_2(c/b, m')\left(\frac{P}{P_0}\right)^{m'}. \tag{4.2}$$

In Eq. 4.2, P_0 is the plastic collapse load and the function h_2 is tabulated in Ref. 3. Equation 4.2 was applied to the case of an axial crack in a relatively long steam generator tube by replacing the remote stress with the nominal hoop stress $\sigma = \frac{\Delta p R}{h}$ (R and h are the mean radius and thickness of the tube, and Δp is the pressure differential), the collapse stress with σ_0/m (m is the bulging factor), and by putting c/b = 0, i.e.,

$$\delta = c h_2(0, m')\frac{\alpha\varepsilon_0}{(\sigma_0)^{m'}}(m\sigma)^{m'}. \tag{4.3}$$

Equation 4.3 is expected to give reasonable estimates of crack opening displacements as long as the pressure is small compared to the unstable burst pressure.

Equation 4.3 can be generalized for the high-temperature creep case as follows. If the material obeys a power law creep rate equation, i.e.,

$$\dot{\varepsilon} = A\sigma^n, \tag{4.4}$$

where A and n are the creep-rate coefficient and exponent, respectively, then the crack opening rate is given by analogy with Eqs. 4.1 and 4.3 as follows:

$$\dot{\delta} = Ach_2(0, n)(m\sigma)^n \tag{4.5}$$

A similar procedure, i.e., using $m_p\sigma$ as the stress in a formula to predict ligament rupture of tubes with part-throughwall axial cracks at room temperature, has been used successfully at high temperature in the past and should work for calculating crack opening displacement rates.[2]

Creep rate equation

The INEEL creep rate data are plotted in Fig. 4.71.[4] The data at three temperatures can be collapsed onto a bilinear plot (log-log basis) by using an activation energy of 65 kcal/mole and plotting the stress normalized by the Young's modulus at temperature, as shown in Fig. 4.71.

Crack opening area for axial cracks

The h_2 (c/b, n) function is plotted as a function of c/b for three values of n in Fig. 4.72a. Since our interest is in the value of $h_2(0,n)$, the graphs are extrapolated to c/b = 0 by polynomial fits and the results plotted as a function of n in Fig. 4.72b.

Calculated (by Eq. 4.5) variation of crack opening rate with crack length is shown in Fig. 4.73a for steam generator tubes at 700°C subjected to internal pressure of 16.2 MPa (2350 psi). Note that the crack opening rate increases exponentially beyond a crack length of 10 mm (0.4 in.).

Crack opening area as a function of crack length for a SG tube subjected to a SBO Case 6RU[5] transient up to final temperatures of 700 and 750°C is shown in Fig. 4.73b. For a final temperature of ≥750°C, cracks longer than 15 mm (0.6 in.) will have crack opening areas that are greater than the tube cross-sectional flow area 143 mm^2 (0.47 $in.^2$) for a 22,2-mm (7/8-in.)-diameter tube.

4.3.2 Validation tests on specimens with circumferential notches at high temperature

It is extremely difficult to carry out creep tests on tubular specimens with throughwall axial notches subjected to internal pressure. Because the approach followed in this report depends critically on our ability to predict crack opening displacement rates in rectangular plates, validation tests should ideally be conducted on rectangular plates with notches at high temperature. However, validation tests can also be conducted on axially loaded tube specimens with two symmetrical throughwall circumferential EDM notches (Fig. 4.74a) if the

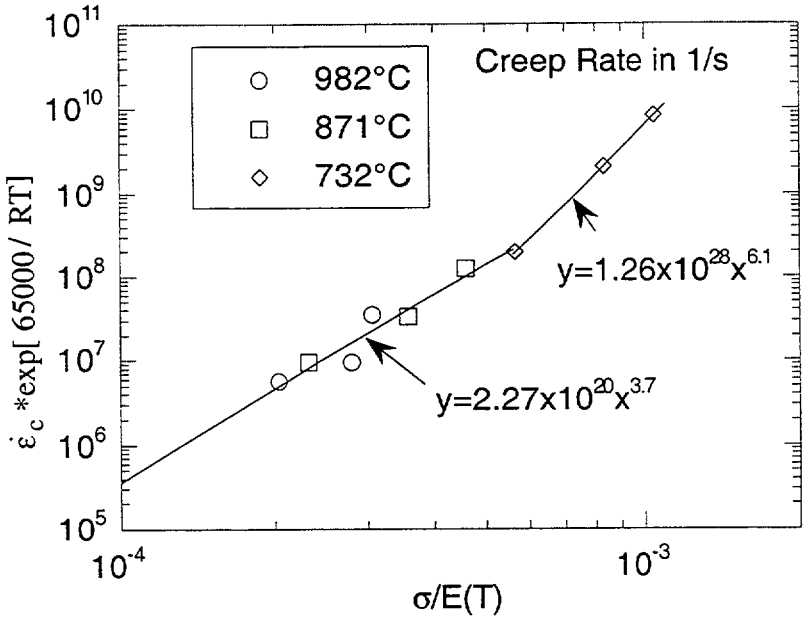

Fig. 4.71. INEEL data on creep rate of Alloy 600 vs. stress plotted using activation energy of 65 kcal/mole and stress normalized by Young's modulus at temperature.

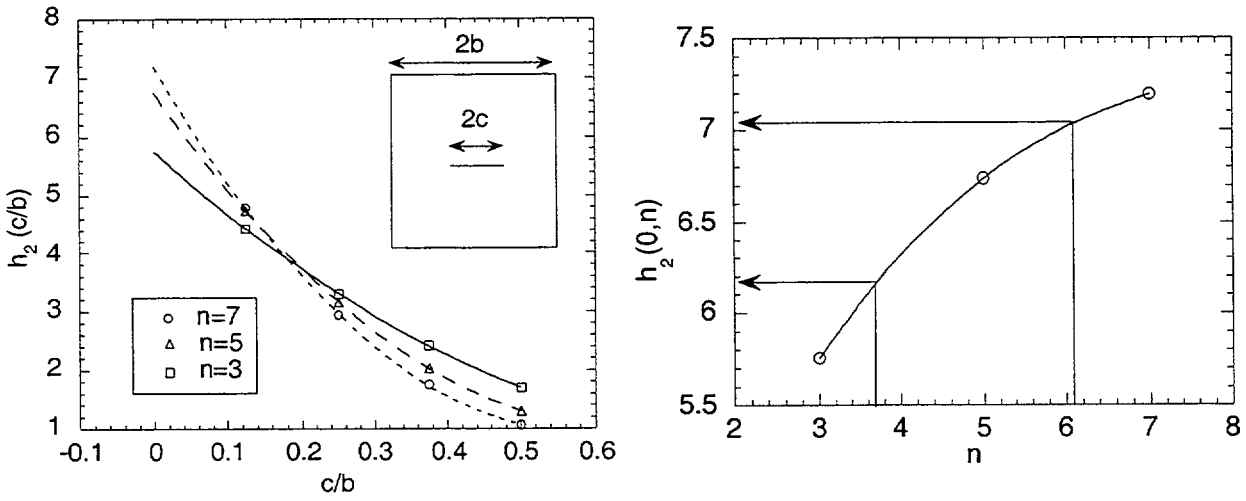

Fig. 4.72. (a) Variation of h_2 (c/b,n) with c/b for various values of n and (b) variation of h_2 (0,n) with n. Values of h_2 (0,n) are 7.03 and 6.16 for n = 6.1 and 3.7, respectively.

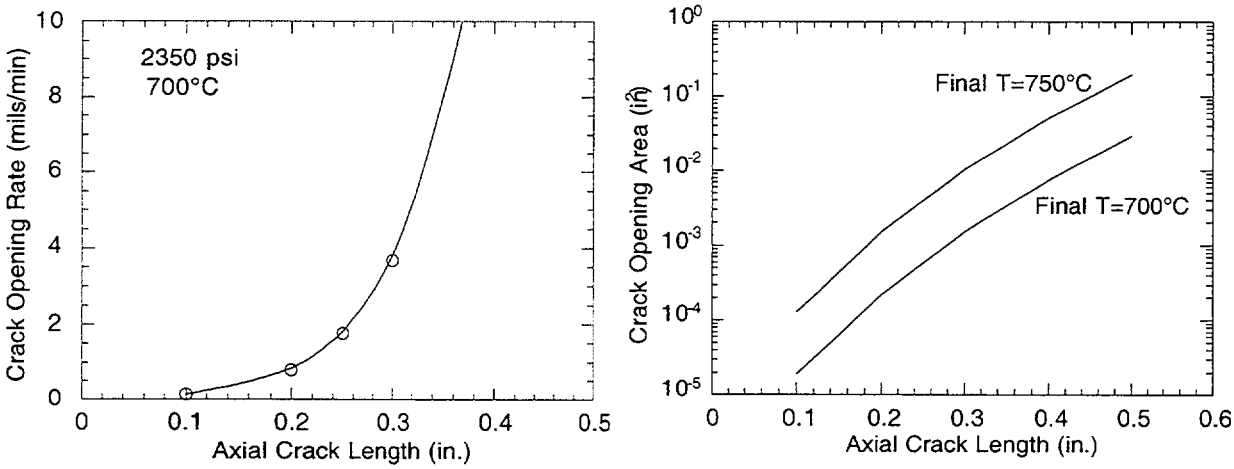

(a) (b)

Fig. 4.73. Variations of (a) crack opening displacement rate with throughwall axial crack length for tube subjected to internal pressure of 16.2 MPa (2350 psi) at 700°C and (b) crack opening area with crack length at final temperatures 700 and 750°C for tube subjected to Case 6RU transient.

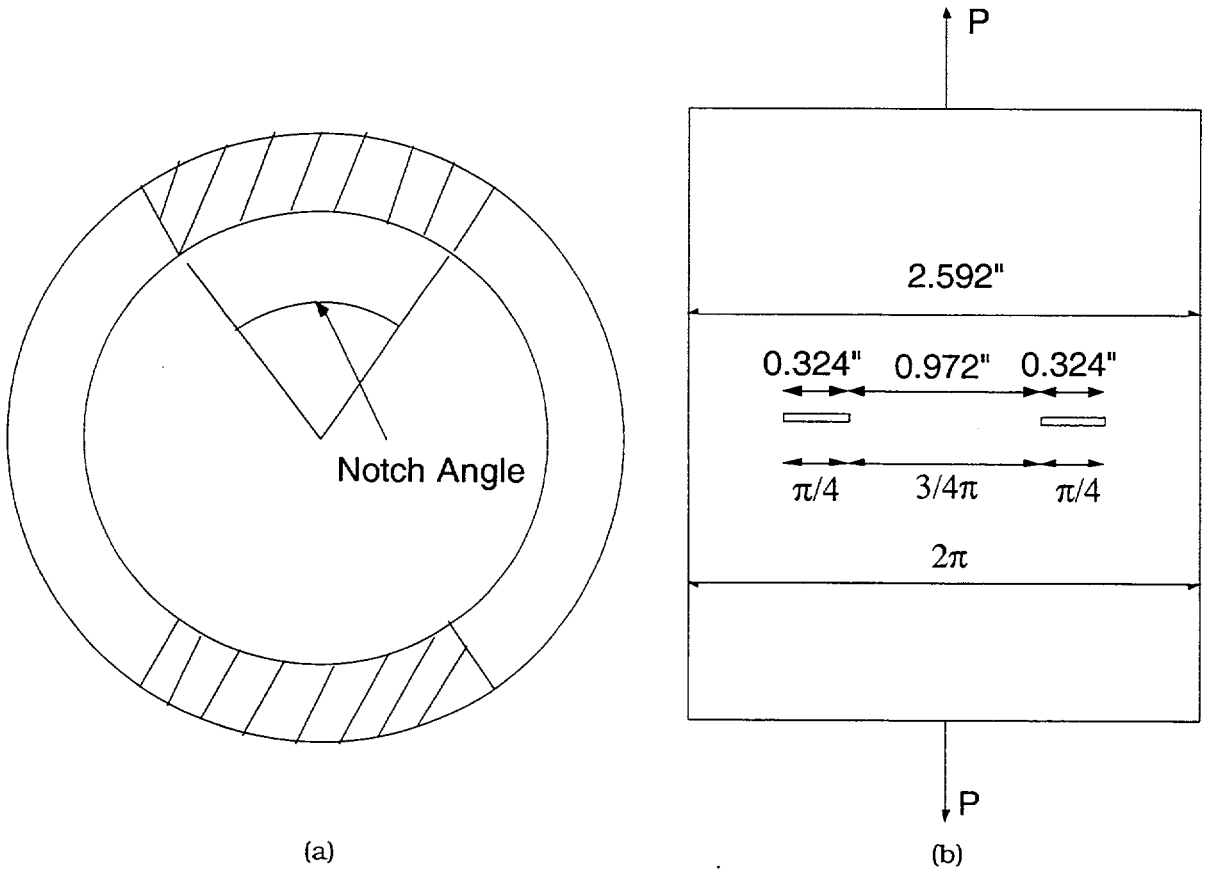

(a) (b)

Fig. 4.74. (a) Tube with two symmetrical throughwall circumferential notches and (b) axial loading on tube with two symmetrical 45° notches plotted after making axial cut and unfolding the tube circumference into a plane.

notch lengths are small. By keeping the notch lengths small, the effects of tube curvature can be minimized and the equations for calculating opening rates of throughwall cracks in rectangular plates can be applied. The small interaction between the two notches can be taken into account by using equations applicable to cracks in rectangular plates of finite width (Fig. 4.74b). Since the equations used are applicable to cracks in rectangular plates subjected to remotely applied uniform tensile stress without bending, two symmetrical circumferential notches were used in the tube specimens to minimize bending.

As mentioned earlier, the peculiarity of the circumferential crack geometry requires that the corresponding rectangular plate be of finite width (Fig. 4.74b). In general, the equation for COD of cracks in plates of finite width is given by Eq. 4.2. For the current geometry, the remotely applied axial load $P = 2\pi Rh\sigma$ and the plastic collapse load $P_0 = 2(\pi-2\theta)Rh\sigma_0$, and Eq. 4.2 reduces to:

$$\delta = ch_2\left(\frac{c}{b}, m'\right)\frac{\alpha\varepsilon_0}{(\sigma_0)^{m'}}\left(\frac{\pi}{\pi-2\theta}\sigma\right)^{m'},$$

where σ is the remotely applied axial stress, 2θ is the angular length of each circumferential crack, R and h are the mean radius and thickness of the tube, and

$$\frac{c}{b} = \frac{2\theta}{\pi} \quad (c/b = 0.25 \text{ for } 45° \text{ cracks}). \tag{4.7}$$

As before, under creep conditions, Eq. 4.6 is replaced by analogy,

$$\dot{\delta} = Ach_2\left(\frac{c}{b}, n\right)\left(\frac{\pi}{\pi-2\theta}\sigma\right)^{n}. \tag{4.8}$$

Variation of the function h_2 (c/b, n) with c/b is shown in Fig. 4.75 for the two values of n applicable to Alloy 600. In contrast to axial cracks that were considered earlier, $c/b \neq 0$ for the circumferential notches.

Test results

Two tests with 45° circumferential EDM notches were first conducted. The variations of calculated notch opening with time for two symmetrical 45° circumferential cracks at two applied axial loads are compared with experimentally observed notch openings in Figs. 4.76a-b. The test under an axial load of 910 kg (2440 lb) (Fig. 4.76a) was started initially at 695°C, but changed to 685°C after 1 h. The test under an applied axial load of 101 kg (2700 lb) (Fig. 4.76b), was conducted at 665°C with less variation in temperature. Agreement between experimentally measured notch openings and predicted values was reasonably good.

The temperature control for the specimen was subsequently improved. The next series of tests involved 2 x 6.35 mm (0.25 in.) and 2 x 5.1 mm (0.20 in.) circumferential notches subjected to 895 kg (2400 lbs) at a constant temperature of 700°C. Figures 4.77a-b show a comparison between measured and predicted notch opening with time for specimens with two symmetrical circumferential notches of length 6.35 and 5.1 mm (0.25 and 0.20 in.), respectively, each subjected to an applied axial load of 895 kg (2400 lb). As before, the predicted openings are close to the measured values.

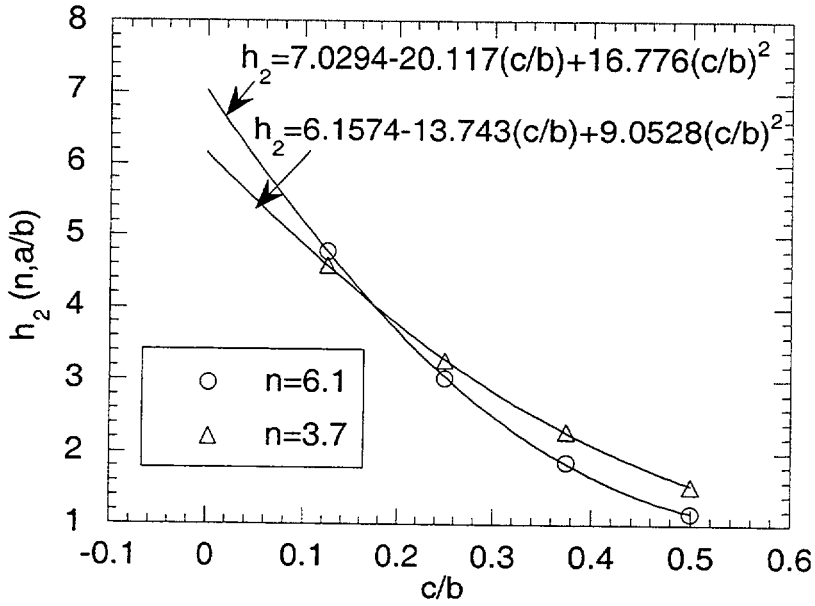

Fig. 4.75. Variation of h_2 with c/b for creep rate exponents n = 3.7 and 6.1.

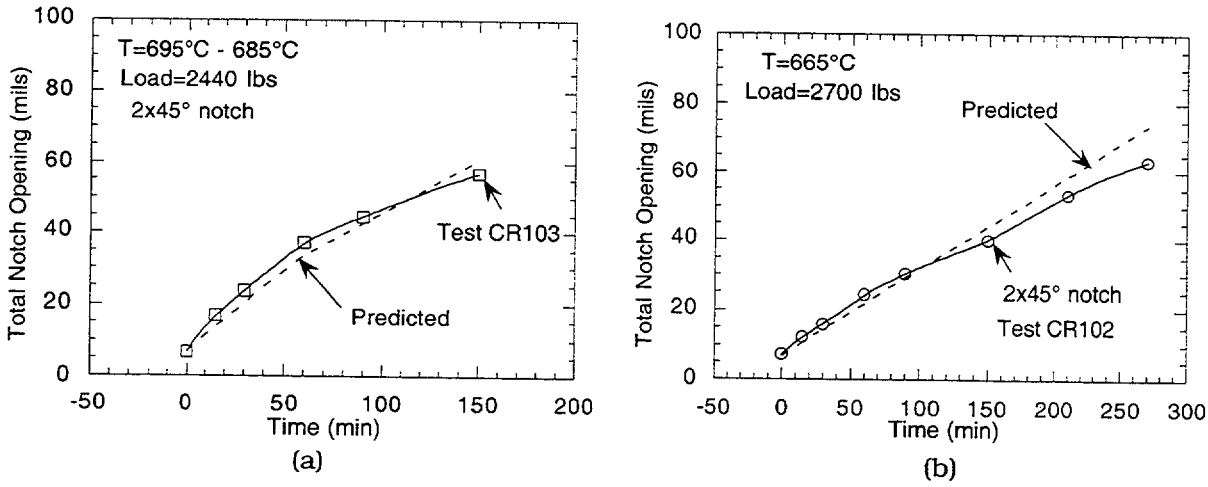

Fig. 4.76. Experimentally measured and predicted variation of total notch opening with time for specimens with two circumferential notches, each 45° in extent (2 x 45° notches), loaded at (a) 1107 kg (2440 lb) and (b) 1225 kg (2700 lb).

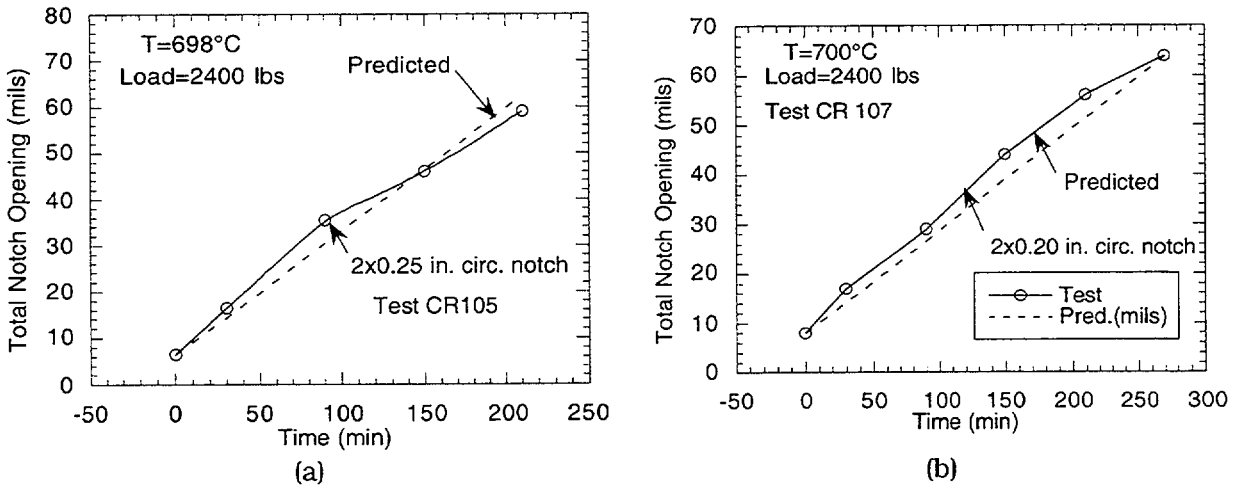

Fig. 4.77. Experimentally measured and predicted variation of total notch opening with time for specimens with 2 symmetrical circumferential notches loaded at 1108 kg (2400 lbs) for notch lengths (a) 6.35 mm (0.25 in.) and (b) 5.1 mm (0.20 in.).

All the tests reported so far were conducted isothermally. Finally, to validate the model for nonisothermal loading, two tests were conducted in which the temperature was ramped following the Case 6RU transient (Fig. 4.78). Both tests had a constant axial load of 1362 kg (3000 lb). Test CR 106 had 2 x 6.35 mm (0.25 in.) circumferential notches and Test CR 108 had 2 x 5.1 mm (0.20 in.) circumferential notches. The predicted notch opening displacement vs. temperature plots for the two tests are given in Figs. 4.79a-b, which also include the measured notch opening displacements at the end of the tests. One of the predicted notch openings is close to the measured value, and the other one is off by 20%.

4.3.3 Conclusions for high-temperature tests

A model for calculating crack opening area at high temperature was developed. Prediction of time-dependent variation of crack opening displacement was validated with four isothermal and two nonisothermal tests on tubes with two symmetrical circumferential notches under constant axial load. Based on these tests, it was concluded that the proposed model gives reasonable estimates of variations of crack opening displacement and crack opening area with time at high temperature for isothermal and nonisothermal loadings.

The model was used to predict the variation of crack opening area with time for tubes with axial cracks subjected to a severe accident transient referred to as Case 6RU. The results show that for a final temperature ≥750°C, crack opening areas of throughwall cracks >15 mm (0.6 in.) long are greater than the tube cross-sectional flow area (143 mm^2 [0.47 $in.^2$]) of a 22.2–mm (7/8-in.)-diameter tube.

4.4 Comparison of EDM and Laser-Cut Notches at Room Temperature

A series of ligament-rupture tests on specimens with single rectangular EDM and laser-cut notches were conducted at room temperature in the High-Pressure Test Facility at ANL. Following ligament rupture, bladders and, if necessary, 0.13-mm (0.005-in.)-thick brass foil, were inserted into the specimens, which were then pressurized until unstable burst.

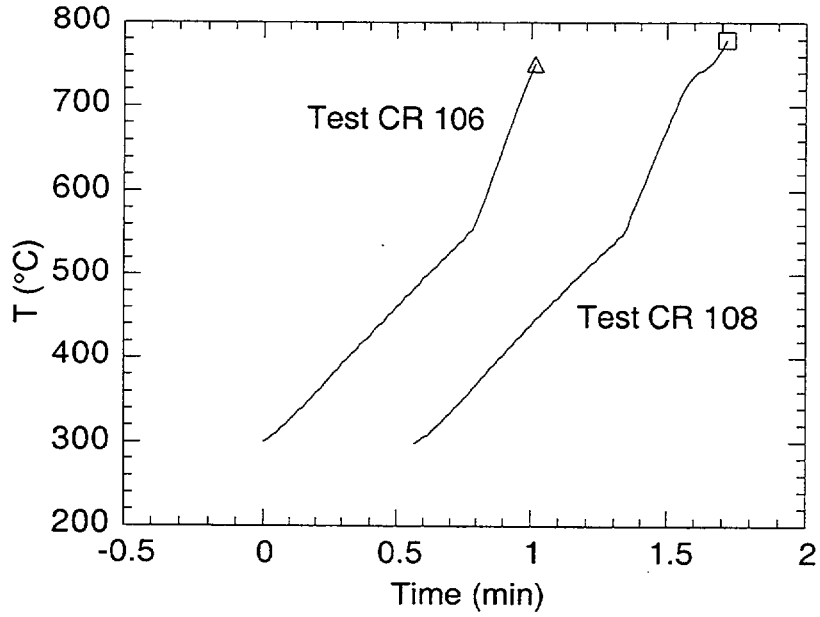

Fig. 4.78. Time vs. temperature plot for tests CR 106 and CR 108. Curve for CR 108 has been displaced in the horizontal direction for clarity.

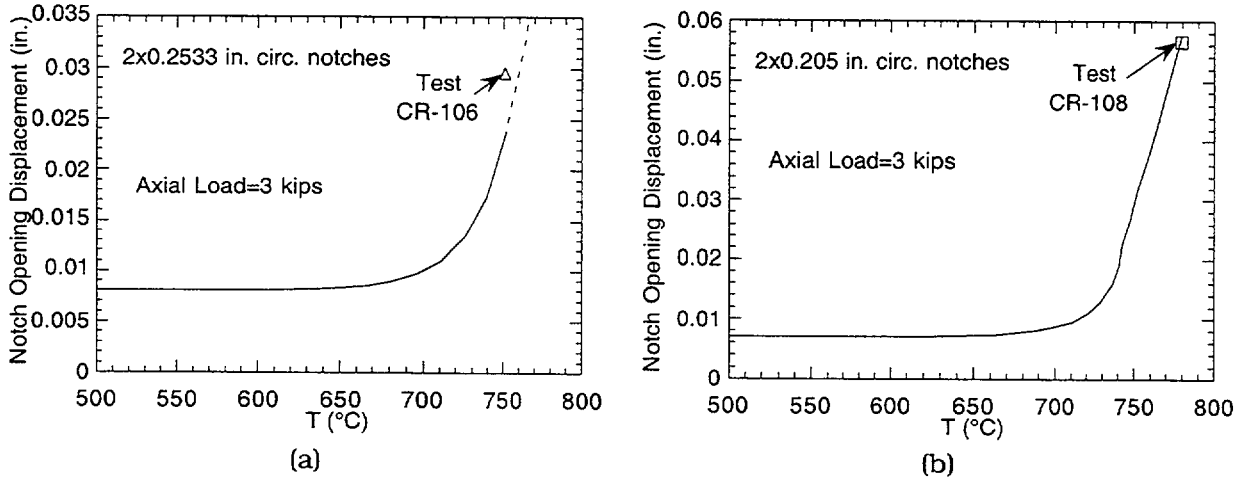

Fig. 4.79. Comparison of predicted (solid line) and experimentally measured (symbols) notch opening displacements for (a) Test CR 106 and (b) Test CR 108.

4.4.1 Ligament rupture pressure

The correlation for predicting ligament rupture pressure of part-throughwall axial notches and cracks is:

$$\sigma_{lig} = \bar{\sigma}, \tag{4.9}$$

where $\bar{\sigma}$ = flow stress = $k(S_y + S_u)$ with k = 0.55, σ_{lig} is the average ligament stress, which for an axial crack is given by

$$\sigma_{lig} = m_p \sigma , \tag{4.10}$$

where m_p is the ligament stress magnification factor, and σ is the nominal hoop stress (calculated by using the mean radius). The following ANL correlation for m_p was proposed in Ref. 2:

$$m_p = \frac{1 - \alpha \frac{a}{mh}}{1 - \frac{a}{h}} \tag{4.11}$$

$$\alpha = 1 + \beta \left(\frac{a}{h}\right)^2 \left(1 - \frac{1}{m}\right), \tag{4.12}$$

where a is crack depth and m is the bulging factor, and β is an empirical parameter determined by comparison with experimental data.[2]

EDM notches

The value of β was originally determined from the failure tests conducted at PNNL, which did not contain many short deep flaws.[6] The prediction of the failure pressure includes a second empirical parameter k, the flow stress factor in addition to β. In the original analysis, the value of k = 0.55 was chosen based on prior PNNL work, and β was determined to be 0.9. ANL has conducted a number of tests on tubes with short and deep (6.35-, 8.9-, and 12.7-mm [0.25-, 0.35-, and 0.5-in.]-long and 60, 80 and 90% TW) EDM notches. A plot of the normalized test failure pressures (i.e., test failure pressures divided by predicted failure pressures) is shown in Fig. 4.80a for various values of β. The mean and standard deviation, plotted in Fig. 4.80b, show that β = 1 is the best-fit value for these tests. Reanalysis of the PNNL data, together with the new ANL data on short and deep notches, have also shown that with k = 0.55, the best-fit value for β = 1. R. Keating from Westinghouse* noted that based on a large data base on burst pressure of unflawed tubes, they found k = 0.595. If only the unflawed tubes are considered, k = 0.595 also gives a slightly better fit for the PNNL data. If this value of k is chosen, the best–fit to the failure data for the flawed tubes gives β = 0.83.

*Private Communication, R. Keating, Westinghouse, to W.J. Shack, Argonne National Laboratory, February 15, 2000.

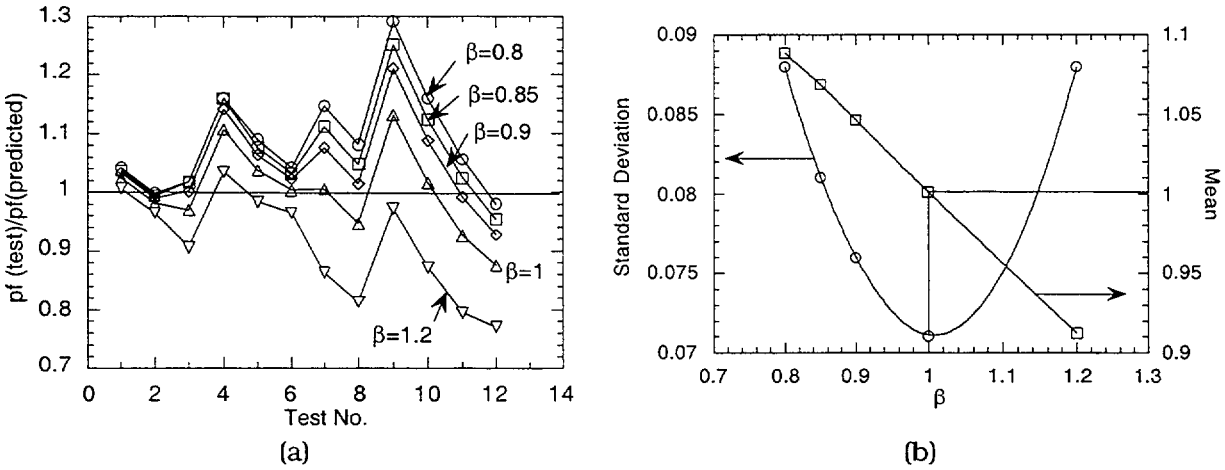

Fig. 4.80. (a) Variation of test failure pressures divided by predicted failure pressures corresponding to various values of β for the ANL tests and (b) variation of mean value and standard deviation of test failure pressure divided by predicted failure pressure with β.

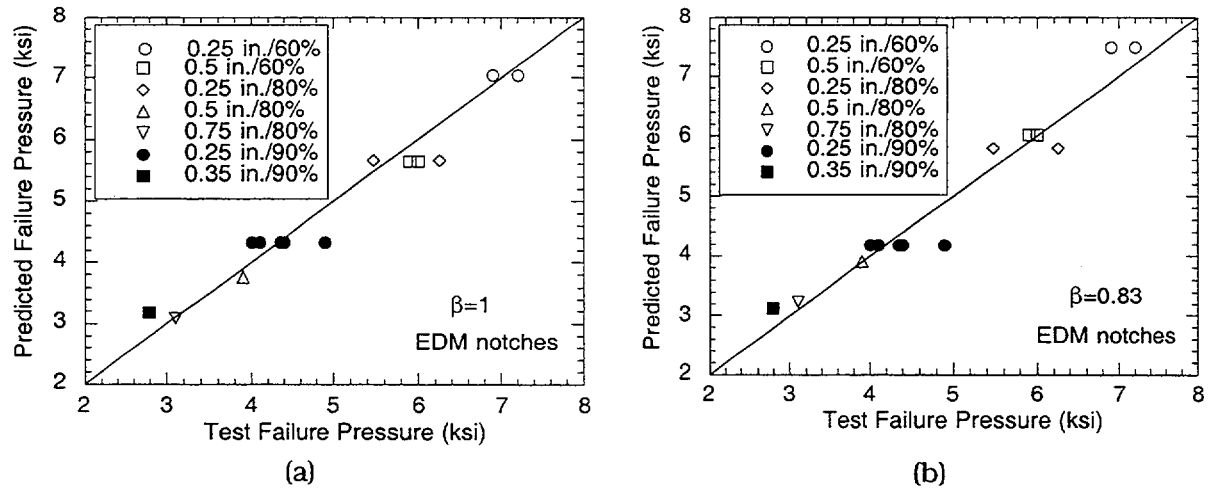

Fig. 4.81. Observed vs. predicted ligament rupture pressures for tubes with EDM notches using (a) k = 0.55 and β = 1 and (b) k = 0.595 and β = 0.83.

Equations 4.9-4.12 were used to predict the ligament rupture pressures of the tests recently conducted at ANL on specimens with EDM notches, using both sets of values of k and β. A plot of observed versus predicted ligament rupture pressures for β = 1 and k = 0.55 is shown in Fig. 4.81a. A similar plot using β = 0.83 and k = 0.595 is shown in Fig. 4.81b. Both sets of β and k provide comparable predictions. Both sets of parameters were used for comparisons with other recent test data on laser-cut notches.

Laser-cut notches

There is a complicating factor with the laser-cut notches in that each notch tip of the laser cut notches has a tiny throughwall pinhole through which small leakage occurs at very low pressure (0.34 MPa or 50 psi). Two specimens with 12.7-mm (0.5-in.)-long laser-cut notches, which were examined destructively after ligament rupture but prior to unstable burst,

showed the presence of these throughwall pinholes. To evaluate the effect of these pinholes on the ligament rupture pressure, duplicate tests were conducted on specimens with 80% TW, 12.7-mm (0.5-in.)-long EDM notches containing 0.13-mm (5 mil)-diameter drilled throughwall pinholes at the notch tips. Both tests had ligament rupture pressures that were comparable to (actually slightly greater than) the ligament rupture pressure of specimens without the drilled holes at the notch tips. Therefore, it was concluded that the effect of the pinholes on the ligament rupture pressure of specimens with laser-cut notches is negligible.

The average depths of the laser-cut notches were measured by post-test fractography. The pre-test maximum depths of the same notches were measured by EC. The difference between peak and average depths, as measured by EC, for these notches should be small because the through-thickness pinholes at the notch tips are too small to affect the EC signal significantly. A comparison between the maximum depths estimated by EC and the average depths measured by fractography is shown in Fig. 4.82. The maximum flaw depths measured by EC are ±0.06 mm (2.5 mil) (i.e., ±5% wall thickness) of the average depths measured by fractography for the laser-cut notches. Depths estimated by EC and fractography were used for all calculations with laser-cut notches. For plotting purposes, the pressure at which there was an abrupt and large increase in leak rate was taken as the ligament rupture pressure.

Comparison of observed versus predicted ligament rupture pressures using both sets of notch depths are shown in Figs 4.83a-b. The predicted ligament rupture pressures are within 10% of the observed rupture pressures if $\beta = 1$ and $k = 0.55$ (k is the flow stress factor) are used together with the notch depths measured by fractography. Predictions are less accurate if the notch depths measured by EC are used. In all cases, the test ligament rupture pressures are overestimated. Note that the test ligament rupture pressures are overestimated even more if $\beta = 0.83$ and $k = 0.595$ are used (Figs. 4.84a-b). The test and predicted ligament rupture pressures of laser-cut and EDM notches are plotted as functions of notch depth and notch length in Fig. 4.85. The solid lines in this figure are predicted ligament rupture pressures based on $k = 0.55$ and $\beta = 1$. Ligament rupture pressures for the laser-cut notches tend to fall at the lower end of the scatter band of the EDM notches. This may be due to melting at the notch tip during the laser cutting process, but post-test microhardness tests failed to reveal any loss of flow stress of the material at the notch tip conclusively.

4.4.2 Unstable burst pressure

The tests on both the EDM and laser-cut notches were conducted in two stages. First, the ligament rupture pressures were determined by testing without internal bladder. After ligament rupture, internal bladders and brass foils (if necessary) were inserted, and the specimens were pressurized until unstable burst. A relatively large data base for unstable burst pressure of tubes with single throughwall EDM notches have been generated. The number of tests on tubes with a single laser-cut notch is limited, but 12 tests were conducted on specimens with multiple laser-cut axial notches of various configurations. After the first stage, all the multiple axial notches coalesced into a single 12.7-mm (0.5-in.)-long notch. These specimens were then pressurized until unstable burst. Comparisons of observed vs. predicted unstable burst pressures using $k = 0.55$ and $k = 0.595$ are shown in Fig. 4.86a and Fig. 4.86b, respectively. Figure 4.86a shows that although the unstable burst pressures of the shorter (6.35- and 8.9-mm [0.25- and 0.35-in.])-long laser-cut notches tended to be at the lower end of EDM notches, the burst pressures for the larger number of specimens with

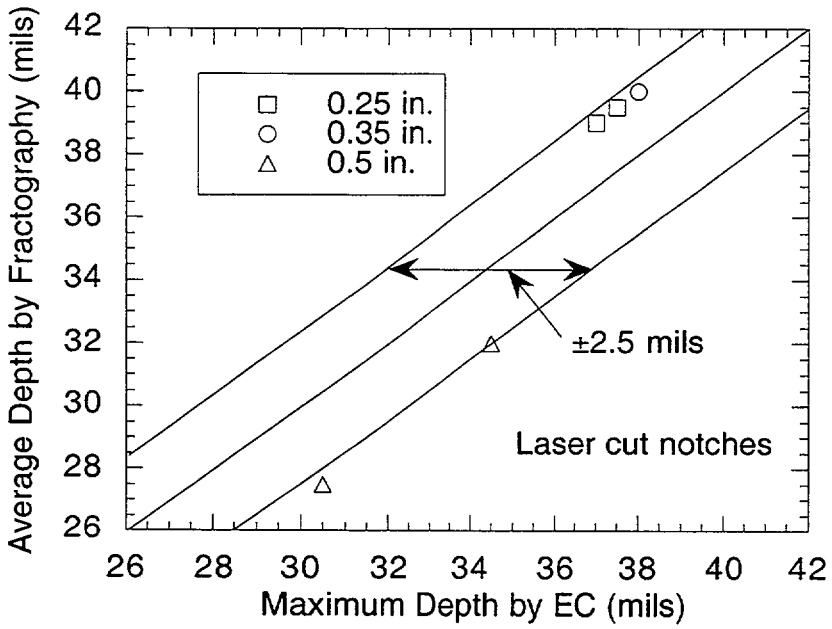

Fig. 4.82. Comparison of notch depths of laser-cut notches as measured by EC with those by fractography.

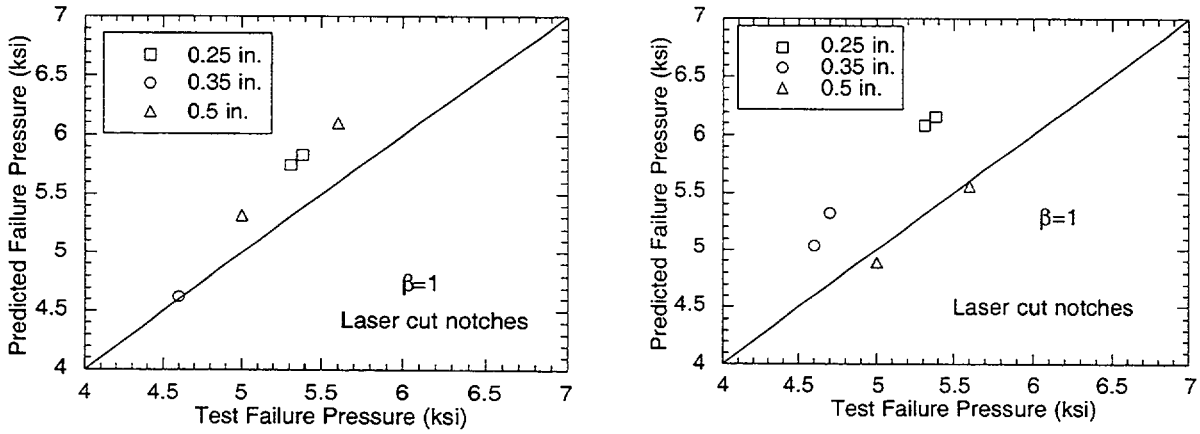

Fig. 4.83. Observed versus predicted ligament rupture pressures (with $\beta = 1$ and $k = 0.55$) for tubes with laser-cut notches using notch depths from (a) fractography and (b) EC measurements.

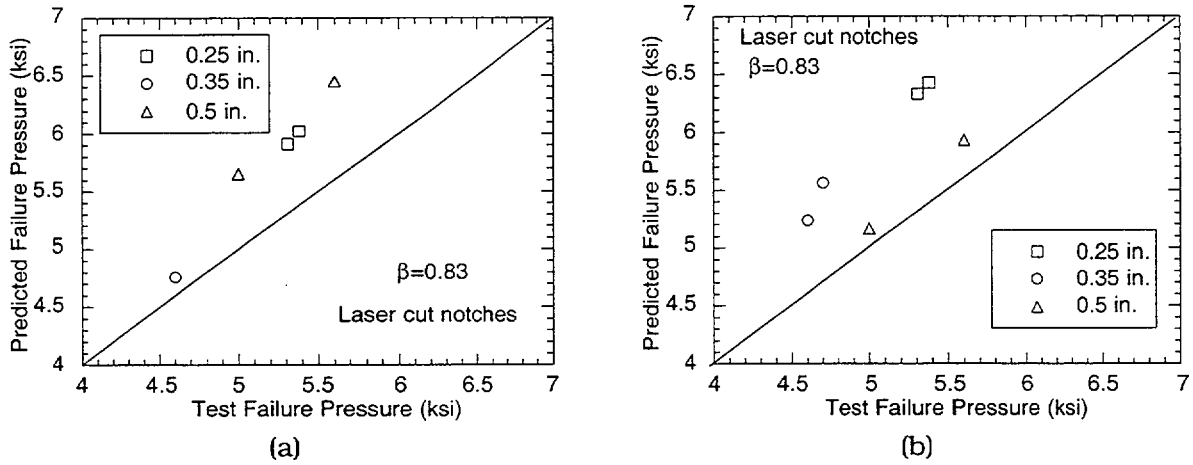

Fig. 4.84. Observed versus predicted ligament rupture pressures (with $\beta = 0.83$ and $k = 0.595$) for tubes with laser-cut notches using notch depths from (a) fractography and (b) EC measurements.

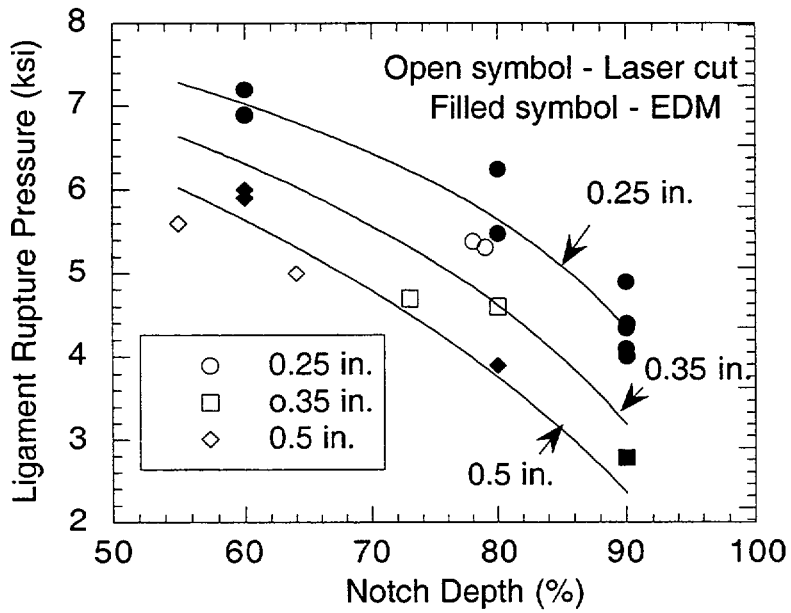

Fig. 4.85. Comparison of ligament rupture pressures for EDM and laser-cut notches of various lengths and depths with predicted values (solid lines).

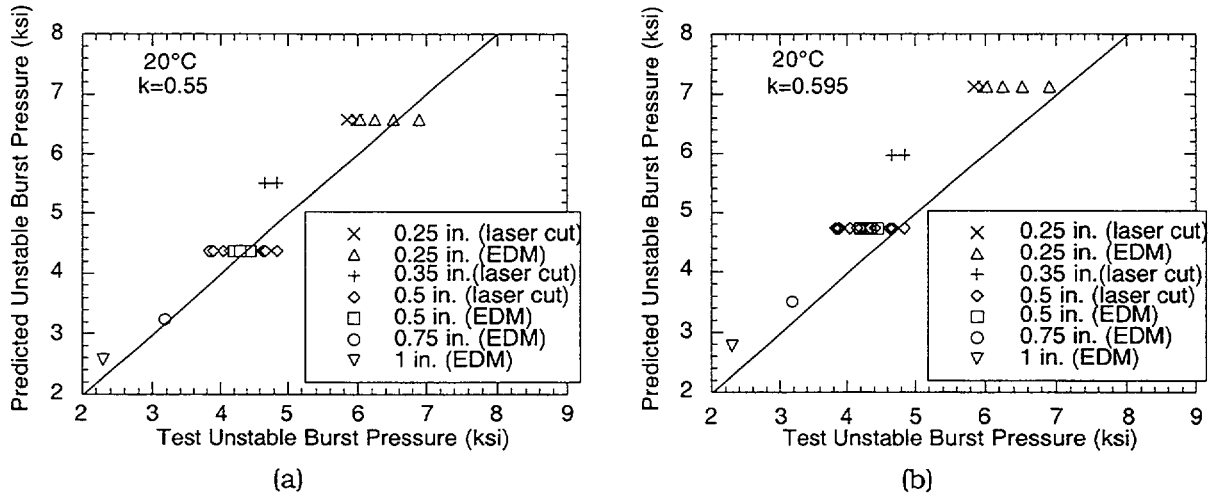

Fig. 4.86. Observed vs. predicted unstable burst pressures for tubes with throughwall EDM and laser-cut notches using (a) k = 0.55 and (b) k = 0.595.

12.7 mm (0.5-in.)-long laser-cut notches were scattered equally above and below those of the EDM notches. Overall, the unstable burst pressures of the EDM and laser-cut notches of equal length are comparable. Figures 4.86a and b show that unstable burst pressures are better predicted by k = 0.55 than by k = 0.595.

4.4.3 Conclusions for EDM and laser-cut notches

Pressure tests at room temperature were conducted on notched tubes in the ANL High-Pressure Test Facility. In addition to part-throughwall EDM notches, laser-cut notches were used. A significant number of specimens with short and deep notches were tested. The tests showed that the ligament rupture pressures of the laser-cut notches were within, but at the lower end of, the scatter band of the EDM notch data. The factor β used in the ANL correlation for m_p was updated on the basis of the tests. It was determined that either k = 0.55 and β = 1 or k = 0.595 and β = 0.83 gave reasonable predictions for the ligament rupture pressures. However, k = 0.55 gave more accurate predictions for unstable burst pressures of throughwall notches than did k = 0.595

4.5 Equivalent Rectangular Notch for Trapezoidal Notches

An approach based on the concept of equivalent rectangular crack length and depth for calculating ligament rupture pressure of arbitrarily-shaped stress corrosion cracks was presented in Ref. 7. An Excel-based visual basic code has been written for determining the equivalent rectangular crack geometry for cracks and notches with nonrectangular geometry. For stress corrosion cracks, EC +Point depth profile data are used as input. The procedure uses a "brute force" method, i.e., it chooses every possible crack length, determines the corresponding average depth, and picks the one that gives the largest m_p. All five SCC specimens (SGL-104, SGL-177, SGL-195, SGL-219, and W2-10) that have been tested to date were reanalyzed by this procedure. It was found that the equivalent rectangular crack geometry and effective m_p factors for all cases were virtually the same as those previously determined manually.

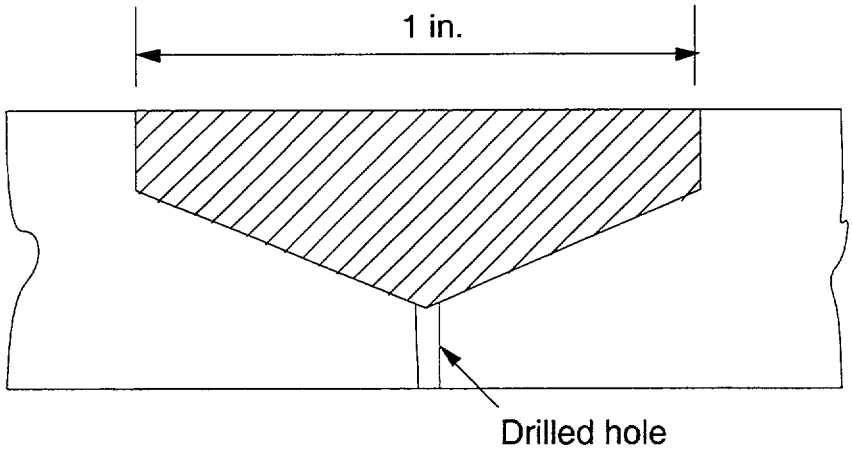

Fig. 4.87. Trapezoidal notch geometry with drilled hole at center of notch.

The procedure was used to calculate the equivalent notch geometry and ligament rupture pressure for three tests on specimens with trapezoidal EDM notches (Fig. 4.87). All three notches were 25.4 mm (1 in.) long at the OD surface. The notch in Specimen T-29 was 90% TW at the center and 82% TW at the tips. Specimens T-30 and T-31 had notches that were 90% TW at the center and 50% TW at the tips. The notches were intended to simulate the non-uniform ligament thicknesses of stress corrosion cracks. The only difference between Specimens T-30 and T-31 was that Specimen T-31 had a 0.13-mm (0.005-in.)-diameter throughwall hole drilled at the center of the notch (Fig. 4.87). The drilled hole was intended to simulate throughwall segments that are often observed for deep stress corrosion cracks. Like stress corrosion cracks, Specimen T-31 did not leak water until high pressure was applied. All tests were conducted at room temperature with pressurized water in the ANL High-Pressure Test Facility. Each test specimen was pressurized quasi-statically without bladder until ligament rupture and continued until the leak rate exceeded the pump capacity (47.3 L/min [12.5 gpm]). The test results are summarized in Table 4.6. Specimen T 29 experienced a small leak at the initial leakage pressure, but the pump was able to keep up with the leakage until a larger ligament rupture event occurred at a higher pressure. The other two specimens experienced abrupt large leaks at the pressures noted in Table 4.6.

Calculations for equivalent crack length and depth are given in Table 4.7. The yield and ultimate tensile strengths of the material are 296 and 676 MPa (43 and 98 ksi), respectively. In all cases, the ligament rupture pressure is overestimated by the equivalent rectangular crack method. Ligament rupture pressure for Test T-29 is actually slightly lower than that for a 90% TW rectangular crack (10.6 MPa or 1.54 ksi). The variation of m_p with crack length for the two types of specimens is shown in Fig. 4.88. The effective m_p, which is defined by the maximum value of m_p, has a rather broad maximum. Note that the equivalent crack lengths are overestimated and the effective m_p' values are underestimated for the specimens without a drilled hole at the center. In contrast, both are predicted reasonably well for Specimen T-31, which had a drilled hole at the center. Although the number of tests is too limited to conclude anything definitively, the sharp discontinuity of the EDM notch at the center may play a role in these tests. Drilling a small hole at the center of the notch in T-31 may effectively reduce the stress concentration effect of the discontinuity.

Table 4.6. Summary of test results on specimens with trapezoidal notches.

Spec. No.	Initial Leak Pressure, MPa (ksi)	Leak Rate, L/min (gpm)	Final Test Condition		
			Pressure, MPa (ksi)	Leak Rate, L/min (gpm)	Crack Length, mm (in.)
T-29	8.79 (1.276)	small	9.58 (1.390)	>47.3 (>12.5)	21.2 (0.836)
T-30	18.30 (2.654)	>47.3 (>12.5)	18.30 (2.654)	>47.3 (>12.5)	13.7 (0.540)
T-31	21.76 (3.156)	>47.3 (>12.5)	21.76 (3.156)	>47.3 (>12.5)	18.3 (0.720)

Table 4.7. Summary of equivalent notch geometry and predicted ligament rupture pressure.

Spec. No.	Equiv. Notch Length, mm (in.)	Equiv. Notch Depth, % TW	Eff. m_p	Predicted Ligament Rupture Pressure, MPA (ksi)
T-29	25.4 (1.0)	87.0	4.86	13.3 (1.93)
T-30	17.3 (0.68)	76.4	2.59	25.0 (3.63)
T-31	17.3 (0.68)	76.4	2.59	25.0 (3.63)

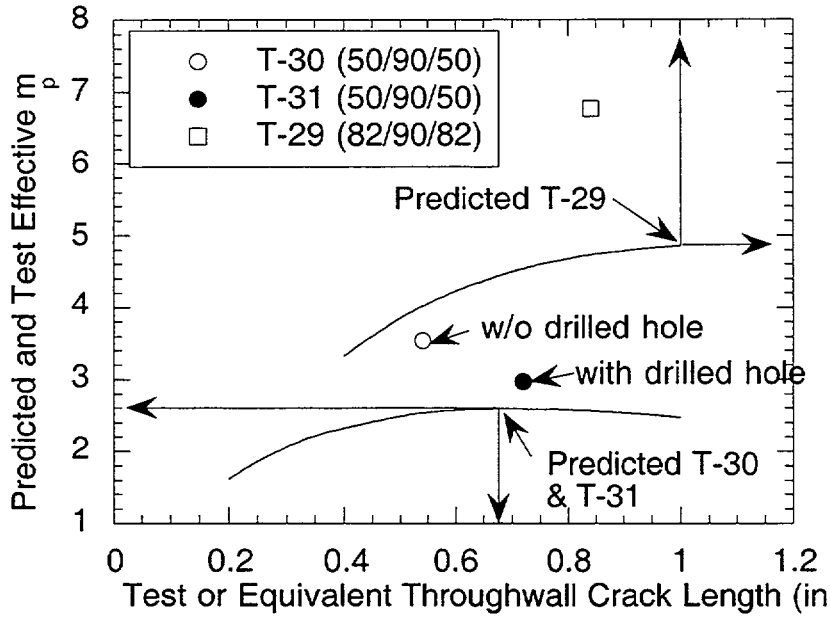

Fig. 4.88. Comparison of predicted vs. observed effective m_p for tests with trapezoidal notches.

References

1. D. R. Diercks, S. Bakhtiari, K. E. Kasza, D. S. Kupperman. S. Majumdar, J. Y. Park, and W. J. Shack, *Steam Generator Tube Integrity Program, Semiannual Report, October 1998-March 1999*, NUREG/CR-6511, Vol. 7.

2. S. Majumdar, W. J. Shack, D.R. Diercks, K. Mruk, J. Franklin, and L. Knoblich, *Failure Behavior of Internally Pressurized Flawed and Unflawed Steam Generator Tubing at High Temperatures—Experiments and Comparison with Model Predictions*, NUREG/CR–6575, ANL–97/17, Argonne, IL, 1998.

3. V. Kumar, M. D. German, and C. F. Shih, *An Engineering Approach for Elastic-Plastic fracture Analysis*, EPRI NP-1931, Electric Power Research Institute, 1981.

4. J. L. Rempe, S. A. Chavez, G. L. Thinnes, C. M. Allison, G. E. Korth, R. J. Witt, J. J. Sienicki, S. K. Wang, L. A. Stickler, C. H. Heath, and S. D. Snow, *Light Water Reactor Lower Head Failure Analysis*, NUREG/CR-5642, EGG-2618, Idaho National Engineering Laboratory, Idaho Falls, ID, Oct. 1993.

5. SGTR Severe Accident Working Group, *Risk Assessment of Severe Accident-Induced Steam Generator Tube Rupture*, NUREG-1570, U.S. Nuclear Regulatory Commission, Washington DC, 1998.

6. J. M. Alzheimer, R. A. Clark, C. J. Morris, and M. Vagins, *Steam Generator Tube Integrity Program Phase I Report*, NUREG/CR–0718, PNL-2937, Richland, WA, Sept., 1979.

7. D. R. Diercks, S. Bakhtiari, K. E. Kasza, D. S. Kupperman. S. Majumdar, J. Y. Park, and W. J. Shack, *Steam Generator Tube Integrity Program, Semiannual Report, October 1997-March 1998*, NUREG/CR-6511, Vol. 5 (April 1999).

NRC FORM 335 (2-89) NRCM 1102, 3201, 3202

U.S. NUCLEAR REGULATORY COMMISSION

BIBLIOGRAPHIC DATA SHEET

(See instructions on the reverse)

1. REPORT NUMBER (Assigned by NRC, Add Vol., Supp., Rev., and Addendum Numbers, if any.)

NUREG/CR-6511, Vol. 9

2. TITLE AND SUBTITLE

Steam Generator Tube Integrity Program, Semiannual Report,October 1999-March 20 00

3. DATE REPORT PUBLISHED

MONTH	YEAR
June	2002

4. FIN OR GRANT NUMBER

W6487

5. AUTHOR(S)

D. R. Diercks, S. Bakhtiari, K. E. Kasza, D. S. Kupperman, S. Majumdar, J. Y. P ark, W. J. Shack

6. TYPE OF REPORT

Technical

7. PERIOD COVERED *(Inclusive Dates)*

Oct, 99-Mar 00

8. PERFORMING ORGANIZATION - NAME AND ADDRESS *(If NRC, provide Division, Office or Region, U.S. Nuclear Regulatory Commission, and mailing address; if contractor, provide name and mailing address.)*

Argonne National Laboratory
9700 South Cass Avenue
Argonne, IL 60439

9. SPONSORING ORGANIZATION - NAME AND ADDRESS *(If NRC, type "Same as above"; if contractor, provide NRC Division, Office or Region, U.S. Nuclear Regulatory Commission, and mailing address.)*

Division of Engineering Technology
Office of Nuclear Regulatory Research
U.S. Nuclear Regulatory Commission
Washington, DC. 20555-0001

10. SUPPLEMENTARY NOTES

Joseph Muscara, NRC Project Manager

11. ABSTRACT *(200 words or less)*

This report summarizes work performed by Argonne National Laboratory on the Ste am Generator Tube Integrity Program for the period October 1999 through March 2000. The program is divided into five t asks: (1) Assessment of Inspection Reliability, (2) Research on ISI Technology, (3) Research on Degradation Modes and Integrity , (4) Development of Methodology and Technical Requirements for Current and Emerging Regulatory Issues, and (5) Prog ram Management. Under Task 1, progress is reported on the round-robin analysis of the steam generator tube mockup, in which a total of seven teams have participated to date. The format for the tables necessary to carry out the statistical anal ysis of the round-robin data has also been established. Activities under Task 2 were concerned primarily with multiparame ter analysis of eddy current NDE results. Calculations were performed on the applicability of pseudoinverse filters for i mproving the spatial resolution of rotating probes, analytical procedures for the elimination of unwanted signals were explored, th e conversion of data analysis results into calibrated profiles for more direct deduction of estimated flaw size and extent was examined, and inspection data obtained from laboratory-degraded tubes were analyzed. Under Task 3, the production and characterization of laboratory-degraded tubes continued. Further testing of tubes with electro-discharged machined and laser cut notches, as well as laboratory-degraded tubes, was carried out in the High-Pressure Test Facility, and an exploratory test was conducted to evaluate the potential for erosion resulting from a jet of water from a leaking tube impinging on an adjacent tube. Finally, a model was developed to calculate crack-opening area as a function of time for a xial cracks under severe-accident conditions, and the ligament-rupture behavior observed in laboratory tests on tubes with ED M and laser-cut notches was modeled.

12. KEY WORDS/DESCRIPTORS *(List words or phrases that will assist researchers in locating the report.)*

Steam generator tubing, steam generator, inservice inspection, NDE, stress corr osion cracking

13. AVAILABILITY STATEMENT

unlimited

14. SECURITY CLASSIFICATION

(This Page) unclassified

(This Report) unclassified

15. NUMBER OF PAGES

16. PRICE

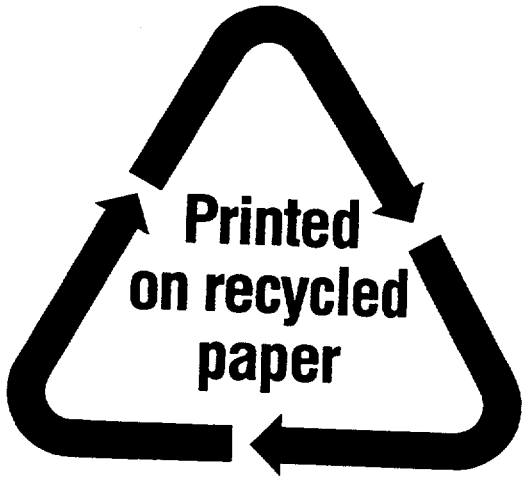

Federal Recycling Program

UNITED STATES
NUCLEAR REGULATORY COMMISSION
WASHINGTON, DC 20555-0001
